A patient-specific stem cell model of neurovascular interaction for vascular dementia CADASIL

A thesis submitted to the University of Manchester for the degree of

Doctor of Philosophy (PhD)

In the Faculty of Biology, Medicine and Health

Wenjun Zhang

2020

School of Biological Sciences

Contents

Word count: 55,115

List of Figures

List of Tables

List of abbreviations

Acronym	Full name
ABC	ATP-binding cassette
Aβ	amyloid-β
AD	Alzheimer's disease
ADM	Astrocyte Differentiation Medium
AJs	Adherens junctions
ALS	Amyotrophic lateral sclerosis
AMM	Astrocyte Maturation Medium
APCs	astrocytes progenitor cells
APP	amyloid precursor protein
AQP4	Aquaporin 4
ASL-fMRI	Arterial spin labelling-functional Magnetic resonance imaging
Aza-C	Azacytidine
BBB	Blood-brain barrier
BMECs	Brain Microvascular endothelial cells
BMP4	bone morphogenetic protein 4
CAA	Cerebral amyloid angiopathy
CADASIL	Cerebral Autosomal Dominant Arteriopathy with Subcortical Infarcts and Leukoencephalopathy
CARASIL	Cerebral Autosomal Recessive Arteriopathy with Subcortical Infarcts and Leukoencephalopathy
CBF	Central blood flow
C/F/W	collagen IV/ fibronectin /water
CNN	Calponin1
CNS	Central nervous system
Cx	Connexin
DAG1	Dystroclycan
DMD	Dystrophin
DMEM	Dulbecco's Modified Eagle Medium
DMSO	dimethyl sulfoxide
DSL	Delta-like serrate LAG2 domain
EBs	embryoid bodies
ECM	Extracellular Matrix
ECs	Endothelial cells
EGF	Epidermal growth factor
ER	Endoplasmic reticulum
ESCs	Embryonic stem cells
ETA	Efflux transporter activity
fAD	familial AD
FBS	Foetal Bovine Serum
FD	Fabry disease

FTD	frontotemporal lobar dementia
GBA	glucosidase beta acid
GFAP	Glial fibrillary acidic protein
GJs	Gap junctions
GLAST	glutamate-aspartate transporter
GLT-1	Glutamate transporter 1
GOM	Granular osmisophilic Material
GWAS	Genome-wide association studies
HCAECs	Human coronary arterial endothelial cells
HD	Huntington's disease
HDFs	Human dermal fibroblasts
HEK	Human embryonic kidney
hESC	Human embryonic stem cell
hESFM	Human Endothelial serum free medium
HS	Human Platelet Poor Plasma-derived Serum
HTRA1	HtrA serine peptidase/protease 1
HUVECs	Human umbilical vein endothelial cells
ICH	Intracerebral hemorrhage
iPSCs	Induced pluripotent stem cells
JAMs	Junctional adhesion Molecules
KOSR	KnockOut Serum Replacement
LDL	Low-density lipoprotein
LRRK2	leucine-rich repeat kinase 2
MID	Multi-infarct dementia
MSCs	Mesenchymal stem cells
NaF	sodium fluorescence
N3ECD	NOTCH3 extracellular domain
NC	Neural crest
NCSCs	neural crest stem cells
NE	Neural ectodermal
NEAA	Non-essential amino acids
NECD	NOTCH extracellular domain
NESs	Neuroectodermal spheres
NG2	Neuron-glial antigen 2
NICD	NOTCH intracellular domain
NIM	Neural induction Medium
NINDS	National Institute of Neurological Disease and Stroke
NMM	Neural Maintenance Medium
NO	nitric oxide
NPC	Neural progenitor cell
NSCs	Neural stem cells
NVU	Neurovascular Unit
OST	Oligosaccharyltransferase

PARK2	parkin RBR E3 ubiquitin protein ligase
PBS	Phosphate Buffered Saline
PD	Parkinson's disease
PDGF	Platelet derived growth factor
Pe	permeability of fluorescein
PFA	Paraformaldehyde
PGE	prostaglandins
p-gp	p-glycoprotein
PINK1	PTEN-induced putative kinase 1
PNS	Peripheral nervous system
PSEN1	presenilin 1
qRT-PCR	Quantitative real time polymerase chain reaction
RA	Retinoic acid
rBMP4	Bone Morphogenetic Protein 4
ROS	Reactive oxygen species
RVCL	Retinal vasculopathy with cerebral leukodystrophy
sAD	sporadic AD
S100β	S100 calcium-binding protein β
SEM	Standard error
SMTN	smoothelin
SNCA	synuclein alpha
SNP	Single nucleotide polymorphism
SP	Signal peptide
SVD	Small vessel disease
TEER	Trans-endothelial electrical resistance
TGF-β	Transforming Growth Factor-β
TH	thyroid hormone
TJs	Tight junctions
TREX1	Three Prime Repair Exonuclease 1
TSA	Trichostatin A
UM	Unconditioned Medium
VaD	Vascular dementia
vECs	Vascular endothelial cells
VEGF	vascular Endothelial growth factor
VIM	vimentin
vMCs	vascular Mural cells
vSMCs	vascular Smooth Muscle cells
VTN-N	Vitronectin Recombinant Human Protein
WMH	White Matter lesion
α-SMA	alpha-Smooth Muscle actin

Abstract

Cerebral Autosomal Dominant Arteriopathy with Subcortical Infarcts and Leukoencephalopathy (CADASIL), as the most common hereditary stroke syndrome caused by NOTCH3 mutation, represents a valuable model to explore the pathogenesis of vascular dementia (VaD) and genetic small vessel diseases (SVDs). To date, several cell and animal models have been developed for CADASIL, but none of them could effectively recapitulate the brain phenotype of this condition. Induced pluripotent stem cells (iPSCs) provide the opportunity to model CADASIL from patients with the ability to retain the genetic background of the patient especially the NOTCH3 mutation. Currently three studies established iPSC-derived CADASIL models have focussed on vascular mural cells (vMCs) and vascular endothelial cells (vECs). Investigations suggest defect may exist in the neurovascular interactions in CADASIL, which rely on the communications between the neurovascular unit (NVU) cells including vMCs, brain microvascular endothelial cells (BMECs), astrocytes and neurons. However, previous models have never stressed this condition and the underlying mechanisms.

This thesis demonstrates the development of an *in vitro* iPSCs model of CADASIL using NVU cell types differentiated from three control and two CADASIL (Arg153Cys and Cys224Tyr) iPSC lines. The data in this thesis shows that vMCs, BMECs, astrocytes and neurons can be generated from iPSCs and these NVU cells can mimic blood brain barrier (BBB) in CADASIL when co-culturing on the Transwell settings. Using the trans-endothelial electrical resistance (TEER) measurement assay, we demonstrated that the BMECs barrier function was obviously promoted by co-culturing with vMCs, astrocytes or neurons. This *in vitro* BBB model revealed barrier function defect in CADASIL BMECs that could not be restored by co-culturing with other NVU cells. Moreover, it was observed in the Transwell co-culturing system that CADASIL vMCs failed to support BMECs barrier function.

Altogether the data presented in this thesis has shown BMECs defect and vMCs dysfunction in CADASIL BBB. Understanding the molecular mechanisms of this condition is vital in identification of therapeutic targets and developing future treatments. The established iPSC-BBB model for CADASIL represents a valuable platform that could be further applied to understand neurovascular interactions in CADASIL pathology as well as other genetic SVDs.

Declaration Statement

No portion of the work referred to in the thesis has been submitted in support of an application for another degree or qualification of this or any other university or other institute of learning.

Copyright Statement

Acknowledgements

I would like to express my deepest gratitude to my supervisor Prof. Tao Wang for providing me this opportunity to conduct this great project in her group under her excellent supervision. Her consistent support, guidance, encouragement and insights in this field have made this an inspiring experience for me.

I would also like to thank my co supervisor Prof. Nigel Hooper for providing me the opportunity to work in the stem cell lab and valuable guidance throughout my PhD. Without his support the stem cell work would not have been going forward smoothly.

I would especially like to thank Dr. Adam Mitchell for his devotion to my thesis writing and revision, as well for all his support to my project. And it's my pleasure to work with all the group members in the Tao Lab from past to the present. Thanks Jerry Zheng for assisting me with qRT-PCR and data analysis. Thanks for the support from Dr. Jianzhen Ren, Dr. Joseph Kelleher and Victor Yan Zhi Lin Hu. Thank you Luis Larrea, Xiangjun Zhao, Nadim Luka, Xuting Ye, Chaowen Yu, Katie Newman and Amerikos Argyriou. I will miss the Domino's meatball pizza we shared during evening lab work.

I would also really like to thank Hooper Lab members. Great thanks for Dr. Kate Kellett for her efforts especially on the astrocytes differentiation. Thanks Alys Jones for guiding me entered into the wonderful world of neurons differentiation in the lab. Thank you Nicola Corbett, Helen A Rowland, Kate Fisher, Laura Castro-Aldrete, Sam Moxon, Geoff Potjewyd, Nishtha Chandra and Monica Seif, for your support and accompany in the stem cell lab.

I would like to thank for China Scholarship Council and the University of Manchester joint scholarship (CSC-UOM) for the funding opportunity to support my PhD life in UK.

I would also like to thank my dearest friends Yaqing Ou, Yang Qin and Yang Xiao for their generous help during my thesis writing and during COVID-19 lockdown. Thank you my friends Jingshu Liu, Fuhui Chen and Junzhe Zha. I will never forget the wonderful times we shared.

My last gratitude goes to my parents, and my sister, for your tremendous support and encouragement during the last four years. Thank you for your love throughout my life. Thank you for giving me the strength to chase my dreams.

1. Chapter 1: General introduction

1.1. Vascular dementia

Dementia describes a syndrome of neurodegeneration recognised by patterns of decline in memory and thinking impairment [1]. The World Health Organization estimates that 35.6 million people suffer from dementia [2]. Symptoms vary among people with different dementias. Depression syndromes are most commonly followed by anxiety neurosis and paranoid psychosis. Ageing is the largest risk factor for dementia. Studies suggest several factors are responsible for dementia, such as hypertension, type 2 diabetes and obesity [3, 4]. Dementia can be roughly divided into many subtypes with the most common ones being Alzheimer's disease (AD), vascular dementia (VaD) and mixed-type dementia. Other conditions such as Parkinson's disease (PD), Huntington's disease (HD) and Creutzfeldt-Jacob disease can also result in dementia at late stages. Mixed-type dementia refers to dementia displaying symptoms and brain abnormalities associated with more than one type of dementia [5]. For example, it was reported about half of people with AD also had brain defects of other dementias, most commonly VaD [6, 7]. Dementia incidence has been increasing especially in less developed regions of the world [8]. However, currently no known effective curative or preventive measure has been discovered for any type of dementia. Therefore, there is great importance for better understanding of the disease and the development of effective therapies.

VaD is recognised as the second most prevalent type of dementia. In Europe AD is the leading cause of progressive dementia and VaD is the second leading cause, whilst in Asia, VaD may be as common as AD [9]. VaD is responsible for nearly 20% of all cases of dementia [10]. Currently the incidence of VaD around the world is rising, however, the underlying pathogenesis has not been fully understood, therefore, no effective treatment is available [11]. The risk factors of VaD include vascular factors that can be treated, such as heart disease (including coronary artery disease, myocardial infarction and heart failure), hypertension, diabetes and atrial fibrillation. Risk factors that cannot be effectively treated are primarily genetic factors [12, 13]. In recent years, polymorphisms were found in the *APOE* gene family, of which *APOE4* can increase the level of total cholesterol and low-density lipoprotein of plasma, so as to accelerate the formation of atherosclerosis, thus contributing to VaD incidence [14, 15]

Owing to the various pathological mechanisms causing VaD, the classification of VaD is complicated. Currently, VaD can be divided into the following categories depending on pathological changes. Multi-infarct dementia (MID) is the main type of VaD caused by the bilateral multiple brain infarction. Single cerebral infarcts dementia is caused by cerebral artery occlusion. Small vessel dementia includes but not limited to multiple lacunar infarction, Binswanger disease, cerebral amyloid angiopathy (CAA) and Cerebral Autosomal Dominant Arteriopathy with Subcortical Infarcts and Leukoencephalopathy (CADASIL). Low perfusion dementia often leads to watershed cerebral infarction caused by acute cerebral hemodynamic change [16].

1.2. Cerebral small vessel disease

The term cerebral small vessel disease (SVD) refers to a range of pathological processes with various aetiologies that impact the small arteries, arterioles, venules, and capillaries of the brain with the neuroimaging features ranging from little to focal neurological symptoms including stroke, finally leading to neurological dysfunction and dementia. SVD account for about a fifth of all strokes and contributes to ~ 45% of all dementias [17, 18]. The main clinical features of SVD include stroke, cognitive decline, dementia, psychiatric disorders, abnormal gait, and urinary incontinence [19, 20]. SVD plays an important role in cerebrovascular disease and is one of the leading causes of cognitive decline and functional loss in old people. Currently, there are no specific preventive or therapeutic measures to improve this condition. SVD should be a main target for preventive and treatment strategies, but all types of presentation and complications should be taken into account [19, 20].

1.2.1. Sporadic SVD

Majority of SVDs are sporadic intrinsic processes affecting small cerebral arterioles, capillaries and sometimes venules [20]. Sporadic SVD contributes considerably to stroke, cognitive impairment, dementia, and other disabilities seen in the elderly including depression, motor and gait disturbances, urinary symptoms, and functional impairment[21]. Two pathologic changes that are most common involved in sporadic SVD are arteriolosclerosis and cerebral small vascular atherosclerosis [19]. Arteriolosclerosis is an age-related SVD associated with vascular risk factors and is the most common small vessel alteration in aged brains [19]. The severity of arteriolosclerosis increases with aging and is aggravated by hypertension and diabetes [22]. The other one, cerebral small vascular atherosclerosis is characterised by a loss of vascular smooth muscle cells (vSMCs) from the

tunica media, degeneration of internal elastic lamina, deposits of collagens, thickening of the vessel wall and narrowing of the lumen and others, all of which leading to the vessels becoming elongated and inflexible [20]. By far, the underlying molecular mechanisms of sporadic SVD have not been clearly uncovered.

1.2.2. Genetics of SVD

Genome-wide association studies (GWAS), a relatively new technique, have shed light on the identification of genetic variants that are associated with SVD or potential disease mechanisms that involving the white matter and several important genetic loci in relation to SVD [23]. For example, a nonsynonymous SNP (single-nucleotide polymorphism) in PRKCH (protein kinase C eta) was found to increases the risk of cerebral lacunar infarction [24]. A meta-analysis of GWAS involving 9,361 stroke-free individuals identified 6 novel SNPs on chromosome 17 could increase the white matter lesion (WMH) burden, including *WBP2, TRIM65, TRIM47, MRPL38, FBF1*, and *ACOX1* [25]. Woo et al. identified chromosome 1q22 as a susceptibility locus for intracerebral hemorrhage (ICH), a region that contains genes *PMF1* and *SLC25A44* [26]. In addition, several single gene disorders leading to SVD have been discovered, including CADASIL, cerebral autosomal recessive arteriopathy with subcortical infarcts and leukoencephalopathy (CARASIL), collagen IV-associated (*COL4A*) SVD, autosomal dominant retinal vasculopathy with cerebral leukodystrophy (RVCL), and Fabry disease. All these findings could play a crucial role in our understanding of SVD pathogenesis and their causes.

1.2.3. Common genetic of SVD

The most common single gene SVD is CADASIL, a late onset condition of the cerebral small blood vessels caused by mutations in the *NOTCH3* gene on chromosome 19q12 [27]. The main clinical features of CADASIL include recurrent ischemic stroke, migraine with aura, mood disturbances, psychiatric symptoms, progressive cognitive decline and VaD [28]. Migraine as the most common primary symptom usually begins around age 20 years and will develop in most patients by age 40 [29].

CARASIL is a recessive hereditary single gene disorder of SVD, which is characterised by mood disturbances, recurrent ischemic stroke, early-onset lacunar stroke, cognitive deficit, gait disturbance and systemic symptoms including alopecia and low back pain Lacunar stroke [30]. CARASIL is caused by mutations in the *HTRA1* gene encoding HtrA serine peptidase/protease 1 (HTRA1) [31]. Mutations in the *HTRA1* gene have been identified can

result in decreased level of protease activity leading to an increase in Transforming Growth Factor-β (TGF-β) signaling, thus leading to degeneration of vSMCs, as TGF-β plays vital role in the differentiation of vSMCs [23].

Other less commonly seen SVDs includes *COL4A*-related cerebral SVD, RVCL and Fabry disease. Mutations in genes encoding type IV collagen α chain 1 and 2 (COL4A1 and COL4A2) were associated with porencephaly and infantile hemiparesis and will later lead to SVD. These mutations can affect multi organs as collagen IV is a basement membrane protein widespread in the body [32]. RVCL is caused by heterozygous, frame-shift mutations in the C-terminus of *TREX1* encoding three Prime Repair Exonuclease 1 (TREX1), which is a DNA-specific exonuclease DNase III in the and also involved in the regulation of N-linked protein glycosylation via C-terminal interactions with the oligosaccharyltransferase (OST) complex [33]. The clinical features of this disease include dementia, progressive visual loss, psychiatric symptoms, migraine, and renal dysfunction [34]. Fabry disease (FD) is caused by mutations in *GLA* gene encodes lysosomal α-galactosidase A on chromosome Xq22. The symptoms of FD include chronic pain, hearing loss, kidney damage, gastrointestinal problems, heart damage and dementia [23].

1.3. CADASIL

Many families with early-onset VaD of the SVD type have been reported in the form of CADASIL. CADASIL is the most common form of hereditary stroke and VaD caused by mutations in the *NOTCH3* gene on chromosome19, typical clinical manifestations of CADASIL are recurrent ischemic strokes that lead to cognitive decline, eventually progressing to dementia. The disease has a young to middle-aged onset with an average age of onset about 45 years old. The mean death age of CADASIL patients is around 65 [35]. The presence of granular osmisophilic material (GOM) deposits and NOTCH3 accumulation in the vSMCs can be seen under electron microscopy. Although peripheral tissue biopsies for evidence of protein accumulations are a valuable diagnostic method, diagnosis of CADASIL relies on the identifications of *NOTCH3* mutations by DNA sequencing [36].

1.3.1. CADASAIL pathology and molecular mechanisms

The pathogenesis of CADASIL remains obscure. Current research endeavours have revealed an accumulation of NOTCH3 extracellular domain in the small arterial walls of CADASIL patients, the degeneration of arterial SMCs, and the deposition of GOM at basal membrane could be responsible for CADASIL pathology. Dominant mutations in *NOTCH3* were found

in CADASIL. Mutations of NOTCH3 lead to abnormalities in the number of cysteine residues, causing disulfide bridge disruption and receptor misfolding [37]. NOTCH3 is expressed mainly in vascular mural cells (vMCs) including pericytes and vSMCs of the small arteries of the brain [38]. Normal *NOTCH3* gene encodes a 2,321-amino acid single pass transmembrane receptor that is expressed in pericytes of brain capillaries and vSMCs of small arteries. Pathogenic mutations alter the number of cysteine residues in the extracellular domain of NOTCH3, resulting in its abnormal accumulation in the small arteries of patients. The accumulation of the mutated NOTCH3 around vSMC appears to be a key pathological mechanism for CADASIL, by binding to components of the extracellular matrix (ECM), which results in their aggregation near vSMC [39]. Cerebral arteries are consistently narrowed by thickening and expansion of the ECM in CADASIL patients, accompanied by disruption and degeneration of vSMCs in vessel wall and the deposition of the GOM [40].

CADASIL patients may also demonstrate reduced clearance of NOTCH3 extracellular domain (N3ECD) from the plasma membrane of vMCs, mutant protein aggregates that cause endoplasmic reticulum (ER) stress with formation of reactive oxygen species (ROS), that affect cell growth and proliferation and prevent impaired cell replacement, which results in the accumulation of N3ECD within the tunica media of arterioles [41, 42]. In mutant *NOTCH3* cell lines it was shown that these cells are also more sensitive to stress inducers such as hypoxia, oxidative stress and glucose deprivation, which may induce proteasome dysfunction, activation of apoptotic pathways and cell death [42].

1.4. NOTCH signalling

1.4.1. NOTCH receptor family

The NOTCH receptors are evolutionarily highly conserved transmembrane proteins. A typical NOTCH gene encodes a single transmembrane receptor in its extracellular region of up to 36-epidermal growth factor (EGF)-like repeats and three juxtamembrane repeats known as Lin-12-Notch (LN) repeats (**Figure 1.1 A**) [43]. Some of the EGF-like repeats mediate interactions with ligands while LN repeats modulate interactions between the extracellular and the membrane-tethered intracellular domains [44, 45]. Additionally, many EGF repeats bind calcium, which plays an vital role in determining the structure of NOTCH to its ligands [46]. Humans have four NOTCH receptors (NOTCH1-NOTCH4) and five different NOTCH ligands (JAGGED1, JAGGED2, DLL1, DLL3 and DLL4), which are also transmembrane proteins (**Figure 1.1 B**). All NOTCH receptors contain a NOTCH extracellular domain

(NECD) and NOTCH intracellular domain (NICD) [47]. The NECD contains the EGF-like repeats that participate in ligand binding to other NOTCH receptors and lin-12 repeats that prevent ligand-independent activation of NOTCH receptors [48]. The NICD localises to the nucleus, regulating gene expression in association with the DNA-binding protein CSL [49-51].

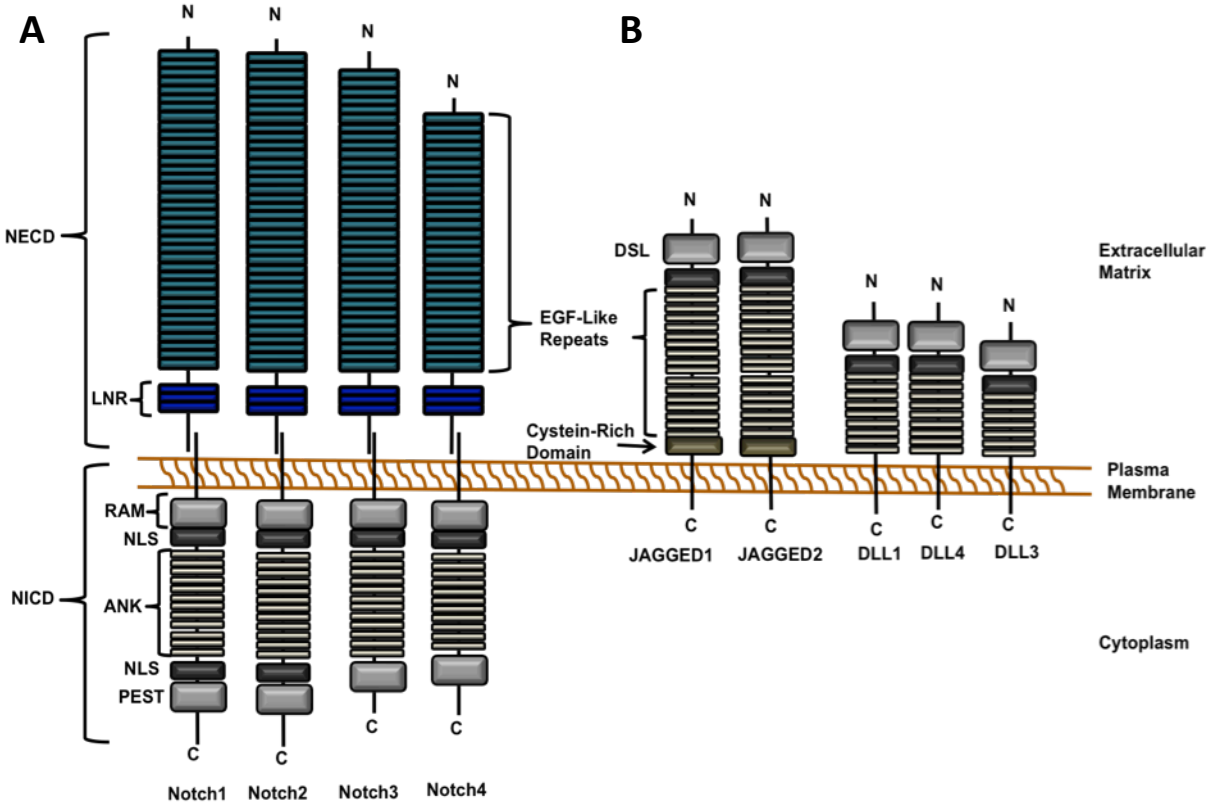

Figure 1.1 Structure of NOTCH receptor family and its ligands

(A). Structure of four human NOTCH receptors contains 7 domains that are conserved across all NOTCH receptors. The EGF-like repeats on the NECD vary between NOTCH receptors with 36 repeats in NOTCH1 and NOTCH2, 34 repeats in NOTCH3 and 29 repeats in NOTCH4. (**B).** There are five NOTCH ligands within two families, the JAGGED and the DLL family. The ligands structure consists of a signal peptide (SP) delta-like serrate LAG2 domain (DSL).

Abbreviations: LNR, cysteine-rich Lin12/NOTCH repeats; NLS, nuclear localization sequence; DSL, Delta/Serrate/LAG-2; DLL, delta-like. Adapted from (Steinbuck and Winandy, 2018, A Review of Notch Processing With New Insights Into Ligand-Independent Notch Signalling in T-Cells).

1.4.2. NOTCH signalling pathway

The NOTCH signalling pathway is highly evolutionarily conserved which functions as a mediator of cell-cell communication and is critical for cell fate determination during embryonic development [52]. The NOTCH signalling pathway involves a complex process of proteolytic cleavage events leading to transcriptional activation of target genes. Current evidence suggests that NOTCH3 first undergoes constitutive cleavage at S1 by a furin-like convertase to form a functional heterodimeric receptor. Receptor ligands include JAGGED1, JAGGED2 and Delta-like1, 3, 4 (DLL1, 3 and 4). Upon the NECD interacts with a ligand, ADAM10, which is an ADAM-family metalloprotease, NOTCH receptor is cleaved at the S2 site [53]. The S2 site cleavage releases the NECD, which continues to interact with the ligand. After the S2 site cleavage, γ-secretase cleaves the receptor at the S3 site where NICD is released from the plasma membrane [47]. In summary, the interaction between the NOTCH receptors and ligands results in a second and third cleavage of the receptors at S2 and S3 sites, which results in the generation of an NICD. The NICD translocates to the nucleus, where it interacts with CBF1/RBP-Jk to activate transcription of target genes *HES* and *HESR* (or *HRT*) [54] (**Figure 1.2**).

CADASIL is caused by mutations in *NOTCH3* while the underlying mechanisms of how those mutations impact the NOTCH signalling pathway is not fully uncovered. NOTCH3 shares the canonical NOTCH signalling pathway with other members of the family, however, majority of *NOTCH3* mutations in CADASIL do not alter the activity of the canonical NOTCH signalling [55]. In CADASIL patients, an accumulation of N3ECD protein was observed in the perivascular region. Evidence indicates that EC dysfunction may also result in N3ECD accumulation within perivascular spaces [56]. Thus, it is of great importance to consider how NOTCH signalling impacts cell behaviour affected by *NOTCH3* mutation in CADASIL.

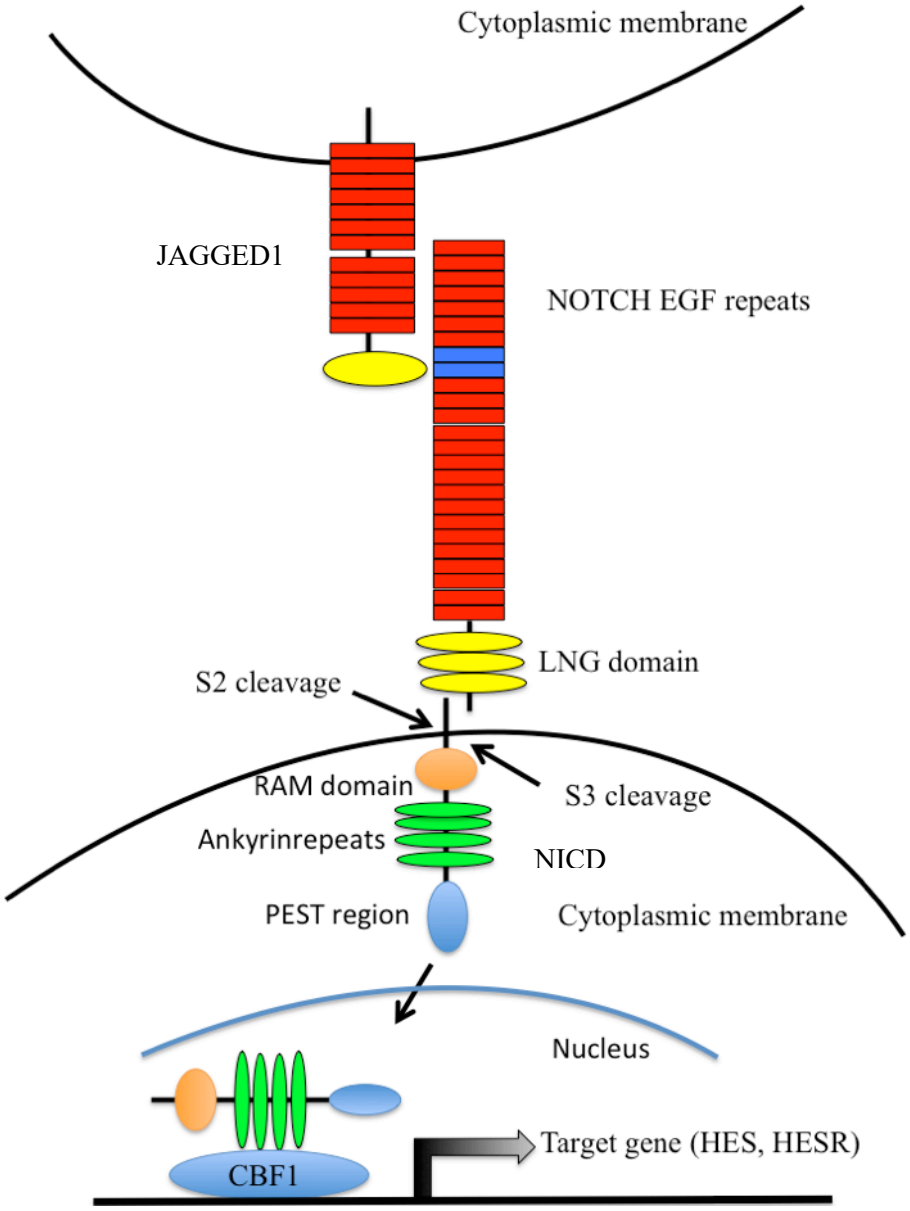

Figure 1.2 The NOTCH signalling pathway.

NOTCH firstly undergoes constitutive cleavage at S1 by a furin-like convertase to form a functional heterodimeric receptor. JAGGED1 is a NOTCH3 ligand that locates on adjacent cells such as ECs or vSMCs. The ligand binding of NOTCH3 results in the ADAM family of transmembrane proteases (S2) and proteolytic cleavage of the receptor by γ-secretase (S3). This cleavage releases the NICD inside the cell where it translocates to the nucleus together with transcription factors, where it interacts with CBF1/R/RBP-Jk to activate transcription of target genes HES and HESR (or HRT). NECD is still bound to the ligand and endocytosed into the ligand-expressing cell for degradation. Adapted from (Wang, 2008, An overview of Notch3 function in vascular smooth muscle cells).

1.4.3. NOTCH signalling in vascular development

Previous studies has made it clear that the NOTCH signalling pathway plays an important role in vascular development and maintenance, including EC and vSMC functions [57]. The proper functioning of the vascular system, composed of a complex network of arteries, veins, and capillaries, involves precise coordination of cells especially ECs and vSMCs. EC precursors differentiate and aggregate into a primary vascular network in the early stage of development and then expand into a highly branched vascular system [58]. In the arteries and veins, mature vSMCs play a crucial role in the regulation of vessel functions, such as, blood pressure and blood flow [59].

The NOTCH signalling pathway plays a role in regulating vascular development and was initially demonstrated in *Notch* mutant mouse models [60]. *Notch1* and *Notch4* knock out mouse models demonstrated a role for Notch signalling in embryonic vascular development while *Notch3* knock out did not influence embryonic development in mice [60-62]. However, further investigation into *Notch3* knout out mice found that *Notch3* is required to generate functional arteries by regulating differentiation and maturation of vSMCs [63]. In a 3-dimensional model of angiogenesis, it was discovered that NOTCH3 expression in vMCs is robustly induced by co-culture with vascular endothelial cells (vECs). The authors demonstrated NOTCH3 contributes to the angiogenic abilities of vMCs co-cultured with vECs and that upregulation of NOTCH3 is dependent on cell-cell contact between vMCs and vECs. VECs expressing JAGGED1 bound to NOTCH1 expressed on vSMCs, promoted the upregulation of NOTCH3 within the vMCs. JAGGED1 can also promote arterial vSMC gene expression and the upregulation of *JAGGED1* in vMCs [64].

The Notch signalling pathway is vital in promoting angiogenic tubule structure formation [65]. The NOTCH pathway plays a role in regulating early embryonic vascular development and is intertwined with vascular endothelial growth factor A (VEGFA), which is a glycoprotein that can induce angiogenesis and also regulates blood vessel homeostasis [66, 67]. VEGFA is a ligand for the VEGFR2 and VEGFR1, binding to VEGFR2 stimulates angiogenesis in ECs whilst binding of VEGFR1 prevents angiogenesis [68, 69]. VEGFA binding initiates a signalling cascade, which activates PI3K/AKT, protein kinase C and PKC/ERK and NFkB signalling pathways. VEGFR2 signalling can also facilitate the expression of Notch receptors including NOTCH1 and ligands DLL4 and Jagged1 [70]. Studies on the formation of vessels in the zebrafish embryo revealed that reduction of Vegf

activity resulted in loss of expression of arterial markers from the dorsal aorta and ectopic arterial expression of vein markers [71].

1.4.4. NOTCH signalling in other brain cell types

Apart from vascular cell types including vMCs and vECs, NOTCH signalling has been reported to be important in other brain cell types. Several studies have provided important evidence about the roles of NOTCH signalling in neural development. Early findings on Notch signalling in central nervous system (CNS) development were performed mainly in D. melanogaster [72]. A report in 1937 indicated that Notch mutations can lead to the failure of neural cell segregation in early Drosophila embryos [73]. Later, Notch signalling was found to be critical for neural progenitor cell (NPC) maintenance and self-renewal based on mutation and knockout models of *Drosophila melanogaster* embryos [74]. In the CNS, neurons and glial cells are generated from the neuroepithelium. Notch signalling plays a role in neuronal progenitor maintenance, neuronal and glial lineage fate decision and the behaviour of differentiated neurons, as well as contributing to aspects of brain morphogenesis and might even affect neuronal migration [75].

Embryonic stem cell-derived neurosphere models have revealed that Notch1, Presenilins and RBP are key Notch signalling molecules and these Notch pathway molecules are essential for the maintenance of neural stem cells [76]. It was found inactivation of Notch-regulated genes such as Hes1 and Hes5 induced neuronal differentiation during brain development [77]. Most of these studies investigated the NSCs from non-human animals rather than humans, while in recent years the role of Notch signalling has been studied in human embryonic stem cells (hESCs) derived neuroectodermal spheres (NESs). It was found that Notch signalling is required for maintaining stem cell features of neuroprogenitor cells derived from hESCs [78]. Apart from its role in the CNS development, evidence shows that Notch signalling is also involved in neuronal apoptosis, neurite retraction, and neurodegeneration of ischemic stroke in the brain [79]. However, the Notch 3 function on other NVU brain types was rarely been reported.

1.5. CADASIL disease modelling

Cell models for CADASIL

Currently, several *in vitro* cell models for CADASIL have been reported, predominantly using human embryonic kidney (HEK) cells. In 2004, Joutel *et al*. generated 293T cells (a

variant of HEK cells that overexpress the SV40 large T antigen) or NIH3T3 cells (a murine fibroblast cell line) transfected with CADASIL *NOTCH3* mutations distributed in various EGF repeats (Arg90Cys, Cys212Ser, Cys428Ser, Cys542Tyr and Arg1006Cys). It was concluded that mutations in *NOTCH3* affect JAGGED1 binding and NOTCH3 signalling via the RBP/JK pathway [80]. Meanwhile, Peters *et al.* established a CADASIL cell model with three mutations (Arg133Cys, Cys183Arg and Cys455Arg) in cell line NIH3T3 and the vSMCs line A7r5, they found that CADASIL-associated *NOTHC3* mutations have distinct effects both on ligand binding and ligand-induced Notch3 receptor signalling through RBP-Jk [81]. Chuang *et al*. built a CADASIL model based on HEK293 and SH-SY5Y cells expressing wild type or mutant NOTCH3 (Arg90Cys, Arg133Cys, Cys185Arg and Arg449Cys) and found that the arteriopathy in CADASIL is caused by other mechanisms not necessarily involving NOTCH3 processing and activation [82]. These findings collectively indicate that CADASIL mutations could impair downstream NOTCH3 signalling and the impairment varies depending on different mutation site on the chromosome.

More recently, Takahashi *et al*. established a HEK293 cell model containing wild type *NOTCH3* and two CADASIL mutants (Arg133Cys and Cys185Arg). It was revealed that both mutants of NOTCH3 were prone to aggregation and retained in the ER and that the cells exhibited impaired proliferation and increased sensitivity to proteasome inhibition resulting in cell death [83]. Opherk et al. also applied the HEK293 cell line to express multiple various CADASIL mutations and found that mutated NOTCH3 had an increased ability to oligomerize with other NOTCH3 receptors [84].

These findings help understand how NOTCH3 mutations affect cells behaviour. However, as these experiments were carried out in HEK cells, which are dissimilar to the vSMCs that are affected in CADASIL. Future work is required to assess influence of mutations on cells that are closer to CADASIL patients.

Mice models for CADASIL

A few mice models of CADASIL have been generated to understand the physiological role of NOTCH3. Consistent with the pathobiology of human CADASIL, *Notch3* knockout mice develop vMCs loss and dysfunction [85, 86]. Domenga *et al*. established adult *Notch3* knockout mice that showed an increased dilation and resistance in arteries in response to flow, suggesting that NOTCH3 plays a role in flow mediated vasodilation [63]. However, these mice did not develop age related stroke and GOM deposition in the tunica media of vessels.

While in human CADASIL patients vECs show degenerative changes in addition to vSMCs, transgenic mice carrying the Arg90Cys mutation of *Notch3* showed no evidence of prominent brain parenchyma damage. Thus this transgenic mice model can only recapitulate the certain characteristic and specific aspects of the CADASIL vasculopathy and modelling the early stage of CADASIL before onset of clinical symptoms and brain parenchyma damage [87]. Moreover, mice models expressing the Notch3 Arg142Cys mutation failed to show apparentphenotypes of CADASIL [88].

In summary, although recent models appear more improved, the CADASIL mice failed to phenocopy the full clinical features seen in CADASIL patients, especially the brain pathologies. It is of great important to employ alternative methodologies for CADASIL disease modelling that can recapitulate the disease phenotype more vividly.

1.6. Neurovascular interactions

The brain is the most complex organ in the human body. The nervous system plays a leading role in the regulation of our bodies' physiological functions and consists of two parts: the CNS and peripheral nervous system (PNS). CNS is composed of the brain and the spinal cord, while PNS is the neuronal network connecting the CNS to all the other organs in the body. CNS is divided into white and gray matter, which can be seen macroscopically on brain tissue. The white matter consists of myelinated axons, few neuronal cell bodies and oligodendrocytes, while the gray matter consists of a large number of neuronal cell bodies and unmyelinated fibres. Astrocytes may be involved with both the clearance of metabolites as well as nutrient perfusion and transport of various substances to neurons from the capillaries of the brain. More glial cells are found in white matter rather than in the gray matter, which are often referred to as supporting cells of the central nervous system. Different types of glial cells function differently, glial cells of the oligodendrocyte lineage acting during neurogenesis as a support for neuroblasts growing, while others, such as microglia, are involved in the clearance of various metabolites from the brain tissue as well as the immune system of the brain [89].

In the CNS, changes in blood supply based on neuronal demand are accomplished by the neurovascular unit (NVU), which is a cluster of cells of both vascular and neural origin. Understanding the structure and function of the NVU is central in our understanding of neurodegenerative disease.

1.6.1. Neurovascular Unit

Ischemic stroke, one of the main symptoms of dementia, has been shown to be caused by a disruption in neural and vascular interactions [90]. Early clinical trials to treat dementia focused on pharmaceuticals to treat the neural deficit alone but were largely unsuccessful [91]. The study of neural and vascular interactions has coalesced around the concept of the NVU, which encompasses neuron-astrocyte-capillary interactions as a unique entity [92, 93]. This combination of both neuronal and vascular cell types may reflect various structures and function of brain constitutions more comprehensively and rapidly and thereafter became a hotspot in the understanding of stroke pathology as well as new therapy development [94].

The concept of NVU was refined in 2002 by Harder as a structure that consists of neurons, interneurons, astrocytes, microglia, and basal lamina covered with vSMCs and pericytes, vECs and ECM [95], which are structurally and functionally linked to one another, resulting in an effective system of regulation of brain blood flow [96] [97]. In 2003, the concept of NVU was expanded upon by Lo *et al* [93], which emphasised the dynamic interactions among cerebral blood vessels and the neurons they serve, being regarded as important in achieving an integrated response to central nervous system ischemic injury [92]. The term NVU, as officially defined by the National Institute of Neurological Disease and Stroke (NINDS), was used as an integrated target for stroke research and treatment, representing the fundamental structural and functional unit for nervous system[98].

The NVU is mainly composed of brain microvessels that are encompassed by pericytes, astrocyte end-feet, and neurons. The structure formed by ECs functions as a physical barrier between the blood and brain parenchyma creating what is known as the blood brain barrier (BBB). The BBB also, possesses an active transport system where ECs use membrane transport proteins to regulate the influx and efflux of molecules across the BBB. Additionally, basement membranes and other cell types in the NVU are essential in regulating the precise function of the BBB. The BBB, a vital structure in the NVU, is constituted by brain microvascular endothelial cells (BMECs) connected tightly with each other and intertwined with surrounding pericytes and astrocytes [99] (**Figure 1.3.**).

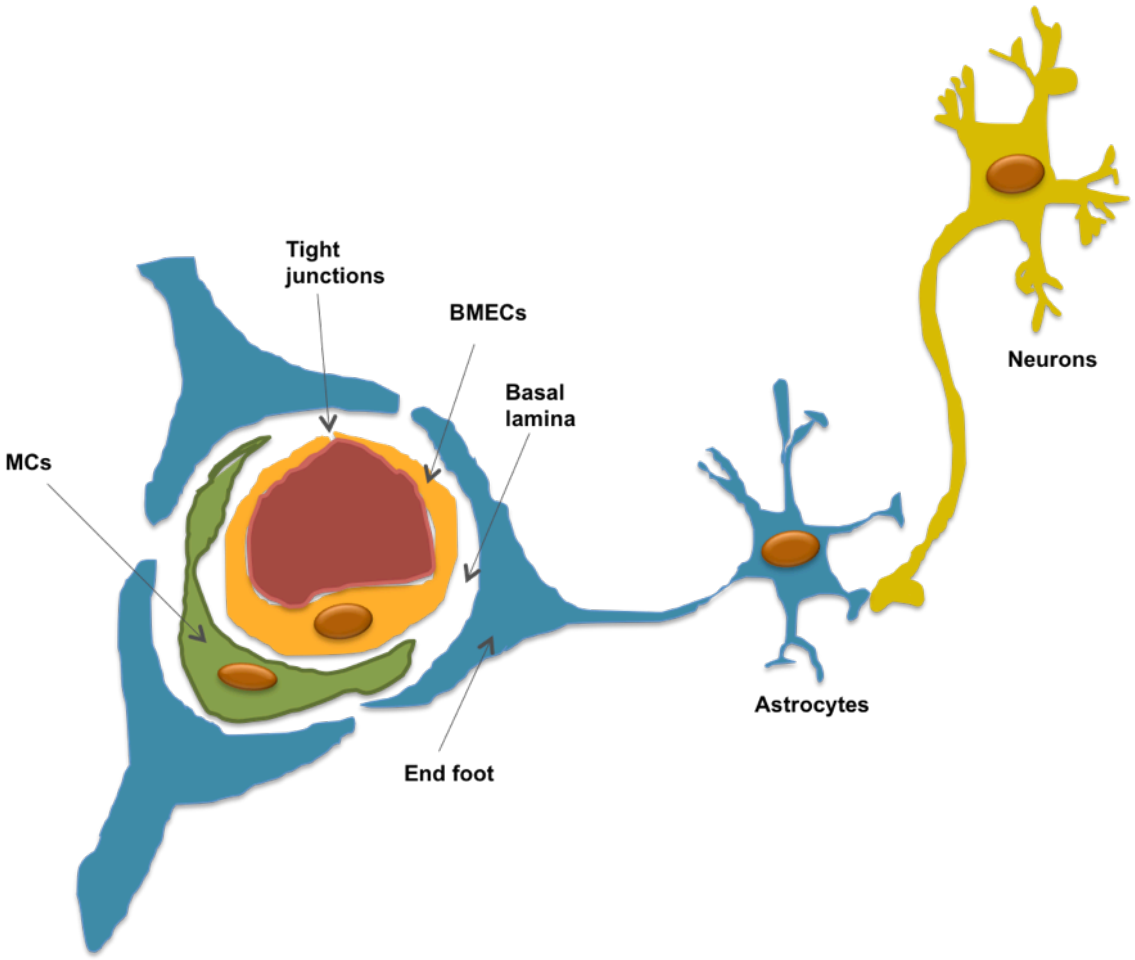

Figure 1.3 The constituents of neurovascular unit.

BMECs make up the capillaries in the CNS while pericytes (vMCs, green) incompletely cover the surface. VMCs are distributed along the length of the cerebral capillaries and partially surround the BMEC monolayer. BMECs form tight junctions between one another, which prevent paracellular diffusion between cells. Astrocytes communicate with local neurons and synapses and also extend foot-like processes that encase cerebral vessels. Extracellular matrix (basal lamina) is between the astrocytes and blood vessels [100]. Adapted from (Abbott, 2009, Structure and function of the blood-brain barrier).

1.6.2. Brain microvascular endothelial cells

VECs are derived from the mesodermal germ layer, differentiating into various types according to their localisation and function in the body [101]. VECs of different tissues have distinct structures and functions while the core elementary unit of the BBB is the BMECs. BMECs in the CNS have unique properties compared with vECs in other tissues, which allow BMECs to tightly regulate the exchange of ions, molecules, nutrients and cells between the blood and the brain. BMECs are held together and form a monolayer by tight junctions (TJs), which strictly limit the paracellular flux of materials [102].

Compared with peripheral vECs, BMECs show several vital distinctive features summarised below:

(a). Connections between cells are much closer, greatly limiting paracellular transport [102-104]. BMECs undergo extremely low rates of transcytosis compared with peripheral vECs, which greatly restricts the transcellular movement of solutes [105].

(b). The proteins BMECs express have a distinct luminal/ablumenal distribution resulting in cellular polarity, consequently ensuring an efficient active transport of substances between the brain and blood [106, 107].

(c). More membrane protein transporters are expressed in BMECs, which can be divided into two categories. Members of the ATP-binding cassette (ABC) efflux transporter family, such as p-glycoprotein, is expressed in vascular lumen surface. These transporters transport materials outside the brain, thus can take a lot of cerebral lipid and harmful substances into the blood [108-110]. Glucose transporters including GLUT 1 and GLUT 3 transmits materials into the brain, which can transport necessary nutrients such as glucose, amino acid and pyruvic acid for neural cells growth and activities into the brain [110].

(d). The expression of leukocyte adhesion molecule is quiet low that greatly limits the peripheral immune cells getting into the CNS, thus preventing brain from damage when it comes across inflammation [111].

1.6.3. Vascular mural cells (Pericytes and vSMCs)

VMCs include vSMCs that surround the large vessels and pericytes that incompletely cover BMECs [112]. Pericytes are located at the interface between the brain parenchyma and the blood vessels to facilitate communications between neuronal/glia and vascular cells therefore are vital to NVU function [113]. While it is commonly recognised that pericytes have many

important functions in the CNS vasculature, their engagement in the BBB function and regulation of central blood flow (CBF) remains not fully understood [114]. Though CNS pericytes have a developmental origin distinct from vSMCs [115, 116], the morphological and genetic markers of pericytes are not distinct compared to vSMCs. Pericytes are characterized by an elongated flattened morphology, expressing markers such as platelet-derived growth factor receptor-beta (PDGFRβ), Neuron-glial antigen 2 (NG2), alpha-smooth muscle actin (α-SMA), desmin and Calponin1 (CNN) [114]. However, expression of these markers varies among pericytes derived from different tissues and studies have found that a subclass of the CNS pericytes express proteins related to cellular contraction including α-SMA and desmin [114]. Current findings suggest there is confusion in distinguishing pericytes and vSMCs based on the expression of molecular markers that identify whether these cells are a subset of vSMCs that cover the arterioles or are genuine capillary pericytes [117]. As vSMCs and pericytes share many molecular markers, identification of novel molecular markers that distinguish vSMCs and pericytes in the cerebral vascular will be a valuable tool in the future to figure out the role of both cell populations in the brain during CNS pathologies.

CNS pericytes can be derived from different germ layers. Ectopic transplantation between quail and chicken embryos demonstrated that the pericytes in the forebrain are mainly differentiated from neuroepithelium, while pericytes from the midbrain, brain stem, and spinal cord are derived from mesoblast [118-121]. A recent study on adult mice showed that bone marrow precursor cells that exist in the cyclic system could provide pericytes for CNS [122]. Similarly, the heterogeneity of vSMCs is related to their different developmental origins during development, including vSMC progenitors arise from distinct embryonic sources including splanchnic mesoderm, somitic mesoderm, neural crest (NC), mesothelia, and other embryonic cell types [123]. Among them the NC is one of the major sources of vSMCs [124].

At the arterial level, vSMCs are the main components that wrap around the outside of cerebral blood vessels and the major dedicators to basal tone maintenance, blood pressure and blood flow distribution [125]. However, most of the studies on vMCs function in the NVU were focused on pericytes. In the CNS, pericytes can regulate and maintain the BBB through the release of signalling factors in determining BMECs tight junctions numbers and directing the polarization of astrocyte endfeet [126]. Pericytes can change CBF in response to localized changes in neuronal activity [127]. A reduction in pericyte numbers can cause losing of tight

junctions between BMECs, leading to increased BBB permeability and decreased barrier function [128]. Moreover, pericytes can control the motion of substances between the blood and the brain side, such as the clearance of toxic materials out of the brain [129].

1.6.4. Astrocytes

Astrocytes, a major glial cell subtype in the brain, have long been thought to be critical in the development and maintenance of BBB structure and function [130]. Astrocytes located in proximity to blood vessels will extend protrusions, the end of which forms the swollen endfeet that wrap around vECs and pericytes[131]. Astrocytes participate in wrapping 99% of the blood vessels of the NVU and interact with vECs to confer BBB properties by increasing tight junctions expression as well decreasing gap junctions expression [132].

Astrocytes are essential for many metabolic processes in the CNS such as promoting neurovascular coupling, attracting cells through the release of chemokines (chemotactic agents that activate receptors on other cells) [133], releasing of gliotransmitters (chemicals that act on adjacent neurons, vessels and glial cells including glutamate, ATP and cytokines and others) [133], releasing of glutamate by calcium signalling, control of brain pH, dopamine metabolism by monoamine oxidases, and the uptake of glutamate and γ-aminobutyricacid (GABA) [134]. Astrocytes can also function as a bridge between neurons and blood vessels by interacting with the synapses of neurons, regulating the functions of pericytes and vascular endothelial cells in response to neural activity[135].

Astrocytes are characterized by the expression of the intermediate filaments vimentin (VIM) and glial fibrillary acidic protein (GFAP) and S100 calcium-binding protein β (S100β). Several functional proteins are expressed in astrocytes end-feet, such as dystroclycan (DAG1), dystrophin (DMD) and aquaporin 4 (AQP4) [136, 137]. The dystroclycan-dystrophin complex connects the astrocyte endfeet to the ECM secreted by BMECs, pericytes and astrocytes, while AQP4 regulates cerebral water balance [138]. Although a high heterogeneity exists among astrocytes, there are two main types in the CNS: protoplasmic astrocytes in the grey matter which wrap neuronal bodies and synapses, and fibrous astrocytes in the white matter that connect with the nodes of oligodendroglia [139-141].

1.6.5. Neurons

Neurons play important role in the CNS due to its extremely complicated mechanisms, however the exact nature of neurons in BBB is largely uninvestigated. In one of the early studies about neural involvement in the BBB, Stewart *et al.* found that BMECs developed BBB characteristics in answer to some aspect of the neural environment [142]. Yoshida et al. supposed that the primary demand for blood vessels in nervous tissue seems to be connected with neuroblast formation. The developing neural cells including neuroblasts and glial cells affect the BMECs by changing their morphology [143]. Later on, Tontsch *et al*. investigated the implications of membrane contact between neural cells and BMECs as well as the importance of paracrine signalling. The results showed that the plasma membranes of glial or neuronal cells can induce BBB-related enzyme activities in cultured vECs, which indicates that not only glial cells but also neurons interact with BMECs during CNS ontogenesis and thus contributing to the formation of the metabolic and structural characteristics of the BBB [144].

The NVU regulates changes in CBF in response to neural activity. NVU is thought to be regulated by direct interactions between neurons and BMECs or through complex neurogliovascular signalling pathways [145]. Lecrux *et al.* summarised the interrelationships between interneurons and astrocytes in the BBB [146]. Moreover, neurons can detect tiny variations in their supply of nutrients and oxygen, and transfer the signals to adjacent interneurons or astrocytes [98]. In other aspects as reported, Glucose gets into the brain via Glut1 transporter expressed by BMECs and is taken up by neurons via Glut3 [147]. In summary, neurons play important roles in the function of NVU through co-relationship with other NVU cell types.

1.6.6. Extracellular matrixes (ECMs)

ECM is composed of ECM proteins such as collagens and laminin forming the basement membrane between (BMECs and pericytes) and (astrocytes and pericytes). The matrix surrounding the outside of pericytes and BMECs can be as thick as 30-40 nm. The sheath that pericytes create around BMECs is discontinuous, where there is a shared single basement membrane between astrocytes and BMECs in the gaps left by pericytes. Culturing endogenous ECM and vECs *in vitro* could strengthen the barrier function of vECs. The secreteome of vECs might theoretically be influenced by the ECM, which represents a conducive environment to the diffusion of ions, neurotransmitters and ATP [148-150].

However, ECM secreted by glial cells can better maintain the barrier function of BMECs as opposed to peripheral vECs [151]. This also indicates a difference between BMECs and peripheral vECs.

For proper NVU and BBB functioning, ECM and the protein supportive components of the basement membrane are essential to mediate the activation process of many cell receptors. Several CNS diseases such as cerebral haemorrhage and small vessel disease, which can be caused by an inherited mutation in genes that encode collagen *COL4A1* and *COL4A2*, are associated with degradation and dysfunction of the basement membrane and leading to SVD [32]. In conclusion, ECMs are important components of the NVU function especially affect BMECs barrier function.

1.6.7. Blood-brain barrier (BBB)

The BBB is a special barrier system formed by BMECs that connect tightly with each other by various ligands and intertwine with vMCs and astrocytes [152]. The BBB strictly limits neurotoxic substances, inflammatory factors and immune cells from the blood to flow into the CNS. At the same time, BBB helps discharge metabolites and neurotoxins created in the CNS into the blood. Through such precise control in the exchange of substances between blood and brain, the BBB functions to maintain ion balance, water balance, neurotransmitter and hormone levels in the CNS [153].

The BBB is composed of an BMEC monolayer making up the capillary wall, astrocyte endfeet ensheathing the capillary, and vMCs (pericytes in capillaries and vSMCs in arterioles and arteries) embedded in the capillary basement membrane (**Figure 1.3.)** [132]. The BBB has tightly sealed contacts between cells that result in high trans-endothelial electrical resistance (TEER) and low paracellular transport abilities. This is due to the selectivity of the tight junctions formed between the BMECs composed of occludin, claudins, amongst other junctional adhesion molecules that all serve to limit paracellular diffusion [154]. This selective barrier capacity allows BBB ECs to rigidly regulate CNS homeostasis that is vital for protecting the CNS from toxins, pathogens, inflammation, injury, and disease [155].

Abnormal development and function of the BBB can damage the homeostasis of the brain microenvironment, leading to neuronal death and neurological dysfunction. The breakdown of the BBB is found in brain diseases such as AD, PD, CADASIL and amyotrophic lateral sclerosis (ALS) [156]. The low permeability of the BBB also makes it a natural barrier against drug delivery to the brain. Consequently, numerous studies have focused on this

nature of BBB and developed new drug carriers to deliver drugs to CNS [157-162]. Given the properties of the BBB and its disruption in disease states an in-depth study of BBB will provide important theoretical foundation for the diagnosis and treatment of nervous system disease.

1.6.8. Junctions between NVU cells

As previously discussed, the BBB is a highly complicated and dynamic barrier that regulates the entry of solutes from the blood into brain and maintains ionic homeostasis within the CNS microenvironment. One of the primary properties of BBB is a strict regulation of paracellular transport, regulated by the presence of junctional proteins (tight, adherens and gap junctions) between the NVU cell types [163] (**Figure 1.4.)**.

Tight junctions

The tight junctions (TJs) between BMECs form an elaborated structure with a branching network of protein sealing strands. The general function of TJs is to prevent leakage of transported solutes and water from the blood sealing the paracellular pathway. In the normal BBB the TJs are located along the lateral membrane to seal the inter-BMECs cleft completely. There are at least 40 different proteins composing the TJs consisting of both transmembrane and cytoplasmic proteins [164]. The three major transmembrane protein groups are Occludin, Claudins (Claudin5, Claudin3, Claudin12 and Claudin1), and junction adhesion molecule proteins (JAMs), which connects the cytoskeletons of adjacent BMECs in association with cytoplasmic proteins such as ZO-1 located on the intracellular side of plasma membrane and anchors the strands to the actin component of the cytoskeleton [164].

Occludin was the first transmembrane TJ protein described that plays a key role in cellular structure and barrier function. Structurally, occludin consists of four transmembrane domains with two extracellular loops and one intracellular loop, a short N-terminus and a long C-terminus. These loops help regulate paracellular permeability while the terminus is involved in interactions with scaffolding proteins and the actin cytoskeleton [165, 166]. The 2nd extracellular loop is involved in regulating adhesion between cells. Moreover, Occludin does not have the ability to build organized strands by itself and it is mostly associated with Claudin strands, which indicates the function of Occludin in BMECs is regulatory rather than adhesion by itself [167, 168].

Claudins are the principal sealing components of transmembrane TJs with more than 24 isoforms identified. They have a structure similar to that of Occludin in that they have four

transmembrane domains and similar loop structure, which plays a significant role in the tight junction's ability to seal the paracellular space. Claudin 5 is the major constitutive Claudin in the BBB [169, 170]. Nitta *et al*. found Claudin 5 deficient mice died in the first 10 hours after birth due to brain edema and other Claudins including Claudin 3, Claudin 1 and Claudin 12 are not able to recover the Claudin 5 deficit and maintain BBB integrity indicating that Claudin 5 is indispensable for normal BBB function [170, 171].

JAMs are part of the immunoglobulin superfamily and are structurally composed of a single membrane spanning domain, an IgG-like extracellular domain, an extracellular N-terminus crucial for dimerization, and a short cytoplasmic C-terminus important for interaction with the TJ protein ZO-1 [172-174]. The JAMs help to regulate the paracellular pathway function of tight junctions and is also involved in maintaining cell polarity. JAM A/B/C are indicated as important molecules for tubule formation and establishing TJ complexes as well as in regulating leukocyte adhesion and trans-migration [175].

Other TJ proteins important for BBB function include scaffolding proteins, which include a family of membrane associated kinases, zonula occludens 1, 2 and 3 (ZO-1, ZO-2 and ZO-3). Structurally, TJ ZO proteins have three core regions: a SH3 domain responsible for binding signalling proteins, a guanylate cyclase, for catalyzing the ATP-dependent transformation and a PDZ domains that bind to the C-terminal ends of transmembrane proteins. ZO proteins are recognised as indispensable in regulating the assembly of claudins, occludin and JAM-A in TJs [176, 177].

Gap junctions

Gap junctions (GJs) are a specialized intercellular connection formed by members of the connexin (Cx) family composed of several transmembrane hexamers [178]. Cx37, Cx40 and Cx43 are expressed in BMECs. Connexins commonly function as hexamers at the plasma membrane following oligomerization in the ER. Studies have characterised the distribution of Cx43 across BMECs and pericytes, establishing the structural foundation for vascular cell connectivity [179]. GJs are critical for intercellular communication, when formed between cells, GJs create hydrophilic channels that allow ions and various small molecules pass through GJ plaques and transduce signals between neighbouring cells. Electrotonic pulses that propagate along the network of pericytes and BMECs are regulated by GJ-mediated communication [180]. While the N-terminus of connexins regulates their oligomerization in the ER, the C-terminal cytoplasmic tail regulates channel closing in response to changes in

pH [181, 182]. Many studies have demonstrated that the C-terminal cytoplasmic tail of Cx43 also play important role such as in cell proliferation and migration independent of Cx43's channel function [183].

Adherens junctions

Adherens junctions (AJs) are cell-cell junctional complexes located in the apical region of EC membranes, which regulate adhesion between the ECs and contributes to the overall junction arrangement. AJs have a similar structure to TJs. AJs contain transmembrane proteins, cadherins, which are responsible for the adhesion between cells and scaffolding proteins. In BMECs, the major AJ transmembrane protein is VE-cadherin, with low levels of N-cadherin and E-cadherin [172, 184, 185]. VE-cadherin is an EC-specific AJ protein known for its function in promoting early stages of vascular connection and fusion. Increasing evidence points to a role of VE-cadherin in the maintenance of cell-cell junction stabilization and regulation of vascular barrier integrity. Additionally, VE-cadherin is responsible for the maturation and remodelling of embryonic angiogenesis [186, 187].

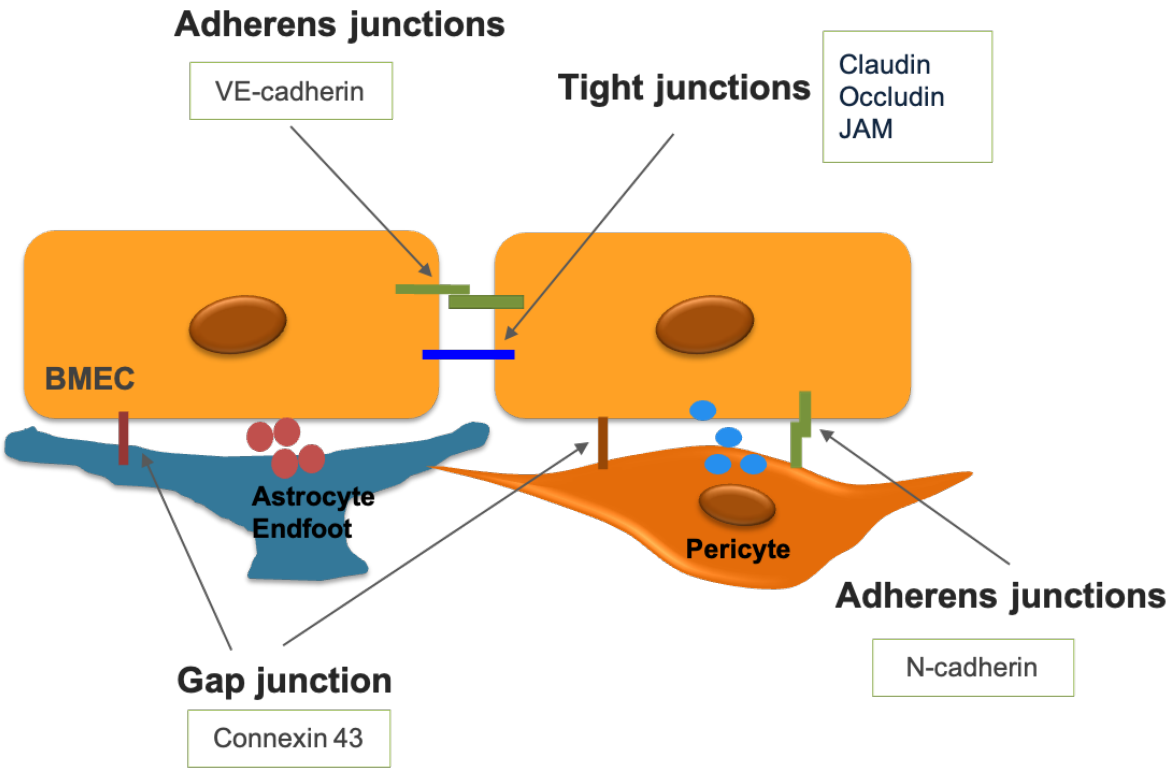

Figure 1.4 The composition and localisation of junction proteins in neurovascular unit.

The primary components of the NVU are vascular cells (BMECs, vMCs), astrocytes and neurons. Pericytes and astrocyte endfeet surround BMEC microvessels. The interactions between NVU cells rely on junction proteins. Adjacent BMECs are connected by TJs and AJs. TJs are mainly composed of Claudins, Occludin, and junctional adhesion molecules (JAM), whereas the AJs are composed of VE-cadherin and N-cadherin. Gap junctions are expressed in all the three cell types and are responsible for interactions between BMECs and astrocytes or BMECs and pericytes.

1.7. Neurovascular interaction and CADASIL pathology

1.7.1. NOTCH function in blood brain barrier

As NOTCH signalling play vital role in both vascular and neuronal cell types, it may affect the function of the neurovascular interaction and the blood brain barrier BBB. PDGF is a ligand for the receptor tyrosine kinases PDGFR-α and PDGFR-β, which play important role in recruitment of mural cells by neovessels, regulating maturation of the infarct vasculature [188]. Recent studies on Pdgfb and Pdgfrb mutant mice models have shown that loss of pericytes led to increased ECs transcytosis and a significant transport of blood-borne tracers

across the BBB [116, 189]. In one study a *Notch3*−/− mice model was generated which demonstrated an enhanced and continuous rate of apoptosis may lead to loss of vSMC in these mice which during adulthood was linked to localised impairment of the BBB [190]. Pericyte loss in aging brain can lead to brain vascular damage causing decreased capillary perfusion, impaired CBF response to stimulus and BBB breakdown [191]. Moreover, pericyte loss and subsequent increase of vessel permeability may also promote neurodegeneration in the aging brain. In a *Notch3* mutant Zebrafish model it was revealed that the mutant Zebrafish suffer from brain hemorrhage and fail to form a tight BBB caused by failure of pericyte expansion, which indicates that Notch3 signalling may help determine pericyte coverage of BBB [192].

These studies revealed important functions of Notch3 signalling in maintaining BBB integrity, however, most of the data was generated using pericytes, excluding other BBB cells. It's still unknown how EC dysfunction in CADASIL happens and how it is related to BBB functions. Therefore, to better understand the full range of CADASIL pathology it will be important to study the interactions between all of the NVU cells that make up the BBB.

1.7.2. NVU and CADASIL pathology

Increased cerebrospinal fluid/serum albumin ratio, a marker of BBB breakdown, has been involved in VaD [193, 194]. CADASIL as the most common hereditary VaD [39, 195], was found that the extensive loss of vSMCs and MCs ECM deprives the NVU of its structural and functional ability to regulate CBF and is therefore involved in the development of CADASIL [196].

Accumulated evidence has shed light on the relations between NVU and CADASIL. Mitrajit and his colleagues examined CADASIL mutant mice and controls to check out Notch3 aggregation in pericytes, astrocytes endfeet, BBB integrity and the protein expression of GJs and AJs respectively in astrocytes and ECs [86]. As a result, pericytes as well the coverage of capillaries they process was found to be significantly reduced in mutant mice caused by mutant Notch3 aggregation around pericytes. This result infers that pericytes may be the first cells affected by Notch3 accumulation and may lead to BBB and microvascular dysfunction in CADASIL mice. Another team found up-regulation of pericytes that expressing PDGFR-β in microvessels of CADASIL patients' microvessels, which may be response for loss of vSMCs in CADASIL[197].

Neurovascular interaction is a complex biological process underlying blood flow increases in response to neural activation, which is termed functional hyperemia, was mostly investigated at the early stage of CADASIL. An early reduction in functional hyperemia in response to whisker stimulation has consistently been observed in CADASIL mice prior to vSMCs loss [198, 199]. Therefore, defects in NVU may represent one of the earliest manifestations of CADASIL. Huneau *et al*. discovered that alterations of neurovascular coupling occur early in CADASIL, which can be assessed by arterial spin labelling-functional magnetic resonance imaging (ASL-fMRI) using a simple marker of vascular dysfunction [200].

VMCs express PDGFRb, which is responsible for the function and survival of vECs and for adequate expression of TJ proteins. Thus, vMCs play a key role in maintaining microvascular perfusion and the proper functioning of the BBB. In a *Notch3* mutant mice model of CADASIL, *Notch3* aggregation in vMCs, vMC numbers, capillary density, BBB integrity, astrocytic endfeet, and the expression of astrocytic GJs and ECs AJs protein was compared between CADASIL and control mice using immunostaining and western blot analysis. The results showed that pericytes are the primary cells affected by Notch3 aggregation in CADASIL mice thus causing breakdown of the BBB and microvascular dysfunction. However, it was noted that alterations in NVC, specifically, detachment of astrocytic endfeet from brain microvessels, resulted in leakage of plasma proteins, reduction in expression of AJs protein, and diminished microvascular reactivity to CO_2 [201].

Data from these studies indicate that not only vascular cells (vMCs and vECs) are responsible for CADASIL, but that neurons and glial cells are also involved. This may manifest as defects in astrocytes or neurons or neurovascular coupling. However, the precise order in which pathological changes occur or whether these defects are a symptom or cause of the disease remains largely unknown.

1.8. iPSCs and disease modelling

Induced pluripotent stem cells (iPSCs) were first discovered by the Yamanaka Lab in 2006. This pioneering work defined a minimum of 4 transcription factors: Oct4, Sox2, Klf4 and c-Myc were required in reprogramming somatic cells to pluripotency cells and making these iPSCs capable of generating tissues of all three germ layers. [202]. Since then, various donor cell types were applied to generate iPSCs by other researchers including skin cells, neuronal cells, adipose stromal cells and others [203-205]. The discovery of iPSCs has made it easier and more reliable to study human genetic diseases in patient-specific cells using *in vitro*

models. As discussed before, though previous models of primary cells or immortalized cell lines and animal models were used to model CADASIL, these methods have several drawbacks, including difficulties in isolating primary cells from the cerebrovascular system and difference between human and animal cerebrovascular structure thus they cannot fully recapitulate what happens in CADASIL. Therefore the successful generation of objective cells derived from iPSCs has provided a more efficient and reproducible model for diseases than previous *in vitro* approaches. iPSCs disease modelling allows researchers to obtain tissue from patients in sufficient number to conduct *in vitro* cellular assays of diseased cells to study their altered cell function [206]. In the case of CADASIL this would be the cell of the cerebral vasculature (vECs and vMCs). Deriving patient specific tissues *in vitro* may be utilised in drug toxicology and efficacy screening, allowing drug companies to create tailored drugs to the genetic background of patients.

1.8.1. iPSC disease modelling

Stem cells commonly used in disease modelling include mesenchymal stem cells (MSCs), embryonic stem cells (ESCs), iPSCs and brain derived neural stem cells (NSCs).

Potential cell sources for VaD disease modelling include MSCs and NSCs. While human NSCs cultures are considered to be a perfect standard for modelling neurological disease, limited access to tissues at source impedes the use of NSCs for disease modelling. Neither surgical nor post-mortem removal of brain tissues can provide sufficient biomaterial for large-scale cell-based drug screening.

ESCs possess a capacity for unlimited self-renewal and have the ability to differentiate into all types of somatic cells in the body, including neuron-like cells [207, 208]. Such cells not only carry congenital mutations for specific disease but can also be subjected to genetic modification in order to model disease-specific alterations. Preimplantation genetic diagnosis derived human ES cells are derived from blastocysts left over from *in vitro* fertilisation, have been developed to model CNS related disorders such as AD and ALS. These cell lines provide a valuable source of ES cells as well as neurons, glia, and other somatic cells for investigations of the cause, effect, and treatment for brain disease [209].

However, the ethical implication of destroying blastocysts to generate ESCs, the potential for immune rejection if those cells were used as a treatment hinder their use. The generation of iPSCs solves the problems.

As discussed, current cell models and mice models for CADASIL cannot faithfully mimic the disease pathology, iPSCs could provide a valuable tool to address this deficit as they can be generated directly from CADASIL patients. The concept of iPSCs is for the first time been report in 2006 by Japanese scientist Takahashi and Yamanaka, who successfully generated iPSCs using retroviruses with four transcription factors (Klf4, Sox2, Oct4 and c-Myc) [202]. This process takes use of exogenous transcription factors to reprogram differentiated somatic cells and induces them into iPSCs. At present many novel technologies have improved the transfection efficiency and clinical safety of iPSCs. This method is of great significance for the construction of *in vitro* model for neurodegenerative diseases.

iPSCs derived from patients with genetic diseases can be induced to differentiate into various cell types that can be used in the *in vitro* study of the cellular and molecular changes caused by the disease. Using iPSCs to explore disease pathogenesis could ultimately lead to the development of in vitro drug screening platforms[210].

1.8.2. iPSC differentiation into NVU cell types

Recent work has shown that iPSCs can be differentiated into various BBB cell types. Lippmann established the first iPSC-BMECs differentiation protocol using a strategy of EC and neural cell co-differentiation in unconditioned medium, followed by a BMEC specification and expansion stage in EC growth media. Then BMECs can be selectively purified on a mixture of collagen and fibronectin on Transwell membranes for BBB modelling [211]. Advancement has been made with the addition of retinoic acid (RA) during the BMEC differentiation that increases both the differentiation efficiency and barrier properties of the resulting BBB layer [212] (Summarized in **Figure 1.5**). Further refinement including optimizing initial iPSC seeding density, accelerating the differentiation time and more recent efforts have been made to improve in vivo angiogenesis by adding a small molecule against Wnt/β-catenin, CHIR99021 [213]. Other recent advancements in the differentiation of iPSC-BMECs include the application of defined cell culture medium, modification of sorting strategies to promote BMEC purity, and the preservation of differentiated cells [214]. The BMECs generated in these protocols were characterized with TEER measurement, passive diffusion of sodium fluorescence (NaF) through the BBB, efflux transporter activity (ETA), and expression of essential BBB junctional proteins (claudin-5, ZO-1, occludin, VE-Cadherin), transporters (P-gp, GLUT1), and other factors (PECAM-1, VEGFR2, vWF).

Although the BMECs are the main cell type that constitutes the BBB interface, other cell types of NVU contribute significantly to regulating BBB phenotype and function including MCs, astrocytes, and neurons. vSMCs, or related pericytes, can be differentiated from mesoderm and neural ectodermal lineages. iPSCs differentiated through the neural ectodermal lineage were demonstrated to produce vSMCs and pericytes more closely resembling those found in the brain [215]. Cheng *et al*. published a differentiation protocol to generate neural ectodermal (NE) derived vSMCs producing a neural ectodermal-like population that was positive for Nestin and SOX1. These NE cells were then differentiated further to a vSMC-like cell following TGFβ and PDGFB treatment. The NE-vSMCs generated, expressed the vSMC specific markers CNN1, αSMA, SM22 and smoothelin (SMTN) [216].

Since the discovery of iPSC technology, several differentiation protocols to obtain human neurons and astrocytes from iPSCs or ESCs have been established. Meanwhile, these protocols are continuously being updated in various aspects such as the cell seeding density at plating, the substrate, media composition, the timing and concentration of growth factors. Among the most commonly used techniques, both neurons and astrocytes differentiation from iPSCs normally start with neuronal induction to generate stable human NPC populations. To mimic the *in vivo* mechanisms of early neurogenesis of NPC formation, two protocols are mainly utilized: an EB-based technique with or without SMAD inhibition and a monolayer-based dual SMAD inhibition method [217, 218]. The cells are induced in the neural induction medium (NIM) usually consists of the neurobasal medium and/or DMEM/F12 medium with either LDN or noggin to inhibit the BMP pathway and SB431542 to inhibit the TGF-ß pathway. NPCs are arranged into polarized neuroepithelial sheets called neural rosettes, which are then selected and cultured for several passages and then cryopreserved or directed toward neuronal or astroglial fates in defined culture medium with different combinations of morphogens.

Citation	Differentiation Protocol	Characterisations
Lippmann et al., 2012 *Nature Biotech.*	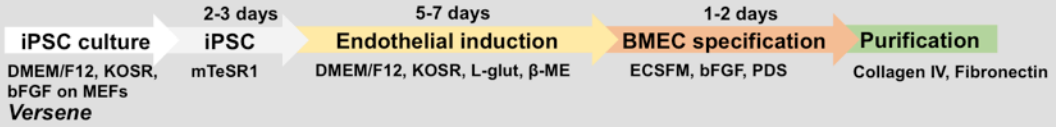	**TEER**: ~400 Ωxcm² (mono) ~1400 Ωxcm² (co-culture) **IF**: GLUT-1, CD31, CLDN5, OCLN, ZO-1 **Functions**: Tube, LDL, FC, ETA (P-gp)
Lippmann et al., 2014 *Scientific Reports*	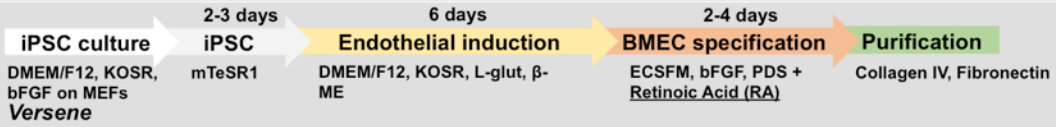	**TEER**: ~3,000 Ωxcm² (mono) ~5,300 Ωxcm² (co-culture) **IF**: GLUT-1, CD31, CLDN5, OCLN, CDH5 **Functions**: ETA (P-gp), FC, qPCR
Wilson et al., 2015 *FBCNS*	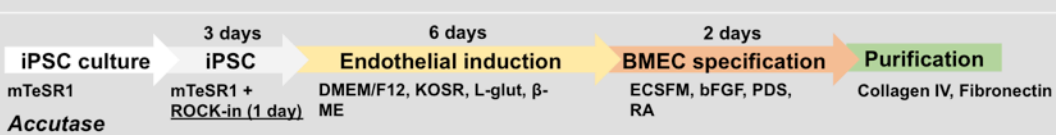	**TEER**: ~2,300 Ωxcm² (mono) **IF**: GLUT-1, CD31, CLDN5, OCLN, CDH5 **Functions**: ETA (P-gp), FC
Qian et al., 2017 *Science Advances*	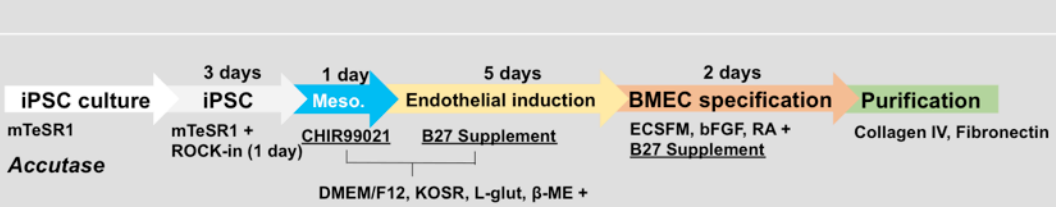	**TEER**: ~3,000 Ωxcm² (mono) ~3,900 Ωxcm² (co-culture) **IF**: GLUT-1, CD31, CLDN5, OCLN, ZO-1, KDR **Functions**: RNAseq, tube, LDL, FC
Neal et al., 2019 *Stem cell reports*	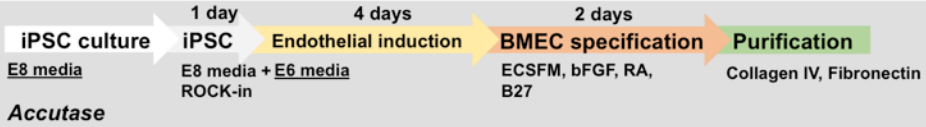	**TEER**: ~8,000 Ωxcm² (mono) ~10,500 Ωxcm² (co-culture) **IF**: GLUT-1, CD31, CLDN5, OCLN, CDH5 **Functions**: ETA (P-gp), Sodium permeability
Park et al., 2019 *Nature Comm.*	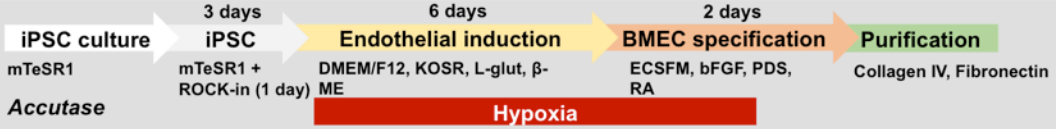	**Impedance**: ~25,000 Ω (co-culture) **IF**: GLUT-1, CD31, CLDN5, ZO-1 **Functions**: ETA (P-gp), drug delivery
Praca et al., 2019 *Stem Cell Reports*	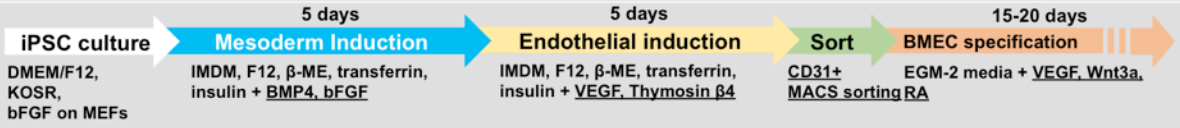	**TEER**: ~55 Ωxcm² (mono) ~55 Ωxcm² (co-culture) **IF**: GLUT-1, CD31, CLDN5, OCLN, vWF, CDH5 **Functions**: ETA (P-gp)

Figure 1.5 Schematic summaries of differentiation protocols for BMECs from iPSCs.

Main advancements from previous protocols are strengthened in bold. Abbreviations: bFGF: basic fibroblast growth factor, MEF: mouse embryonic fibroblast, KOSR: knockout serum replacement, L-glut: L-glutamine, β-ME: β-mercaptoethanol, ECSFM: endothelial cell serum free media, PDS: platelet-poor plasma derived serum, VEGF: vascular endothelial growth factor, TEER: transendothelial electrical resistance, IF: immunocytochemistry, ETA: efflux transporter activity, FC: flow cytometry. Adapted from Workman, 2020 (Recent advances in human iPSC-derived models of the blood–brain barrier).

1.8.3. iPSC modelling of BBB

Currently there are several methods established for the differentiation of BMECs from stem cells including iPSCs as discussed before. Previous studies have demonstrated BBB models being established based on iPSC-derived peripheral ECs co-cultured with iPSC-derived pericytes, astrocytes, and neurons [219]. However, none of the previous studies demonstrated a robust process for generating human BMECs exhibiting functional BBB phenotypes. Recent iPSC-BBB models mainly followed or refined from the neural co-differentiation protocol developed by Lippmann *et al.* [220, 221]. This method was based on the hypothesis that simultaneous differentiation of iPSCs to both neural and endothelial lineages could lead to iPSC-derived ECs with BBB attributes. This protocol described the generation of pure iPSC-derived BMECs through co-differentiation of iPSCs to neural and endothelial progenitors, followed by selective purification of the BMECs. It also demonstrated addition of RA during BMEC differentiation could enhance the barrier properties.

Because of species differences between humans and animals, research results based on animal models may not always be successfully translated into clinical applications. In modelling CADASIL, efforts have been made to construct human BBB and CADASIL vMCs using iPSCs in recent two years. BBB is mainly comprised of BMECs, pericytes, astrocytes and neurons. VaD was indicated to be associated with BBB dysfunction as we discussed before. Lippmann was the first to have reported the properties of hiPSCs-derived BBB *in vitro* with a success rate of 60%.

Currently only 3 iPSC-mural cells models for CADASIL have been reported, all of them were published in recent three year. Ling et al. built the CADASIL iPSCs-vSMCs model and found gene expression changes associated with disease phenotypes, including activation of the NOTCH and NF-κB signalling pathway, cytoskeleton disorganization and excessive cell

proliferation [222]. Kelleher et al. from our group demonstrated for the first time a failure of the CADASIL iPSC-derived vMCs in engaging and stabilizing endothelial capillary structures [223, 224]. In a more recent research an iPSC-derived CADASIL vMCs model was built, which could recapitulate CADASIL pathology [225].

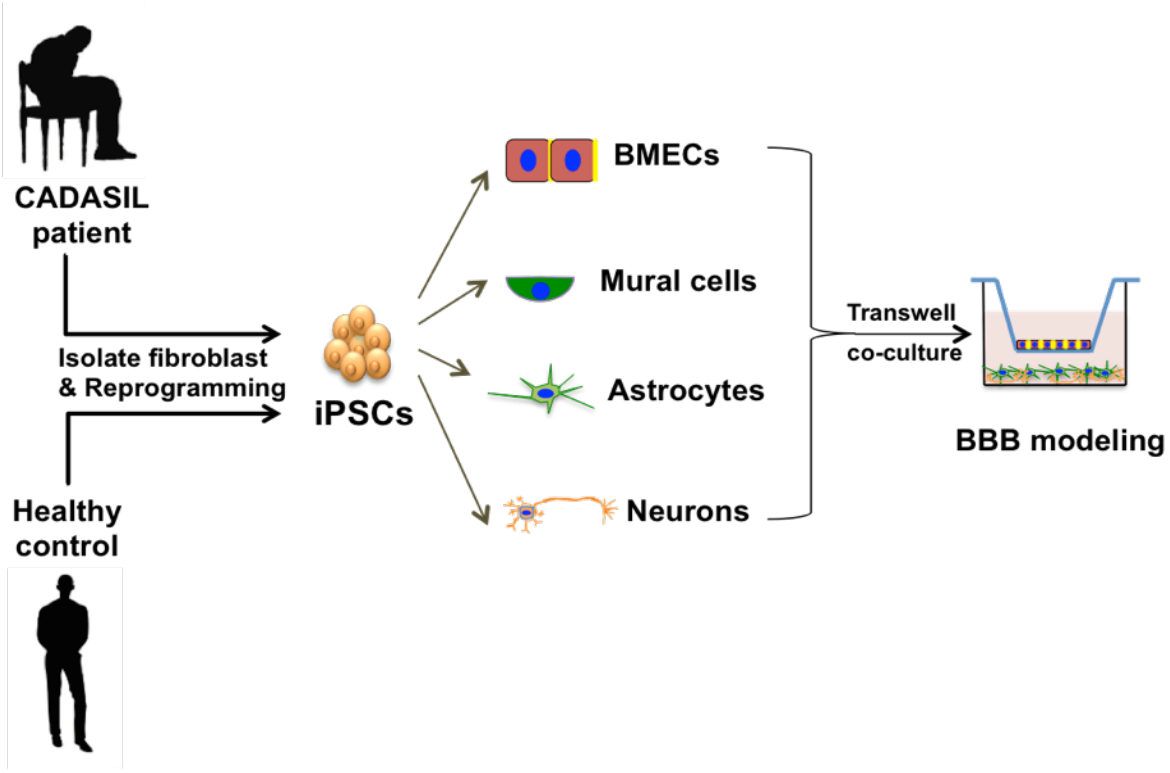

Figure 1.6 Schematic drawing of modelling CADASIL with iPSC-NVU cells.

Fibroblasts from patients or healthy individuals can be reprogrammed to iPSCs and subsequently differentiated into all major NVU cell types for in vitro studies. These cell types can then be co-cultured on Transwell settings to mimic the BBB. Such studies can be applied to investigating cellular functions and how they are impacted by CADASIL pathologies or notch3 mutations. The co-culture models allow for examination of interactions between cell types to better model BBB processes occurring *in vivo*. This model holds promise for better understanding the relevant mechanisms underlying CADASIL and can be applied to the development of drug screening for effective therapeutics.

1.9. Aim and objectives

1.9.1. Summary and aims

While cell models and animal models have disadvantages to faithfully recapitulate CADASIL pathologies and human NVU cells are difficult to be isolated from the brain, iPSCs provide the possibility to investigate disease mechanisms using autologous cells with genetic background of the patient. Studies have found defects in BBB integrity may exist in CADASIL as discussed before. However, most of the studies mainly revealed vMCs deficiency in CADASIL, which left the other NVU cell types and BBB dysfunction largely un-investigated.

Therefore, it is hypothesized that patient-specific iPSCs provide a valid *in vitro* disease model to recapitulate CADASIL pathology, and impaired neurovascular coupling contributes to the development of CADASIL dementia phenotype. Through the set up and refinement of differentiation protocols for cells constituting the NVU from iPSCs, it is anticipated that the iPSC disease models will help better understanding of CADASIL disease pathology which can be generalised to the study of other common or sporadic VaDs and neurodegenerative disorders that involve vascular contributions to the pathologies. Factors if identified as able to rescue the disease phenotype will have therapeutic potentials for CADASIL and, possibly, VaDs in general.

Therefore the main aim of this project is to generate an *in vitro* patient-specific iPSC model of neurovascular interactions for CADASIL in order to investigate the cellular and molecular changes in the iPSC derived NVU cells and their interactions (**Figure 1.6**). With understanding the molecular mechanism, we aim to identify therapeutic insights for future treatment of CADASIL.

1.9.2. Objectives

1. To differentiated iPSCs into NVU cell types including BMECs, vMCs, astrocytes and neurons.

Protocols for the differentiation of BMECs and astrocytes will be achieved by reviewing and optimising the already published methods in literatures. The differentiation of vMC and neuron from iPSCs, will be carried out by following protocols that are well established in the lab. The differentiated cells will be characterised by measuring the expression of cell type specific marker genes and protein expression by qRT-PCR and immunofluorescence staining.

The function of iPSC-BMECs will be confirmed by their ability to form tubule structure *in vitro*, uptake acetylated low-density lipoprotein and BBB barrier function via TEER measurement as well as sodium fluorescence permeability assay.

2. To develop an *in vitro* iPSC-BBB model.

The iPSC-BBB model will be established by culturing iPSC-BMECs in Transwell settings. The contribution of neurovascular interactions to the function of BBB will be determined by co-culturing the iPSC-BMECs with or without iPSC-vMCs, iPSC-astrocytes or iPSC-neurons. The functional integrity of BMECs will be partially assessed by immunefluorescent staining of the junctional proteins on BMECs. The barrier function of iPSC-BBB models will be determined by the TEER measurement and sodium fluorescence permeability assay.

3. To investigate whether CADASIL vMCs have detrimental effect on BMECs barrier function.

The CADASIL or control iPSC-vMCs will be co-cultured with control iPSC-BMECs and TEER as well as sodium fluorescence permeability will be measured.

2. Chapter 2: Materials and methods

2.1. Cell line and cell culture

2.1.1. Primary cell culture

Primary human coronary arterial endothelial cells (HCAECs) (PromoCell, C-12222) or primary human umbilical vein endothelial cells (HUVECs) (PromoCell, C-12250) were cultured in 6-well plates (Corning, 3516) with 2 mL Endothelial Cell Growth Medium MV2 (PromoCell, C-22121) and maintained at 37°C incubator with 5% CO_2. The HCAECs were subcultured when they reached 70-80% confluence, approximately every 3-5 days, as follows. Cell culture medium was discarded and the cells rinsed with Dulbecco's Phosphate Buffered Saline (PBS) (Sigma, D8537). HCAECs were incubated with 0.5 mL TrypLE (Gibco, 12604021) Express Enzyme for 3 minutes at 37°C. The cells were detached from the culture surface by pipetting and 1 mL cell culture medium added. The cells were collected into a falcon tube and centrifuged at 300 g for 4 minutes. Supernatant was discarded and cells were resuspended in pre-warmed fresh cell culture medium. The cell suspension was passaged 1:3 to a new cell culture plate. Medium was changed every 3 days. HCAECs were frozen by resuspending 1 x 10^6 cells in per mL freezing medium containing 60% cell culture medium with 10% dimethyl sulfoxide (DMSO, Sigma) and 30% KnockOut Serum Replacement (KOSR) (10828028, ThermoFisher). Cryotubes were stored at -80°C freezer for 24 hours before transfer to liquid nitrogen for long-term storage.

2.1.2. Immortalised cell line culture

HEK 293T cells were provided by Forbes Manson Group (University of Manchester, UK). Cells were cultured in Dulbecco's Modified Eagle Medium (DMEM) (Gibco, 31966021) supplemented with 10% Foetal Bovine Serum (FBS) (Gibco, 10500064). Cells were passaged at 80-90% confluence using TrypLE as described above. Cells were frozen by resuspending 1 x 106 cells in 1 mL freezing medium containing 90% growth medium and 10% DMSO.

2.1.3. Culture of iPSC cell lines

Both normal control and CADASIL patient iPSC lines (AGD-14) were previously established and characterised in our lab [226]. Both SW lines and AGD-14 lines were reprogrammed using Sendai virus. Control iPSC lines EIPL1 and SOJD3 are purchased from HipSci and characterised (https://www.hipsci.org/lines/#/lines/HPSI0314i-sojd_3). Wide type iPSC line

OX1-19 was provided by the Hooper Lab (University of Manchester, UK), which has been characterised previously [223]. Control iPSC lines SW171A and SW174A were provided by the Kimber Lab (University of Manchester, UK). All iPSC lines were cultured in 6-well plates with 2 mL medium and maintained at 37°C with 5% CO2. The OX1-19 iPSCs were plated onto Matrigel (Corning, 354277) pre-coated wells and cultured in mTeSR1 complete medium (85850, STEMCELL Technologies). The AGD-14 iPSC lines were maintained on Vitronectin Recombinant Human Protein (VTN-N) (ThermoFisher, A14700) pre-coated wells in presence of TeSR-E8 medium (Life Technologies, 05990). Both Matrigel and VTN-N were made according to the manufacturers' recommendations. Medium was changed daily and cells were passaged every 3 to 5 days when iPSCs reached 70% confluence or cell colonies were becoming too large and merging with one another. Colonies were passaged into small clumps using 0.5 mM UltraPure EDTA dissociation solution (Invitrogen, 15575020) and incubated for 3-5 minutes, and then cells were seeded with 2 mL of fresh culture medium with 10 μM. Rho kinase (ROCK) Inhibitor (Y-27632) (Sigma, SCM075). Cells were maintained and used during 18 to 50 passages.

All iPSCs were frozen in PSC Cryopreservation medium that was made according to the manufacturers' recommendations (Gibco, A2644601).

2.2. Differentiation of neurovascular unit (NVU) cells from iPSCs

2.2.1. iPSC-vMCs differentiation

iPSCs colonies with around 10-20 cells per cluster were seeded at 20% confluence on VTN-N pre-coated wells in TeSR-E8 medium containing 10 μM Y-27632. When reaching 30% confluency, the cells in smaller colonies were ready for differentiation, designated day 0. On day 0 of differentiation, TeSR-E8 medium was removed and replaced with Essential 6 medium (E6) (Life Technologies, A1516401) supplemented with 10 ng/mL Recombinant Human FGF-basic (FGF2) (PeproTech, 100-18C) and 10 μM SB431542 (Tocris, 1614). Medium was changed every day and cells were passaged (1 well split into 10 wells of 6-well plate) at day 5 using 10 μM EDTA solution and incubated at 37°C for 5 minutes until colony edges were slightly folded. Cell culture medium was added and pipetted to detach all the colonies and break them into single cells. Cell culture medium remained the same as day 0 until day 8 and was replaced daily, after which medium was replaced by E6 medium containing 10 ng/mL human Platelet-Derived Growth Factor BB (PDGF-BB) (PeproTech,

100-14B) and 2 ng/mL Recombinant Human Transforming Growth Factor-β1 (TGF-β1) (PeproTech, 100-21). Cells were passaged when reaching 70% confluency.
Cells were frozen at days 8 and15 in freezing medium containing 60% E6 medium with PDGF-BB and TGF-β1, 30% KOSR and 10% DMSO for future experiments. Mature iPSC-vSMCs after day 18 were used for experiments. After day 18, cells culture medium can be changed to Smooth Muscle Cell Growth Medium 2 (Promocell, C-22062).

2.2.2. iPSC-neuronal progenitor cell induction

A summary of the 'three-step' neuronal differentiation procedure is shown in **Figure 2.1**. iPSCs were dissociated with EDTA and seeded on 12-well plates (Corning) pre-coated with Matrigel prior to differentiation. iPSCs were induced to NPCs by suppression of the SMAD signalling pathway [227]. When cells reached 100% confluence, they were washed once with PBS and 1.5 mL of neural induction medium (NIM) was added per well. NIM was a combination of 1 μM Dorsomorphin (3093, Tocris) and 10 μM SB431542 in neural maintenance medium (NMM). NMM was a 1:1 mixture of N2 (Thermo Fisher Scientific, 17502001) and B27 medium (Thermo Fisher Scientific, 17504044). N2 medium consisted of DMEM/F-12 GlutaMAX medium (Life Technologies, 31331), 1 x N2, 5 μg/mL insulin (Sigma, I9278), 1 mM L-Glutamine (Life Technologies, 25030024), 100 μM Non-essential amino acids (NEAA) (Life Technologies, 11140), 100 μM 2-mercaptoethanol (Life Technologies, 31350) and 0.5% Penicillin-Streptomycin (10,000 U/mL) (Life Technologies, 15140). B27 medium consists of 1 x Neurobasal medium (Life Technologies, 12348), 1 x B27, 200 mM L-Glutamine and 0.5% Penicillin-Streptomycin. NMM was stored at 4°C for up to 3 weeks while NIM was stored at 4°C for up to 5 days.
On day 10-12 after induction, the cells formed a dense neuro-epithelial sheet and were passaged with 0.5 mL Dispase (Life Technologies, 17105) incubated for up to 7 minutes. After centrifuge at 300 g for 5 minutes, cells were resuspended and seeded at a ratio of 1:1 with 2 mL of fresh NIM onto Laminin (Sigma, L2020) pre-coated 6-well plate. After 24 hours incubation the medium was changed to NMM with 20 ng/mL FGF2 for 3-4 days. FGF2 was withdrawn when neural rosettes appeared and cells were incubated with NMM from then on. Cells were passaged 1:3 with Dispase into Laminin pre-coated well. Rosettes were isolated from cultures using Neural Rosette Selection Reagent (Stemcell Technologies, #05832), this was the NPC stage.

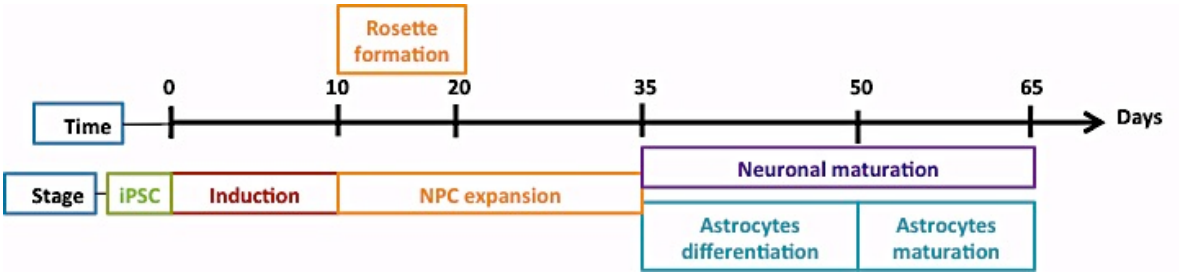

Figure 2.1 Schematic summary of neurons and astrocytes differentiation.

Schematic workflow shows differentiation process and timeline of iPSCs starting at day 0 with a bifurcation at day 35 for neural/astrocyte differentiation.

2.2.3. iPSC-neuron differentiation

On day 25 after induction, cells were dissociated into single cells with Accutase (Stemcell Technologies, #07920) and seeded onto Laminin pre-coated wells at a ratio of 1:1 in NMM, changed every other day. Mature neurons after day 60 were used for all experiments. Neuronal progenitor cells were frozen for future use at day 35 in neural freezing medium (10% DMSO in NMM + 20 ng/mL FGF2) per 35 mm dish of cells. Cells were not passaged after day 35 to avoid cell death.

2.2.4. iPSC-astrocyte differentiation

During neuron differentiation, selected neural rosettes were seeded onto Laminin pre-coated wells in 2 mL of NMM, incubated at 37°C for 24 hours, this was marked as day0 of astrocyte differentiation. On day1, medium was changed to 2 mL of complete STEMdiff™ Astrocyte Differentiation Medium (ADM) (Stemcell Technologies, #08540). On day7, when cells reached 90% confluence, cells were passaged with Accutase and incubated at 37°C for 5 minutes. After centrifuge at 300 g for 5 minutes, cells were resuspended in ADM onto Laminin pre-coated wells at a density of 1 x 10^5 cells/cm^2. On day14 cells were passaged again as described above. ADM was changed every other day. At day 21 the cells reached an immature astrocyte phenotype and were ready to passage again for astrocyte maturation.

On day 21, cells were passaged using Accutase and seeded onto Laminin pre-coated wells at a density of 1 x 10^5 cells/cm^2 in complete STEMdiff™ Astrocyte Maturation Medium (AMM) (Stemcell Technologies, #08550). Cells were passaged twice on days 28 and 35. AMM was changed every other day. After day 35, mature astrocytes were observed. Cells were frozen during maturation in astrocyte freezing medium (10% DMSO in AMM) for future use.

2.2.5. iPSCs differentiation to vECs

iPSCs colonies (approximately 8-12 colonies) with around 10-20 cells per cluster were seeded on to VTN-N pre-coated (overnight) T75 flasks in E8 medium containing 10 μM Y-27632. Cells were cultured for 24 hours undisturbed at 37°C in CO_2 incubator. At 30% confluency, the cells were ready for differentiation, termed day 0. On day 0 of differentiation, E8 medium was removed and replaced with Essential 6 medium supplemented with 6 uM CHIR99021 (Tocris Bioscience, 4423), 20 ng/mL Bone Morphogenetic Protein 4 (rBMP4) (PeproTech, 120-05) and 10 ng/mL FGF2. Cells were incubated in this medium for 3 days for mesoderm induction. On day 3, medium was replaced with 'Vascular Specification media', E6 supplemented with 50 ng/mL vascular endothelial growth factor (VEGF) (PeproTech, 100-20), 10 ng/mL FGF2 and 20 ng/mL rBMP4. Medium was changed at day 5. At day 7, medium was changed to 'Endothelial Amplification media', E6 medium supplemented with 50 ng/mL VEGF, 10ng/mL FGF2 and 10 μM SB431542. The same medium was changed at days 9 and11.

At day 12, endothelial cells were purified using a CD31 MicroBead Kit (Miltenyi Biotec, 130-091-935), described below. The purified cells were further cultured with Promocell endothelial cell medium (MV2) until use. Cells were frozen between days 12-14 after purification in freezing medium containing 90% MV2 medium and 10% DMSO at a density of 1 x 10^6 cell per mL.

2.2.6. MACs dynabead purification of iPSC-ECs

At day 12 of iPSC-EC differentiation, MACs $CD31^+$ dynabead kit was used to purify mature ECs. 5mL Trypsin-EDTA (Sigma, T392) was added to cells for per T75 flask for dissociation and incubated for 5-10 minutes. When all cells were detached from the bottom of the flask, 5 mL EC Growth Medium was added to inactivate the trypsin. Cells suspensions were passed through a filter (40 μm pore size) (Fisher Scientific, 10737821) to harvest single cells. A cell count was performed by taking 10 μL of the cell suspension and mixed with 10 μL trypan blue and counted using a Countess™ II FL Automated Cell Counter (Invitrogen, AMQAF1000). Volumes given are for up to 1 × 10^7 cells. The cell suspension was centrifuged at 300 g for 5 minutes. A maximum of 1 × 10^7 cells were resuspended in 60 μL of medium to which was added 20 μL of FcR Blocking Reagent and 20 μL of $CD31^+$ MicroBeads. After 15 minutes of incubation in 4°C, 1 mL of E6 medium was added and cells were centrifuged at 300 g for 3 minutes. The cell pellet was resuspended in 1 mL of E6

medium. LS Columns were placed in the magnetic field of a MidiMACS Separator and rinsed with 3 mL E6 medium. The cell suspension was applied onto the column and unlabelled cells that passed through were collected. The column was washed with 3 × 3 mL of medium to ensure the removal of all unlabelled cells. Columns were removed from the separator and placed on a suitable collection tube. Cells bound to $CD31^+$ beads were collected by addition of 5 mL of Endothelial Cell Growth Medium MV2 to the column and flushed through by a plunger. The labelled cells can be directly taken into culture. The cells were ready for experiment when confluent.

2.2.7. Differentiation of iPSC into brain microvascular endothelial cells (BMECs)

iPSCs were cultured using TESR-E8 medium on Matrigel pre-coated wells. At a cell density approximately 25,000-400,000 per well of 6 well plates differentiation was induced, termed day 0. From day 0 to day 5 the medium was changed daily with 2 mL Unconditioned Medium (UM) containing DMEM/F-12, 20% KOSR, 1 x NEAA, 0.5 x L-glutamine and 0.1 mM β-mercaptoethanol. UM was stored at 4°C for up to two weeks. Cultures at day 5 contain a mixed endothelial and neural progenitor cell population. From day 6 to 8 the BMEC population was expanded. At day 6, medium was changed to 3 mL EC + retinoic acid (RA) medium containing Human Endothelial serum free medium (hESFM) (Invitrogen, 11111) with 1% filter sterilised Human Platelet Poor Plasma-derived Serum (HS) (Sigma, P2918), 20 ng/mL FGF2 and 10 uM All-trans RA (Sigma, R2625). Medium was not changed at day 7. At day 8, BMECs were purified by subculturing onto a Transwell to establish an in vitro BBB model as described below.

2.2.8. In vitro BBB model

An In vitro BBB model was established by growing iPSC-BMECs on the insert of the Transwell as mentioned above. Once a confluent layer of BMECs was formed on the filter membrane of the insert, a simulated BBB was formed between the upper and lower chambers of the Transwell culture. On day 8 of the BMECs differentiation, Collagen IV (Sigma, C5533) was prepared by dissolving of Collagen IV in 0.5-2.0 mg/mL acetic acid to 1 mg/mL which was used to make a collagen IV/fibronectin (Sigma, F1141)/ water (C/F/W, 4:1:5) solution to pre-coate the 0.4 μm insert membrane of a 12-well Corning polyester Transwell plate (Sigma, CLS3460). For 6-well plate pre-coating the C/F/W solution can be diluted 5 times. The iPSC-BMECs were then dissociated using Accutase (Invitrogen, A1110501) at 37°C for 20-60 minutes (typically 45 minutes), until 90% cells visibly detached from plates. The cell

suspension was then collected and centrifuged for 5 minutes at 300 g. Cells were then resuspended in EC+RA medium and 1.1 x 10^6/cells were seeded on to the C/F/W pre-coated 12-well Transwell filters. The lower chamber of the Transwells received 1.5 ml EC+RA medium, thus, an *in vitro* BBB model was formed. A proportion of the iPSC-BMECs were seeded onto cover slips or 6-well plates for immunofluorescence staining, qRP-PCR and co-culture experiments described below. From day 9, medium was changed to hESFM medium with 1% HS (without FGF2 or RA) daily before TEER measurement or sodium fluorescein permeability assay as described below.

2.2.9. Co-culture of iPSC-NVU cell types in Transwell settings

NVU cells were co-cultured in Transwells. iPSC-derived BMECs at day 8 were singularized with Accutase for 40 minutes and seeded onto 0.4 μm pore diameter 12-well Transwell inserts coated with C/F/W at a density of 1 x 10^6 cells/cm^2. In the iPSC-BMECs and iPSC-vMCs co-culture system, 1 x 10^5 cells per well iPSC-vMCs were seeded two days before seeding iPSC-BMECs either on the bottom of the 12-well plates (mimicking indirect contact) or onto the bottom side of the Transwell (mimicking direct contact) both pre-coated with Vitronectin. For the direct contact co-culture model, iPSC-vMCs were grown on the bottom side of the Transwell for 24 hours with the Transwells upside down. Then the Transwells were placed into 12-well plates with fresh Smooth Muscle Cell Growth Medium 2. The top chamber of the Transwell was then pre-coated with 200 uL Matrigel and incubated in a CO^2 incubator for at least 1 hour. iPSC-BMECs were seeded into the top chamber afterwards. In the iPSC-BMECs and iPSC-neurons or iPSC-astrocytes co-culture system, 1 x 10^5 cells per well iPSC-neurons or iPSC-astrocytes were seeded onto the bottom side of the 12-well plates pre-coated with Laminin at least one week before BMECs seeding.

Immediately following iPSC-BMEC seeding, BMEC-coated Transwells were then placed into plates with either no cells, iPSC-vMCs mimicking direct and indirect contact, iPSC-neurons, iPSC-astrocytes or with 2 cell types. All experimental groups were cultured in hESFM supplemented with 1% HS and 20 ng/mL FGF2 with or without retinoic acid for an initial 24 hours and switched to hESFM supplemented with 1% HS for the remainder of the experiment. The upper chamber of the Transwells contained 0.5 mL of medium and the lower chamber 1.5 mL medium.

2.2.10. Direct co-culture of iPSC-NVU cell types

Control iPSC-BMECs at day 10 of differentiation grown on C/F/W pre-coated plates were washed with PBS and dissociated with 1 mL Accutase solution for 20-40 minutes. Cells were counted using Countess™ II FL Automated Cell Counter. After centrifugation at 300 g for 5 minutes, 1 x 10^5 BMECs were resuspended in 1 mL hESFM supplemented with 1% HS for each well. Then cells were seeded onto 3 wells of C/F/W pre-coated 12-well plates and incubated for 24 hours in a CO^2 incubator. After 24 hours, iPSC-vMCs at day 18 of differentiation were dissociated with 0.5 mL TrypLE solution and incubated in 37°C for 3 minutes. iPSC-vMCs were collected and centrifuged at 300 g for 5 minutes with the addition of 5 mL Smooth Muscle Cell Growth Medium 2. Cells were counted using Countess™ II FL Automated Cell Counter and 1 x 10^5 cells were resuspended in 0.5 mL fresh Smooth Muscle Cell Growth Medium 2 for each well. Then the medium for iPSC-BMECs was replaced with 0.5 mL fresh hESFM supplemented with 1% HS. iPSCs-vMCs in 0.5 mL Smooth Muscle Cell Growth Medium 2 were seeded directly onto iPSC-BMEC monolayers. Co-cultured cells were incubated in a 37°C CO_2 incubator for 24 hours. Cell morphology images were acquired at 24 hours after co-culture on an EVOS™ XL Core Imaging System microscopy using 4x and 40x objectives.

2.2.11. SiRNA knockdown of NOTCH3 in iPSC-BMECs

The *NOTCH3* specific siRNA (FlexiTube GeneSolution, GS4854) targeting the NM_00435 transcript (precursor of Notch3 receptor) and a scrambled negative control siRNA were purchased from Qiagen. Notch3 siRNA 5'-ATGCCTAGACCTGGTGGACAA-3' and negative control was delivered into HCAECs and iPSC-BMECs by electroporation using a SF Cell Line 4D-Nucleofector System (Lonza, V4XC-2032). Briefly, HCAECs or iPSC-BMECs were trypsinised for counting and collected, as previously described, in aliquots of 1 x 10^6 cells. After centrifuge AT 300 g for 5 minutes the cells were resuspended in 100 uL of Nucleofection Solution SF solution (Lonza, V4XC-2032) (1 x 10^6 cells/sample) with 300 nM of N3 construct (stock 10 μM). Then the samples were transferred into a nucleocuvette (Lonza) using pasteur pipettes (Lonza) to avoid bubbles. The nucleocuvette was loaded into the 4D nucleofector system. Pre-set program CM-137 and CA-137 were used respectively for HCAECs and iPSC-BMECs transfection. After electroporation 500 uL pre-warmed cell culture medium was added to the nucleocuvettes and mixed gently to resuspend the cells.

Cells were then seeded dropwise into wells with pre-warmed medium and incubated for up to 48 hours to ensure sufficient down-regulation of NOTCH receptor for analysis.

2.3. Immunofluorescent staining

Cells were washed twice with PBS and fixed with 4% paraformaldehyde (PFA) (11400580, Alfa Aesar™) for 15 minutes at room temperature. PFA was removed and cells were washed 3 times with PBS. IPSCs were then permeabilised in PBS containing 0.2% Triton X-100 for 3 minutes (10 minutes for non-iPSCs) at room temperature to allow detection of intracellular proteins. Cells were gently rinsed twice with PBS and then incubated in blocking buffer (10% donkey serum diluted in PBS) and placed on a shaker for 3-4 hours at room temperature or overnight at 4°C. Cover slips were transferred onto parafilm in a moist chamber and incubated with 40 uL primary antibody diluted in blocking buffer for 1 hour at room temperature or overnight at 4°C. For antibody details see **Table 1**. Cells were washed 3 times with PBS. The appropriate fluorescent conjugated secondary antibodies (1:500) were diluted in blocking buffer and applied to cells (200 µL/coverslip) for 1 hour in the dark at room temperature. Cover slips were washed 3 times with PBS followed by 2 times with ddH_2O and left to dry before mounting coverslips face down onto a slide using prolong gold with DAPI (Thermo Fisher Scientific, P36935). Images were collected on an Olympus BX51 upright microscope using an objective (20x / 0.5 UPlan FLN) and captured using a Coolsnap ES2 camera (Photometrics) through Metavue v7.8.4.0 software (Molecular Devices). Specific band pass filter sets for DAPI, FITC and Texas red were used to prevent bleed through from one channel to the next. Images were then processed and analysed using Fiji ImageJ (http://imagej.net/Fiji/Downloads).

For the BMEC junctional protein immunofluorescent staining, BMECs were fixed and stained for junctional proteins (Occludin, ZO1) as described above. To quantify tight junction continuity, images were blinded and the area fraction index was determined using imageJ. In addition, images were blinded, and the number of frayed junctions was manually counted.

2.4. Quantitative real time polymerase chain reaction (qRT-PCR)

2.4.1. RNA extraction

Total RNA from cells (less than 1 x 10^7) was extracted using a RNeasy mini kit (Qiagen, 74104) following the manufacturer's protocol. Cells were dissociated and centrifuged at 300 g for 5 minutes. The supernatant was completely discarded and the cell pallet was lysed in buffer RLT. Lysate was homogenised by centrifugation through Qiashredder columns

(Qiagen, 79654) at 10,000g in a table-top centrifuge for 3 minutes. An equal volume of 70% ethanol was added to the lysate and the total volume of the sample was mixed well by pipetting then transferred to the RNeasy Mini spin column and centrifuged at 8,000 g for 15 seconds. Flow-through was discarded and buffer RW1 was added to the column then centrifuged again and the flow-through discarded. Two additional wash steps were performed by adding buffer RPE and centrifuged at 15 seconds and 2 minutes respectively in order to remove the salts in lysis buffer which could interfere with reverse transcription of mRNA and polymerase chain reaction of cDNA. Then an additional centrifugation was carried out to remove any remaining liquids. The RNA was eluted by addition of 20-30 uL of RNase free water to the membrane of the spin column and centrifuged at 8,000 g for 1 minute. The RNA concentration and purity were measured using the SimpliNano spectrophotometer (Biochem, 29061711) according to the manufacturer's instructions. RNase free water was used for calibration.

2.4.2. cDNA synthesis

A High-Capacity RNA-to-cDNA™ kit (Thermofisher, 4387406) was used for the reverse transcription of mRNA to cDNA according to the manufacturer's protocol. Reverse transcription reactions consisted of 10 µL of RT buffer mix (x2), 1 uL of RT enzyme mix (x20), 200 ng RNA with the remaining volume RNase free water up to 20 µL total (Table 2). After a brief vortex, tubes were centrifuged briefly and transferred to the QuantStudio 3 (Applied Biosystems) Real-Time PCR System for cDNA synthesis. The reaction conditions can be found in **Table 2.2**. When cDNA synthesis was finished the samples were stored at -20 °C.

2.4.3. qRT-PCR

Ten ng/ml cDNA was combined with 10 ul PowerUp™ SYBR™ Green Master Mix (A25742, Thermofisher) and primers purchased from Eurofins Genomics (**Table 2.4**), used at a final concentration of 1 uM/uL. The volume was made up to 20 uL with DEPC-Treated water. Each sample was prepared in triplicate in 96-well plate. A plate seal film was used to cover the plate. After a brief centrifuge the plate was transferred into the QuantStudio 3 (Applied Biosystems) Real-Time PCR System. Samples were held for 10 minutes at 95°C. For PCR 40 cycles of 95°C for 15 seconds then annealing step at 60°C for 1 minute were conducted. The melt curve stage kept samples at 95°C for 15 seconds before holding at 60°C for 60 seconds (**Table 2.3**).

Data was analysed using the ΔΔCt method. The endogenous control was *GAPDH* while untreated or wild type samples were used as calibrators. Ct values of the gene of interest (GOI) in both control and test samples were normalized using the endogenous control (norm) gene Ct. The resulting ΔΔCt value was shown to determine the fold difference in expression compared to the calibrator:

Fold difference = $2^{-\Delta\Delta Ct}$

$\Delta Ct_{\text{sample}} - \Delta Ct_{\text{calibrator}} = \Delta\Delta Ct$

$Ct_{GOI}{}^{s} - Ct_{norm}{}^{s} = \Delta Ct_{\text{sample}}$

$Ct_{GOI}{}^{c} - Ct_{norm}{}^{c} = \Delta Ct$ calibrator

2.5. iPSC-NVU cell functional assays

2.5.1. Angiogenesis tube formation assay for endothelial cells

Briefly, 1 x 10^4 HCAECs/ HUVECs/ iPSC-derived ECs or BMECs in 200 µL cell culture medium was plated onto a thin layer of Matrigel (50 µL per well) (354234, Corning) in 96-well plates. The Matrigel was pre-coated overnight. Respectively, iPSC-ECs at day 14 or iPSC-BMECs at day 10 of differentiation were used for tube formation. Accutase was used for cell dissociation as previously described. After cell counting and centrifuge at 300 g for 5 minutes, HCAECs were seeded in 200 µL Endothelial Cell Growth Medium MV2. iPSC-ECs were seeded in E6 supplemented with 5 ng/mL VEGF-165 and 2 ng/mL FGF2. iPSC-BMECs were seeded in hESFM with 50 ng/mL VEGF-165 without RA or FGF2. Phase-contrast images were acquired at 3, 6, 24, 48 and 72 hours of culture in a CO2 incubator on an EVOS™ XL Core Imaging System microscopy (AMEX1000, ThermoFisher Scientific) using 4x objectives.

2.5.2. Low density lipoprotein (LDL) uptake assay

Differentiated BMECs at day 10 were analysed with the Dil-ac-LDL dye (J65597, Alfa Aesar). Culture medium was aspirated then incubated in medium containing 12 µg/mL Dil-ac-LDL for 4 h at 37°C, 5% CO2. Cells were then washed three times with PBS, fixed with 4% paraformaldehyde for 10 minutes. Cells were then washed two times and incubated with 0.1% Triton X-100 for 5 minutes, followed by 30 minutes blocking with 10% donkey serum. Cells were then stained with donkey anti-Rabbit 594 secondary antibody at 1:500 dilution. Images were taken with a fluorescent microscope with excitation and emission wavelengths of 591 nm and 614 nm, respectively.

2.5.3. Calcium wave imaging of astrocytes

At day 100, astrocytes derived from OX1-19 iPSCs were labeled using the Ca^{2+} indicator dye Fluo-4 AM (Invitrogen, ThermoFischer Scientific) with incubation at 37°C and 5% CO^2. The excitation/emission wavelengths were set to 494/506 nm in Ca^{2+}-bound form. Recordings were made by confocal time-lapse microscopy under a Zeiss LSM 880 Biolumi confocal laser scanning microscope with a 40x oil objective (Carl Zeiss, UK). The fluo-4 AM dye was loaded at 20 μM for 30-60 minutes depending on absorption rate of individual cells until the basal fluorescence of fluo-4 in all cells plateaued to a constant level. Spontaneous activity of cells was recorded for 10 minutes. Five random fields were chosen under microscopy and averaged for each sample. Time-lapse recording and images were analysed using Zeiss microscopy software ZEN, MicroExcel and ImageJ.

2.5.4. Assessing barrier function by transendothelial electrical resistance (TEER) measurement

Barrier tightness was measured by the voltage difference from the movement of ions across the Transwell membrane on 12-well Transwell inserts with a 0.4 μm pore size. From day 9 to day 13 of iPSC-BMECs differentiation, TEER measurements were taken at 24, 48, 72, 96 and 120 hours after cell seeding using an Epithelial Volt/Ohm Meter EVOM2™ (EVOM with STX2 electrodes, World Precision Instrument) following the manufacturer's instructions. TEER was measured one plate at a time to avoid temperature decreases. Medium was changed 30 minutes before measurement.

TEER measurements were normalized by subtracting the background (TEER from a blank well) and then multiplied by the surface area (1.12 cm^2) of the Transwell filter and reported as ohms/cm^2. All TEER experiments were performed with at least 3 triplicate wells, and at least three independent differentiations. The peak TEER represents the TEER value at the time point that the average of the technical replicates yielded the maximum TEER value (typically at 48 hours).

2.5.5. Assessing barrier function by sodium fluorescein permeability assay

Sodium fluorescein permeability was measured at day 10 in 12-well Transwell settings as described previously [228]. At day 8, cells were cultured onto C/F/W pre-coated Transwells at a density of 1.1 x 10^6 cells per well of 12-well Transwell. The permeability coefficient of the cells was indicated as Pe (centimeters per minute). A blank pre-coated Transwell was set up as control to determine the Pe value for each experiment. TEER was measured at 48 hours

for the maximum TEER value before the permeability assay. The medium was then removed and pre-warmed hESFM with 1% HS was added to the top chambers (0.5 mL) and the bottom wells (1.5 mL). The cells were incubated for 60 minutes at 37°C, followed by TEER measurement to ensure the starting barrier tightness. Sodium fluorescein salt (F6337, Sigma) was diluted to 10 uM in hESFM with 1% human serum. Medium in the top chamber was removed and replaced with 500 uL of the fluorescein loaded medium. After briefly pipetting up and down, 150 uL medium from the bottom well was collected at 15, 30, 45 and 60 minutes then transferred to a 96-well plate. After each sampling 150 uL fresh pre-warmed cell culture medium was added to the bottom well. After 60 minutes, 150 uL of medium was collected from the top Transwell chamber and pipetted into a 96-well plate. As a control 150 uL of hESFM including 1% HS without sodium fluorescein was placed in the 96-well plate. The 96-well plate was placed in a Fluorescent plate reader (Synergy HT platereader, BioTek) and readings taken at 485 nm excitation/530 nm emissions.

2.6. Statistics

Statistical significance was set at $p<0.05$ and was considered to be normally distributed and further statistical tests were then applied. Comparisons of two groups were made using an unpaired t-test. Levene's test for equality of variances was applied, and where appropriate Welch's correction was used to account for unequal variance. For comparisons of data sets above two samples, one-way or two-way ANOVA was used were performed followed by the Tukey's post-hoc test or Bonferroni post-hoc test to confirm the differences between two groups. The data analysis was performed with using Prism version 7 (GraphPad Software, La Jolla, CA) unless otherwise indicated. Data are shown as mean ± standard error (SEM) unless otherwise indicated. n represents the number of samples.

Table 2.1 Antibodies information for immunofluorescent staining

Role	Antibody	Host	Localization	Supplier	Dilution
Pluripotency markers	OCT4	Rabbit	Nucleus	Abcam Ab109884	1:500
	SOX2	Rabbit	Nucleus	Abcam Ab109884	1:500
	SSEA4	Mouse	Cytoplasm	Abcam Ab109884	1:200
	Nanog	Rabbit	Nucleus	Abcam Ab109884	1:200
SMC markers	CNN1	Rabbit	Cytoskeleton	Abcam EP798Y	1:200
	α-SMA	Goat	Cytoskeleton	Abcam ab21027	1:200
NPC markers	PAX6	Mouse	Nucleus	Covance PRB-278P	1:500
	FOXG1	Mouse	Nucleus	Abcam Ab18259	1:500
	SOX1	Rabbit	Nucleus	Abcam ab87775	1:500
Neuronal markers	TBR1	Rabbit	Nucleus	Abcam ab31940	1:500
	MAP2	Mouse/Chicken	Cytoplasm	Abcam Ab92434	1:600
	β-TUB	Rabbit	Cytoplasm	Abcam ab18207	1:500
Cell surface marker	CD44	Rabbit	Membrane	Abcam ab157107	1:250
Astrocyte markers	GFAP	Chicken	Cytoplasm	Abcam ab4674	1:600
	S100β	Rabbit	Cytoplasm/ Nucleus	Abcam ab52642	1:200

EC/ BMEC / Junctional markers	PECAM-1	Mouse	Membrane	Bio Techne BBA7	1:200
	VE-Cadherin	Mouse	Membrane	Bio Techne MAB9381	1:200
	ZO-1	Mouse	Membrane/ Tight junction	Life Technologies 617300	1:200
	GLUT-1	Mouse	Membrane	Life Technologies MA511315	1:50
	Occludin	Mouse	Membrane/ Tight junction	Life Technologies 331500	1:200
	Claudin-5	Mouse	Membrane/ Tight junction	Life Technologies 352500	1:100
	Connexin 43	Rabbit	Membrane/ Gap junction	Abcam ab11370	1:500
Notch signaling marker	NOTCH3 ECD	Mouse	Cytoplasm	Abnova H00004854-M01	1:200
	NOTCH ICD	Rabbit	Nucleus	Abcam Ab23426	1:200

Secondary antibody

Donkey pAb anti-Rabbit Alexa Fluor® 594	Abcam	ab150064	1:500
Donkey pAb anti-Mouse Alexa Fluor® 488		ab150105	
Goat pAb anti-Chicken Alexa Fluor® 647		ab150175	
Donkey pAb anti-Goat Alexa Fluor® 488		ab150029	

Table 2.2 cDNA synthesis system

Reagent	Volume
RT buffer mix (x2)	10 µL
RT enzyme mix (x20)	1 µL
RNA	200ng (Up to 9 µL)
DEPC-Treated Water	To a total volume of 20 µL

Temperature	Time
37 °C	60 minutes
95 °C	5 minutes
4 °C	Hold

Table 2.3 qRT-PCR reaction system

Reagent	Volume
PowerUp™ SYBR™ Green Master Mix	10 µL
Forward Primer	0.5 µL (final 1 µM)
Reverse Primer	0.5 µL (final 1 µM)
cDNA	1 µL
DEPC-Treated Water	8 µL

Stage	Cycles	Steps	Temperature	Time
Hold	1	Initial denaturation	95 °C	10 minutes
Cycling	40	Denature	95 °C	15 seconds
		Annealing	60 °C	60 seconds
Melt Curve	Step and Hold	Extension	96-60	30 minutes

Table 2.4 Primers used in qRT-PCR

Target genes	Forward sequence (5'-3')	Reverse sequence (5'-3')
OCT4	CGAGAGGATTTTGAGGCTGC	CGAGGAGTACAGTGCAGTGA
NANOG	TTAATAACCTTGGCTGCCGT	GCAGCAAATACGAGACCTCT
SOX2	GGAGCTTTGCAGGAAGTTTG	GCAAGAAGCCTCTCCTTGAA
PECAM	GAGTATTACTGCACAGCCTTCA	AACCACTGCAATAAGTCCTTTC
Ve-cad (CDH5)	GGTCCCTGAACGCCCTGGTAA	GGAGTGGAGTATGGAGTTGGAGCA
GLUT1	AGGTGATCGAGGAGTTCTAC	TCAAAGGACTTGCCCAGTTT
MAP2	AAACTGCTCTTCCGCTCAGACACC	GTTCACTTGGGCAGGTCTCCACAA
βIII-TUBULIN	CCCGTTATCCCAGCTCCAATATGCT	ATGGCTTGACGTGCGTACTTCTCC
GFAP	GTCCCCCACCTAGTTTGCAG	TAGTCGTTGGCTTCGTGCTT
S100b	TGTAGACCCTAACCCGGAGG	TGCATGGATGAGGAACGCAT
ALDH1L1	TCACAGAAGTCTAACCTGCC	AGTGACGGGTGATAGATGAT
GLT1	CTGGGCTTTATGCAGGATTC	CAATGGGGATTGTGAATGTG
GLAST (EAAT-1)	ACCCCAAGCATTCTGTGC	TTCCGAAATAGAGCCTCGAC
NOTCH3	CATCTCCGACCTGATCTGCC	GTCTGTAGAGCGGTTTCGGA
Brachyury (T)	GGGTGGCTTCTTCCTGGAAC	TTGGAGAATTGTTCCGATGAG
KDR	GGGAAAGCATCGAAGTCTCA	CGTCCTCCTTCCTCACTCTG
MESP1	TGTACGCAGAAACAGCATCC	TTGTCCCCTCCACTCTTCAG
ISL1	AGATTATATCAGGTTGTACGGGATCA	ACACAGCGGAAACACTCGAT

OCLN	GACTTCAGGCAGCCTCGTTAC	GCCAGTTGTGTAGTCTGTCTCA
CLDN5	GTTCGCCAACATTGTCGTCC	GTAGTTCTTCTTGTCGTAGTCGC
TJP1 (Zo-1)	ACCAGTAAGTCGTCCTGATCC	TCGGCCAAATCTTCTCACTCC
P-glycoprotein (ABCB1)	CTCATCGTTTGTCTACAGTTCG	AAGACATTTCCAAGGCATCA
SOX1	CCTCCGTCCATCCTCTG	AAAGCATCAAACAACCTCAAG
CNN1	GTCCACCCTCCTGGCTTT	AAACTTGTTGGTGCCCATCT
α-SMA	TGACAATGGCTCTGGGCTCTGTAA	TTCGTCACCCACGTAGCTGTCTTT
SM22α	CGCGAAGTGCAGTCCAAAAT	CAGCTTGCTCAGAATCACGC
SMMHC	GACTTCCCTGCTCAATGCCT	GGACCTCTTCTCGTGGTTGG
SMTN	CGGCTGCGCGTGTCTAATCC	CTGTGACCTCCAGCAGCTTCCG
GAPDH	CATGTTCGTCATGGGTGTGAACCA	ATGGCATGGACTGTGGTCATGAGT

3. Chapter 3: Differentiation and characterisation of iPSC-BMECs

3.1. Introduction

3.1.1. iPSC model for VaD

CADASIL is the most common type of vascular dementia and currently there's no treatment for this condition. The main pathological changes in CADASIL include vSMCs degeneration, NOTCH3 accumulation, ECs dysfunction and CBF dysregulation [229, 230]. Previous cell models of CADASIL are mainly based on overexpression of the mutant NOTCH3 protein, mainly by HEK cells. Although it has been found in these cell models how mutations affected NOTCH3 protein activity, CADASIL pathologies, *in vivo*, are in vSMCs [42]. Thus, it's necessary to develop mutant NOTCH3 models in vSMCs to assess how mutations affect cell functions in the relevant cell type.

Although several knock-in, knockout or transgenic mice models of CADASIL with different *Notch3* defects have been generated, they cannot faithfully mimic the human phenotype. One transgenic CADASIL mice model carrying mutant NOTCH3 Arg90Cys developed CADASIL pathological features such as NOTCH3 accumulation and deposition of GOM. However, the phenotype was more obvious in the tail arteries than in the brain and these mice did not undergo stroke [231, 232]. Another mice model carrying an Arg142Cys NOTCH3 knock-in mutation did not develop a CADASIL-like phenotype. The mutant NOTCH3 receptor was processed normally and did not appear to accumulate the extracellular domain, which has been observed in CADASIL patients [233]. Therefore, further work is required to explore new models for CADASIL with NOTCH3 mutation to investigate the pathologies of the disease.

The discovery of iPSCs with their capabilities of differentiation to various cell types have provided a promising platform for disease modelling and cell therapy. The Nobel Prize winning discovery was made in 2006 when Japanese scientist Yamanaka successfully generated iPSCs from somatic cells for the first time through induction with 4 transcription factors [234]. Moreover, the generation of iPSCs from somatic cells of patients with certain disease and differentiation to related cell types provides a platform for *in vitro* disease modelling and the discovery of new drugs [235]. From current reports, for neurodegenerative diseases such as AD, PD and HD, patient specific iPSCs have been used to generate neuronal cell types and build disease models to investigate the disease mechanisms or potential

therapies [236-239]. However, the application of iPSCs on SVDs and VaDs has been poorly explored.

Currently, only two papers, both published in 2019, demonstrating the use of iPSC-derived vMCs models to investigate CADASIL pathology. One of the models used vMCs differentiated from CADASIL-specific iPSCs, which showed gene expression changes associated with disease phenotypes, including activation of the NOTCH and NF-κB signalling pathway, cytoskeleton disorganization, and excessive cell proliferation. In comparison, these abnormalities were not observed in vECs derived from the patient's iPSCs [240]. In the other model, iPSCs were differentiated into vMCs and vECs carrying NOTCH3 mutations and it was demonstrated for the first time a failure of the patient iPSC-vMCs in engaging and stabilizing endothelial capillary structures. The patient iPSC-vMCs had reduced PDGF-BB expression and decreased secretion of the angiogenic factor VEGF, and could also induce apoptosis of adjacent vECs [223]. The two models of iPSC-CADASIL demonstrated disease pathologies with vMCs and vECs derived from patients. However, the endothelial cells involved in both researches are peripheral rather than BMECs.

Considering from natural history of CADASIL (Figure.3.1) [241], it is yet to be explained why migraine with aura first starts at young age around 30 years while ischaemic events happen between 50 and 60 years. This suggests that CADASIL may not only involve vascular cell dysfunction, there might be defects in neurovascular interactions as well. Previous CADASIL research mainly focused on vSMCs and mutant NOTCH3 protein, leaving the neurovascular pathology poorly investigated. Moreover, identifying the molecular and cellular mechanisms underlying the neurovascular interaction defects in CADASIL will advance our understanding of the vascular contributions to other dementias.

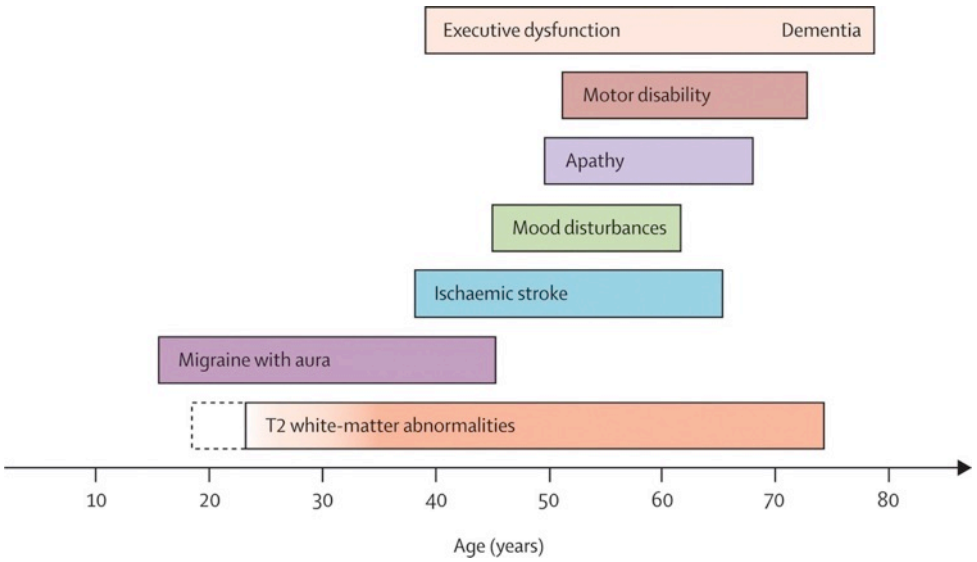

Figure 3.1 Natural history of the main clinical manifestations of CADASIL [239]

The exact age at earliest onset of T2 white-matter abnormalities is uncertain represented by the dashed line. The frequency of T2 white-matter abnormalities increases gradually and becomes constant by around 35 years in all patients. Migraine with aura can happen at very young age between 10-20 years old while ischemic stroke can occur from middle age and progressively leads to dementia.

3.1.2. iPSC-BMECs model in vascular dementia

The NVU comprises BMECs, vMCs, neurons, astrocytes and glial cells, the functional connections between which are involved in the formation of the BBB [242]. The NVU controls BBB permeability, CBF and neuroinflammation [243]. The BBB is a specialised structure in the cerebral vasculature and is not seen in other organs. The BBB functions due to the TJs complexes between the BMECs and the interaction with other NVU cell types. VMCs play an important role in the BBB function through direct contact with BMECs[244].

The BBB serves to limit the entry of toxic agents, blood cells and pathogens into the cerebral parenchyma, thus protecting the brain from harmful substrates in the blood that may cause injury, whilst also protecting the brain from systemic hormones and neurotransmitters [245]. During embryonic development, the BBB barrier possess a TEER from 500 Ωxcm^2 to around 1500 Ωxcm^2 with decreased permeability to water-soluble compounds such as mannitol, potassium or urea [246, 247]. The adult BBB boasts an elevated TEER as a result of adult brain microenvironment, where pericytes, neuronal cells and astrocytes play important roles in BBB maturation and maintenance, measured at values between 1000–6000 Ωxcm^2 and a

lower passive permeability to small molecules [246, 247]. These mature BMECs also express a series of molecule transport proteins including nutrient influx transporters and efflux transporters such as p-glycoprotein (p-gp) [248].

Current mouse disease models for BBB largely relied on knockout of mutated genes but failed to recapitulate phenotypic alterations. Because of the limitations of *in vivo* models, *in vitro* models have been developed to mimic BBB and study the cerebral vascular disease pathologies. Due to the difficulty in the removal of primary BMECs from the brain and their survival after isolation, an alternative method is to use immortalised BMEC lines such as the hCMEC/D3 (Human Cardiac Microvascular Endothelial Cells) cell line and the mouse bEnd.3 cell line [249]. However, while these immortalised cell lines have high capacity of expansion and maintain many aspects of primary BMEC properties, they failed to show significant barrier function [250, 251]. As a result, it would be useful to use iPSCs as a new approach to obtain a human in vitro BBB disease model.

Currently there are several methods established for the differentiation of BMECs from stem cells including iPSCs. Previous studies have shown that human BMEC-like cells can be generated from stem or progenitor cell sources [213], including hematopoietic stem cells [219], endothelial progenitors [252], and iPSC-derived peripheral ECs co-cultured with iPSC-derived pericytes, astrocytes, and neurons [219]. However, none of the previous studies demonstrated a robust process for generating human BMECs exhibiting functional BBB phenotypes. Recent iPSC-BBB models mainly followed or refined from the neural co-differentiation protocol developed by Lippmann *et al.* [220, 221]. This method was based on the hypothesis that simultaneous differentiation of iPSCs to both neural and endothelial lineages could lead to iPSC-derived endothelial cells with BBB attributes. This protocol described the generation of pure iPSC-derived BMECs through co-differentiation of iPSCs to neural and endothelial progenitors, followed by selective purification of the BMECs. It also demonstrated addition of RA during BMEC differentiation could enhance the barrier properties.

Mature iPSC-derived BMECs should not only exhibit EC properties, including the expression of CD31, formation of tube-like structures on Matrigel, uptake of LDL, but also express junctional proteins and show barrier function. Interactions between the NVU cells can be assessed by both direct contact that relies on the junctional proteins and indirect contact via secretion of growth factors between these cells.

3.1.3. CADASIL and control iPSC source

Various iPSC lines were used for experimental work. The CADASIL iPSC lines (AGD-14-01 and AGD-14-04) and control iPSC lines AGD-14-02 used in this project had already been established in the Tao Wang lab. Briefly, human dermal fibroblasts (HDFs) obtained from skin biopsy samples of two CADASIL patients carrying mutations of NOTCH3 (Arg153Cys or Cys224Tyr) and two control individuals, were successfully reprogrammed into iPSCs using Sendai virus [223]. CytoTune-iPS 2.0 Reprogramming Kit purchased from Life Technologies was used for the reprogramming of these iPSCs, which utilised Sendai virus to deliver two vectors c-Myc and 'KOS' (carries KLF4, OCT4 and SOX-2) into the cells.

The characterisation for pluripotency of iPSCs used in all the experiment is vital for the successfully differentiation of iPSCs into neuronal and vascular cells described in this thesis. It's also important to ensure the genomic integrity of the patient iPSCs be maintained before using them for disease modelling experiment. As iPSCs have the ability of self-renewing and differentiating to three germ layers, iPSCs pluripotency could be assessed by embryoid body formation in vitro for the spontaneous differentiation of iPSCs into three germ layers including ectderm, mesoderm and endoderm.

iPSCs are characterised by their expression of pluripotency markers, self-renewal and ability to differentiate along the three germ layers, ectoderm, mesoderm and endoderm. Additionally, the genomic integrity of iPSCs must be assessed to ensure optimal differentiation [253]. The characterisation of the iPSCs used in this study was conducted previously [223]. Previous studies in our lab have shown that these iPSCs lines were successfully reprogrammed from fibroblasts and could maintain their pluripotency properties grown on VTN-N and Matrigel cell culture substrates by monitoring the morphological changes over time and characterising the pluripotency markers expression including OCT4, SOX-2, NANOG and SSEA4. It was also confirmed these iPSCs are free of Sendai virus by PCR and karyotype assessed to be normal. Meanwhile, the iPSC lines demonstrated the ability to differentiate into three germ layers with the markers expression of ectodermal, mesodermal and endodermal confirmed by immunofluorescence staining [223]. Control iPSC line, OX1-19, which has previously been characterised [254], was provided by Sally Cowley (University of Oxford, UK).

3.1.4. Aims

The aim of this project is to build an iPSC-derived CADASIL model for neurovascular interactions to investigate the neurovascular dysfunction in CADASIL and the pathologies of this condition. In order to achieve this goal, successful differentiation of neuronal and vascular cells from CADASIL and control iPSCs is essential. To mimic the brain pathology of CADASIL, successful differentiation of BMECs from iPSCs is required. In this chapter, successful BMECs differentiation from CADASIL and control iPSCs and characterisation will be discussed. The differentiation process is refined based on the Lippmann protocol. Characterisations on these iPSC-BMECs will be performed by immunofluorescence microscopy and qRT-PCR of specific proteins and genes of tight junctions (Claudin5, Occludin and ZO-1). To determine the BBB properties of differentiated BMECs, iPSC-BMECs will be cultured on Transwell settings and barrier function will be measured by TEER and NaF permeability assay.

In summary, the aim of this project is to establish an iPSC-BBB model for CADASIL. In order to build iPSC-derived neurovascular interaction for CADASIL, we need to differentiate CADASIL and control iPSCs to NVU cell types. In this chapter we showed successfully differentiation and characterisation of BMECs from iPSCs.

3.2. Results

3.2.1. iPSCs cell morphology and pluripotency characterisation

Skin fibroblasts from CADASIL patients and unaffected individuals (control) were reprogrammed to iPSCs, which have already been established in Tao Lab. Colonies generated from the fibroblasts exhibited typical iPSC morphology and maintained a normal phenotype after continuous expansion. Representative phase microscopy images of control line and CADASIL line are shown in **Figure 3.2**.

Immunofluorescent staining verified all cell lines expressed pluripotency markers NANOG, OCT4, SSEA4 and SOX2, with low expression of PAX6 (neuronal progenitor cells marker) that works as a negative control (**Figure 3.3 and 3.4**).

Figure 3.2 Morphology of iPSCs.

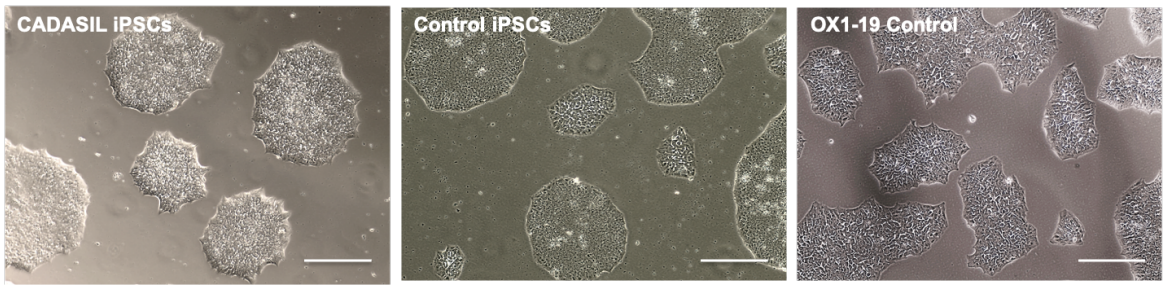

Phase microscopy photographs show morphology of iPSCs. Scale bar represents 200 μm.

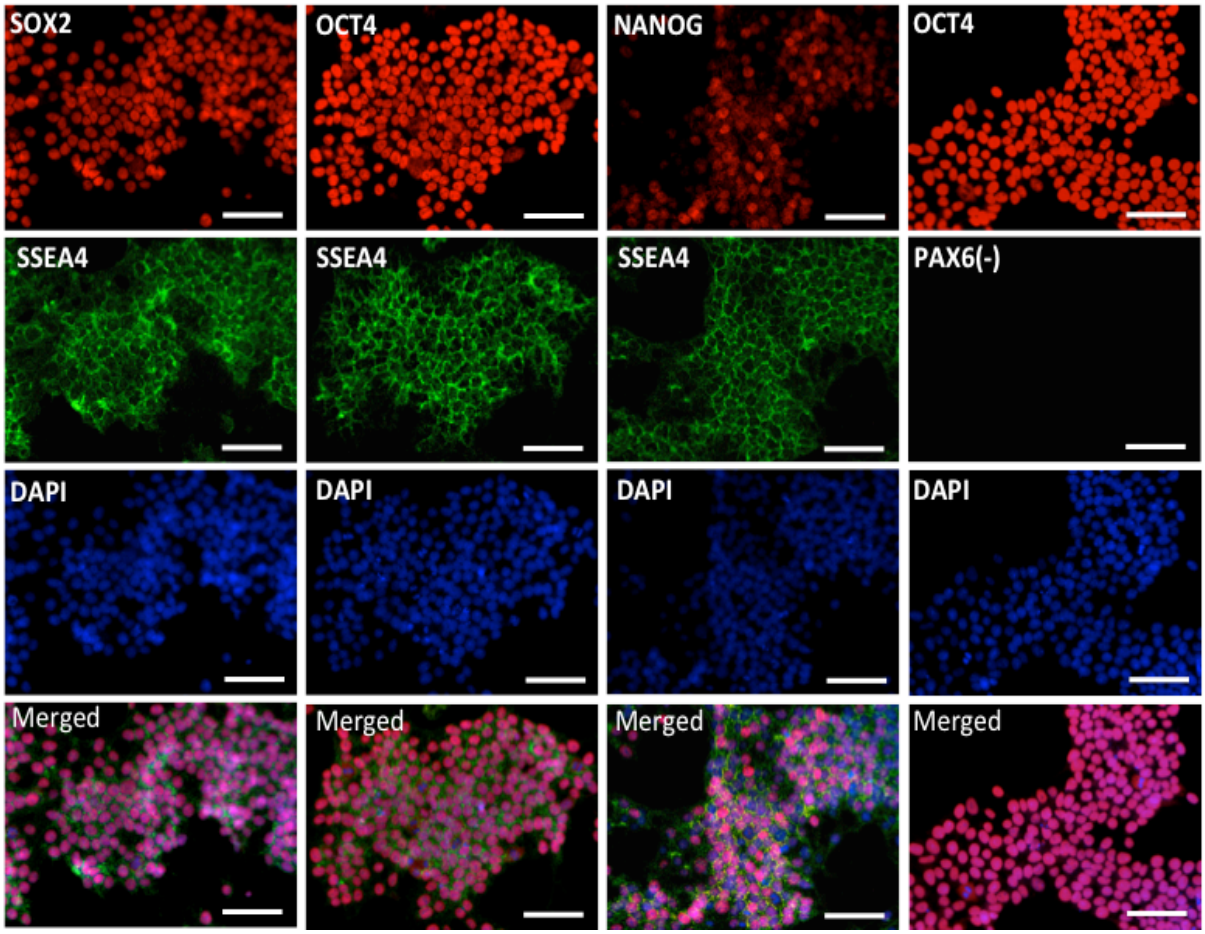

Figure 3.3 Pluripotency marker protein expression in control iPSC line.

Immunofluorescent staining microscopy images show pluripotency marker protein expression for control iPSCs line (AGD-14-02-C3). Markers including OCT4, SOX2, SSEA4 and NANOG are all expressed in iPSCs with PAX6 as a negative control, DAPI was counterstained to show nuclei. Membrane and nuclear markers were double-stained as shown in the merged photos. Scale bars, 100 μm.

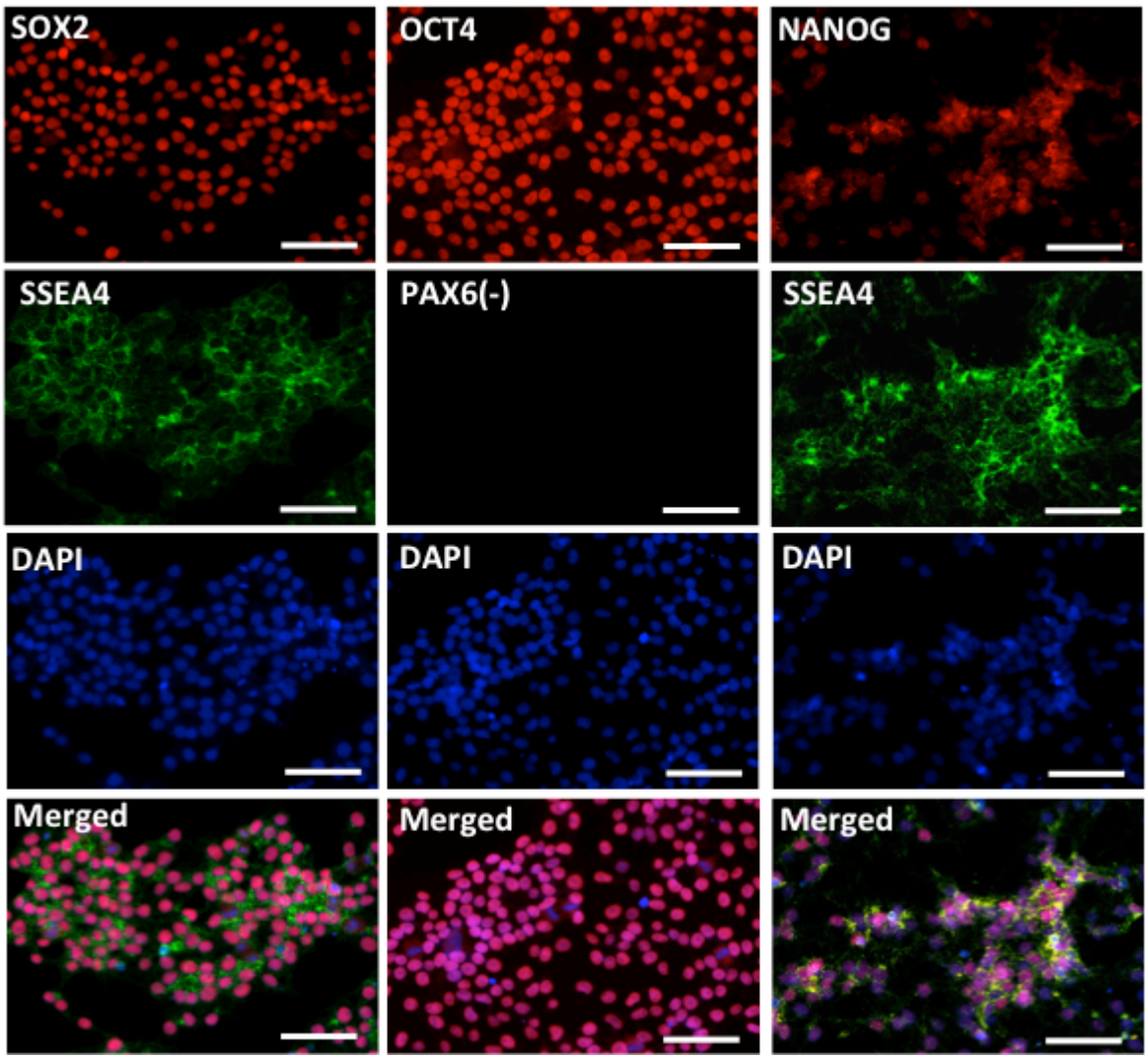

Figure 3.4 Pluripotency markers expression of control iPSC line.

Immunofluorescent staining microscopy images show pluripotency marker protein expression for OX1-19 control line. Markers including OCT4, SOX2, SSEA4 and NANOG are all expressed in iPSCs with PAX6 as a negative control, DAPI was counterstained to show nuclei. Membrane and nuclear markers were double-stained as shown in the merged photos. Scale bars, 100 μm.

3.2.2. Human brain microvascular endothelial cells can be differentiated from iPSCs

IPSCs were differentiated into BMECs using previously described methods [212, 220, 228]. The strategy of this method was a two-dimensional iPSC differentiation approach that promotes neural and endothelial co-differentiation, providing a microenvironment mimicking the embryonic brain *in vitro*. The differentiation strategy was initially established using AGD-14-02-C3 iPSC control line with 3 times replications.

IPSCs were expanded on Matrigel-coated plates in E8 medium for 2-3 days. To initiate neural and endothelial co-differentiation, iPSCs colonies were grown in unconditioned medium for 6 days (**Figure 3.5A**). At day 5 cells expanded to be confluent (**Figure 3.5B**). At day 6 cells were then selectively expanded by switching medium to endothelial cell growth medium supplemented with RA from day 6 to day 8. To purify BMECs, cells were sub-cultured at day 8 onto C/F/W Transwell filters or culture plates (**Figure 3.5A**). BMECs selectively adhered to the C/F/W gel.

At day 9, a monolayer of pure BMECs was formed (**Figure 3.5B**). Immunofluorescence staining for day 9 BMECs showed the expression of typical BMECs marker proteins GLUT1, ZO-1, Occludin and Claudin-5, with visually the vast majority of cells positively stained (**Figure 3.5C**).

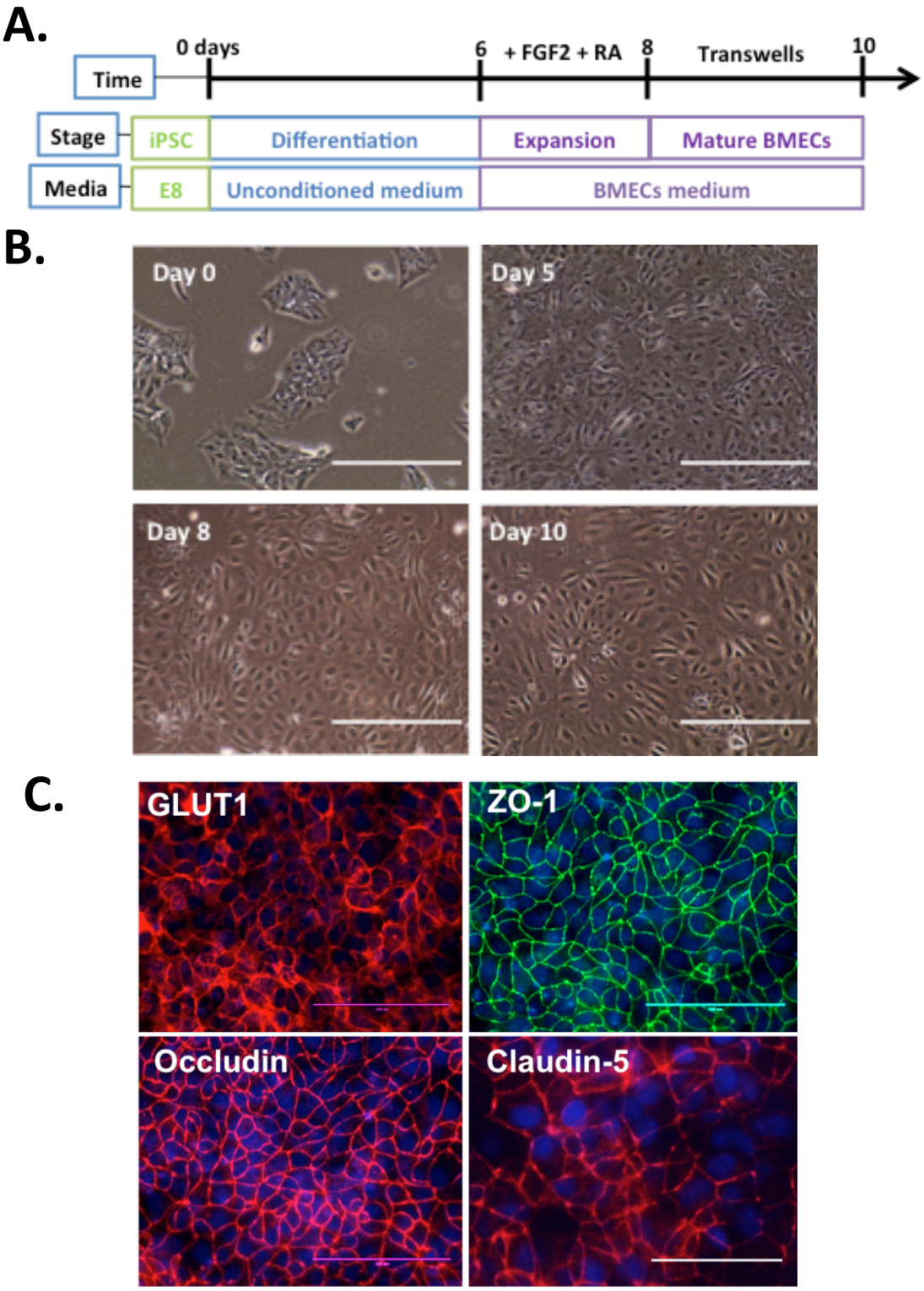

Figure 3.5 Differentiation of BMECs from iPSCs

(A) Schematic summary of the BMEC differentiation process. iPSCs were seeded onto Matrigel in E8 medium for 2-3 days to allow adherence and cell expansion and then cultured in unconditioned medium for 6 days until large colonies merged with typical endothelial cell morphology observed. At day 6, BMEC purification was induced by culturing in hESFM supplemented with RA and FGF2 for 2 days, followed by subculture onto C/F/W matrix for purification.

(B) Phase contrast microscopy photographs show morphology changes of cells during BMEC differentiation at day 0 (iPSCs stage), day 5 (after 5 days in unconditioned medium), day 8 (after 2 days in EC expansion medium before purification) and day 10 (2 days after purification, mature BMECs were obtained). Cells showed an endothelial-like morphology at day 8 and day 10. Scale bars, 200 μm.

(C) Expression of mature BMEC and junctional marker proteins GLUT1 (red), ZO-1 (Green), Occludin (Red) and Claudin-5 (Red) at day 9 of iPSC-BMEC differentiation DAPI (blue) was counterstained to show nuclei. Scale bars, 200 μm.

3.2.3. Gene expression profile of iPSC-BMECs

The expression of pluripotency and BMEC markers was assessed throughout BMEC differentiation. There was a significant decrease in the expression of all pluripotency markers by day 10, *SOX2* and *NANOG* ($p<0.0001$), *OCT4* ($p<0.001$) (**Figure 3.6 A, B, C**). Meanwhile, a significant increase in the expression of BMECs markers GLUT1 and CD31 was observed between Day0 and Day10 BMECs ($p<0.001$), there was no significant difference in gene expression between day 0 and day 8 (prior to BMEC purification) (**Figure 3.6 D, E**). Transcripts encoding tight junction protein *ZO-1*, *OCLN* and *CLDN5* as well as *ABCB1* (p-glycoprotein) were significantly up-regulated from day 0 to day 8 ($P<0.0005$),

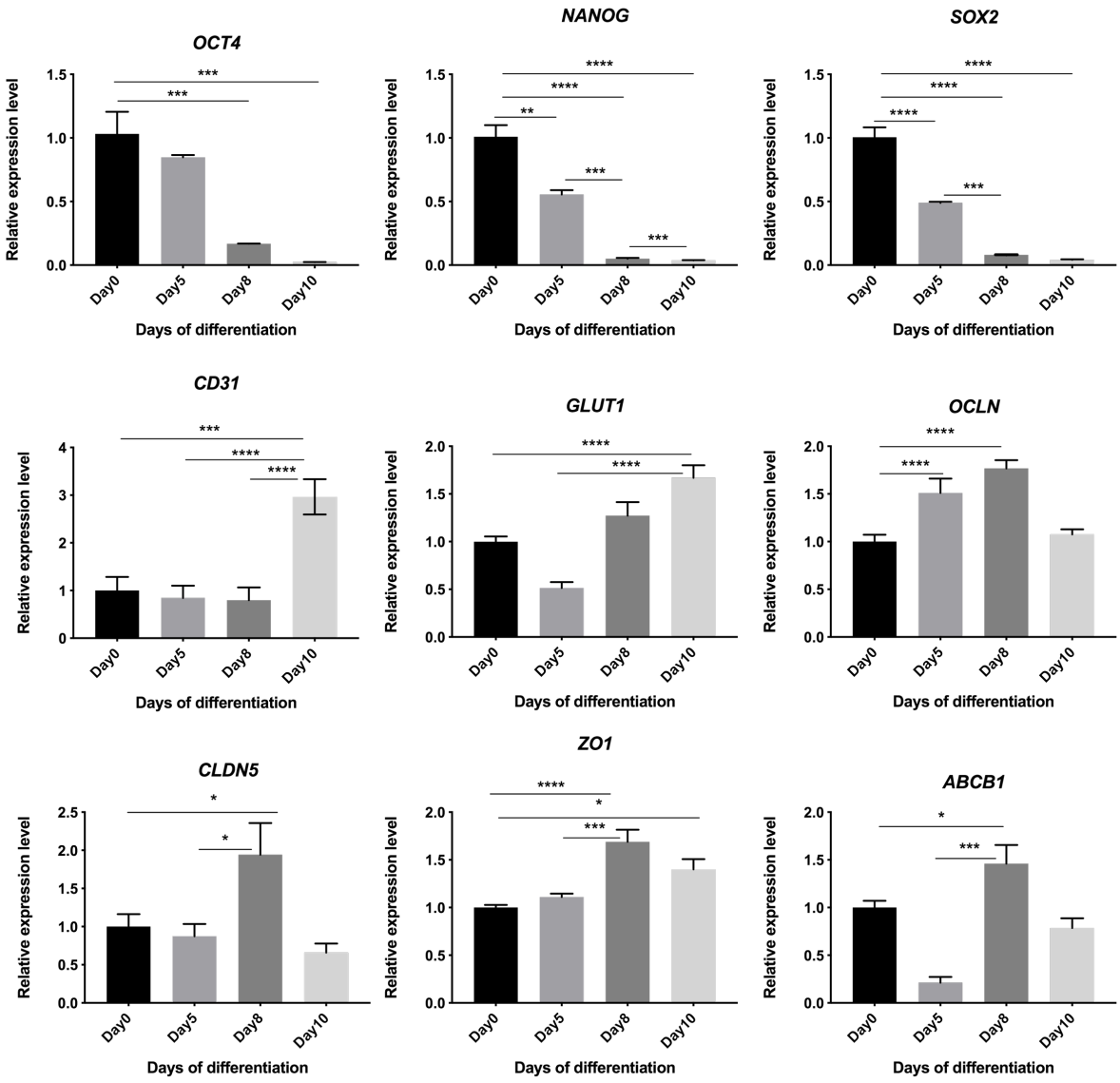

Figure 3.6 Gene expression profiles of BMECs markers during iPSC-BMECs differentiation.

qRT-PCR quantification of endothelial cell specific marker gene CD31 and BMEC specific markers *GLUT1*, *OCLN*, *CLDN5*, *ABCB1* and *ZO-1* expression. Data shows gene expression during iPSC-BMECs differentiation over time at day 5 (co-differentiation stage), day 8 (BMECs expansion stage) and day 10 (maturation stage) relative to day 0 (iPSCs stage). Expression is measured relative to *GAPDH*.

Means ±SEM was calculated from triplicate reactions of 3 biological replicates, n=3. *, $p<0.05$, ** $p<0.005$ *** $P<0.0005$, **** $P<0.0001$. Statistical significance was determined by using one-way ANOVA.

3.2.4. iPSC-BMECs exhibit BBB phenotypes

In addition to BMEC gene and protein expression, endothelial cell and BMEC functional characteristics were also assessed. After 8 days of differentiation, cells were purified by selective adhesion on C/F/W-coated plates. To evaluate the angiogenesis ability of iPSC-BMECs, a Matrigel-based angiogenesis tube formation assay was carried out with BMECs and primary ECs as comparison. Endothelial tube formation was observed in all groups (**Figure 3.7B**). Additionally at Day 10, iPSC-derived BMECs exhibited further EC properties including uptake of acetylated LDL (**Figure 3.7A**).

BMECs sub-cultured on C/F/W Transwell membranes can be used to measure TEER starting at day 9 of the differentiation, while other functional assays such as sodium fluorescein permeability were performed on day 10 when TEER reaches a maximum. On day 8 BMECs were seeded onto Transwells pre-coated with C/F/W (**Figure 3.7C**) then TEER value was measured every 24 hours for 5 days. The TEER of HCAECs was also measured as a comparison to BMECs. Initial TEER measurements taken at 24 hours after seeding were 350-400 , indicating a tightening endothelial monolayer started to form (**Figure 3.7D,** Day9**)**. By day 10 the TEER value of the iPSC-derived BMEC monolayers was significantly higher ($p<0.0001$) than the HCAEC control exhibiting maximum TEER of up to 1000 $\Omega x cm^2$. iPSC-BMEC TEER values then decreased gradually in the following 3 days. In comparison, HCAECs did not possess barrier function with the TEER value under 50 $\Omega x cm^2$ throughout 5 days measurement. The maximum TEER of BMECs and HCAECs monolayers at 48 hours after plating is shown in **Figure 3.7E.**

The BBB function is not only characterised by its high TEER, but also by its low permeability to passive diffusion [211]. The permeability of fluorescein (Pe) was less than the threshold of sucrose as a reference (3.4×10^{-5} cm/s) for all lines, with an average of 3.7×10^{-7} cm/s (**Figure 3.7 F**).

A.

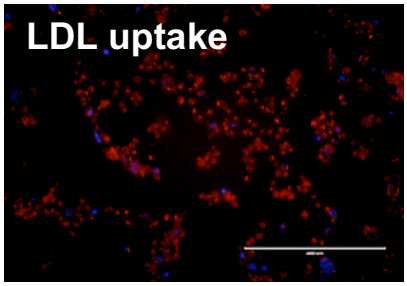
LDL uptake

B.

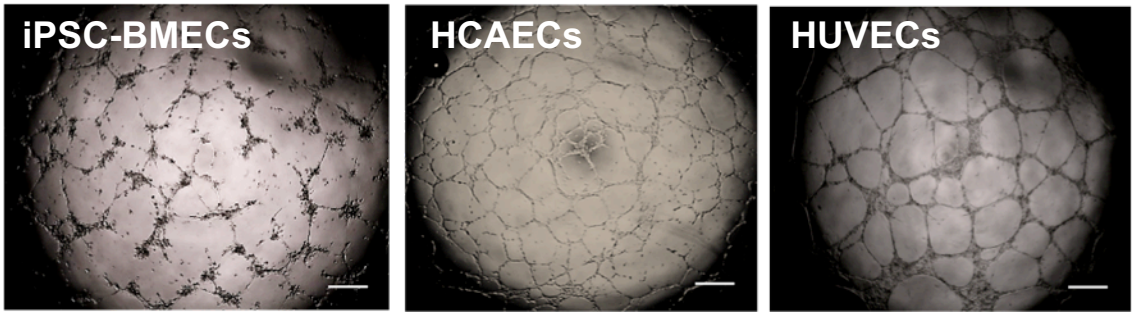
iPSC-BMECs
HCAECs
HUVECs

C.

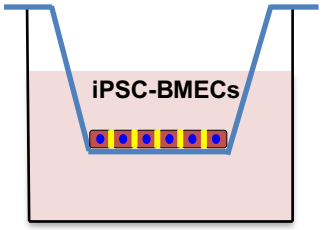
iPSC-BMECs

D.

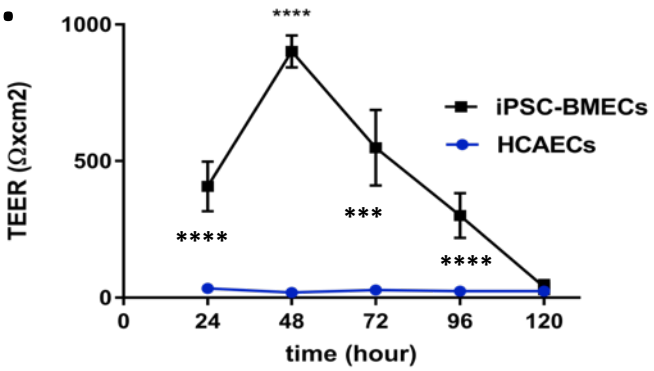
TEER (Ωxcm2)
1000
500
0
0
24
48
72
96
120
time (hour)
****
***
****
****
iPSC-BMECs
HCAECs

E.

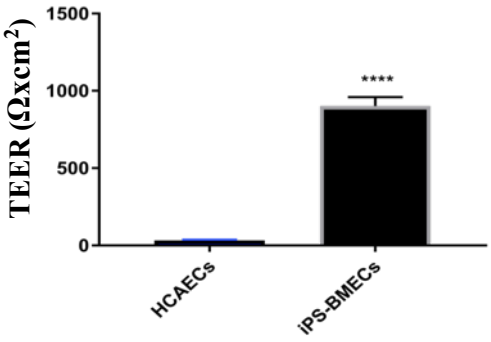
TEER (Ωxcm2)
1500
1000
500
0
****
HCAECs
iPS-BMECs

F.

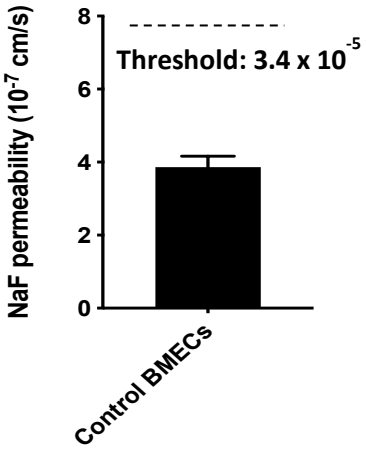
NaF permeability (10-7 cm/s)
8
6
4
2
0
Threshold: 3.4 x 10-5
Control BMECs

Figure 3.7 Functional characterizations of iPSC-BMECs.

(A) iPSC-derived BMECs at day 10 were analysed for LDL uptake assay. LDL is shown in red while DAPI was stained blue (scale bar, 200 μm).

(B) iPSC-derived BMECs were dissociated with Accutase and seeded at 1 x 10^4 cells per well of 96-well plate on Matrigel. Images were taken after 24 hours of culture in hESFM with VEGF165 (50 ng/mL). HCAECs and HUVECs were seeded at the same density in the same medium for comparison (scale bar, 200 μm).

(C) Schematic drawing of *in vitro* BBB model with BMECs.

(D) (E) iPSC-BMECs showed typical barrier function by TEER measurement while HCAECs failed to show barrier function. For each cell type, three Transwell filters were seeded with BMECs, and TEER was measured in three different positions for each filter. Each plot is the result of 3 biological replicates (n = 3) with each daily TEER measurement. Values are reported as mean ± SEM of these collective measurements. Statistical significance was calculated using Student's t-test, ****$p < 0.0001$ versus HCAECs. The TEER at peak value was shown in the bar graph (E).

(F) Sodium fluorescein (Na-F) permeability was measured across BMECs 48 hours after seeding on to coated Transwells. Statistical significance was calculated using Student's t-test. Values are mean ± SEM of 3 biological replicates. Data of three replicates was shown in average.

3.3. Discussion

In this chapter, the differentiation and characterization of BMECs from control iPSCs was described. The data shows BMECs can be differentiated from iPSCs lines and these iPSC-BMECs positively expressed endothelial and BMECs-specific protein markers. It was also demonstrated that these BMECs are able to show BBB barrier function as well as general EC function including LDL uptake and angiogenesis tube formation.

3.3.1. iPSCs can be successfully differentiated into BMECs

A well-defined and repeatable protocol for iPSC-BMEC differentiation is vital in modelling the BBB, particularly for barrier function assessment requiring large numbers of BMECs with consistent quality [255]. This study was based on the BMEC differentiation protocol by Stebbins *et al.* (2016) predicated on the neuronal and endothelial cell co-differentiation of iPSCs. IPSC line for BMEC differentiation progressed from pluripotent state to an intermediate neuronal and endothelial co-differentiation stage, finally to mature BMECs. The pluripotency of iPSCs is essential for their successful differentiation into pure NVU cells, which was confirmed by both immunostaining and qRT-PCR. The pluripotent markers OCT4, SOX2, SSEA4 and NANOG were highly expressed in the control iPSC line involved in this research.

It has previously been shown that during the differentiation of iPSCs to BMECS, variations between line-to-line or batch-to-batch can lead to differences in BMEC purity and phenotype [213]. Accordingly, modifications were made between our iPSCs lines in refining the existing protocol. For example, the iPSCs in this study reached confluence between days 1-4 (typically day 3) and were therefore sub-cultured 1:3 on fresh Matrigel coated plates to prevent cell death and poor differentiation efficiency. In contrast, the iPSCs in the source protocol were maintained without subculture until day8. Finally, E8 and TeSR-E8 medium were used for iPSC maintenance as opposed to mTeSR, which made no difference to the differentiation, as indicated by others [256, 257].

QRT-PCR data demonstrated significant down-regulation of pluripotent gene expression including *SOX2*, *OCT4* and *NANOG* in the process of iPSCs differentiating to BMECs. Meanwhile up-regulation of the EC specific gene *CD31* and BMEC functional genes *GLUT1*, *ZO-1*, *OCLN*, *CLDN5* and *ABCB1* was observed at day 8 of BMEC differentiation compared with day 0. The expression level of junctional proteins, which are responsible for forming

tight junction complexes between cells, should be high in iPSC-derived BMECs at the end of differentiation. However, there appeared to be a tendency of decreased expression of junctional genes *OCLN*, *CLDN5* and efflux transporter gene *ABCB1* at day10, compared with day 8, when BMECs on Transwells reached the maximum TEER (**Figure 3.6**). One possible explanation is that these proteins were already expressed in day 0 iPSCs but needs future validation. Gene expression is not widely reported in studies using iPSC-BMEC differentiation protocols. As a result, additional validation of qRT-PCR on tight junctional genes OCCLUDIN, CLAUDIN5 and efflux transporter gene ABCB1 expression at day10 is needed in future experiment.

Thus, these data present a capacity of making highly reliable source of human BMECs from iPSCs that can be used to generate sufficient cells for disease modelling of the BBB for the PhD project and possible drug screening in the future. This iPSC-derived BMECs differentiation strategy could be adopted by the broader research communities for studies of brain development, disease mechanisms, and drug delivery.

3.3.2. iPSC-BMECs can be used to mimic in vitro BBB models

Recent advances in iPSC differentiation schemes have paved the way for developing more complex *in vitro* BBB models. However, few iPSC-BBB models have been reported for vascular dementia, especially CADASIL using BMECs, though there have been studies based on vECs [223]. The use of ECs though fails to recapitulate normal cerebral vascular properties. Although several iPSC-BMEC protocols rely on co-culture with neural cells to direct ECs toward a BMEC phenotype expressing junctional protein markers Claudin 5, Occludin and ZO-1, these BMECs did not possess barrier function demonstrated by low TEER values [258, 259].

In this chapter, successful differentiation of iPSCs into BMECs was described. These BMECs demonstrated EC functions including tube formation and LDL uptake ability. The iPSC-BMECs were evaluated for BBB phenotype by TEER measurement and sodium fluorescein permeability. BMECs produced by this differentiation protocol reached a maximum TEER above 1000 Ω/cm^2, similar to previously published reports using similar Transwell-based methods [212, 260]. The sodium fluorescein permeability values are in align with previously published values of iPSC-derived BMECs [256, 260], further confirming the passive barrier properties observed by TEER. Importantly, the low sodium fluorescein permeability values of BMECs indicate high barrier functions for the BMEC monolayers, which provide the

potential application of the iPSC-derived BBB model as a drug-screening tool for neurovascular defect disease or vascular dementia. Future testing with various compounds will be needed to fully validate the potential values of the BBB model.

BBB is mainly composed of BMECs that help regulate the flow of substances into and out of the brain. BBB breakdown and dysfunction are associated with a variety of neurological diseases, including AD, stroke, VaD and brain tumours. In this chapter we showed iPSC-derived BMECs possess excellent barrier characteristics including blockage of passive small molecule transit. It is promising this iPSC-BMECs platform could also be useful in drug permeability screening to develop pharmaceuticals or to limit the brain uptake of drugs that may have neurotoxic side effects[211].

As indicated in the natural history of CADASIL, defects in neurovascular interactions may be involved in this condition. Current mouse and cell models failed to mimic the cerebral pathology of CADASIL, thus the overall aim of this project was to build a neurovascular model using iPSC-derived NVU cells. Among NVU cells, BMECs form the inner lining of blood vessels in the brain and are responsible for the neurovascular barrier function through their TJs, AJs and transporter proteins. These junction proteins are used as markers for barrier formation of BMECs and are also useful markers for BBB tightness [258, 261, 262].

3.4. Summary

In summary, these data suggest that BMECs can be differentiated from iPSCs and can be used to model BBB, and this *in vitro* iPSC-BBB model can provide a reasonable simulation of the *in vivo* human BBB.

Overall, the validation of gene expression and tight junction formation, high TEER value and low permeability for small molecules, provide evidence that the iPSC-derived BMECs possess significant BBB characteristics for mimicking prior *in vitro* BBB models.

In order to build a complete iPSC-BBB model for CADASIL, other cell types that constitute BBB structure are essential, including pericytes, astrocytes and neurons. The differentiation of these cell types will be described in following chapters separately.

4. Chapter 4: Differentiation and characterisation of iPSC to astrocytes and neurons

4.1. Introduction

As mentioned earlier, the BBB is an essential regulatory interface in the CNS system mainly composed of BMECs, pericytes, astrocytes and adjacent neurons that create a NVU [134]. Astrocytes play vital roles in BBB function and CNS diseases. Neurons connect with astrocytes' endfeet close to the BBB. The use of iPSC-derived astrocytes and neurons provide a platform to explore the pathologies of both cell types in CNS disease.

4.1.1. Astrocyte phenotype and function in the BBB

Astrocytes are the most abundant glial cells in the brain, the morphology and function of which are extremely specialized and heterogeneous in the CNS [263]. Although huge heterogeneity exists among astrocytes, two main types have been reported in the CNS: protoplasmic astrocytes of the grey matter which wrap neuronal bodies and synapses that contact blood vessels and neurons, and fibrous astrocytes from the white matter that interact with blood vessels, the nodes of Ranvier and oligodendroglia [139, 140, 264, 265]. Astrocytes exhibit various phenotypes when responding to different stimuli including infection, ischemia and neurodegenerative disorders. Non-reactive astrocytes become reactive astrocytes with a range of potential molecular, cellular and functional changes including neurotoxic or neuron-protective conditions, in response to extracellular signals and stress [266].

The BBB is formed of BMECs that form YJs and AJs and are surrounded by a basal lamina, pericytes and astrocytes' end-feet. Astrocytes are essential for the formation and function of the BBB by secreting signalling factors in association with the cells of BBB and the formation of tight junctions [134]. Also, astrocytes have extensive contacts and interactions with blood vessels thus regulating CNS blood flow by producing and releasing various molecular mediators, such as nitric oxide (NO) and prostaglandins (PGE) [135, 267]. Moreover, astrocytes have been shown to be the primary mediators of changes in blood flow within the CNS in response to changes in neuronal activity [268]. Evidence indicates that astrocytes can induce barrier properties in BMECs [269-271]. In summary, as one of the main components in NVU, astrocytes play important role in the BBB function.

4.1.2. Astrocytes in BBB dysfunction

Although the main constituent of the BBB is BMECs, astrocytes contribute to BBB stability through their direct contact with perivascular endfeet between BMECs and pericytes [272]. In healthy conditions, Astrocytes' main tasks are to provide physical and trophic support to other NVU cells, ensuring BBB integrity and proper synaptic maturation and signalling [273, 274].

Propagation of Ca^{2+} waves is a remarkable intercellular communication function in astrocyte networks, bridging neural circuits and vasculature. This process is known to be mediated by gap junction and extracellular ATP. Astrocytes communicate with each other through gap junction proteins, mainly connexin 43 (Cx43) and connexin 30 (Cx30). Mice with down-regulated Cx43 and Cx30 expression on astrocyte endfeet demonstrated a significant loss of AQP4 and β-dystroglycan, a transmembrane receptor anchoring astrocyte endfeet to the perivascular basal lamina. The absence of astroglial connexins weakens the BBB resulting in increased hydrostatic vascular pressure and shear stress. Thus, the astroglial GJ protein connexins are necessary to maintain BBB integrity [275].

Several functional changes in astrocyte properties have been found in the cortex of patients with impaired BBB. These changes include: (1) Reduced expression of potassium inward rectifying channels (Kir4.1) and water channels AQP4; (2) reduced expression of GJs; and (3) impaired glutamate metabolism [276].

Accumulated evidence has indicated astrocytes dysfunction in vascular contributions to cognitive impairment and dementia, including CADASIL [277]. It was observed that GFAP expression was significantly reduced in CADASIL, which may reflect loss of astrocytes or impaired astrocyte function in CADASIL [278]. A recent study showed that astrocytes undergo autophagy-like cell death in CADASIL, with the anterior temporal pole being highly vulnerable [279].

4.1.3. Methods for generating iPSC-astrocytes

Due to the important function of astrocytes in BBB function and the potential dysfunction in CADASIL, it is of great significance to establish a BBB model for CADASIL that incorporating astrocytes. However, animal source of astrocytes have shown differences in morphology, GFAP expression, Ca^{2+} waves propagation and gene expression profiles [280]. GFAP is the hallmark intermediate filament protein in astrocytes, which involved in many

important CNS processes, including cell communication and the BBB functioning [281]. Besides, immortalised human astrocytes fail to fully recapitulate human CNS disease processes and primary neural tissue is difficult to obtain and isolate astrocytes from [263, 282]. Thus, models for iPSC-derived astrocytes represent a valuable technological advance to study CNS disease-related mechanisms.

Considering the limited accessibility to human non-transformed astrocytes for disease modelling and the difference between animal and human astrocytes [283], iPSCs represent an attractive strategy to derive highly enriched astrocyte populations for the study of BBB in CNS disease.

Since the differentiation of neural progenitors from human ESCs was firstly reported in 2001 [284, 285], various differentiation protocols for neural cells including astrocytes from human PSCs have been described [263].

Several protocols exist for generating PSC-derived astrocytes, but these methods are technically complicated, requiring a long time to perform. Early differentiation protocols mainly focused on generating astrocytes from ESCs [284-286], and in recent year they have been adapted for the differentiation of iPSCs [218, 287-290]. Protocols for iPSC-astrocyte generation often constitute four main steps: (1) Induction of the iPSCs into rosette-like NPCs; (2) NPCs purification and long-term expansion either in adhesion or suspension culture; (3) Astrocyte progenitor cell differentiation with growth factors; and (4) Astrocyte maturation and maintenance. In these studies, the dual inhibition of SMAD signalling have been used in adherent iPSCs cultures to obtain NPCs [227, 291].

In most differentiation schema it takes over 60 days to generate mature astrocytes from iPSCs. Thus, there is still a pressing need for quicker, more cost-effective methods to provide robust astrocyte populations to study astroglial contribution to CNS diseases. In one study, an efficient platform for astrocyte differentiation from iPSCs was reported to generate astrocytes within 30 days [292]. However, this method started from NPC stage rather than the iPSC stage, which realistically meant that it still took more than 50 days for iPSC-astrocytes transition.

Immunofluorescent staining and qRT-PCR techniques enable the detection of specific protein and gene expression of markers for characterizing astrocytes. GFAP has become a prototypical marker for identification of iPSC-derived astrocytes. Within or outside the CNS,

GFAP is also expressed by a number of cells that can be considered part of an astroglial family. Therefore further molecular markers are needed for the detection of BBB related astrocytes, including early astrocyte maturation markers S100β and Glutamate transporter 1 (GLT-1), mature astrocyte marker GLAST, and astrocyte specific markers in the human brain Cx43 and ALDH1L1 [293] [274] [294].

4.1.4. Modelling dementia using iPSC-derived astrocytes

BBB breakdown involves a loss in the permeability function of the barrier and phenotype changes in both the BMECs and astrocytes [134]. It has been demonstrated that in AD, the most common dementia worldwide, astrocytes become reactive and exhibit abnormal calcium signalling both in mice AD models and AD patients, also their gene expression profile and metabolism was changed [295]. Besides, elevated levels of GFAP expression, increased GABA production/release have been observed in AD astrocytes [296]. Moreover, amyloid-β (Aβ) accumulation was shown in AD astrocytes [297]. Oksanen *et al.* analysed AD iPSC-derived astrocytes and found they exhibited increased Aβ production, altered cytokine release, and dysregulated Ca^{2+} transients. Furthermore, due to the altered metabolism, the AD iPSC-astrocytes showed increased oxidative stress and reduced lactate secretion [298].

iPSC-derived astrocytes and dopaminergic neurons from PD patients and healthy controls were generated by Di Domenico *et al.* It was demonstrated that α-synuclein secreted from the PD iPSC-derived astrocytes had toxic effects on surrounding dopaminergic neurons, thus leading to neuronal dysfunction [299]. Finally, in a recent paper, an iPSC-based BBB model of MCT8 deficiency was used for modelling psychomotor retardation, indicating a prominent role of MCT8 in BBB function [221]. Juopperi et al. generated iPSCs from patients with HD. The HD iPSC-astrocytes exhibited a vacuolation phenotype, a phenomenon previously observed in primary lymphocytes from HD patients [300].

In summary, various iPSC-astrocytes models have been built to investigate dementia. As we discussed before, astrocytes dysfunction was found to be related to BBB defects in CADASIL pathologies. However, there are few reports on iPSC-astrocyte models for vascular dementia including CADASIL, with the function of astrocytes in BBB especially in these disease conditions being largely unknown.

4.1.5. Neurons function in BBB

Neurons in close proximity to the capillaries and connected with astrocytic endfeet within the

BBB, allows rapid response to the changing local microenvironment, especially in regards to ion balance [301]. It is estimated that nearly every neuron interacts with a capillary [302]. In close relation to BMECs, Neurons play a role in regulating blood flow, microvascular permeability, interact with the ECM, and release factors to stimulate angiogenesis [156].

In the NVU, neurons do not have direct contact with the endothelial barrier. One study demonstrated that neurons help regulate the tightness of the barrier formed by BMECs in culture by accelerating TJs protein synthesis and localization [303]. However, neurons are quite sensitive and vulnerable to ischemic injury because of their high demand on oxygen and nutrition [304], and may function as the initiator for disrupting the BBB when cerebral ischemia occurs [305]. After a vascular injury, signals from neurons and astrocytes can recruit microglia to secrete proinflammatory cytokines that induce neuronal tissue injury [306]. Studies have shown that damaged neurons can produce molecules that activate astrocytes [307], resulting in the production of active factors such as VEGF and cytokines that disrupt the BBB [308].

4.1.6. iPSC-neuron models in dementia

IPSC-derived neurons have been used to model dementia, including AD, PD, and others. AD is the most common cause of dementia and currently there are no effective drugs for this condition. In recent years, several iPSC AD models and disease phenotypes in these iPSC-neurons have been reported [309]. Most studies have mainly focused on familial AD (fAD) and the outcomes of these studies have been reviewed [310, 311]. IPSC-derived neurons were generated from patients with mutations in amyloid precursor protein (APP) or presenilin 1 (PSEN1). In publications modelling fAD, iPSC-derived neurons with PSEN or APP mutations exhibited increased production of amyloid β (Aβ) peptides and changes in the Aβ40/Aβ42 ratio [312]. However, in sporadic AD (sAD) cases, there is evidence that impaired clearance of Aβ contributes more to AD pathogenesis than increased Aβ production [313].

The iPSCs used for PD studies were mainly from patients carrying mutations in synuclein alpha (SNCA), leucine-rich repeat kinase 2 (LRRK2), PTEN-induced putative kinase 1 (PINK1), parkin RBR E3 ubiquitin protein ligase (PARK2), cytoplasmic protein sorting 35 (VPS35), and variants in glucosidase beta acid (GBA) [314]. Apart from iPSC-AD and iPSC-PD models, iPSC-derived neurons were applied to capture some key features of two

neurodegenerative disease ALS and frontotemporal lobar dementia (FTD), and their potential roles in drug discovery was uncovered [315].

4.1.7. iPSC-neuron differentiation for CADASIL

Currently, there is no record of neurons being derived from the iPSCs of CADASIL patients to model VaD. Although patients with subcortical VaD have been shown to have similar metabolic deficits to those with AD, the underlying pathogenesis of these changes is poorly understood [316]. It was reported metabolic deficits and atrophy in AD and subcortical vascular dementia was caused by similar loss of neurons. While the cause of the neuronal loss in AD is related to the deposition of abnormal proteins, the cause in cerebral SVD is unknown [316]. Therefore the generation of iPSC-derived neurons from SVD patients will permit the study of their interaction with the BBB and any dysfunction that arises.

As is common in the differentiation of iPSCs, protocols to produce iPSC-derived neurons do so by mimicking their natural development *in vivo*. Stem cells spontaneously differentiate and form three-dimensional multicellular aggregates called embryoid bodies (EBs) [317]. Most of the neuronal differentiation protocols use either dual SMAD inhibition or embryoid body (EB) formation. Dual SMAD inhibition is particularly used in 2D monolayer cultures that avoids the formation of EBs in order to reduce culture variability[318]. This study was based on a protocol by Shi *et al* which used Dual SMAD inhibition method.[291].

4.1.8. Aims and objectives

Evidence showed that in VaD, defects might exist in astrocytes and neurons or the interaction among NVU cell types. As discussed above, evidence has indicated astrocytes dysfunction in CADASIL, while neurons play important role in the homeostasis of CNS and BBB permeability. iPSCs offer the potential to investigate disease in previously unavailable human cell types. In order to model CADASIL NVU and BBB using iPSCs, neuronal cell types including astrocytes and neurons are essential. In this chapter the differentiation and characterization of astrocytes and neurons will be demonstrated and discussed.

Characterisations on iPSC-astrocytes will be performed by immunofluorescence microscopy and qRT-PCR of specific marker proteins and genes. iPSC-neurons functions were already characterised [319], as a result only immunofluorescence microscopy characterisation results will be shown. To confirm astrocytes functions, calcium imaging results will be demonstrated.

4.2. Results

4.2.1. Refinement of iPSC-astrocytes differentiation

4.2.1.1 Replication of Majumder et al. protocol for iPSC differentiation to astrocytes

NPCs were produced from iPSCs prior to astrocyte differentiation and two approaches assessed for astrocyte maturation thereafter.

OX1-19 iPSC line was used for demonstrating the astrocytes differentiation process. Positive staining for pluripotent markers was confirmed before every neural induction iPSCs were positive for the pluripotent markers OCT4 and SSEA4 by immunofluorescence microscopy, as showed in **Figure 4.1C**. The first of the two astrocytic differentiation protocols tested was based on inhibition of DNA methyltransferases and histone deacetylases by Azacytidine (Aza-C) and Trichostatin A (TSA) [320].

The timeline of the differentiation process is shown (**Figure 4.1A**). iPSCs went through neuronal induction, NPC formation and expansion. Immunofluorescent staining confirmed rosettes at day 20 expressing specific NPC markers MAP2 and PAX6 (**Figure 4.1C**). Cell morphology changed along with differentiation (**Figure 4.1B**).

The expression in astrocytes markers GFAP and S100β was not significant by immunofluorescence staining at day 38 and day 45 of astrocytes differentiation **(Figure 4.1C)**, with pluripotent markers OCT4 and SSEA4 weakly expressed at Day 45 as controls (**Figure 4**.**1C**).

A.

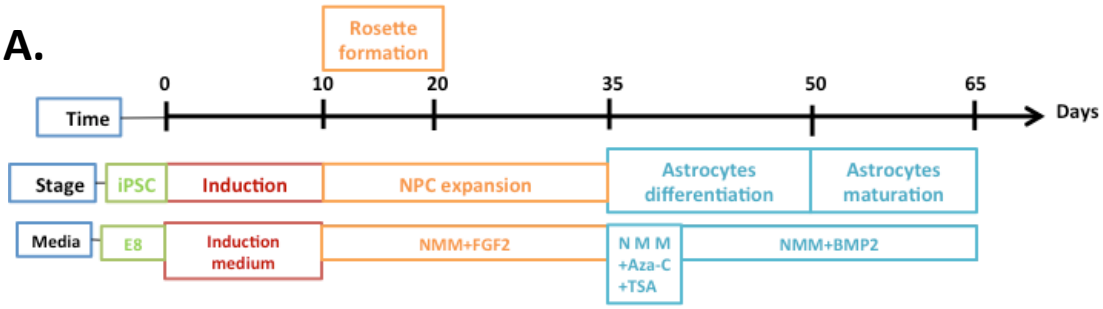
Rosette formation
0
10
20
35
50
65
Time
Days
Stage
iPSC
Induction
NPC expansion
Astrocytes differentiation
Astrocytes maturation
Media
E8
Induction medium
NMM+FGF2
N M M +Aza-C +TSA
NMM+BMP2

B.

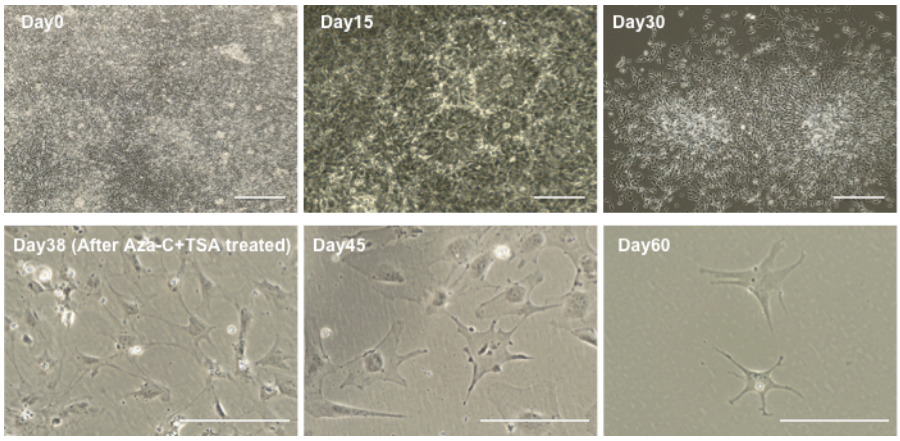
Day0
Day15
Day30
Day38 (After Aza-C+TSA treated)
Day45
Day60

C.

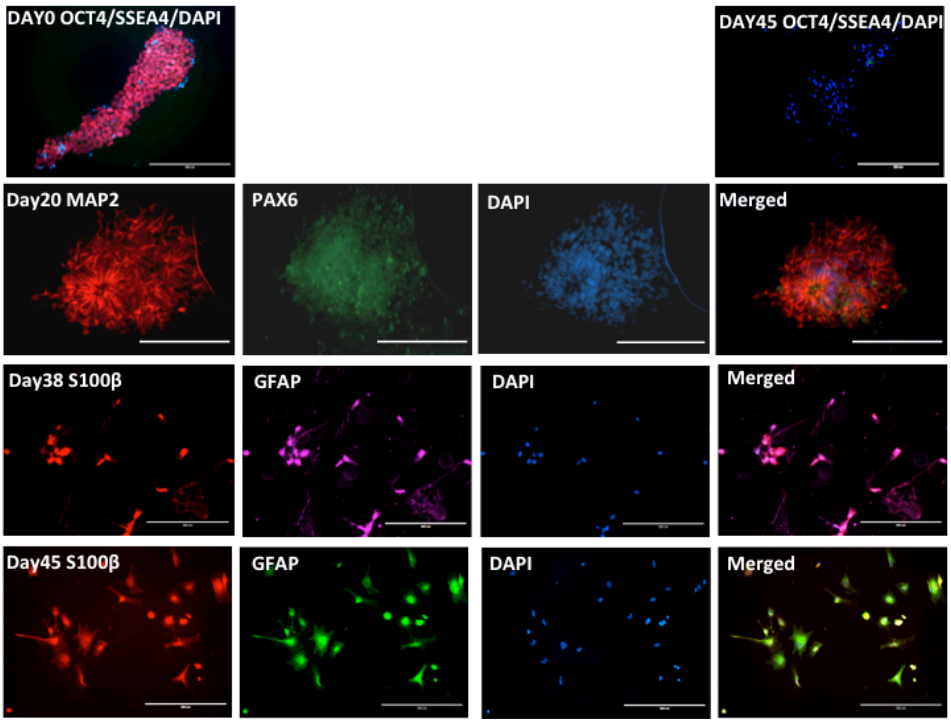
DAY0 OCT4/SSEA4/DAPI
DAY45 OCT4/SSEA4/DAPI
Day20 MAP2
PAX6
DAPI
Merged
Day38 S100β
GFAP
DAPI
Merged
Day45 S100β
GFAP
DAPI
Merged

Figure 4.1 Astrocyte differentiation and characterization from iPSCs using Majumder et al. protocol.

(A) Schematic drawing of the protocol used for iPSC-astrocytes differentiation using Majumder et al. protocol. Cells are directed through developmental identities of iPSCs, progenitor cells and then astrocytes with different treated medium at different stages. **(B)** Phase microscopy photographs show morphology changes of cells during astrocyte differentiation. Scale bars, 200 μm **(C)** Immunofluorescent staining for pluripotency markers OCT4 (red) and SSEA4 (green) at day 0, NPCs markers MAP2 (red), and PAX6 (green) with DAPI (blue) at day 20. Immunofluorescent staining for astrocyte markers S100β (red) and GFAP (purple/green) at day 38 and day 45 of differentiation was demonstrated. Nuclei are stained with DAPI (blue). Pluripotent markers OCT4 (red) and SSEA4 (green) were stained as negative controls for day 45 cells. Markers were double-stained as shown in the merged photos. Scale bars, 200 μm.

4.2.1.2 Differentiation and characterisation of iPSC-astrocytes using StemCell Technologies protocol

Due to poor cell yields using the Majumder et al. protocol, commercially available differentiation and maturation media (ADM2 and AMM2) from STEMCELL Technologies was also tested. Day 35 NPCs were seeded into ADM2 for 2 weeks followed by AMM2 for 2 weeks (**Figure 4.2A**). Typical iPSC, rosette, NPC and astrocyte morphology at day 0, day 15, day 35 and day 60, respectively was observed (**Figure 4.2B**). The differentiation of astrocytes from OX1-19 iPSC line was present as representative. OX1-19 iPSCs expressed pluripotent markers OCT4 and SSEA4 as shown in **Figure 4.2C**. At day 20, immunofluorescent staining confirmed the expression of specific NPC markers MAP2 and PAX6 in rosettes-like NPCs (**Figure 4.2C**). At day 60, cells expressed the astrocyte markers GFAP and S100β (**Figure 4.2C**), at a higher cell yield than the astrocytes generated by the Majumder et al. protocol.

The gene expression profiles of cells throughout astrocyte differentiation demonstrated significant down-regulation of pluripotent gene *NANOG* ($p<0.0005$) (**Figure 4.2D**). Concomitantly, a significant increase in the expression of the astrocyte markers *GFAP*, *S100β* as well as glutamate-aspartate transporter (*GLAST*), an important indicator of functional astrocytes, was observed from day 0 to day 60 along the course of differentiation (**Figure 4.2D**) ($p<0.0005$).

To measure calcium wave propagation astrocytes derived from iPSCs were loaded with Fluo-4, intracellular calcium waves and spikes were instantaneously induced. Fluorescent intensity was observed during mechanical stimulation, with two image series of $Ca2^{+}$ propagation patterns in the result data (**Figure 4.3**).

These findings confirm iPSC-astrocytes were successfully derived using StemCell protocol and they are functional astrocytes. All astrocytes involved in the BBB modelling were derived with this protocol.

A.

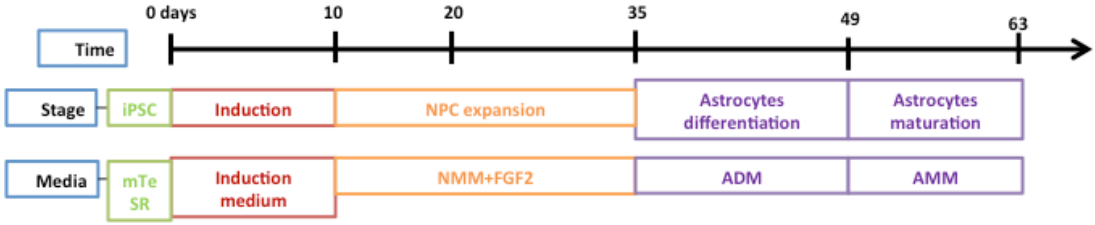
0 days
10
20
35
49
63
Time
Stage
iPSC
Induction
NPC expansion
Astrocytes differentiation
Astrocytes maturation
Media
mTe SR
Induction medium
NMM+FGF2
ADM
AMM

B.

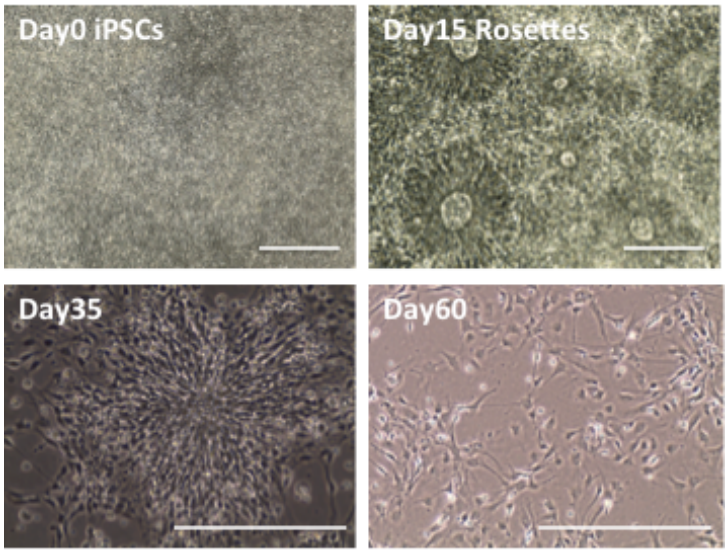
Day0 iPSCs
Day15 Rosettes
Day35
Day60

C.

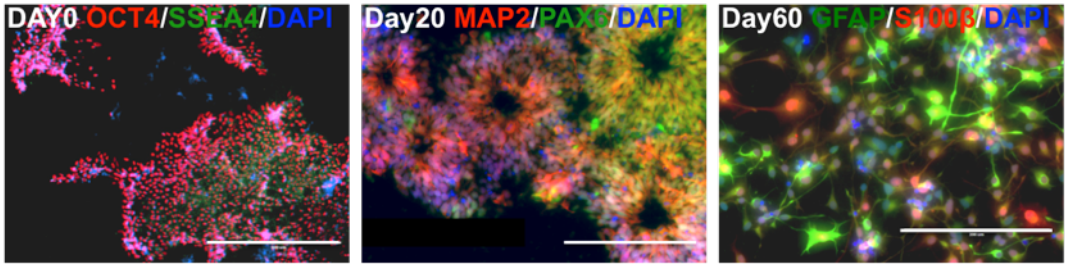
DAY0 OCT4/SSEA4/DAPI
Day20 MAP2/PAX6/DAPI
Day60 GFAP/S100β/DAPI

D.

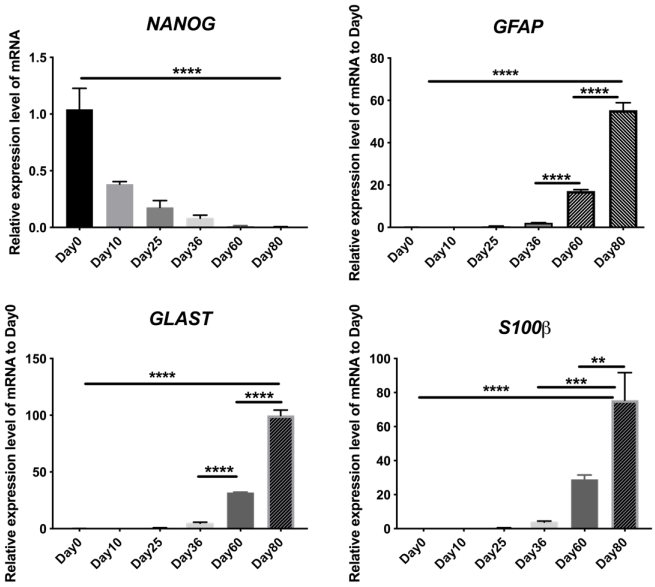
NANOG
GFAP
GLAST
S100β
Relative expression level of mRNA
Relative expression level of mRNA to Day0
Day0
Day10
Day25
Day36
Day60
Day80

Figure 4.2 Astrocyte differentiation and characterization from iPSCs using StemCell Technologies protocol.

(A) Schematic drawing of the protocol used for iPSC-astrocyte differentiation using StemCell Technologies protocol. Cells went through four stages including iPSC, NPC, astrocyte progenitor and mature astrocyte with different media at each stage. **(B)** Phase microscopy photographs show morphology changes of cells during astrocyte differentiation. Scale bars, 200 μm **(C)** Immunofluorescent staining for pluripotency markers OCT4 (red) and SSEA4 (green) at day 0, neural progenitor cell (NPC) markers MAP2 (red), and PAX6 (green) at day 20 and astrocyte markers S100β (green) and GFAP (red) at day 60. Nuclei are stained with DAPI (blue). Scale bars, 200 μm for day 0, 100 μm for day 20 and day 60 images. **(D)** qRT-PCR quantification of astrocytes specific marker genes *S100β*, *GFAP* and *GLAST*. Data shows gene expression during iPSC-astrocyte differentiation at day 25, day 36, day 60 and day 80 relative to day 0 (iPSCs stage). *GAPDH* was used as the endogenous control. Displayed is the mean ± SEM from triplicate reactions of 3 biological replicates, n=3. *, $p<0.05$, ** $p<0.005$ *** $P<0.0005$, **** $P<0.0001$. Statistical significance was determined by using one-way ANOVA.

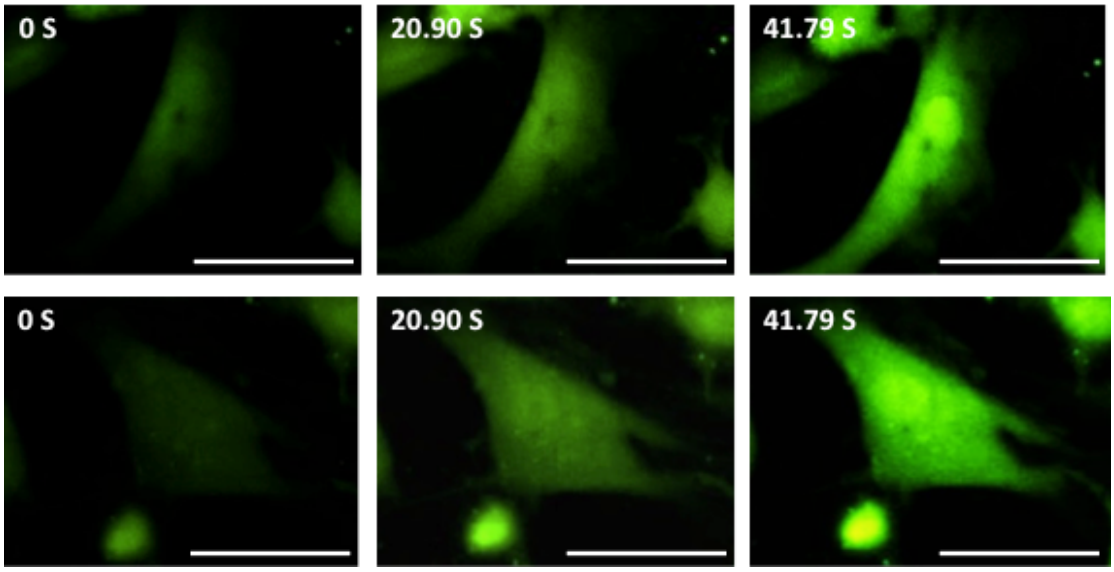

Figure 4.3 iPSC-derived astrocytes exhibited the potential to propagate calcium waves upon mechanical stimulation.

Images show two representative astrocytes plotted over time in seconds. Scale bars, 100 μm.

4.2.1.3 Development a new protocol for quick differentiation of iPSC-astrocytes

In order to pave a way into investigating a new iPSC-astrocytes differentiation protocol that is time and commercially saving, a new protocol was refined based on previous studies. A modified iPSC-astrocytes differentiation protocol was designed for a preliminary test (**Figure 4.4 A**). Typical iPSC, NPC, early and mature astrocyte morphology at day 0, day 10, day 35 and day 65 was observed (**Figure 4.4 B**). At day 6, immunofluorescent staining confirmed the expression of specific NPC markers SOX1 and FOXG1 in NPCs with little expression of astrocytes markers GFAP and S100β (**Figure 4.4 C**). At day 35, immunostaining showed the expression of astrocyte specific markers GFAP and S100β in astrocytes progenitor cells (APCs) (**Figure 4.4 C**), and at day 65, expression of both markers was demonstrated along extensive cellular projections with very little expression of neuronal marker βiii-tubulin.

Gene expression profiles demonstrated a significant increase in the expression of astrocytes markers *GFAP*, *S100β*, *GLAST* as well as *ALDH1L1*, which also differentiates between astrocytes and neurons, from day 0 to day 65 along the course of differentiation (**Figure 4.4D**) ($p<0.05$). The mRNA expression of neuronal marker βiii-tubulin also increased (**Figure 4.4D**) ($p<0.05$).

Collectively, these results proved the feasibility for efficient generation of astrocytes from this new protocol. In order to have an insight into this protocol, several questions need to be answered. **(1)** As we know the iPSC-NPCs differentiation and astrocytes maturation stages are well defined, but what happened during Day 8-Day 18? **(2)** What roles do PDGF and TGF-β play that lead to the occurrence of astrocytes progenitors? **(3)** Do the morphology images need to be collected at more intervals? **(4)** Are more non-astrocytic markers (PAX6 and MAP2) and astrocytes markers needed (CD44, CX43, and GLT-1)?

To answer these questions, a repeat differentiation was conducted looking at more details. Typical iPSC and NPC morphologies were captured at day 0 and day 8 (**Figure 4.5 A**). In order to investigate how PDGF or TGF-β lead to an astrocyte fate, four experimental groups were initiated between day 8-18 of differentiation: E6 only, E6 with PDGF (E6 + P), E6 with TGF-β (E6 + T) and E6 with both (E6 + P + T). The morphology of the cells was observed at days 20, 25, 30, 35, 45, 55, 60 and 65 for all 4 groups (**Figure 4.5 B and C**), which indicated that astrocytes can be generated from E6 + T and E6 + P + T groups while neurons-like cells seem to be generated with E6 only and E6 + P groups.

Immunofluorescent staining at days 35, 45 and 65 showed increasing expression of astrocytic markers GFAP and S100β for the E6 + T and E6 + P + T groups, while the expression of neuronal markers MAP2 and βiii TUBULIN in the E6 only and E6 + P groups was prominent. Conversely, the expression of neuronal markers in the E6 + T and E6 + P + T groups was low at day 65 (**Figure 4.6, 4.7 and 4,8**).

QRT-PCR results showed mRNA expression of astrocytic markers (*S100β*, *GFAP*, *ALDH1L1, GLT-1* and *GLAST*) as well as non-astrocytic markers (*TUBB3* and *α-SMA*) for each group at day 0 (iPSCs stage), day 8 (NPCs stage), day 35, day 45 and day 65 of the differentiation process (**Figure 4.9**). A significant increase in the mRNA expression of *GFAP* and *S100β* was observed in E6 + T and E6 + P + T groups, especially in the E6 + P + T group ($p<0.05$). *ALDH1L1* expression also increased significantly by Day 65 in E6 + T and E6 + P + T groups, but not in E6 and E6 + P groups. The expression of GLAST and GLT-1 increased for all groups at Day 65, however the increase rate in E6 and E6 + P groups is higher (**Figure 4.9**) ($p<0.05$). There was a significant increase ($p<0.0001$) in the expression of α-SMA in all groups between day 0 and 35 followed by a significant decrease ($p<0.0001$) in expression in all groups between day 35 and 65. βiii TUBULIN expression increased at Day 65 for all groups at similar levels (**Figure 4.9**).

A

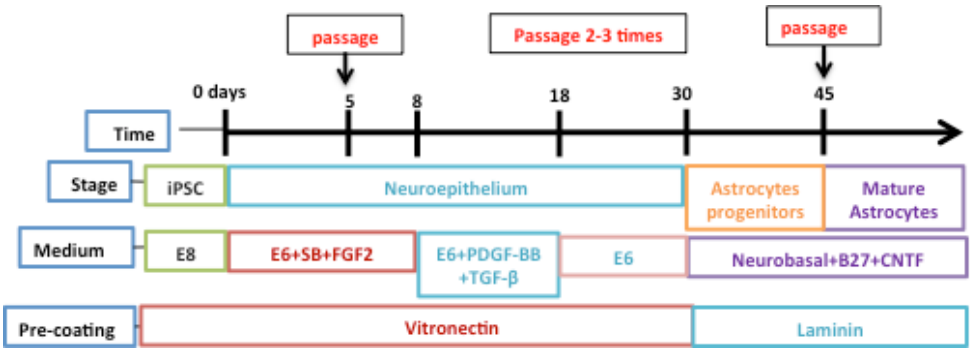
passage
Passage 2-3 times
passage
0 days
5
8
18
30
45
Time
Stage
iPSC
Neuroepithelium
Astrocytes progenitors
Mature Astrocytes
Medium
E8
E6+SB+FGF2
E6+PDGF-BB +TGF-β
E6
Neurobasal+B27+CNTF
Pre-coating
Vitronectin
Laminin

B

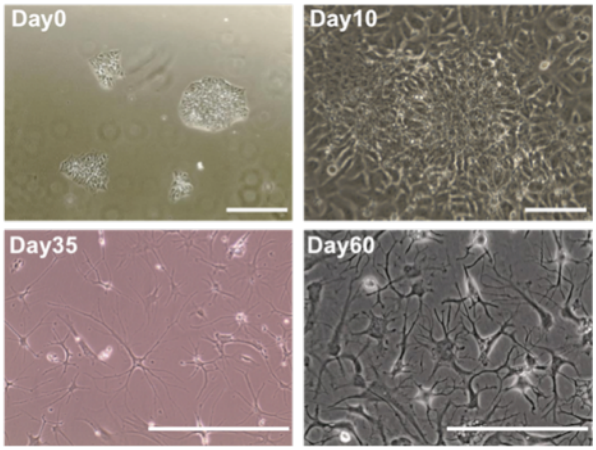
Day0
Day10
Day35
Day60

C

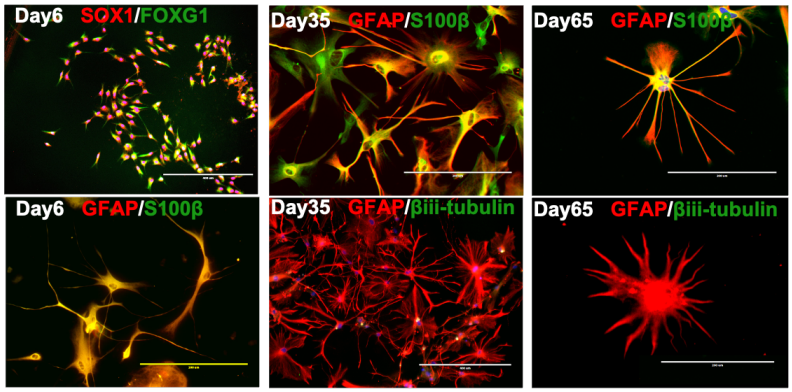
Day6 SOX1/FOXG1
Day35 GFAP/S100β
Day65 GFAP/S100β
Day6 GFAP/S100β
Day35 GFAP/βiii-tubulin
Day65 GFAP/βiii-tubulin

D

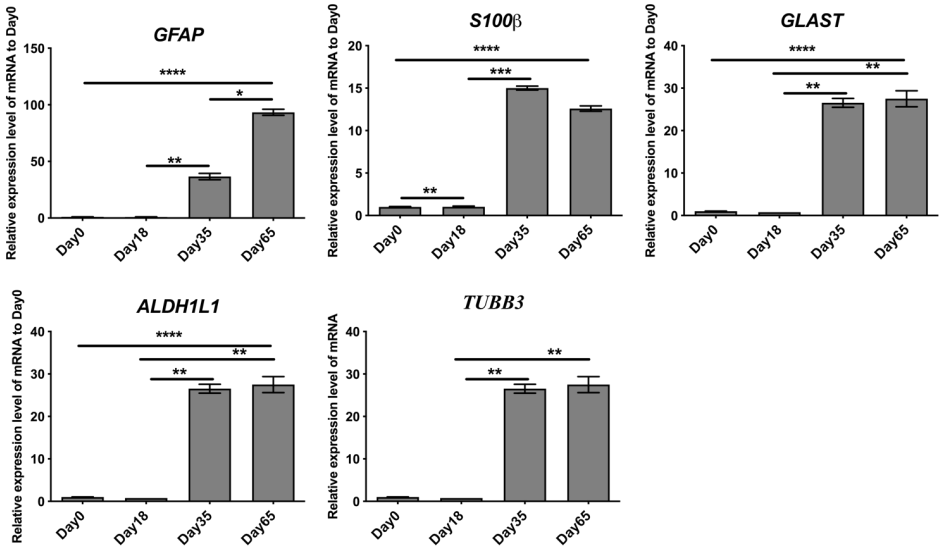
GFAP
S100β
GLAST
ALDH1L1
TUBB3
Relative expression level of mRNA to Day0
Day0
Day18
Day35
Day65

Figure 4.4 Preliminary test for a new iPSC-astrocytes differentiation protocol through SMAD signalling inhibition/ TGF-β1.

(A) Schematic drawing of the new protocol for iPSC-astrocyte differentiation indicating the timeline, differentiation stages, medium and pre-coating material. IPSCs were firstly derived into NPCs through SMAD signalling inhibition in 8 days, under the presence of growth factors SB431542 and FGF2. Then the NPCs were cultured with growth factors PDGF-BB and TGF-β until day 18 to generate neuroepithelium cells, followed by a spontaneous differentiation in E6 medium until day 30. APCs started to form, and finally mature astrocytes were generated after day 45. **(B)** Phase microscopy images show morphology changes of cells during astrocyte differentiation. Scale bars, 200 μm **(C)** Immunofluorescent staining for NPC markers SOX1 (red), and FOXG1 (green) with DAPI (blue) at day 6. Expression of astrocyte markers S100β (green) and GFAP (red) at day 35 and day 65 of differentiation. Nuclei are stained with DAPI (blue). Scale bars, 100 μm. **(D)** qRT-PCR quantification of astrocyte specific marker genes *S100β, GFAP GLAST* and *ALDH1L1* and neuronal marker *TUBB3*. Data shows gene expression during iPSC-astrocyte differentiation at days 18, 35 and 65 relative to day 0 (iPSCs stage). *GAPDH* was used as the endogenous control.

Data displayed as the means ± SEM from 3 biological triplicates each with 3 technical replicates. *, $p<0.05$, ** $p<0.005$ *** $P<0.0005$, **** $P<0.0001$. Statistical significance was determined by using one-way ANOVA.

A

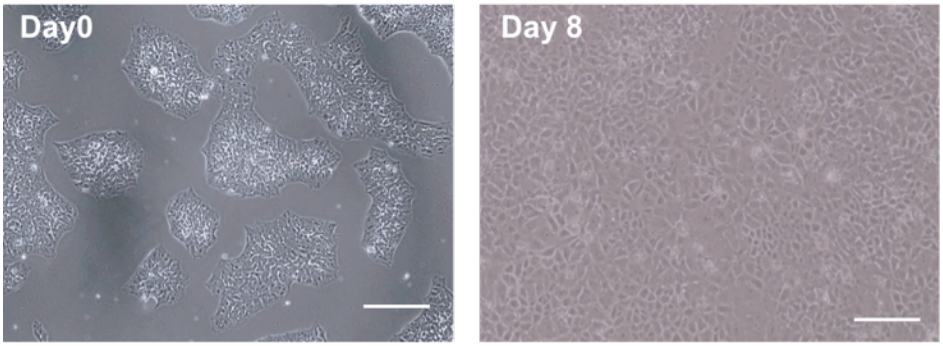
Day0
Day 8

B

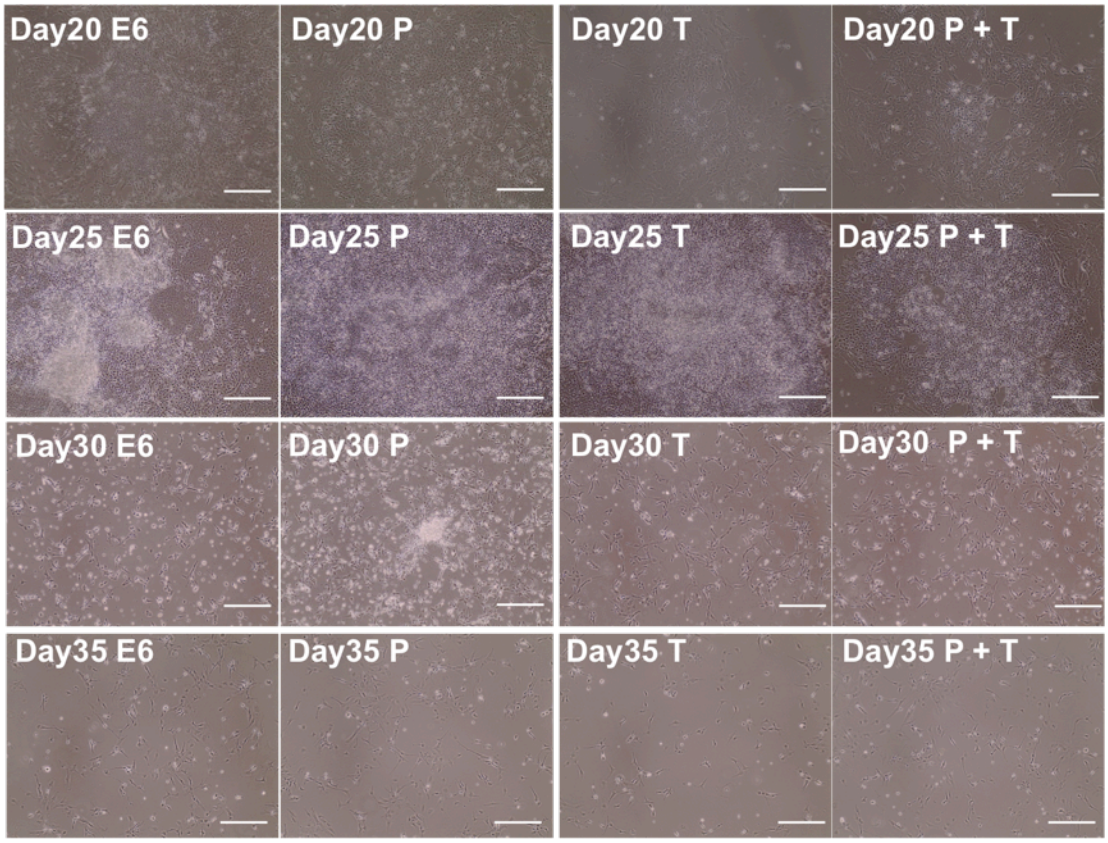
Day20 E6
Day20 P
Day20 T
Day20 P + T
Day25 E6
Day25 P
Day25 T
Day25 P + T
Day30 E6
Day30 P
Day30 T
Day30 P + T
Day35 E6
Day35 P
Day35 T
Day35 P + T

C.

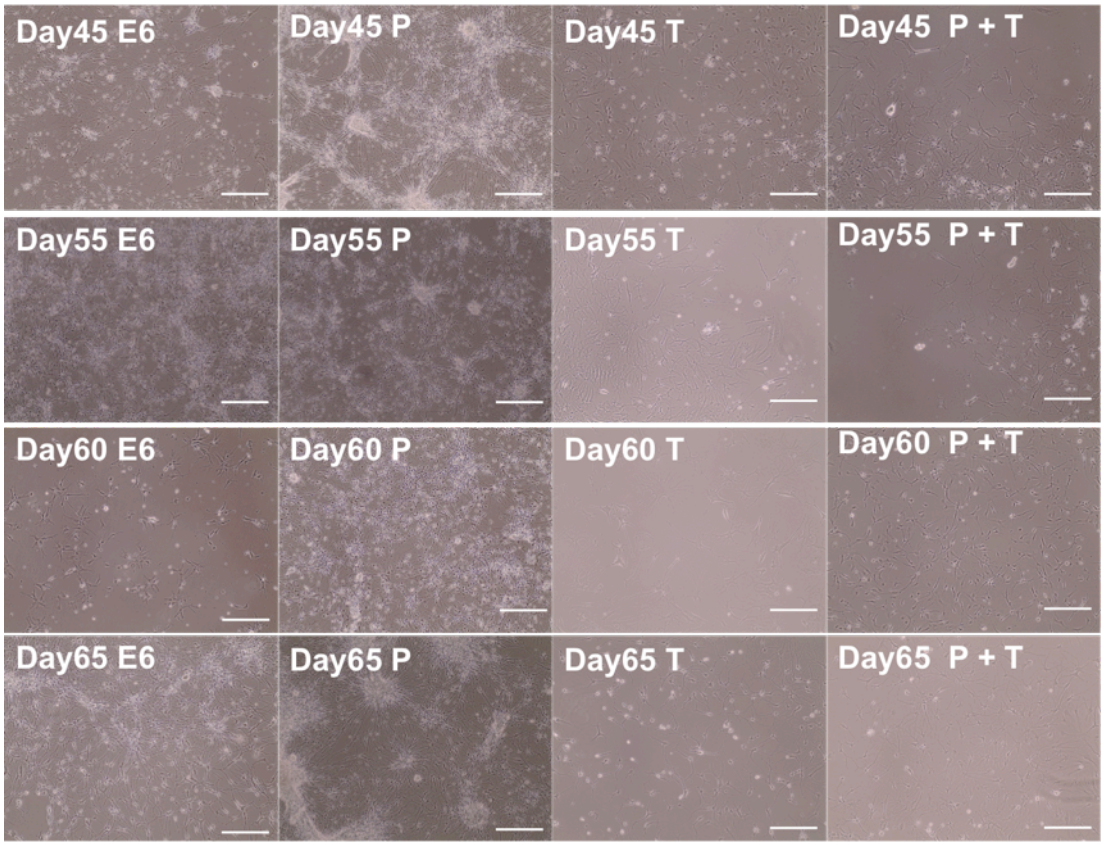

Figure 4.5 Morphology of iPSCs undergoing Astrocyte differentiation via a new protocol under 4 conditions.

(A) Phase microscopy images show morphology changes of cells during astrocytes differentiation at day 0 and day 8. Scale bars, 200 μm.

(B) Morphological changes of cells during astrocyte differentiation at day 20, 25, 30 and 35 under 4 conditions: E6 medium only, E6 + PDGF-BB, E6 + TGF-β and E6 + both growth factors groups. The 4 conditions were applied from day 8 of differentiation. Scale bars, 200 μm.

(C) Phase microscopy images show morphology changes of cells during astrocyte differentiation at days 45, 55, 60 and 65 under 4 conditions: E6 medium only, E6 + PDGF-BB, E6 + TGF-β and E6 + both growth factors groups. Scale bars, 200 μm

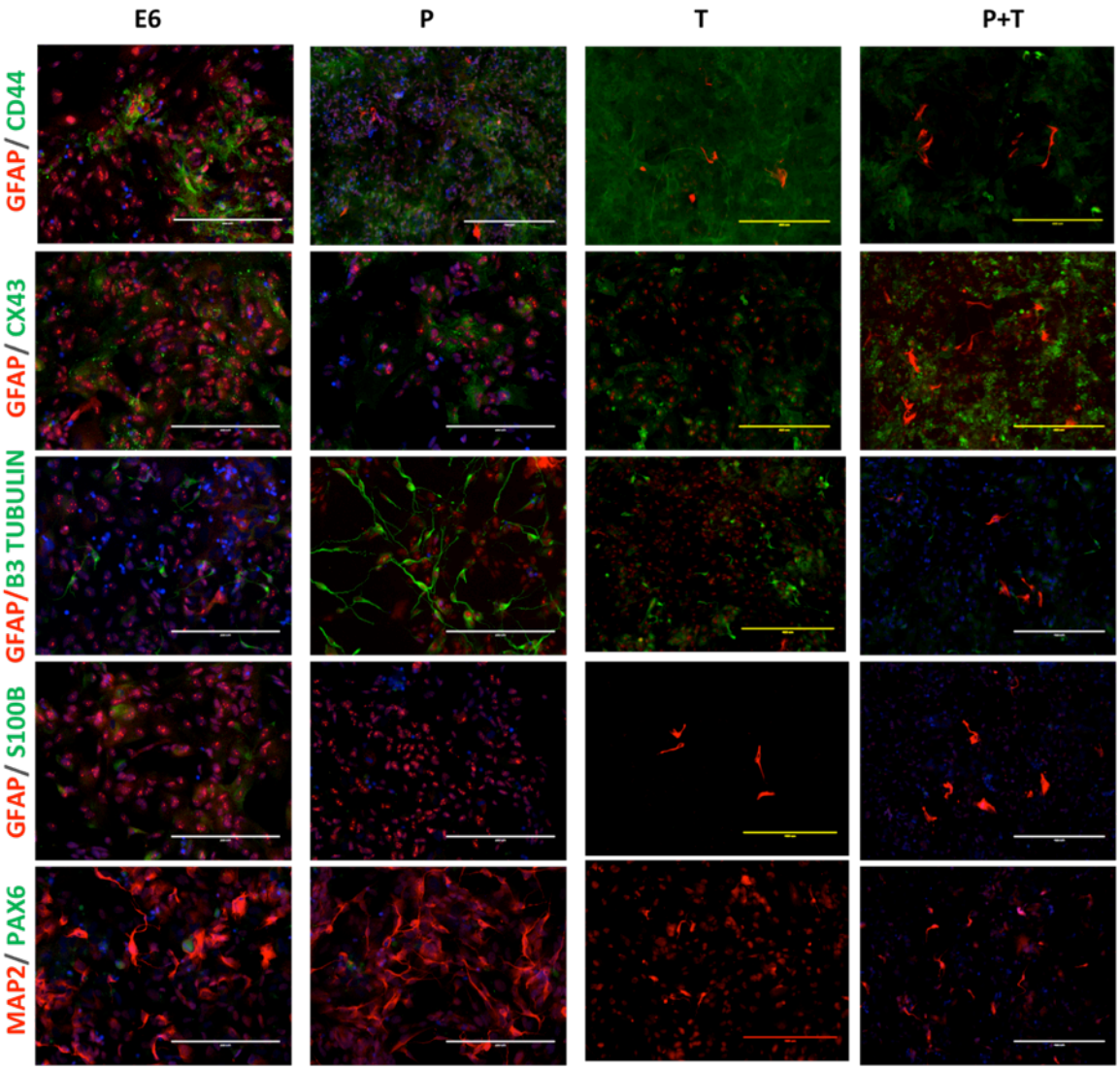

Figure 4.6 Immunofluorescent staining of day 35 iPSC-Astrocytes via a new protocol under 4 conditions.

Immunofluorescent staining images for astrocytic (GFAP, CD44, CX43 and S100β) and non-astrocytic markers (MAP2, PAX6 and βiii TUBULIN) at day 35 of iPSC-astrocytes differentiation under 4 conditions. Markers were double-stained with green and red indicated as labelled. Nuclei are stained with DAPI (blue). Scale bars, 200/400 μm.

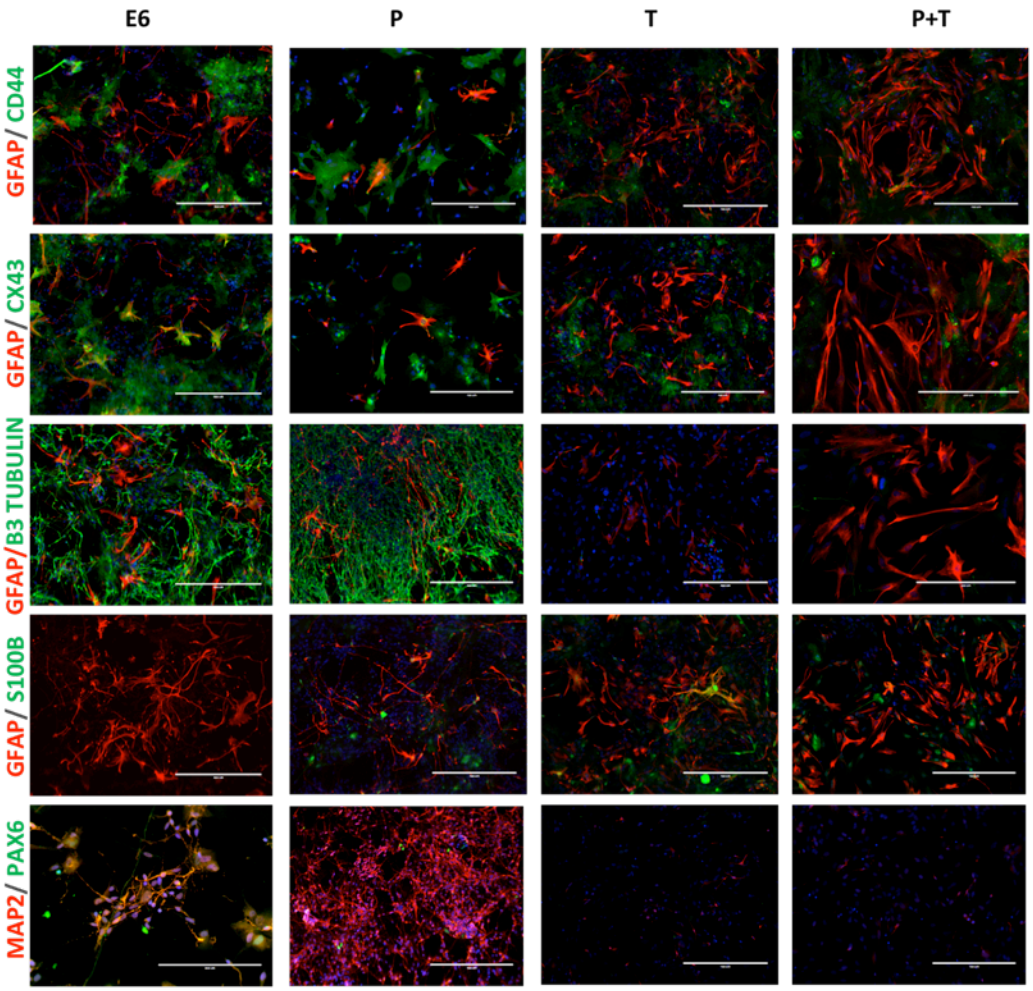

Figure 4.7 Immunofluorescent staining of day 45 iPSC-Astrocytes via a new protocol under 4 conditions.

Immunofluorescent staining images for astrocytic markers (GFAP, CD44, CX43 and S100β) and non-astrocytic markers (MAP2, PAX6 and βiii TUBULIN) at day 45 of iPSC-astrocytes differentiation under 4 conditions. Markers are double-stained with green and red indicated as labelled. Nuclei are stained with DAPI (blue). Scale bars, 200/400 μm.

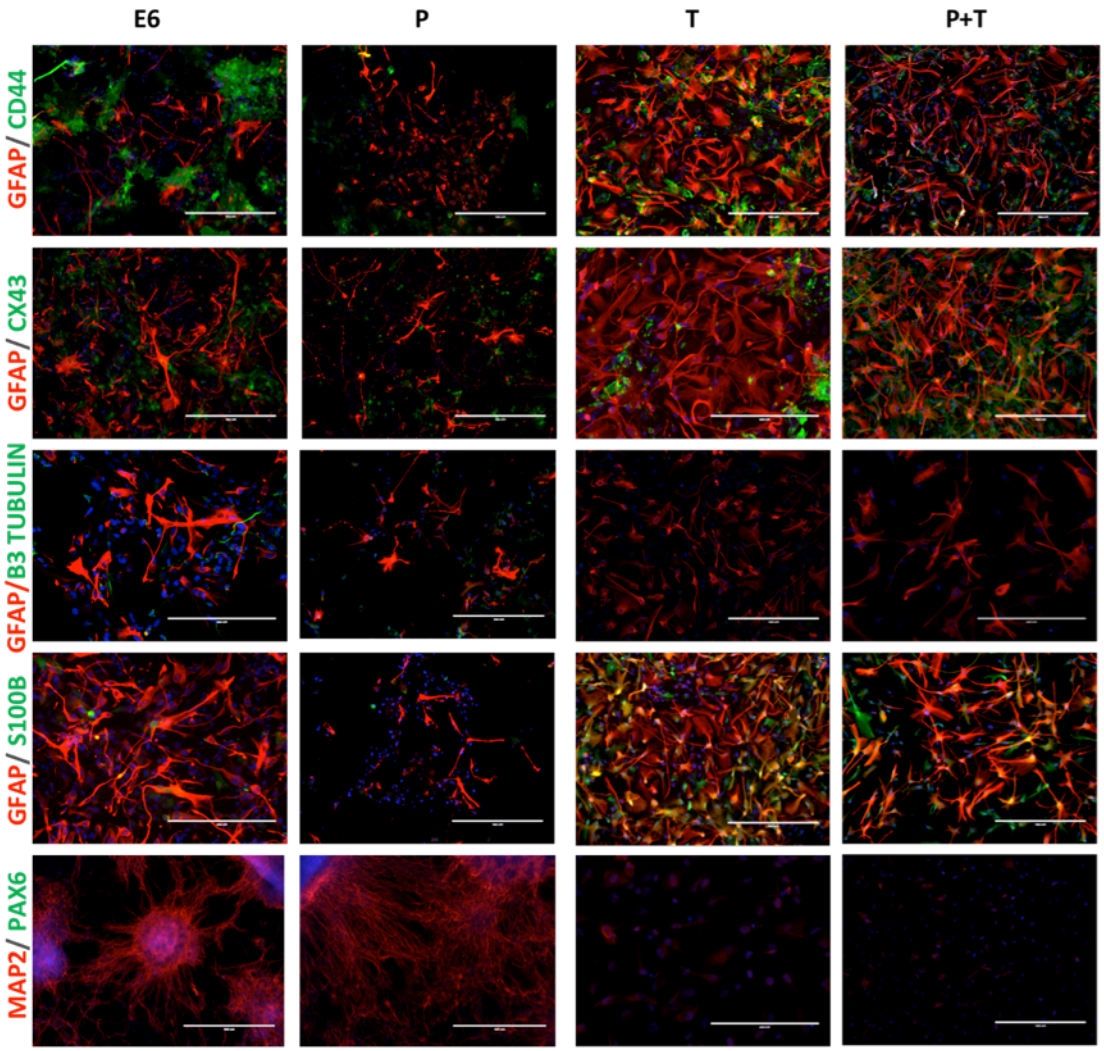

Figure 4.8 Immunofluorescent staining of iPSC-Astrocytes via a new protocol under 4 conditions.

Immunofluorescent staining images for astrocytic markers (GFAP, CD44, CX43 and S100β) and non-astrocytic markers (MAP2, PAX6 and βiii TUBULIN) at day 65 of iPSC-astrocytes differentiation under 4 conditions. Markers are double-stained with green and red indicated as labelled. Nuclei are stained with DAPI (blue). Scale bars, 200/400 μm.

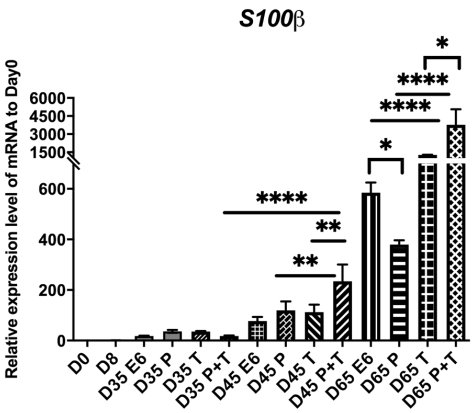
S100β
Relative expression level of mRNA to Day0
6000
4500
3000
1500
600
400
200
0
****
**
**
**
****
****
*
*
D0
D8
D35 E6
D35 P
D35 T
D35 P+T
D45 E6
D45 P
D45 T
D45 P+T
D65 E6
D65 P
D65 T
D65 P+T

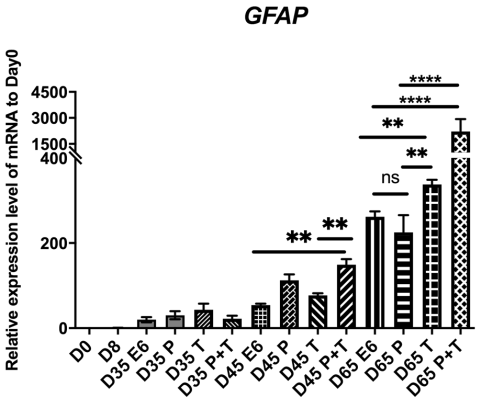
GFAP
Relative expression level of mRNA to Day0
4500
3000
1500
400
200
0
****
****
**
**
**
**
ns
D0
D8
D35 E6
D35 P
D35 T
D35 P+T
D45 E6
D45 P
D45 T
D45 P+T
D65 E6
D65 P
D65 T
D65 P+T

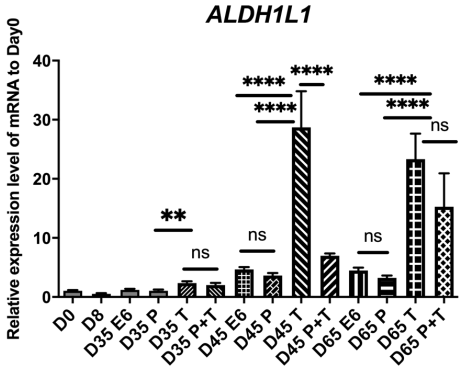
ALDH1L1
Relative expression level of mRNA to Day0
40
30
20
10
0
**
ns
****
****
ns
****
****
ns
ns
D0
D8
D35 E6
D35 P
D35 T
D35 P+T
D45 E6
D45 P
D45 T
D45 P+T
D65 E6
D65 P
D65 T
D65 P+T

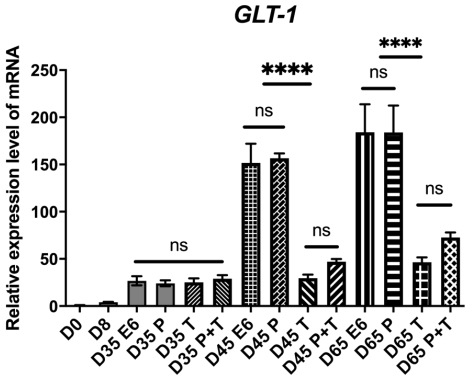
GLT-1
Relative expression level of mRNA
250
200
150
100
50
0
ns
****
ns
ns
****
ns
ns
D0
D8
D35 E6
D35 P
D35 T
D35 P+T
D45 E6
D45 P
D45 T
D45 P+T
D65 E6
D65 P
D65 T
D65 P+T

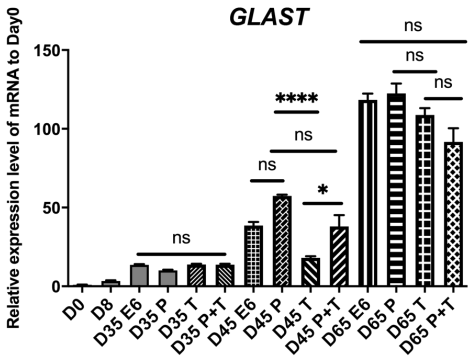
GLAST
Relative expression level of mRNA to Day0
150
100
50
0
ns
ns
ns
****
ns
ns
*
ns
D0
D8
D35 E6
D35 P
D35 T
D35 P+T
D45 E6
D45 P
D45 T
D45 P+T
D65 E6
D65 P
D65 T
D65 P+T

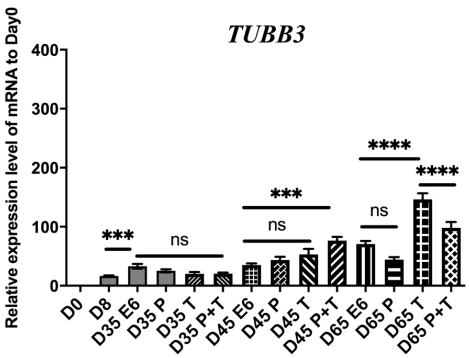
TUBB3
Relative expression level of mRNA to Day0
400
300
200
100
0
***
ns
***
ns
****
****
ns
D0
D8
D35 E6
D35 P
D35 T
D35 P+T
D45 E6
D45 P
D45 T
D45 P+T
D65 E6
D65 P
D65 T
D65 P+T

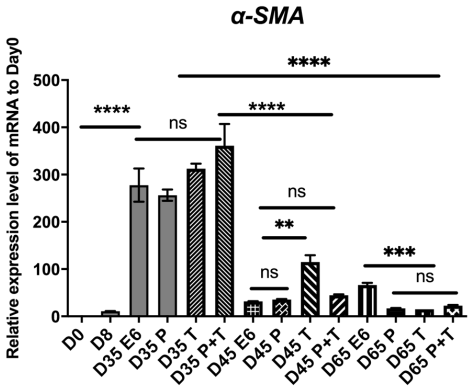
α-SMA
Relative expression level of mRNA to Day0
500
400
300
200
100
0
****
****
ns
****
ns
**
ns
***
ns
D0
D8
D35 E6
D35 P
D35 T
D35 P+T
D45 E6
D45 P
D45 T
D45 P+T
D65 E6
D65 P
D65 T
D65 P+T

Figure 4.9 Gene expression of iPSC-Astrocytes via a new protocol under 4 conditions.

qRT-PCR quantification of astrocytes specific marker genes (*S100β, GFAP GLAST, GLT-1* and *ALDH1L1*), neuronal marker gene *TUBB3* and smooth muscle marker gene *α-SMA*. Data shows gene expression during iPSC-astrocytes differentiation at days 8, 35, 45 and 65 relative to day 0 (iPSCs stage). *GAPDH* was used as the endogenous control.

The data is displayed as the mean ± SEM from a biological triplicate each with 3 technical replicates. * $p<0.05$, ** $p<0.005$ *** $P<0.0005$, **** $P<0.0001$. Statistical significance was determined by using two-way ANOVA.

4.2.2. Differentiation and characterisation of iPSC-neurons

Neurons were differentiated from iPSCs lines following a SMAD inhibition protocol using Dorsomorphin and SB431542 (**Figure 4.10 A**). IPSCs stained positive for pluripotency markers SOX2 and NANOG at day 0 and negative for neuronal marker MAP2 (**Figure 4.10 C**). Cells exhibited typical rosette-like morphology at the NPC stage and stained positive for NPC markers MAP2, PAX6 and FOXG1, with SOX2 and SSEA4 as negative controls (**Figure 4.10 B and C**). For the generation of purified neurons, the neuronal rosettes went through sub-culturing several times at the time points as indicated (**Figure 4.10 A**). NPCs spontaneously differentiated into neurons upon growth factor FGF2 withdrawal. At Day 35, differentiated cells exhibited typical neuronal morphology and stained positive for neuronal markers MAP2, βiii TUBULIN and the functional cortical neuronal marker VGLUT1, (**Figure 4.10 B and C**). iPSCs derived neurons were maintained in culture with cells approximately 80 days after induction of differentiation used for co-culture experiments.

A.

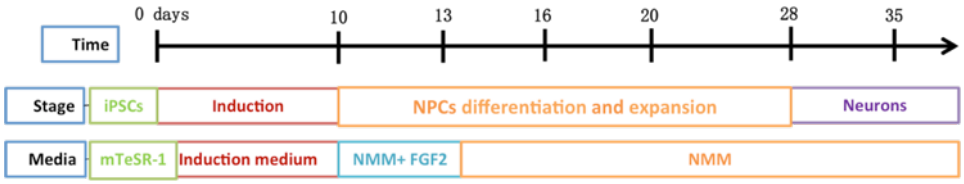
0 days
10
13
16
20
28
35
Time
Stage
iPSCs
Induction
NPCs differentiation and expansion
Neurons
Media
mTeSR-1
Induction medium
NMM+ FGF2
NMM

B.

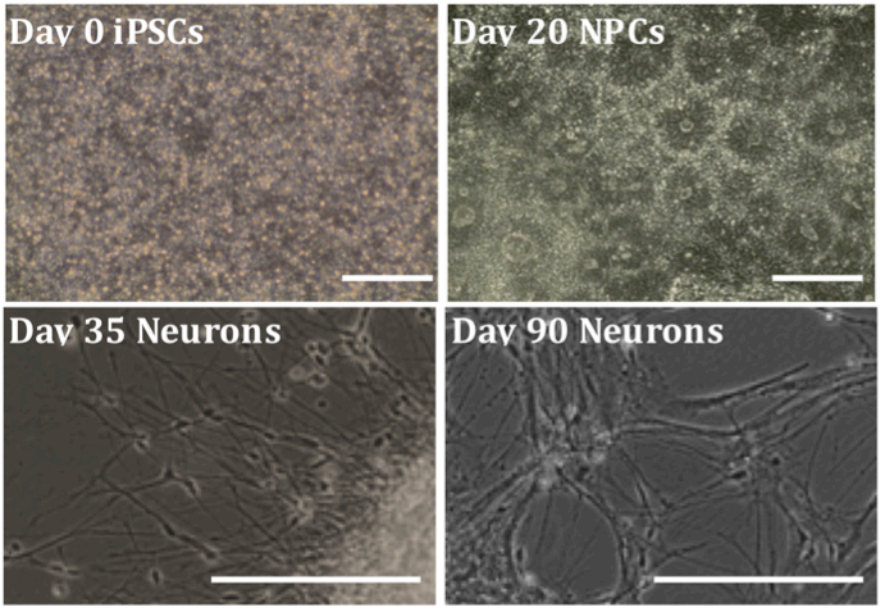
Day 0 iPSCs
Day 20 NPCs
Day 35 Neurons
Day 90 Neurons

C.

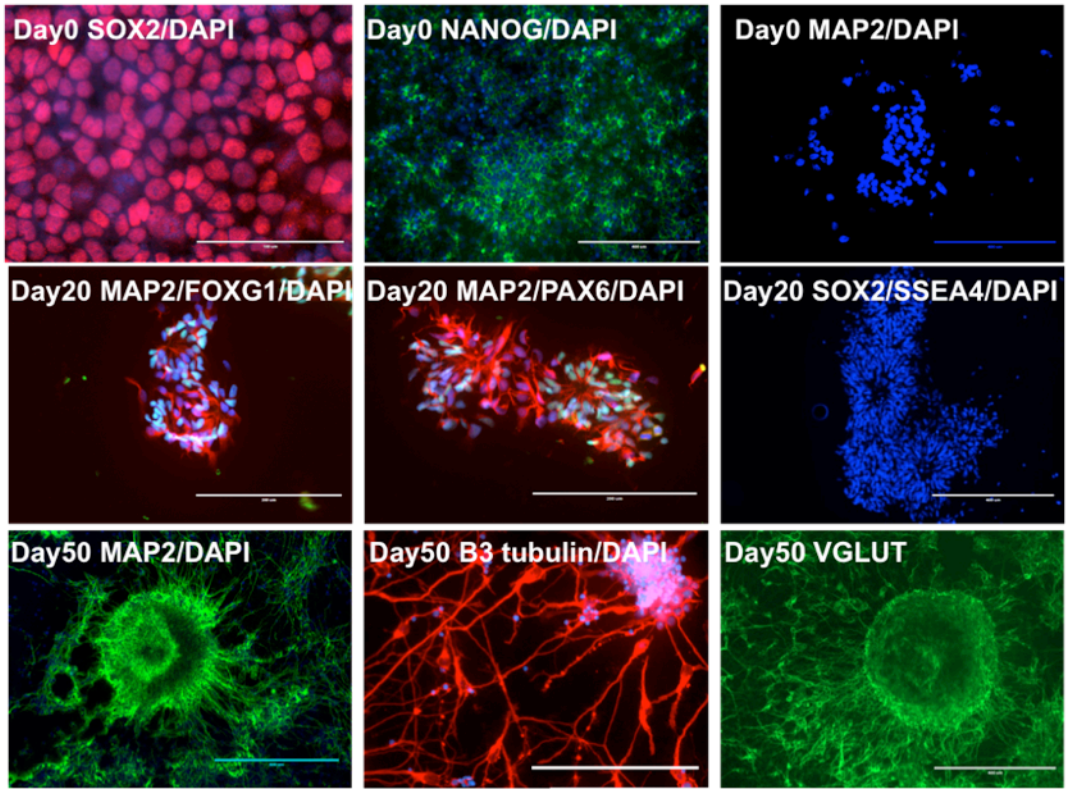
Day0 SOX2/DAPI
Day0 NANOG/DAPI
Day0 MAP2/DAPI
Day20 MAP2/FOXG1/DAPI
Day20 MAP2/PAX6/DAPI
Day20 SOX2/SSEA4/DAPI
Day50 MAP2/DAPI
Day50 B3 tubulin/DAPI
Day50 VGLUT

Figure 4.10 iPSCs-neuron differentiation and characterisation.

(A) Schematic of the iPSC-neuron differentiation protocol. Neural progenitor cells were generated by neural induction for 10 days in NMM with Dorsomorphin and SB431542 (induction medium). Then cells were sub-cultured 3-4 times using Dispase. Medium was changed to NMM with FGF-2 for 3 days after neuronal induction. At Day 28 rosettes were dissociated into single cells using Accutase. Mature neurons were generated after Day 35.

(B) Phase microscopy photographs show morphological changes during iPSCs-neurons differentiation at days 0, 20, 35 and 90.

(C) Immunofluorescent staining day 0 iPSCs, day 20 NPCs and day 50 neurons. day 0 iPSCs were stained for pluripotency markers SOX2 (red) and NANOG (green) as well as neuronal marker MAP2 with DAPI (blue). Day 20 NPCs were stained for neuronal markers MAP2 (red), PAX6 (green) and FOXG1 (green) with DAPI (blue). Pluripotent markers SOX2 (red) and SSEA4 (green) were stained as control. Day 50 neurons were stained for neuronal markers MAP2 (green), βiii TUBULIN (red) and functional neuronal marker VGLUT1 (green). Nuclei were stained with DAPI (blue). Markers were double-stained or triple-stained as shown in the merged photos. Scale bars, 200 μm.

4.3. Discussion

Astrocytes and neurons play key roles in the NVU, as such, the aim of this chapter was the successful differentiation of these cell types from iPSCs. Besides, a new protocol for iPSC-astrocytes deviation was described, which provides an effective way to achieve mature astrocytes from iPSCs with high efficiency and lower expense.

4.3.1. iPSCs can be successfully differentiated to astrocytes

In this chapter three methods of iPSC-astrocytes differentiation were described. The astrocytes differentiated using Majumder et al. protocol were stained positive for astrocyte markers GFAP and S100β (**Figure 4.1**). However, the astrocytes generated could not be maintained longer than 60 days, and the number of cells tended to decrease during differentiation. Poor cell yields meant that conducting further characterisation and co-culture experiments was not possible. The publication on which this method was based did not provide guidance for trouble shooting and systematic optimisation of parameters such as medium composition and sub-culture technique would have taken considerable time therefore this method was abandoned.

Studying NVU interactions with multicellular models requires high numbers of functional and homogenous cells. Another widely published protocol for the production of astrocytes from iPSCs is the commercially available StemCell Technologies protocol. Astrocytes generated with this protocol showed significant expression of astrocytic markers GFAP, S100β and GLAST, confirmed by immunostaining or qRT-PCR (**Figure 4.2**). Functionality was confirmed as these astrocytes exhibited the potential to propagate calcium waves upon mechanical stimulation **(Figure 4.3)**. These results collectively showed that functional astrocytes were generated using the StemCell protocol, though astrocyte identity can be further ascertained by other functional attributes, such as high rate of glutamate uptake and the ability to promote maturation of co-cultured neurons [287]. As a result, the StemCell Tech protocol was applied for generating astrocytes for iPSC-BBB modelling.

4.3.2. Effective generation of iPSC-Astrocytes through SMAD signalling inhibition/TGF-β1

As previously discussed, the methods for the generation of astrocytes from iPSCs are time-consuming and inefficient. The Majumder et al. protocol produced astrocytes with low efficiency and poor astrocytic markers expression taking 60 days. The StemCell

Technologies protocol produced astrocytes with superior function and phenotype at a higher efficiency also within 60 days. However, it is costly and proprietary. Subsequently, a protocol based on SMAD signalling inhibition/TGF-β1 was developed the for rapid and efficient generation astrocytes from iPSCs.

The preliminary experiment showed successful differentiation of iPSCs to astrocytes with typical astrocytic cell morphology formed after Day 35 of differentiation and strong astrocytic specific markers s100β, GFAP and GLAST expression in both protein and mRNA level (**Figure 4.4**). It can be indicated that immature astrocyte precursors at day 35 were generated and finally mature astrocytes were generated at day 65, which can be supported by the mRNA expression of *ALDH1L1* between day 35 and day 65. In order to know whether PDGF and TGF-β1 are required between days 8 and 18, therefore it was investigated what contribution, if any, they made toward astrocyte cell fate. The results indicated TGF-β1 may be essential for successful iPSCs-astrocytes differentiation and addition of PDGF may increase cell proliferation as indicated by immunostaining and *GFAP/S100β* qRT-PCR data at day 65 **(Figure 4.5, 4.6, 4.7, 4.8 and 4.9)**.

These results indicate that the presence of TGF-β may be essential for successful differentiation of iPSCs to astrocytes otherwise cells look neuronal. Besides, addition of PDGF may increase cell proliferation but may also enhance astrocytes differentiation.

Glutamate extracellular levels are regulated by two major specific transporters: GLAST and GLT (glutamate transporters 1 and 2, respectively). As such, GLAST and GLT1 are both markers of functional and mature astrocytes. However, their gene expression profile at the end of differentiation varied between the experimental groups **(Figure 4.9)**. Both GLAST and GLT1 are localised in astroglia and neurons during early brain development [321]. It's surprised to observe *GLAST* and *GLT*-1 mRNA expression in E6 and E6+ P groups are higher than E6 + T and E6+ P + T groups ($p<0.005$) **(Figure 4.9)**. One possible hypothesis could be a lack of neurons in E6 + T and E6+ P + T groups while in E6 and E6+ P groups both neurons and astrocytes existed. It has been reported *GLT-1* and *GLAST* are expressed on morphologically distinct astrocytes and regulated by neuronal activity. The expression of both transporters has been shown to be down-regulated as a consequence of neuronal death or reduced synaptic activity while soluble factors in neuronal-conditioned cell culture medium could restore the expression of the GLT-1 and GLAST proteins [322]. Thus lacking of neurons in E6 + T and E6+ P + T groups could lead to lower expression of GLT-1 and

GLAST compared to E6 and E6+ P groups. Further experimental repeats are needed to confirm the results and mRNA expression of GLT-1 and GLAST on astrocytes with or without co-culture with neurons to test this hypothesis. The immunostaining images further supported the qRT-PCR result as neuronal markers βiii-tubulin and MAP2 expression is obviously increased in E6 and E6 + P groups from day 35 to day 65 while astrocytes markers expression of GFAP and S100β in both groups is low **(Figure 4.6, 4.7 and 4.8)**.

Besides, the expression of mature cortical astrocytes marker *ALDH1L1* at day 65 was much higher in the T and T+P groups compared with E6 and E6 + P groups ($p<0.0005$) **(Figure 4.9),** which further supports that TGF-β1 and PDGF may be required for astrocytes differentiation and also indicates that astrocytes generated with this protocol are possibly cortical subtype.

The data in this study suggest that TGF-β1 and possibly PDGF are required for the successful differentiation of astrocytes from iPSCs via NPCs and SMAD signalling inhibition. Previously a few papers have reported the function of PDGF and TGF-β1 in astrocytes. TGF-β1 acts on astrocytes by increasing the production of laminin and fibronectin, affecting their motility and morphology, promoting the appearance of actin stress fibres, increasing cell actin content, inducing the expression of neuronal and astrocytic cytoskeleton genes such as GFAP and tubulin [323-325]. In one paper it was demonstrated that TGF-β1 is a critical cytokine that regulates radial glial stem cell differentiation into astrocytes *in vitro* and *in vivo*[326]. In another recent publication PDGF-AA was applied for iPSC-astrocytes differentiation and shown to allow NPC spheres to attach onto Matrigel coated plates and permit cell outgrowth [327]. Furthermore, in astrocytes, overexpression of PDGF-BB caused significant increase in proliferation rate of both GFAP-expressing astrocytes and neural progenitors [328]. However, currently there is no published evidence that PDGF-BB could determine stem cells differentiation into astrocytes. All the evidence collectively indicates that TGF-β1 is vital for iPSCs-astrocytes differentiation while PDGF-BB may also contribute to astrocytes differentiation during differentiation but not determine the astrocytic fate. As both NOTCH and TGF-β signalling pathways are critical for astrocyte development [282], it would be interesting to investigate whether NOTCH3 mutations in CADASIL patients affect astrocyte functions and by extension BBB functions.

Though this alternative differentiation protocol has been shown to generate iPSC-derived astrocytes effectively and quickly, further functional properties should be tested such as

calcium imaging, glutamate uptake and promotion of neuronal synaptogenesis. Additionally, further repeats on additional iPSC lines is needed to confirm the results. To further investigate how TGF-β lead to astrocytic fate and if addition of PDGF-BB increases cells proliferation, NPC markers (PAX6, FOXG1+MAP2), astrocyte markers, proliferation markers Ki67 and SMC markers (α-SMA+Calponin) should be assessed between day 5 and 30 to better understand the phenotypic switch that occurs prior the appearance of astrocyte-like cells.

4.3.3. iPSCs can be successfully differentiated into cortical neurons

Differentiation of iPSC-neurons was performed according to Shi *et al*. which mimics cortical development [329]. The pluripotency in iPSCs is essential for successful differentiation and the purity of neurons. Immunostaining images showed OX1-19 iPSCs were positive for pluripotent markers SOX2 and NANOG (**Figure 4.7 C**). During NPCs stage, immunofluorescence microscopy data showed significant increase expression of neuronal marker MAP2 at day 20 compared with Day0 and cells were also positive for early NPC specific markers FOXG1 and PAX6 (**Figure 4.7 C**). By Day 50 iPSC-neurons showed widespread reactivity for neuronal markers βiii-TUBULIN and MAP2. These data suggest that neurons have successfully been derived from iPSCs. There was also positive staining for pre-synaptic markers (VGLUT1) (**Figure 4.7 C**). The presence of synaptic proteins indicates that iPSCs-neurons exhibit functional properties. iPSC-derived neurons from day 80 onwards were used in co-culture experiments and BBB modelling as this was previously determined to be the point of maturation [329].

4.4. Summary

In summary, this chapter demonstrates that functional iPSC-astrocytes and neurons can be derived from iPSCs. A new protocol for iPSC-astrocyte differentiation has been established and optimised for quick and efficient generation of astrocytes. As astrocytes and neurons are key components of NVU structure and play vital roles in BBB function, these iPSC-astrocytes and iPSC-neurons were used for BBB modelling and co-culture experiment, which will be shown in following chapters.

5. Chapter 5: Using an *in vitro* iPSC-BBB model to study neurovascular interaction

5.1. Introduction

In chapters 3 and 4, the successful differentiation of NVU cells from iPSCs including BMECs, astrocytes and neurons were described. The NVU also includes vMCs which composed of vSMCs and pericytes, the differentiation of which is previously published [223] and replicated here. In this chapter the efforts to develop an *in vitro* iPSC-BBB model to study neurovascular interaction in iPSC-derived NVU cells and the advantages of this model will be described.

5.1.1. Differentiation of vascular mural cells from iPSCs

VSMCs and pericytes are collectively called vMCs. vSMCs line arterioles and venules while pericytes are associated with microvessels and capillaries [330]. Previous studies demonstrated *NOTCH3* is expressed on both vSMCs and pericytes and both cell types are severely damaged in CADASIL [331]. However, there is little consensus on how to distinguish vSMCs from pericytes based on the expression of characteristic marker proteins.

To develop the *in vitro* iPSC-BBB model for vascular dementia, iPSC-derived vMCs were required. There are several methods for iPSC-vMCs differentiation. Taura *et al.* were the first to report the generation of vMCs from iPSCs while Lee *et al.* generated the first iPSC lines derived from somatic cells of vascular origin and differentiated them into vSMCs [332, 333]. In a recent publication, Stebbins *et al* described the differentiation of mural cells via iPSC-derived neural crest stem cells (NCSCs) and that these cells develop brain pericyte–like attributes and could induce BBB properties in BMECs [334]. Another recent publication showed induction of mesoderm and neural crest-derived pericytes from iPSCs to study the role of pericytes in BBB dysfunction in AD [335].

A common approach to differentiate vMCs from NCSCs is to supplement basal medium with PDGF-BB and TGFβ1 [216, 336, 337], which was the method being followed by in our iPSC-vMCs differentiation method described in this chapter. Our iPSC-vMCs differentiation protocol was modified by Kelleher et al. which originated from Cheung at al. protocol [223, 338]. This chemically well-defined method is advantageous due to high differentiation efficiency, great reproducibility and relatively simple process.

5.1.2. iPSC-BBB models scheme for neurological disorders

BBB dysfunction and breakdown are observed in various neurodegenerative diseases and likely contributes to the initiation and progression of pathology in many neurological disorders, however the exact mechanisms remain largely unknown [339]. Though animal BBB models have been reported, species differences in the type and expression level of membrane transporter proteins such as P-glycoprotein, multidrug resistance-associated protein 4 and monocarboxylate transporter 1 and others, that form part of the role of the BBB, limit the application of animal models in preclinical studies [340, 341]. *In vitro* BBB models have been established using primary human cells or immortalized human cell lines, however, limitations such as access to post-mortem tissue or lack of sufficient barrier functions of these cells limit their usefulness [342-344].

To overcome these shortcomings, in recent years human iPSC-derived NVU cells have been incorporated into BBB models to investigate the pathology of VaD [345]. In current iPSC-BBB models, iPSC-derived BMECs have been applied alone or co-cultured with either iPSC-derived neural cells and astrocytes or primary pericytes and astrocytes [213, 310, 346-348]. Previously, several groups have found that BMEC barrier function was significantly enhanced after co-culturing with astrocytes, pericytes, and neural cells as measured by TEER and permeability to molecules by passive diffusion [349-351]. However, a fully isogenic model, were all cell types are derived from the same donor, has yet to be described.

The mechanisms underlying many neurological diseases involving BBB dysfunction are still unclear, however, iPSC derived BBB models are beginning to address this issue [352]. BBB dysfunction has been observed in iPSC-derived BBB models of several most common mutations associated neurodegenerative diseases, including AD, PD and ALS [353]. iPSC-BBB models for neurological diseases such as HD and cerebral adrenoleukodystrophy have revealed barrier defects in BMECs differentiated from patient iPSCs of both diseases, suggesting BBB breakdown contributes to disease pathologies [352, 354, 355]. Vatine *et al* found mutations in SLC16A2, which encodes a thyroid hormone (TH) transporter and causes Allan-Herndon-Dudley syndrome, leading to inadequate transport of TH across the BBB [221].

Taken together, these findings indicate that BBB dysfunction is a common feature of many neurological disorders and can be modelled using iPSC-derived BBB cell types. However, there is currently no iPSC-derived BBB model that incorporates all NVU cell types for VaD.

In order to fully model VaD *in vitro* it's necessary to build a BBB model with 4 types of NVU cells derived from iPSC to recapitulate all possible cellular interactions.

5.1.3. Building an iPSC-BBB model for neurovascular interactions

VaD has been associated with BBB dysfunction [356], however, none of the current iPSC-derived CADASIL models used other cell NVU cell types apart from vMCs and vECs. Moreover, the endothelial cells being investigated for CADASIL pathologies in previous studies were peripheral rather than BMECs, which may not faithfully recapitulate the brain pathologies [223]. Among iPSC-BBB models for other CNS disorders, pericytes are the least studied of the cellular components of the BBB despite their tight association with BMECs [357].

To address these limitations, iPSCs were differentiated to BBB cell types including BMECs, astrocytes and neurons, as previously described, and in this chapter the differentiation of iPSC-vMCs will be shown. To assess the effects of different NVU cell types on the iPSC-BBB model, the influence of iPSC-derived astrocytes, neurons and vMCs on the barrier function of iPSC-BMECs can be assessed in different spatial arrangements, such as BMECs co-culture or triple culture with astrocytes or vMCs or neurons. Previous studies have shown that co-culturing BMECs with NPCs, astrocytes and pericytes can enhance BBB properties such as TEER, efflux transporter activity and expression of essential BBB junctional proteins (Claudin-5, ZO-1, Occludin, VE-Cadherin), membrane transporter proteins (P-gp, GLUT1), and other factors (PECAM-1, VEGFR2, vWF) [349, 358-360]. The development of a functional iPSC-BBB model for neurovascular interactions is important not only for understanding mutation linked VaD as well as other CNS disorders leading to BBB dysfunction but also to explore potential drug screening abilities for therapeutics purpose.

5.1.4. Aims and objectives.

BBB dysfunction is a common feature in various dementia and can be modelled using iPSC-derived NVU cell types. However, currently no iPSC-BBB model has been built for VaD or SVD. Most iPSC-derived BBB models have focused on vascular cells and not neuronal cells or astrocytes, left the neurovascular interaction in VaD un-investigated. Therefore the aim of this chapter is to build an iPSC-BBB model for neurovascular interaction.

In previous chapters the differentiation of BMECs, astrocytes and neurons from iPSCs were shown. One of the objectives of this chapter is the replication of the established protocol for iPSCs differentiating into vMCs. Another main objective of this chapter is to build a BBB model with these four NVU cell types differentiated from iPSCs. The barrier properties of this model will be characterised by junction proteins expression by immunostaining and barrier function analysis via TEER measurement and sodium fluorescence permeability assay. The comparison of our iPSC-BBB model with previous models will be discussed to show its advantage.

5.2. Results

5.2.1. Differentiation and characterisation of iPSC-mural cells

The differentiation of iPSCs into mural cells was performed via neuroectodem in order to mimic the embryological origin of cerebral arteries to model CADASIL [224, 361]. The protocol was replicated using control iPSC line (AGD-14-02 C3). A schematic summary shows the process of the differentiation (**Figure 5.1A**). Cells changed from iPSCs morphology to a migratory spindle shape NCSCs by day 8 (**Figure 5.1B**). After treatment with FGF2 and SB431542 (for the inhibition of TGF-β1 receptor) for 7 days, iPSCs changed to triangular-like morphology and gradually differentiated to larger size single cells (**Figure 5.1B**).

Immunofluorescent staining showed cells expressing the NPC markers SOX1 and FOXG1 at day 8 (**Figure 5.1C**), indicating the production of NCSCs. Following these cells were induced to a mural cell phenotype by the addition of TGF-β and PDGF-BB for ten days resulting in cells with an elongated morphology typical of vSMCs (**Figure 5.1B**). Immunofluorescent staining revealed the presence of the SMC markers CNN1 and α-SMA. (**Figure 5.1C**).

qRT-PCR data showed significant down-regulation of pluripotency gene *OCT4* during the differentiation process with d0 vs d7 ($p<0.0001$), d0 vs d18 ($p<0.0001$) (**Figure 5.2**). The expression NCSCs marker genes *SOX2* peaked at Day7: d0 vs d7 ($p<0.05$) then decreased d7 vs d18 ($p<0.0001$), however *SOX1* expression increased at Day7: d0 vs d7 ($p<0.05$) and maintained for a long period d7 vs d18 (ns). The expression of SMC markers *α-SMA, CNN1* and *SM22* showed gradually increased expression during the process (**Figure 5.2**). For *α-SMA*: d0 vs d11 ($p<0.0005$), d11 vs d18 ($p<0.0001$); for *CNN1*: d0 vs d11 ($p<0.0001$), d11 vs d18 ($p<0.0001$); for *SM22*: d0 vs d7 ($p<0.05$), d7 vs d11 ($p<0.0001$), d11 vs d18 ($p<0.0001$).

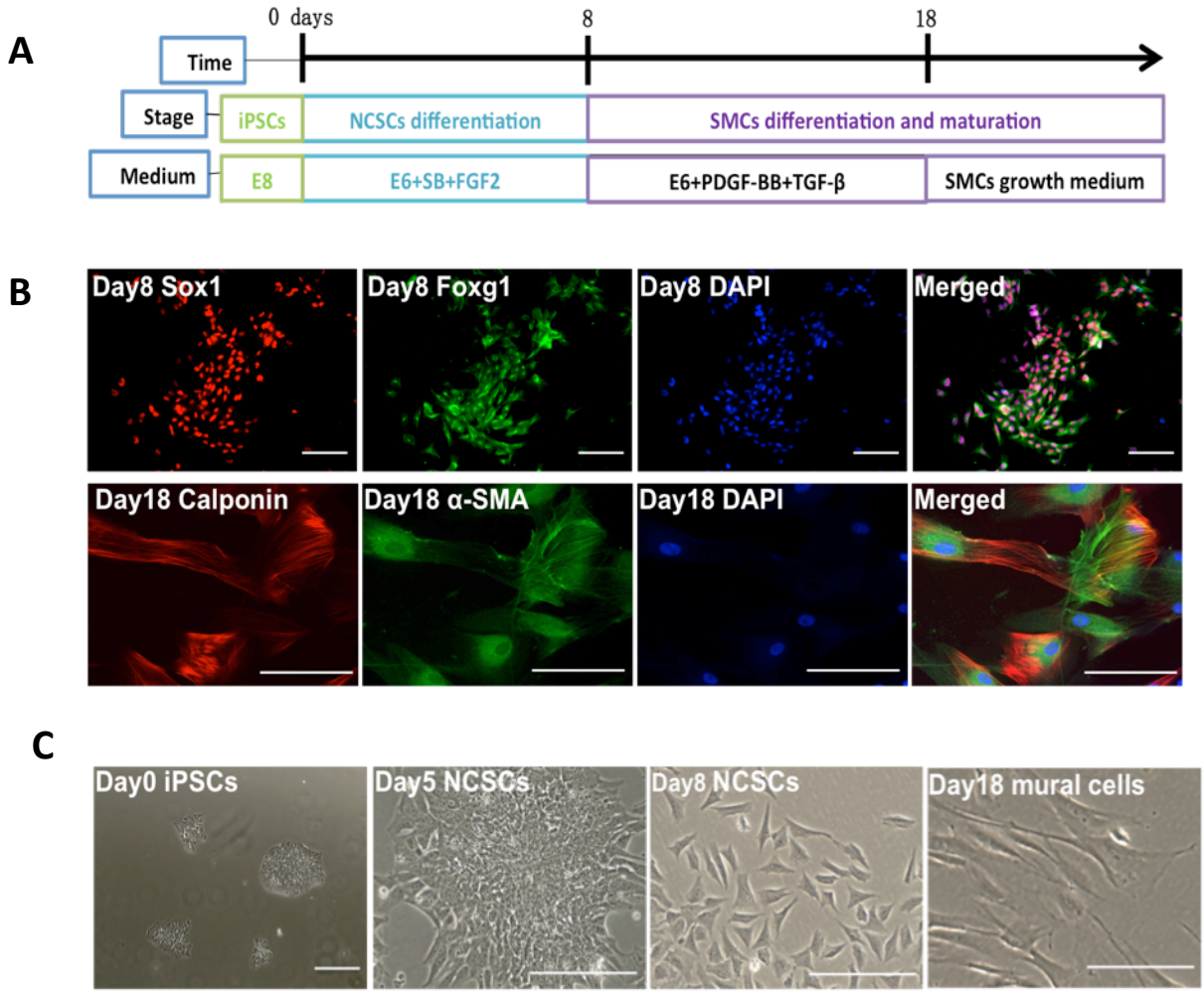

Figure 5.1 Differentiation and characterisation of iPSC-derived vMCs.

(A) Schematic summary of iPSC-vMCs differentiation process. iPSCs were first differentiated to NCSCs for 8 days and then derived into mature vMCs in the presence of PDGF-BB and TGF-β. **(B)** Phase microscopy photographs show morphology change during the differentiation process at day 0 (iPSCs stage), day 5, day 8 and day 18. **(C)** Immunofluorescence staining microscopy shows expression of NCSC markers SOX1 (red) and FOXG1 (green) with DAPI (blue) at day 8 of differentiation and expression of vSMC marker CNN1 (red) and α-SMA (green) at day 18 of differentiation. DAPI (blue) was used as a counterstain and markers were double stained as shown in the merged photos. Scale bars, 200 μm.

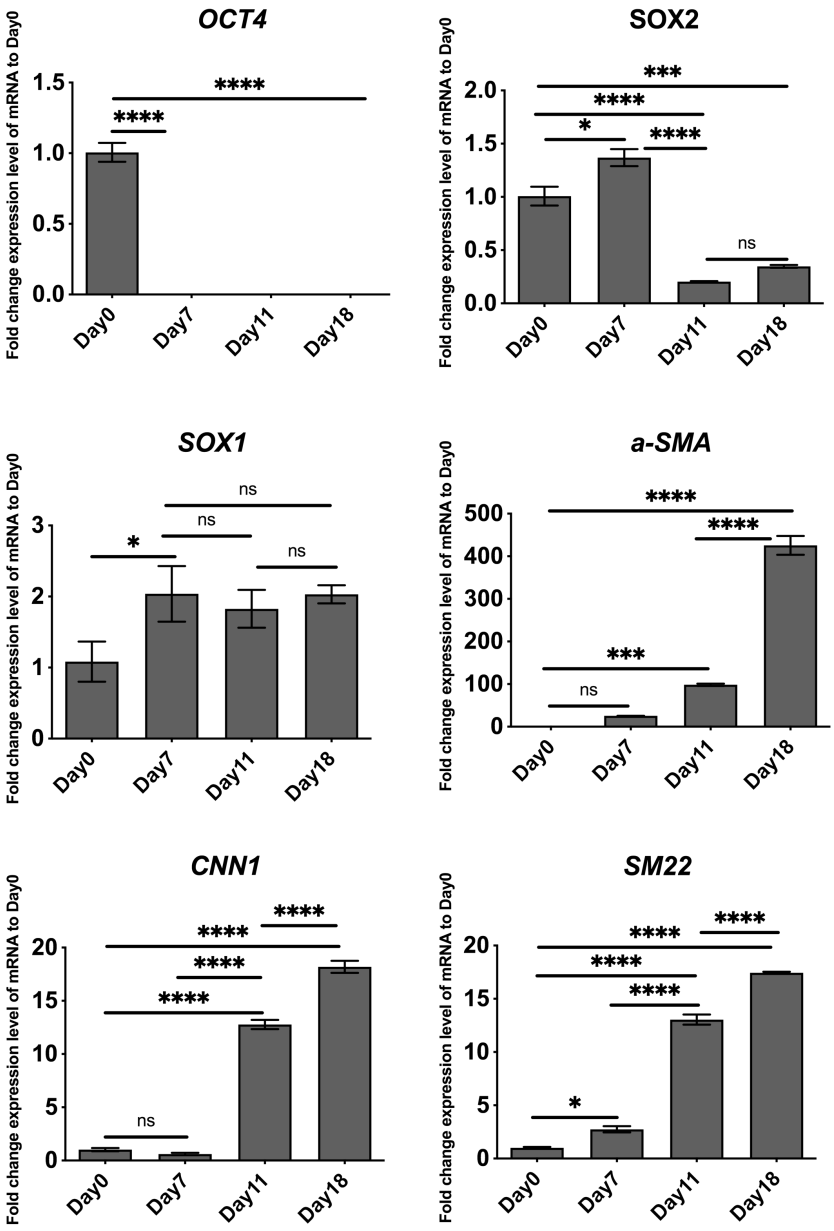

Figure 5.2 mRNA expression profiles of control iPSCs differentiated into vMCs.

qRT-PCR quantification of pluripotency marker gene *OCT4*, NCSC marker genes *SOX1* and *SOX2* and vSMC associated genes *α-SMA, CNN1* and *SM22*. Data shows gene expression during iPSC-vMCs differentiation at day 7, day 11 and ay 18 relatives to Day 0 (iPSCs stage). *GAPDH* was used as the endogenous control. Displayed is the mean ± SEM from triplicate reactions of 3 biological replicates, n=3. *, P<0.05, ** P<0.005 *** P<0.0005, **** P<0.0001. Statistical significance was determined by using one-way ANOVA.

5.2.2. Characterisation of control (AGD-14-02-C9) iPSC-derived BMECs

After prior optimisation of the BMEC differentiation process using control iPSC line AGD-14-02-C3 (chapter 3), further control iPSC lines AGD-14-02-C9, SW171A and SW174A also underwent BMEC differentiation.

AGD-14-02-C9 iPSCs were positive for the pluripotent markers SOX2 and SSEA4 at day 0 of differentiation (**Figure 5.3A**). By day 10, control 02-C9 iPSCs were positive for the functional BMEC and junction protein markers VE-cadherin, GLUT1, occludin, ZO-1 and claudin-5, respectively (**Figure 5.3B, C, D, E and F**). The barrier properties of control iPSC-BMECs was assessed by TEER measurement yielding a maximum TEER value of ~1000 Ω/cm^2 at day10 (**Figure 5.3G**).

5.2.3. Characterisation of control (SW171A) iPSC-derived BMECs

Control line SW171A iPSCs were positive for the pluripotent markers SOX2 and SSEA4 at day 0 of differentiation (**Figure 5.4A**). By day 10, control SW171A iPSCs were positive for the functional BMEC and junction protein markers VE-cadherin, GLUT1, occludin, ZO-1 and claudin-5, respectively (**Figure 5.4B, C, D, E and F**). The barrier properties of control SW171A iPSC-BMECs was assessed by TEER measurement yielding a maximum TEER value of ~ 800 Ω/cm^2 (**Figure 5.4G**).

5.2.4. Characterisation of control (SW174A) iPSC-derived BMECs

Finally, control line SW174A was also induced for BMEC differentiation. The iPSCs were positive for the pluripotent markers SOX2 and SSEA4 at day 0 of differentiation (**Figure 5.5A**). By day 10, control SW174A iPSCs were positive for the functional BMEC and junction protein markers VE-cadherin, GLUT1, occludin, ZO-1 and claudin-5, respectively (**Figure 5.5B, C, D, E and F**). The barrier properties of control iPSC-BMECs was assessed by TEER measurement to demonstrate that BMECs can be applied to model BBB (**Figure 5.5G**).

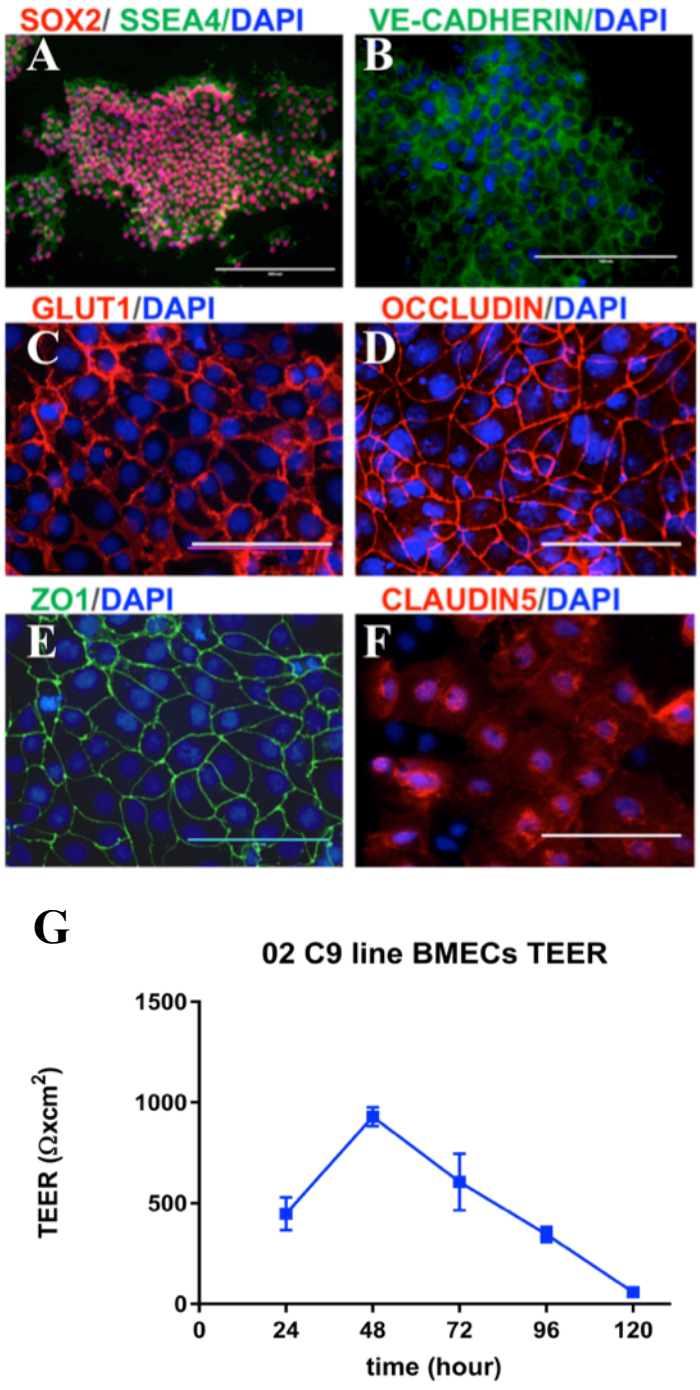

Figure 5.3 BMEC differentiation of iPSC control line AGD-14-02-C9.

Immunofluorescent staining of cells at (**A**) day 0 for SOX2 and SSEA4 and (**B-F**) day 10 for VE-cadherin, GLUT1, occuldin, ZO-1 and claudin-5. Images were counterstaining with DAPI, scale bars 200 µm (A, B, F), 100 µm (C, D, E). **(G)** TEER measurements taken over 5 days of culture on Transwell membranes, n=3, values display the mean ± SEM. Markers were double-stained as colour labelled shown in the merged photos.

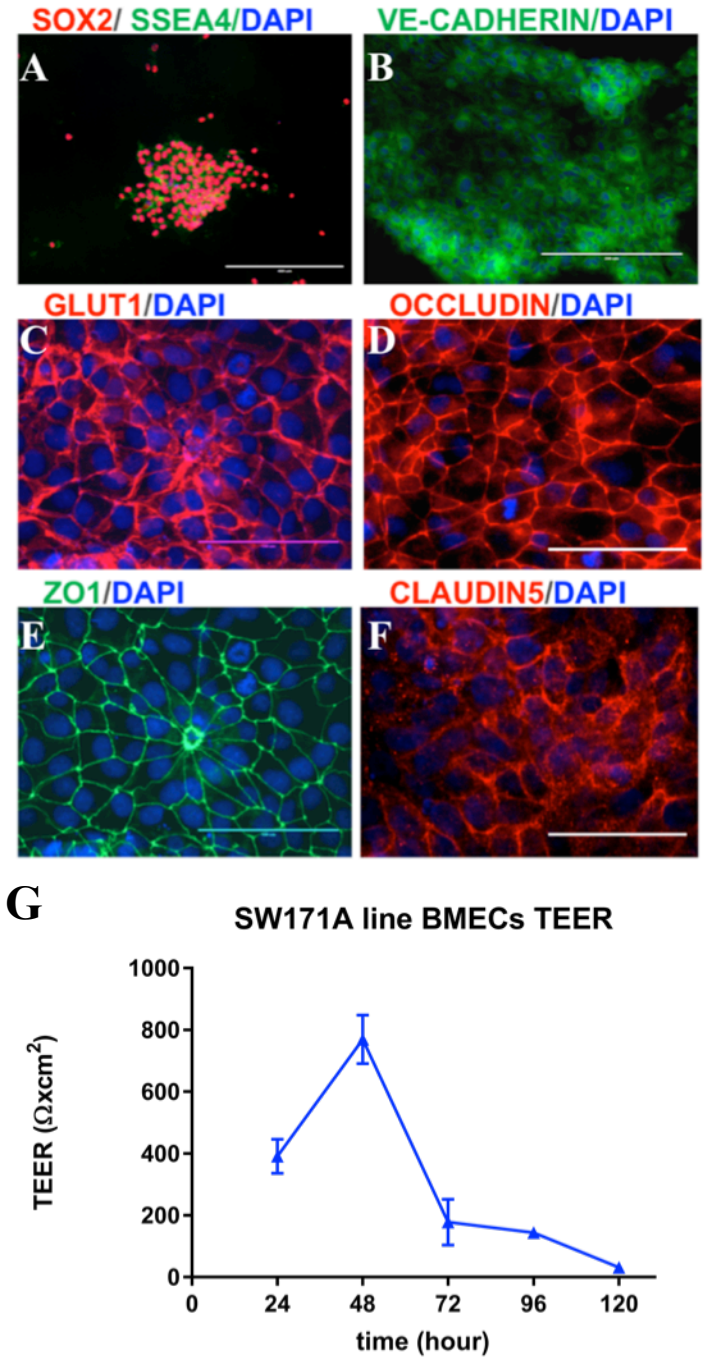

Figure 5.4 BMEC differentiation of iPSC control line SW171A.

Immunofluorescent staining of cells at (**A**) day 0 for SOX2 and SSEA4 and (**B-F**) day 10 for VE-cadherin, GLUT1, occuldin, ZO-1 and claudin-5. Images were counterstaining with DAPI, scale bars 200 µm (A, B), 100 µm (C, D, E, F). **(G)** TEER measurements taken 5 days of culture on Transwell membranes, n=3, values display the mean ± SEM. Markers were double stained as colour labelled shown in the merged photos.

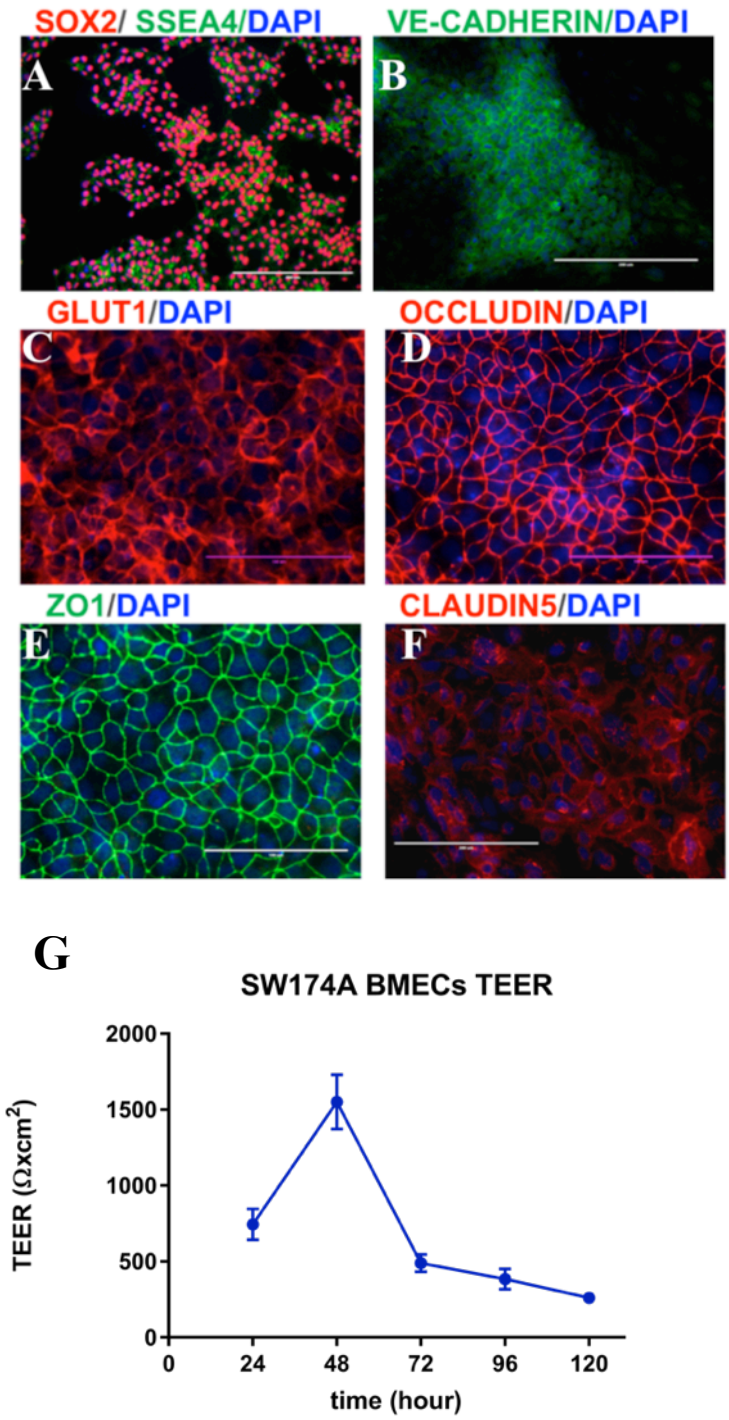

Figure 5.5 BMEC differentiation of iPSC control line SW174A.

Immunofluorescent staining of cells at (**A**) day 0 for SOX2 and SSEA4 and (**B-F**) day 10 for VE-cadherin, GLUT1, occuldin, ZO-1 and claudin-5. Images were counterstaining with DAPI, scale bars 200 µm (A, B, F), 100 µm (C, D, E). **(G)** TEER measurements taken 5 days of culture on Transwell membranes, n=3, values display the mean ± SEM. Markers were double-stained as colour labelled shown in the merged photo.

5.2.5. iPSC-NVU cells can be co-cultured on Transwell membranes to mimic BBB

The BBB is composed of BMECs surrounded by vMCs, astrocytes, and neurons, these cells can be co-cultured in various permutations in Transwell culture plates to simulate the BBB (**Figure 5.6**). The timeline of modelling iPSC-BBB was shown (**Figure 5.7**). To measure the barrier properties induced by co-culture of NVU cells TEER measurements were performed every 24 hours post BMEC seeding onto the Transwell membranes. Immunostaining for junction protein markers and NaF permeability assays were also conducted during co-culture (**Figure 5.6 and 5.7**).

Control iPSC-BMECs (AGD-14-02 C3, AGD-14-02 C9, SW171A and SW174A) were co-cultured with control iPSC-neurons (OX1-19, AGD-14-02 C3), control iPSC-astrocytes (AGD-14-02 C3, AGD-14-02 C9) and control iPSC-vMCs (AGD-14-02 C3, AGD-14-02 C9 and OX1-19) to mimic BBB.

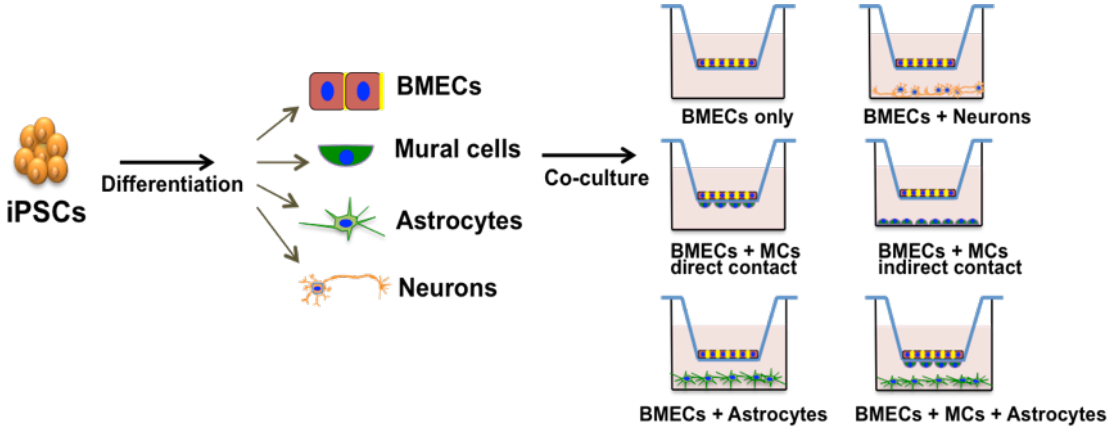

Figure 5.6 Schematic drawing of the co-culture system with four lineages derived from iPSCs.

Schematic drawing of the iPSC-BBB model. iPSC-derived BMECs were seeded onto Transwell filters coated with C/F/W with or without co-culturing with iPSC-derived vMCs, neurons and astrocytes. IPSC-derived neurons or astrocytes were seeded at the bottom of 12-well plates, while iPSC-MCs seeded at the bottom of the well or on the bottom surface of the Transwell.

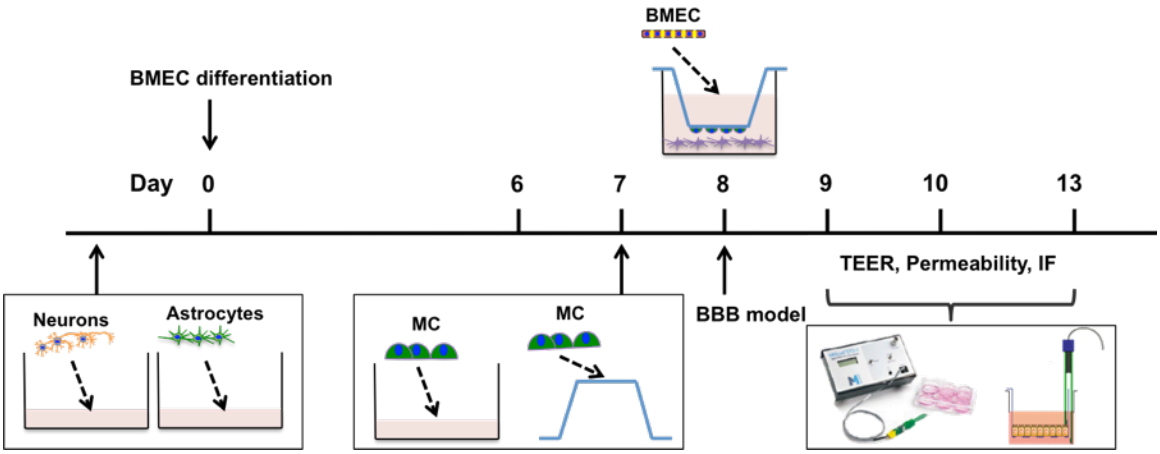

Figure 5.7 Schematic drawing of the timeline of modelling iPSC-BBB.

Day 80-100 iPSC-derived astrocytes and neurons were seeded ahead of BMECs differentiation. Day 18 iPSC-vMCs were seeded 24 hours before BMECs seeding. Functional analysis was performed 24 hours after BMECs seeding.

5.2.6. iPSC-vMCs can enhance BMECs barrier formation

IPSC-derived vMCs were co-cultured either directly or indirectly with iPSC-derived BMECs and barrier formation was monitored by TEER measurement. Initial TEER measurements of iPSC-BMECs derived from control AGD-14-02 C3 line were 1,000 Ωxcm^2 (24 hours' time point). After 24 hours, TEER measurements in direct co-culture with iPSC-vMC line AGD-14-02 C9 significantly increased to 5,000 Ωxcm^2 ($p < 0.05$) compared with that observed in BMEC monocultures (nearly 2,000 Ωxcm^2) (**Figure 5.8A**). Similarly, other two groups also showed direct co-culture with iPSC-vMCs (AGD-14-02 C3 and OX1-19 line) elevated the iPSC-BMECs (AGD-14-02 C3 and SW171A) TEER significantly at 48 hours and the elevation maintained throughout the duration of the experiment ($p < 0.0001$ and $p < 0.0005$ respectively) (**Figure 5.8B and C**).

Three independent co-culturing experiments of control iPSC-BMECs AGD-14-02 C3 in indirect contacted with iPSC-vMCs AGD-14-02 C3 demonstrated increased maximum TEER value compared to the monoculture control iPSC-BMECs, with the initial TEER were 300 Ωxcm^2 (24 hours' time point) and increased to 4500 Ωxcm^2 ($p < 0.0001$) compared with that observed in BMEC monocultures (nearly 800 Ωxcm^2). **Figure 5.9A**. Other two groups also showed indirect co-culture with iPSC-vMCs (AGD-14-02 C9 and SW174A) elevated the iPSC-BMECs (AGD-14-02 C9 and OX1-19) TEER significantly at 48 hours and the elevation maintained throughout the duration of the experiment ($p < 0.0001$ and $p < 0.0005$ respectively) (**Figure 5.9 B and C**).

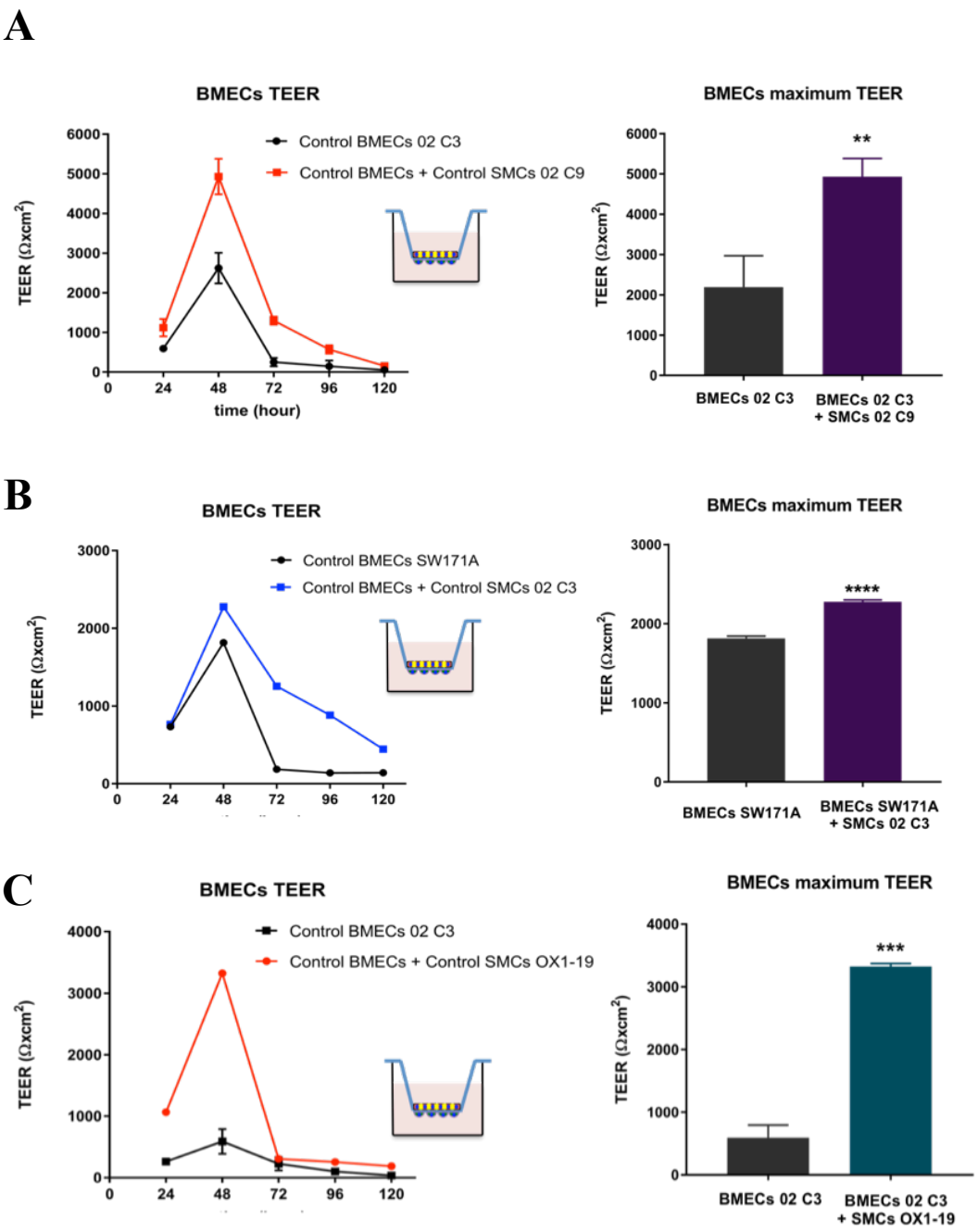

Figure 5.8 The effect of vMCs on BMECs TEER value by direct co-culture.

IPSC-BMECs derived from **(A)** AGD-14-02 C3 line, **(B)** SW171A line and **(C)** AGD-14-02 C3 line were co-cultured directly with **(A)** AGD-14-02 C9, **(B)** AGD-14-02 C3 and **(C)** OX1-19 iPSC-vMCs line and TEER was monitored. Statistical significance was calculated using unpaired t-test, n=3, values display the mean ± SEM. **p < 0.005 versus BMECs monoculture. ** p<0.005 *** P<0.0005, **** P<0.0001.

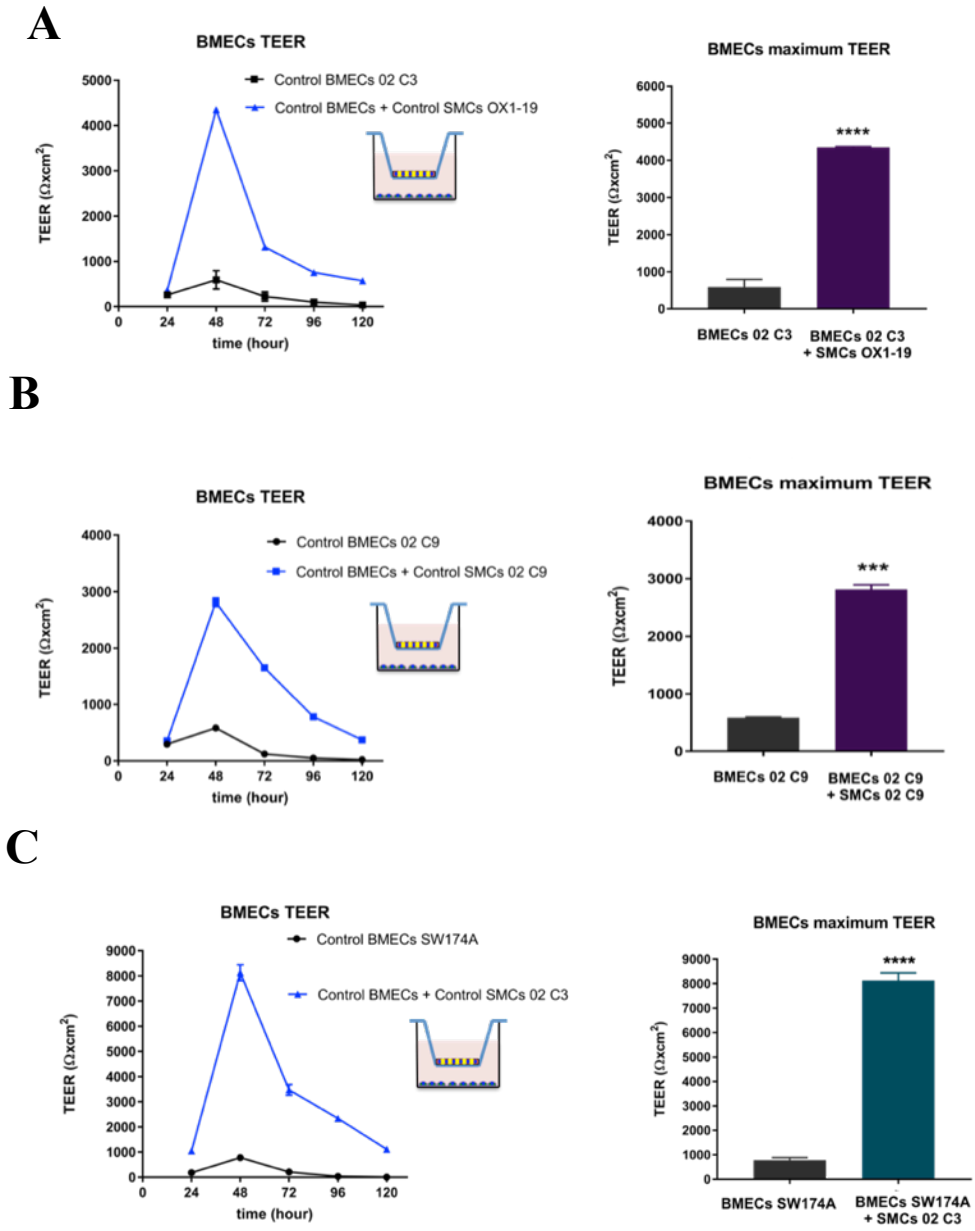

Figure 5.9 The effect of vMCs on BMECs TEER value by indirect co-culture..

IPSC-BMECs derived from **(A)** AGD-14-02 C3 line, **(B)** AGD-14-02 C9 line and **(C)** SW174A line were co-cultured indirectly with **(A)** OX1-19, **(B)** AGD-14-02 C9 and **(C)** AGD-14-02 C3 iPSC-vMCs line and TEER was monitored. Statistical significance was calculated using unpaired t-test, n=3, values display the mean ± SEM. ***p < 0.0005 versus BMECs monoculture. *** P<0.0005, **** P<0.0001.

5.2.7. iPSC-neurons and iPSC-astrocytes promote iPSC-BMEC barrier function

To demonstrate that other NVU cell types were capable of inducing BBB properties, control iPSC-neurons and iPSC-astrocytes were co-cultured indirectly with control iPSC-derived BMECs separately.

TEER measurements following co-culture with iPSC-neurons were compared to mono-cultured iPSC-derived BMECs. Initial TEER measurements of iPSC-BMECs derived from control AGD-14-02 C3 line were 300 Ωxcm^2. After 24 hours, TEER in co-culture with iPSC-neurons OX1-19 line significantly increased to almost 3,000 Ωxcm^2 ($p < 0.0001$), more than 4 times that observed in BMECs monoculture (nearly 700 Ωxcm^2) (**Figure 5.10A**). Starting TEER measurements of iPSC-BMECs derived from control AGD-14-02 C3 line were 300 Ωxcm^2. After 24 hours, TEER in co-culture with iPSC-neurons AGD-14-02 C9 line significantly increased to almost 2,700 Ωxcm^2 ($p < 0.0001$), more than 5 times that observed in BMECs monoculture (nearly 500 Ωxcm^2) (**Figure 5.10B**). Similarly, initial TEER measurements of iPSC-BMECs derived from control SW171A line were 1000 Ωxcm^2. After 24 hours, TEER in co-culture with iPSC-neurons OX1-19 line significantly increased to almost 4,000 Ωxcm^2 ($p < 0.005$), doubled that observed in BMECs monoculture (nearly 2,000 Ωxcm^2) (**Figure 5.10C**).

TEER measurements following co-culture with iPSC-astrocytes were compared to monocultured iPSC-derived BMECs. Initial TEER measurements of iPSC-BMECs derived from control AGD-14-02 C9 line were 300 Ωxcm^2. After 24 hours, TEER in co-culture with iPSC-astrocytes AGD-14-02 C3 line and AGD-14-02 C9 line significantly increased to 4,500-5,500 Ωxcm^2 ($p < 0.05$), almost 7 times that observed in BMECs monoculture (700 Ωxcm^2) (**Figure 5.11A**). The maximum TEER of iPSC-BMEC line SW171A doubled in co-culture with iPSC-astrocytes derived from AGD-14-02 C3 line compared to iPSC-BMECs monoculture (**Figure 5.11C)**. In all 3 groups the elevation maintained throughout the duration of the experiment ($p < 0.05$) (**Figure 5.11A, B and C**).

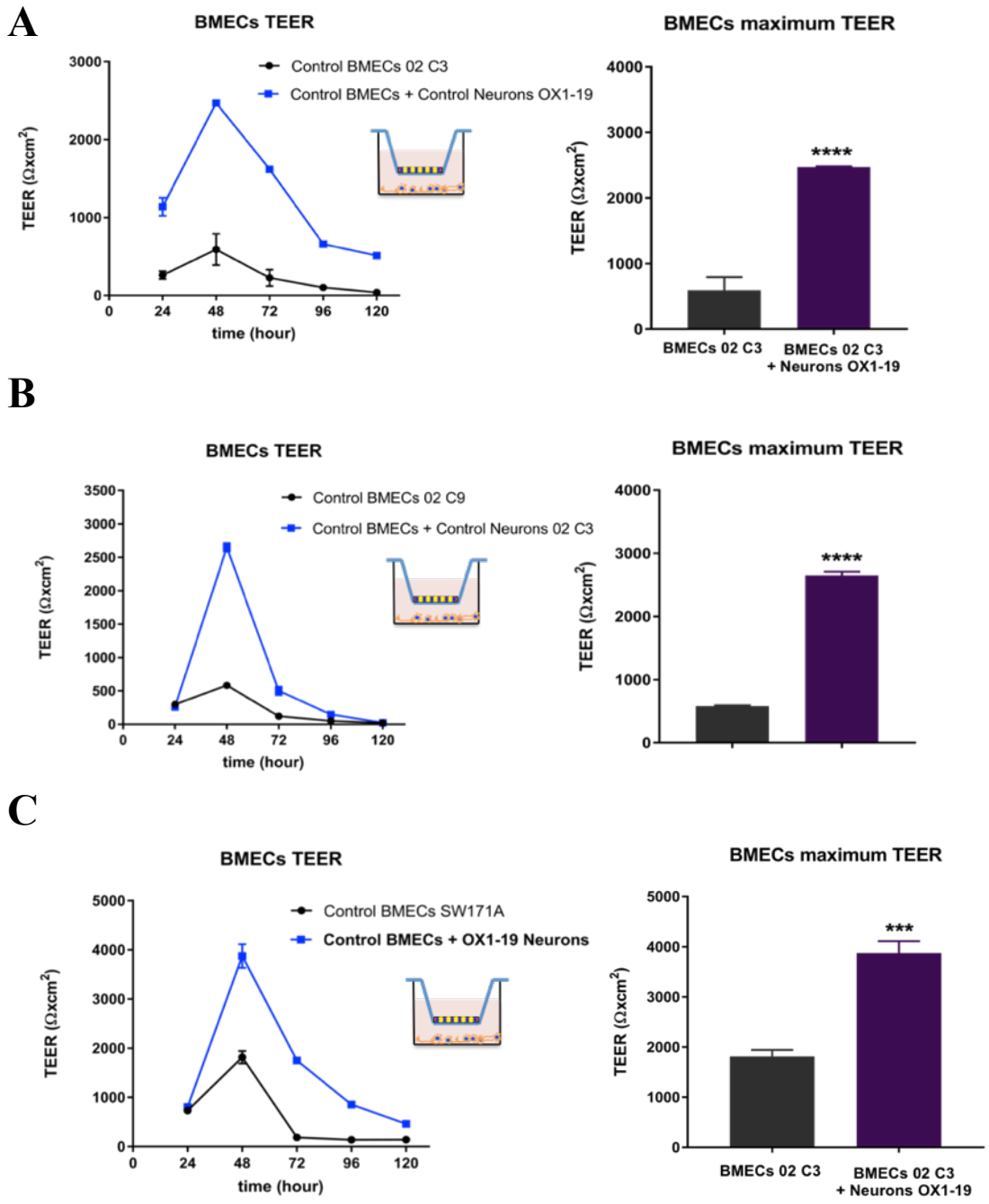

Figure 5.10 The effect of neurons on BMECs TEER value.

IPSC-BMECs derived from **(A)** AGD-14-02 C3 line, **(B)** AGD-14-02 C9 line and **(C)** SW174A line were co-cultured indirectly with **(A)** OX1-19, **(B)** AGD-14-02 C9 and **(C)** OX1-19 iPSC-neurons line and TEER was monitored. Statistical significance was calculated using unpaired t-test, n=3, values display the mean ± SEM. *** P<0.0005 versus BMECs monoculture. *** P<0.0005, **** P<0.0001.

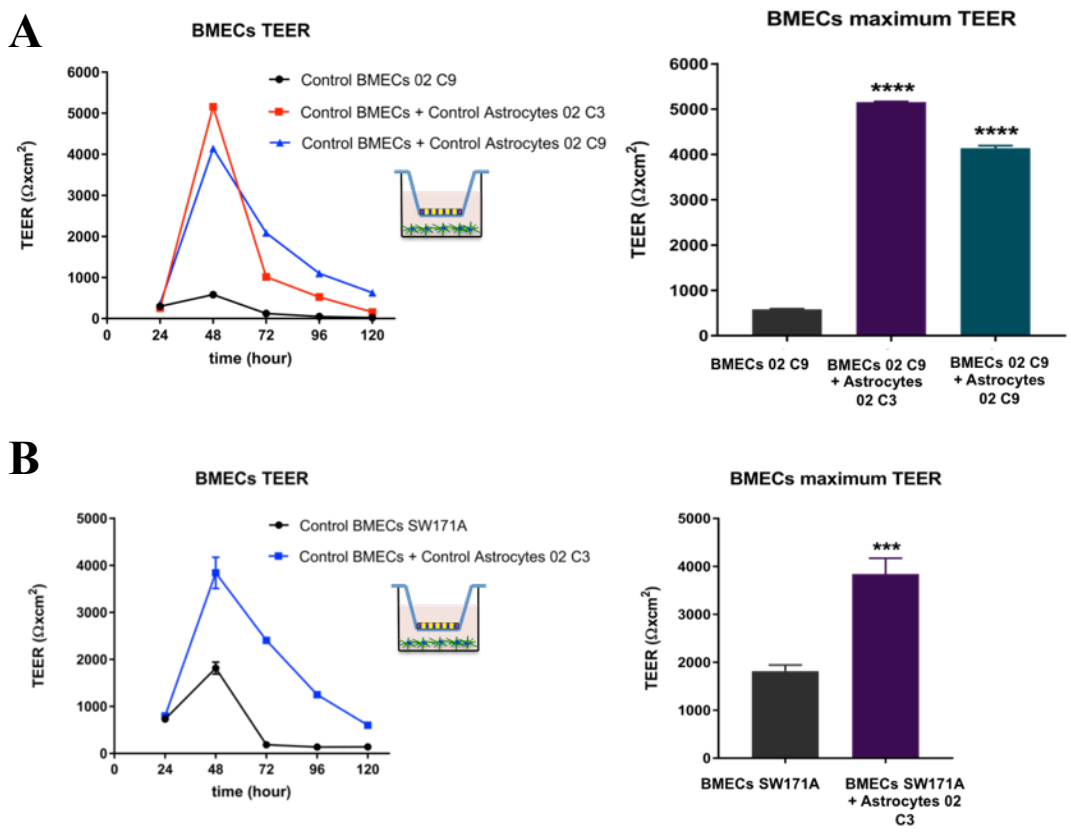

Figure 5.11 The effect of astrocytes on BMECs TEER value.

IPSC-BMECs derived from **(A)** AGD-14-02 C9 line and **(B)** SW171A line were co-cultured indirectly with **(A)** AGD-14-02 C3 and AGD-14-02 C9, **(B)** SW171A and TEER was monitored. Statistical significance was calculated using unpaired t-test, n=3, values display the mean ± SEM. *** P<0.0005 versus BMECs monoculture. *** P<0.0005, **** P<0.0001.

5.2.8. Triple culture of NVU cells further promotes iPSC-BMECs barrier function

The NVU is composed of multiple cell types therefore a tri-culture of vMCs, astrocytes and BMECs was compared with bi-cultures of BMECs with vMCs/astrocytes and TEER measurements taken to assess BMEC barrier formation. Control iPSC-BMECs AGD-14-02 C3 line was cultured with control iPSC-astrocytes AGD-14-02 C3 line seeded in the bottom well and iPSC-vMCs OX1-19 line seeded on the bottom surface of the Transwell membrane. TEER measurements following triple culture were compared to monocultured iPSC-derived BMECs and co-cultured combinations. At 48 hours of seeding, the TEER value of the triple culture was 7000 Ωxcm^2, nearly ten times that observed in iPSC-BMECs monoculture derived from AGD-14-02 C3 line (**Figure 5.12A and B**) ($p<0.0001$). The maximum TEER of triple culture was also significantly higher than various co-culture combinations, BMECs + vMCs (4,500 Ωxcm^2), BMECs + neurons (2,500 Ωxcm^2) ($p<0.0001$, $p<0.0001$ respectively) (**Figure 5.12A and B**). TEER values in the triple culture were significantly higher than all other permutations at all time points ($p < 0.05$) (**Figure 5.12A**).

When normalized to BMECs cultured alone the maximum TEER achieved by BMECs in all co-cultures and triple culture is significantly increased with the biggest increase observed in triple culture ($p<0.05$) (**Figure 5.13**).

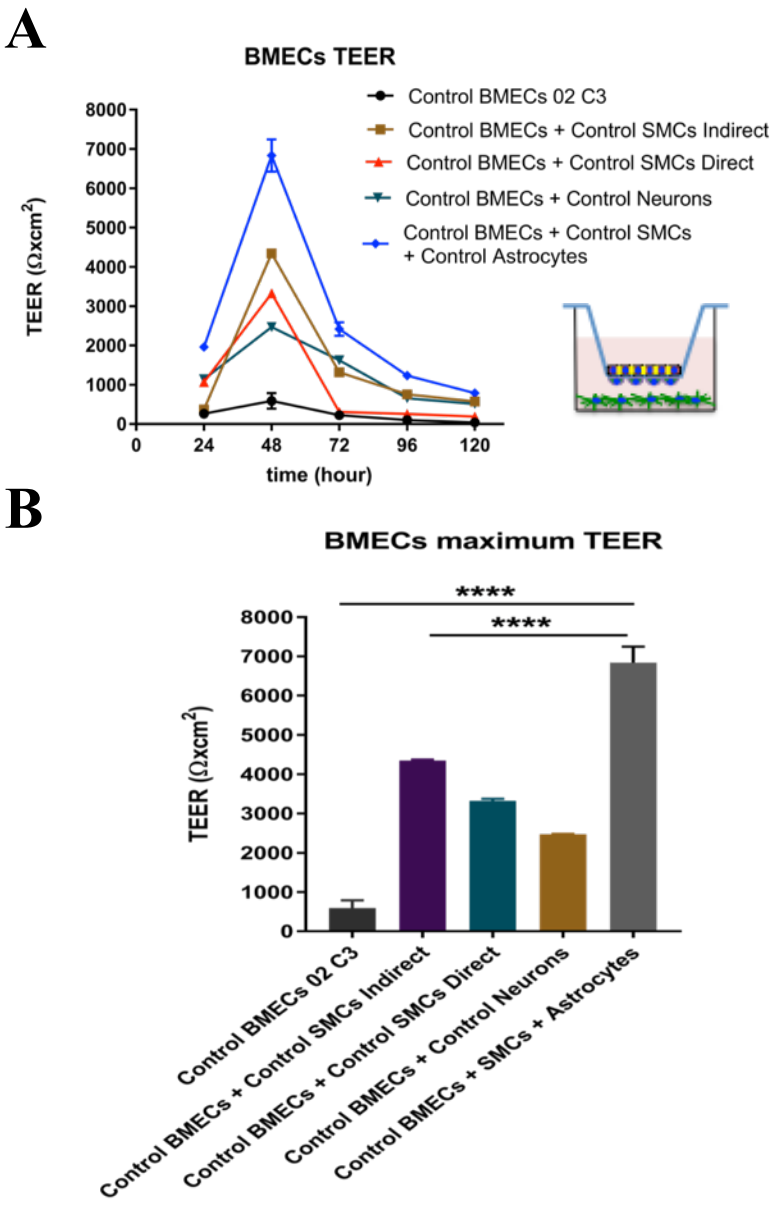

Figure 5.12 Triple culture with iPSC-vMCs and iPSC-astrocytes further increased iPSC-BMECs TEER.

IPSC-astrocytes derived from AGD-14-02 C3 line were cultured on the bottom of the well and iPSC-BMECs derived from AGD-14-02 C3 line were seeded on the Transwell inserts. OX1-19 line iPSC-vMCs were seeded on the bottom surface of the Transwell inserts membrane. **(A)** TEER of the triple culture was compared to BMECs monoculture and co-culture with neurons or vMCs (directly or indirectly) **(B)** Maximum TEER of the triple culture at 48 hours after BMECs seeding was compared to BMECs monoculture and co-culture with neurons or vMCs (directly or indirectly). Statistical significance was calculated using one-way ANOVA, n=3, values display the mean ± SEM. **** P<0.0001 versus BMECs monoculture.

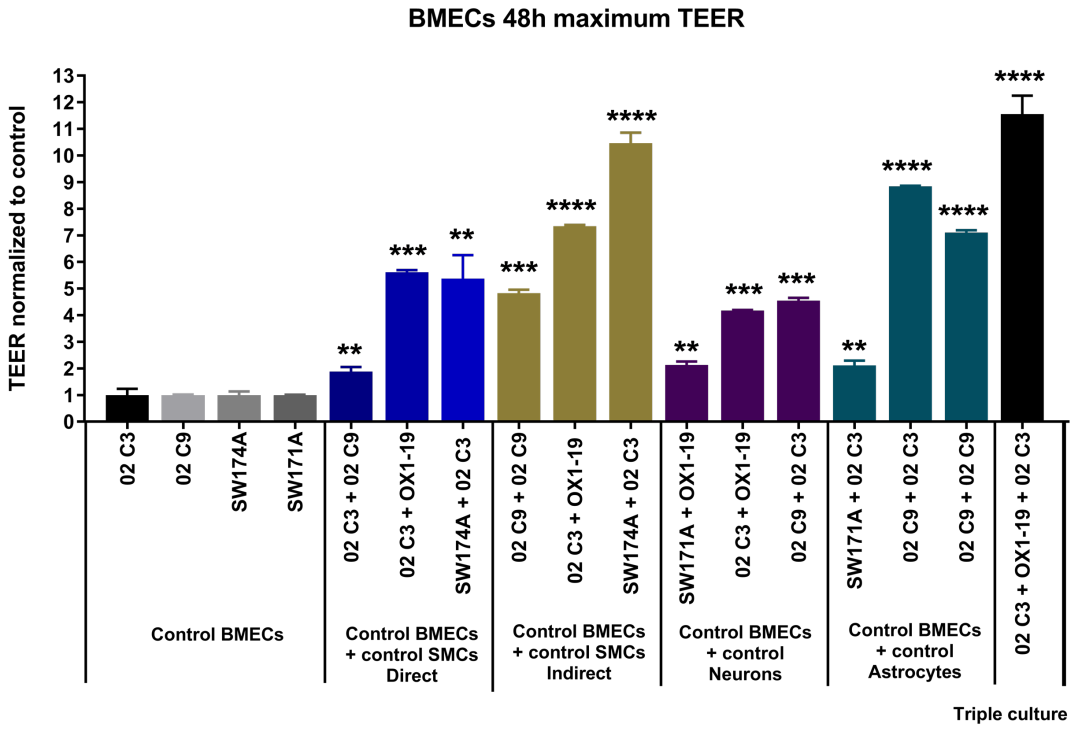

Figure 5.13 Maximum TEER summary of control iPSC-BMECs monoculture compared to co-cultures.

Maximum TEER of control iPSC-BMECs co-cultured with control iPSC-vMCs directly/indirectly, control iPSC-neurons, or control iPSC-astrocytes and triple culture were compared with 4 control iPSC-BMECs lines. Data showed maximum TEER of co-culture groups relative to control BMECs monocultures. Lines were indicated in the graph. Control iPSC-BMECs maximum TEER was normalized as 1.

Statistical significance was calculated using one-way ANOVA. The plot is the result of 3 biological replicates (n=3) with each daily TEER measurement. Values are reported as mean ± SEM of these collective measurements. ** $p<0.005$ *** $P<0.0005$, **** $P<0.0001$ versus BMECs monoculture.

5.2.9. Passive diffusion of the iPSC-BBB model using sodium fluorescein permeability

High electrical resistance as measured by TEER is one of the properties of the BBB, another is low permeability by passive diffusion which can be measured using small fluorescent molecules such as sodium fluorescein (NaF). The diffusion of fluorescein across BMEC monolayers following co-culture with iPSC-derived vMCs directly or indirectly or co-culture with iPSC-astrocytes was compared to monocultured iPSC-derived BMECs.

The amount of fluorescein diffused across monolayers of iPSC-BMECs AGD-14-02 C3 line significantly decreased ~6 times in indirect co-culture with iPSC-vMCs derived from AGD-14-02 C3 line and AGD-14-02 C9 line compared to iPSC-BMECs monoculture ($p<0.005$) (**Figure 5.14A**). However, when BMECs and vMCs were in direct co-culture there was no change in the permeability of the BMEC monolayers (**Figure 5.14B**). Similarly, when BMECs and astrocytes were indirectly co-cultured there was a significant decrease in the permeability of the BMEC monolayer ($p<0.05$) (**Figure 5.14C**).

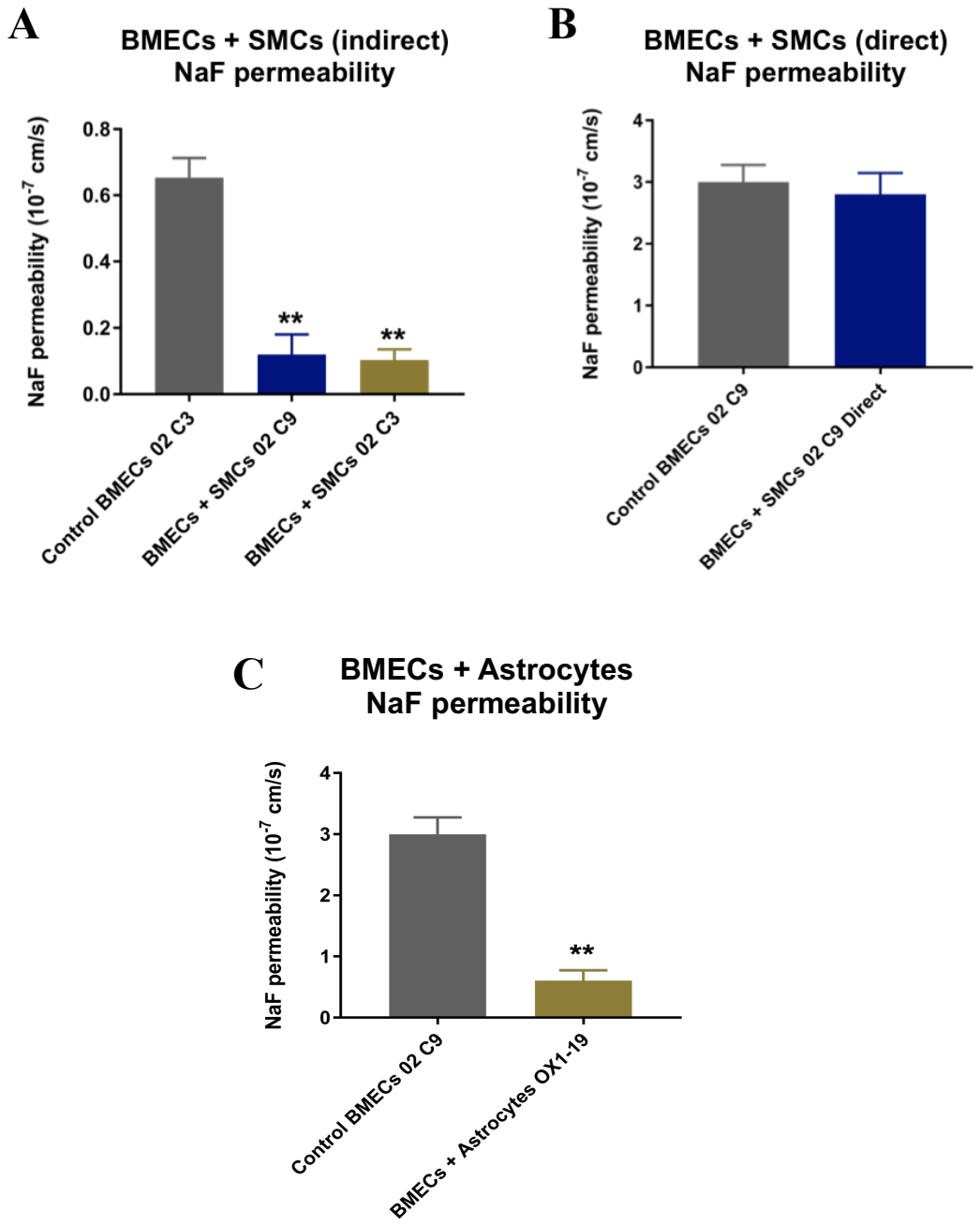

Figure 5.14 Permeability of the iPSC-BBB model tested by sodium fluorescein permeability.

(A) The permeability of indirectly co-cultured BMECs (AGD-14-02 C3 line) with vMCs (AGD-14-02 C9 line) compared with BMECs alone. **(B)** The permeability of directly co-cultured BMECs (AGD-14-02 C3 line) with vMCs (AGD-14-02 C9 line) compared with BMECs alone. **(C)** The permeability of co-cultured BMECs (AGD-14-02 C9 line) with astrocytes (OX1-19 line) compared with BMECs alone.

Statistical significance was calculated using one-way AVOVA **(A)** and unpaired t-test **(B and C)**. Values are mean ± SEM, n=3. ** P<0.005, versus BMECs monoculture.

5.2.10. BBB barrier function is specific to the iPSC-BMECs.

CADASIL is a systemic disease with pathologies that present in multiple organs. As such, previously reported iPSC models on CADASIL focused on iPSC-ECs rather than iPSC-BMECs, which are brain specific. To compare our iPSC-BBB model with existing iPSC-NVU models for CADASIL, non-brain type ECs were differentiated from control iPSCs using already established protocol [223]. The protocol was performed using control AGD-14-02-C3 iPSC line. iPSCs were treated with combinations of growth factors for 11 days as shown in the schematic summary (**Figure 5.15A**).

On day 3, cells started to emerge from the edges of the iPSC colonies. Cells changed from iPSC morphology to migratory spiky shape by day 5 (**Figure 5.15B**). After withdrawal of bone morphogenetic protein 4 (BMP4) and addition of VEGF on day 7 to promote EC differentiation, the cells expanded through the course of differentiation (**Figure 5.15B**). At day 11, ECs were purified out from the differentiated cells using $CD31^+$ labelled microbeads. After sorting, ECs grew healthily after reseeding with expression of endothelial specific marker proteins PECAM1 and VE-cadherin (**Figure 5.15C**).

Over the differentiation period, the expression of pluripotency genes (*OCT4*, *SOX-2* and *NANOG*) decreased progressively ($P<0.0001$) (**Figure 5.15D**). On day 3, a transient expression of the *TBX1* gene, a marker of early mesoderm commitment, was observed. This was followed by an increase in the expression of additional mesoderm markers, *ISL1* and *MESP1* ($P<0.0001$) (**Figure 5.15D**). After addition of VEGF on day 7, the expression of endothelial specific markers *CDH5*, *PECAM1* as well as *KDR* were significantly increased ($P<0.0001$) (**Figure 5.15D**).

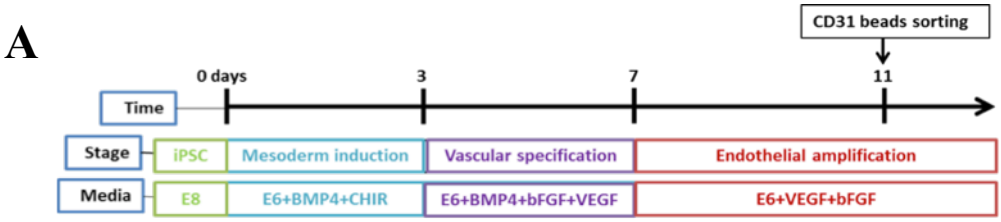
A
CD31 beads sorting
0 days
3
7
11
Time
Stage
iPSC
Mesoderm induction
Vascular specification
Endothelial amplification
Media
E8
E6+BMP4+CHIR
E6+BMP4+bFGF+VEGF
E6+VEGF+bFGF

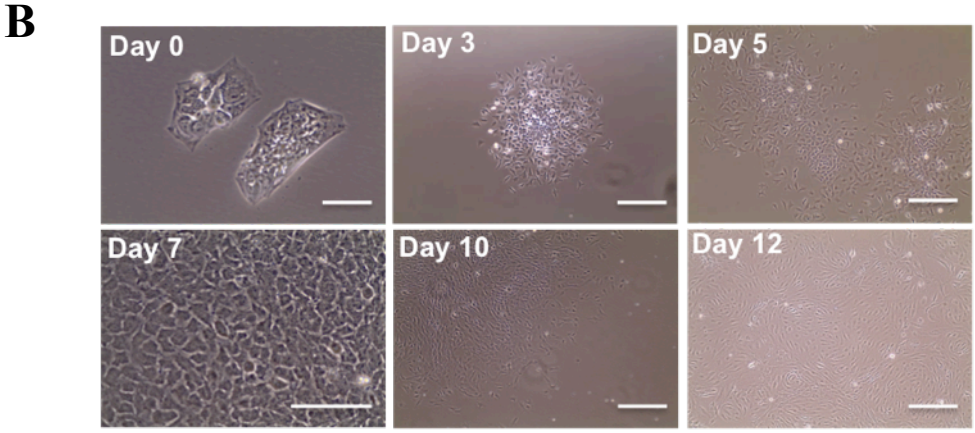
B
Day 0
Day 3
Day 5
Day 7
Day 10
Day 12

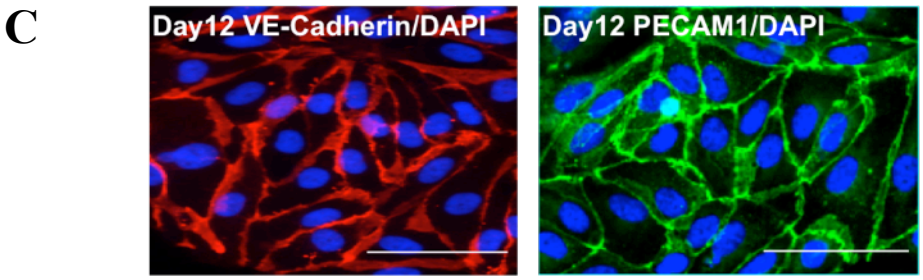
C
Day12 VE-Cadherin/DAPI
Day12 PECAM1/DAPI

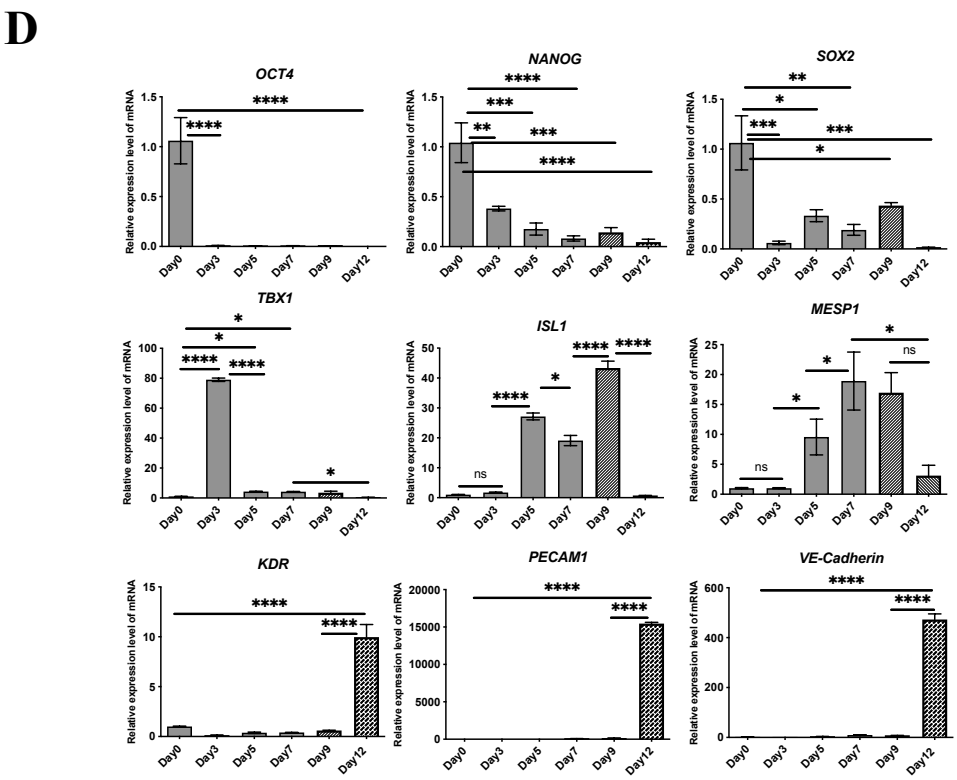
D
OCT4
NANOG
SOX2
TBX1
ISL1
MESP1
KDR
PECAM1
VE-Cadherin
Relative expression level of mRNA
Day0
Day3
Day5
Day7
Day9
Day12

Figure 5.15 Differentiation and characterisation of iPSC-derived ECs.

(A) Schematic summary of iPSC-ECs differentiation process. **(B)** Phase microscopy photographs show morphology change during the differentiation process at Day0 (iPSCs stage), Day3, Day5, Day7 and Day12. **(C)** Immunofluorescence staining microscopy shows EC markers PECAM1 (green) and VE-cadherin (red) with DAPI (blue) at Day 12 of the differentiation. Scale bars, 100 μm. **(D)** qRT-PCR results show changes of gene-expression profiles for pluripotent (*OCT4*, *SOX2*, *NANOG*), mesodermal (*TBX1*, *ISL-1*, *MESP1*, *KDR*), and endothelial (*KDR*, *PECAM-1*, *VE-cadherin*) marker genes relative to GAPDH during the course of iPSC-ECs differentiation.

Statistical significance was calculated using one-way ANOVA, n=3. Values are reported as mean ± SEM of these collective measurements. * $p<0.05$ ** $p<0.005$ *** $P<0.0005$, **** $P<0.0001$.

5.2.11. iPSC-ECs do not exhibit blood brain barrier properties

iPSC-ECs at day12 of differentiation were seeded onto Transwell membranes to mimic the BBB and TEER was measured every 24 hours (**Figure 5.16)**. The results were compared to control iPSC-BMECs and HCAECs as positive and negative controls, respectively. Initial measurements taken after 24 hours showed that iPSC-BMECs possessed a TEER of 350-400 Ωxcm^2 compared with both lower than 100 Ωxcm^2 for iPSC-ECs and HCAECs. After 48 hours iPSC-BMECs exhibited a significantly higher maximum TEER value of 1000 Ωxcm^2 compared with both lower than 100 Ωxcm^2 for iPSC-ECs and HCAECs ($p<0.0001$). After that the TEER measurements from the iPSC-BMECs continued to fall for the next three days converging with ECs and HAECs by 120 hours (**Figure 5.16)**.

To investigate whether the TEER difference in iPSC-ECs and iPSC-BMECs was associated with the expression of functional markers and junctional proteins in both cell types, a qRT-PCR was performed. Over the differentiation period of iPSC-BMECs, the expression of BMECs and tight junction marker genes SLC2A1/GLUT1, *TJP1/ZO1*, *OCLDN/occuldin* and *CLDN5/claudin-5* increased from Day 0 to Day 8 ($P<0.05$) (**Figure 5.17B**). In contrast, during iPSC-ECs differentiation, only the expression of tight junction gene *CLDN5* increased ($P<0.005$) while expression of all the other genes *SLC2A1* (ns), *TJP1* (ns) and *occuldin* (ns) did not show significant change or even decreased (**Figure 5.17A**).

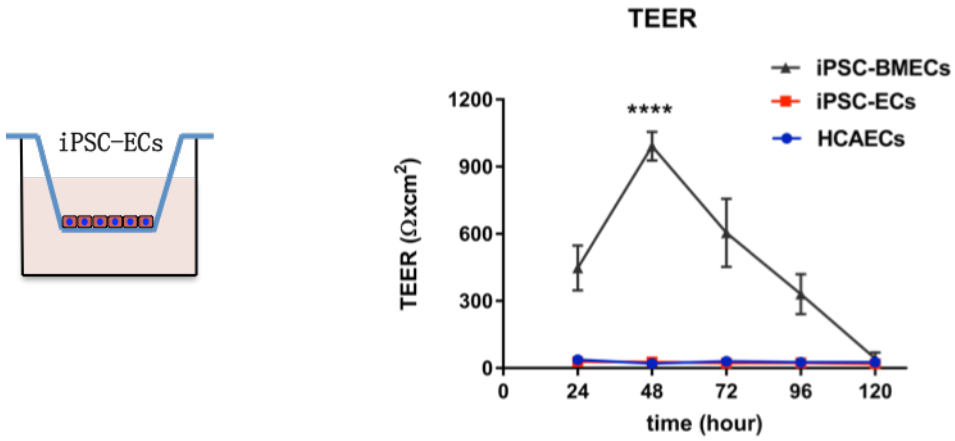

Figure 5.16 TEER of non-brain iPSC-ECs compared to iPSC-BMECs.

Left, Schematic of iPSC-ECs seeding on Transwell settings for TEER measurement. Right, Comparison of TEER value among iPSC-BMECs, iPSC-ECs and HCAECs. Each point in the right plot is the result of 3 biological replicates (n = 3) with each daily TEER measurement. Values are reported as mean ± SEM of these collective measurements. Statistical significance was calculated using unpaired t-test, ****$p < 0.0001$ versus HCAECs.

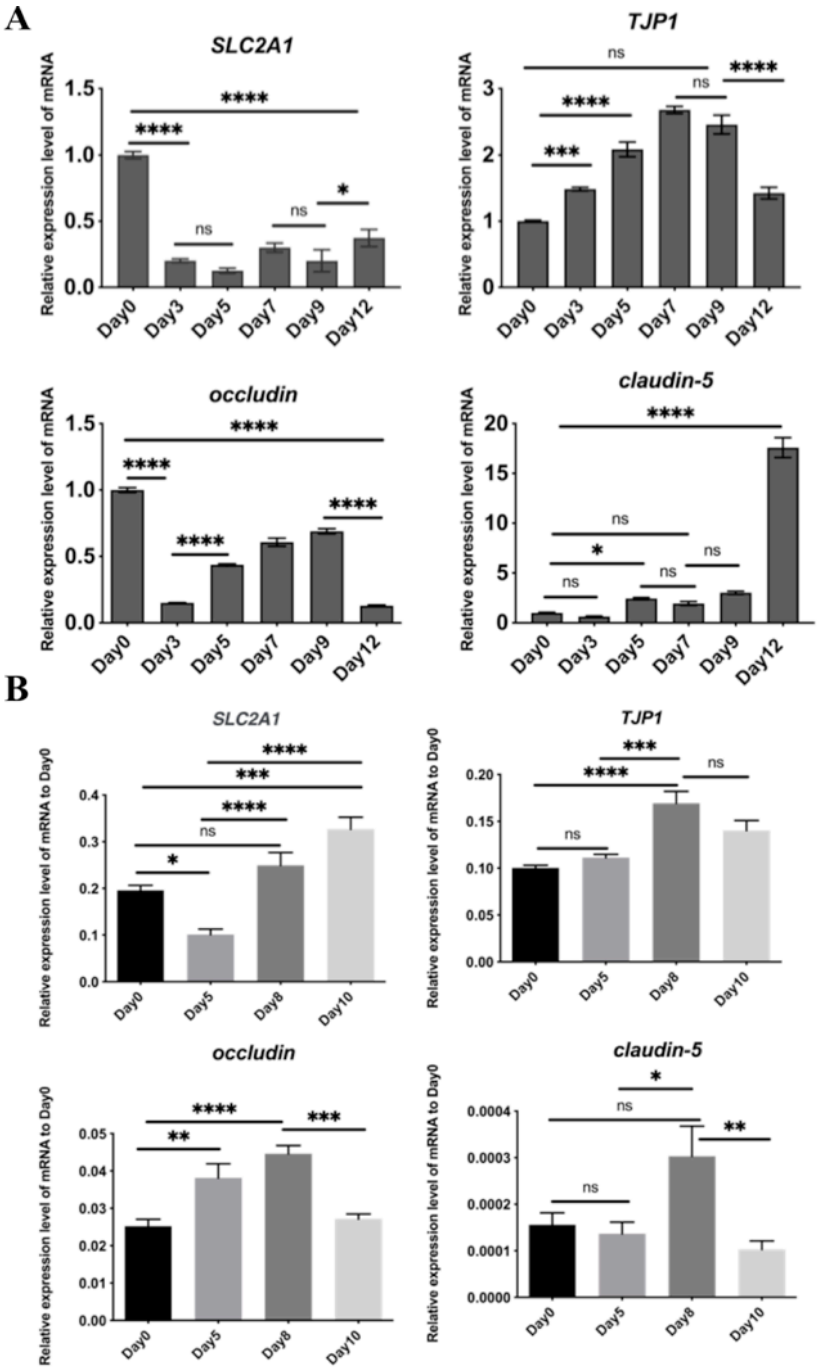

Figure 5.17 Gene expression comparison of BMECs and junction proteins between iPSC-ECs and iPSC-BMECs.

Expression of the BMEC markers *SLC2A1* and tight junction marker *ZO1*, *occuldin* and *claudin-5* during **(A)** iPSC-EC differentiation and **(B)** iPSC-BMEC differentiation. Means ± SEM was calculated from triplicate reactions of 3 biological replicates, n=3. *, $p<0.05$, ** $p<0.005$ *** $P<0.0005$, **** $P<0.0001$. Statistical significance was determined by using one-way ANOVA.

5.3. Discussion

BBB dysfunction is commonly observed in many neurological diseases and can be modelled by NVU cell types derived from iPSCs. Currently only three iPSC models for CADASIL have been reported, however, all three models were based on only vascular cells and the ECs were not brain type. In order to investigate the neurovascular deficit in CADASIL it's important to build an iPSC-derived BBB model that incorporates the 4 main cell types of NVU.

The main aim of this thesis was to build an iPSC-BBB model to study neurovascular interactions in CADASIL. In chapters 3 and 4, the successful differentiation of iPSCs into BMECs, astrocytes and neurons was described. The aim of this chapter was to demonstrate iPSC-vMC differentiation and the construction of a BBB model using all four cell types in order to recapitulate the native BBB as closely as possible. The barrier function of the *in vitro* BBB was measured by TEER or permeability of the BMEC monolayers to sodium fluorescein and compared among various co-culture combinations. The results demonstrated we have successfully built an effective iPSC-BBB model for neurovascular interactions.

5.3.1. Vascular mural-like cells can be differentiated from iPSCs

The differentiation of iPSCs into vMCs was performed using a well-established protocol modified by Kelleher *et al*. based on an earlier protocol from Cheung *et al*. protocol via neuroectodermal intermediary stage [216, 223]. In the original protocol Cheung *et al.* described the cells being differentiated as neural ectodermal derived vSMCs while Kelleher *et al*. assessed the expression of commonly used vascular pericyte (vPCs) associated molecular markers NG2 and PDGFR [216, 223]. However, there are no specific markers that could distinguish vPC from vSMC. It was suggested when differentiating cells to a vSMCs fate, some cells would exhibit a vPC-like phenotype and these cells exhibited a typical pericyte function in supporting EC capillary structures [216, 223, 362]. Due to a lack of markers specifically distinguishing vSMC and vPC, the differentiated cells were referred to as iPSC-vMCs to account for the presence of vPC-like cells within the differentiated population [223].

In this chapter, successful replication of the iPSC-vMCs differentiation protocol was demonstrated. Immunofluorescence microscopy images showed widespread expression of SOX1 and FOXG1 at day 8 of differentiation suggesting a neuroectodermal phenotype (**Figure 5.1 B**), which was further confirmed by a significant increase in the expression of

neuroectodermal marker genes *SOX1* and *SOX2* at day 7 of differentiation compared to day 0 (**Figure 5.2**). Compared with the iPSC-vMCs model for CADASIL developed by Ling et al, the iPSC-vMCs in our model were derived via the neuroectoderm stage, which recuperated more closely of vMCs in the cerebral vasculature where the CADASIL pathology mainly happens [222]. At day 18 of differentiation, the expression of three vMCs markers a-SMA, CNN1, and SM22a were highly expressed as shown in immunofluorescence microscopy images and qRT-PCR results. Taken together, these data suggest that vMCs were successfully derived from iPSCs.

5.3.2. Successful construction of an iPSC-BBB model using all major NVU cell types

BBB is composed of BMECs that regulate the transmission of substances into or out of the brain. The barrier function of BBB relies on tight junction proteins formed between BMECs, resulting in blood vessels exhibiting high TEER and low passive permeability. The characterisation of BMECs derived from control iPSCs lines is essential prior to co-culture in order to generate a reliable iPSC-BBB model. The data shows that all iPSCs were positive for SOX2 and SSEA4 staining indicating that BMEC differentiation was initiated from a pure population of iPSCs (**Figure 5.3, 5.4, and 5.5 A** respectively). This is important, as it is known that contamination of iPSC cultures with spontaneously differentiated cells can result in poorer differentiation. At day 10, cells from 3 iPSC lines were all positive for the functional BMEC and junction protein markers VE-cadherin, GLUT1, occludin, ZO-1 and claudin-5, indicating mature BMECs were generated (**Figure 5.3, 5.4 and 5.5 B, C, D, E and F** respectively). It was further confirmed by barrier function analysis, in which all lines demonstrated high TEER value (**Figure 5.3, 5.4 and 5.5 G** respectively). Another control line AGD-14-02-C3 was also involved in co-culture experiment and the characterisation was shown in Chapter 3.

Transwell-based BBB models typically consist of ECs cultured on a permeable membrane coated with ECM that is suspended within a well of a 12 or 24-well plate. This Transwell platform allows rapidly quantification of barrier integrity by measurement of TEER and permeability screening of molecules or drugs. In the model presented here, BMECs were seeded onto the upper surface of the Transwell membranes to form monolayers with BBB properties and MCs were co-cultured either directly or indirectly with BMECs, with/without astrocytes or neurons seeded onto the bottom wells to mimic the paracrine action of those cells. In comparison with existing BBB models, this iPSC-BBB model showed similar or

higher TEER of control BMECs monoculture and various co-culture settings to the BBB model developed by Lippmann et al. [349].

One physiological aspect this model does not replicate is fluid flow and the sheer stress this induces, which may weaken the effect of cell-cell signalling through soluble factors. Additionally, due to the small pore sizes the permeable membrane of the Transwell inserts may prevent substantial contact between BMECs and other NVU cell types. Future efforts on CADASIL iPSC-BBB model can be made on tissue-engineered 3D NVU model, which utilizing hydrogel-based bioinks with spatial distribution of the different cell types [363].

5.3.3. Co-culturing with iPSC-vMCs, Neurons and astrocytes can promote barrier function of iPSC-BMECs

The co-culture experiments demonstrated that culture of purified iPSC-derived BMECs in the presence of vMCs, neurons or astrocytes could increase iPSC-BMECs barrier formation (**Figure 5.8, 5.9, 5.10, 5.11**). Furthermore, the triple culture of BMECs with vMCs and astrocytes further enhanced barrier formation than co-culture with either cell type alone (**Figure 5.12, 5.13**). These findings were further confirmed by low passive diffusion through the BMEC monolayers by sodium fluorescein (**Figure 5.14**). The tendencies of increased TEER are similar to rodent *in vitro* BBB studies that built up various co-culture combinations of primary isolated pericytes, astrocytes and BMECs [364]. In comparison, this model showed higher TEER value than the rodent model.

5.3.4. Advantages of iPSC-BBB model over current models of neurovascular interaction

Among the current three iPSC-derived models of CADASIL, ECs and MCs were differentiated from iPSCs to model the disease pathologies [222, 223, 225]. However, none of the ECs in the three models exhibit properties found in brain microvascular endothelial cells. In this chapter the iPSC-BBB model built with iPSC-derived BMECs, vMCs, astrocytes and neurons was described. To compare the current three iPSC-ECs models for CADASIL with this model, non-brain iPSC-ECs were differentiated from the same iPSCs lines and TEER measurements compared between both cell types seeded on Transwells. TEER measurements using HCAECs were a negative control as these cells do not naturally possess high electrical resistance *in vivo* (**Figure 5.15)**. The results showed that the iPSC-ECs failed to show BBB properties with a low TEER value similar to HCAECs and low expression of junction genes (**Figure 5.16)**. In comparison, iPSC-BMECs derived from the

same iPSC lines exhibited significantly higher TEER value during differentiation **(Figure 5.17)**. In conclusion, iPSC-BMECs can mimic more closely of neurovascular interactions than iPSC-ECs in the brain, which can be applied to model CADASIL pathology that mainly happens in the brain (will be demonstrated in next chapter). Besides, this model is the first iPSC-BBB model involves neuronal cell types apart from vascular cell types that are all iPSCs derived.

Apart from CADASIL, this iPSC-BBB model can be applied to study the pathologies of other VaD and neurological disorders. Previous BBB models are mainly based on NVU cell types sourced from immortalized cell lines or cells isolated from non-human animals. For example, Thomsen *et al*. developed a Transwell BBB model incorporating primary BMECs, pericytes, and astrocytes [365]. Several recently reported Transwell models for BBB incorporated one or more cell types derived from iPSCs. For instance, a quadruple culture BBB model encompassing iPSC-derived BMECs, iPSC-derived and primary astrocytes and neural stem cells, and primary pericytes exhibited increased TEER and increased expression of the *GLUT1* compared to BMECs monoculture [350]. Recently, Canfield *et al*. demonstrated the differentiation of BMECs, neurons, and astrocytes from the same iPSC line, but pericytes as the main component of BBB were not included [366]. In general, none of these models applied NVU cells including BMECs, pericytes, neurons and astrocytes that are all iPSCs sourced. Current non-primate BBB models fail to adequately recapitulate human BBB function because of species-specific differences as was discussed before. Our iPSC-BBB model is the first to have incorporated 4 cell types all derived from iPSCs, which has more relevance to human biology than immortalized cell lines or cells isolated from animals for modelling human neurovascular disease.

5.4. Summary

This chapter demonstrates the iPSC-BBB model for neurovascular interaction was successfully built using control BMECs. Replication of the iPSC-MCs differentiation protocol was described. iPSC-derived BMECs, vMCs, astrocytes and neurons were co-cultured or triple cultured in Transwell settings to mimic BBB. Barrier function of BMECs after the co-culture or triple culture was obviously increased compared to BMECs monoculture. This iPSC-BBB model showed advantages in barrier function compared to other iPSC-derived models for CADASIL. The application of this iPSC-BBB model on investigating the CADASIL pathologies will be shown in Chapter 6.

6. Chapter 6: *in vitro* blood brain barrier constructed with iPSCs derived from CADASIL patients exhibit impaired barrier properties

6.1. Introduction

Previous studies have revealed that CADASIL pathologies include vSMC degeneration in the brain, abnormal *NOTCH3* accumulation and endothelial dysfunction [367], but the mechanism underlying these changes, particularly endothelial dysfunction, are unclear. One study investigated the effect of *NOTCH3* mutations and its role in vSMC dysfunction, and it also showed increased BBB permeability in a CADASIL animal model [192]. However, no study has revealed BBB dysfunction in human CADASIL models.

In previous chapters, the differentiation of four types of NVU cells including BMECs, MCs, astrocytes and neurons from iPSCs was described. An iPSC-BBB model was then built with four cell types derived from control iPSCs in the Transwell settings. Having validated the iPSC-BBB model, the aim of this chapter was to generate an iPSC-BBB using iPSCs derived from CADASIL patients to investigate if NOTCH3 mutations disrupt the BBB.

6.1.1. iPSC-BBB cell models for CADASIL

As we discussed before, human *in vitro* BBB models using iPSCs derived from CADASIL patients are required, as animal models may not faithfully simulate the VaD phenotype due to species differences. CADASIL as the most common type of VaD, is caused by mutations in *NOTCH3* mainly effecting vMCs [27].

Currently only 3 models of iPSC-vMCs for CADASIL have been reported. Ling *et al* built the CADASIL iPSCs-vSMCs model with a NOTCH3 mutation Arg1076Cys and found gene expression changes associated with disease phenotypes, including activation of the NOTCH and NF-κB signalling pathway, cytoskeleton disorganization and excessive cell proliferation. However, these abnormalities were not observed in vECs derived from the CADASIL patient's iPSCs. Moreover, they found the abnormal upregulation of NF-κB target genes in CADASIL vSMCs could be rescued by a NOTCH pathway inhibitor, which provide a potential therapeutic target for CADASIL [222]. Kelleher *et al.* built an iPSC-CADASIL model with the NOTCH3 mutation Arg153Cys and Cys224Tyr from two CADASIL patients and demonstrated for the first time a failure of the CADASIL iPSC-derived vascular mural cells in engaging and stabilizing endothelial capillary structures [223, 224]. The CADASIL iPSC-vMCs were highly susceptible to apoptotic insults, and could induce

apoptosis of adjacent iPSC-vECs [223]. In a more recent research, an iPSC-derived CADASIL mural cells model was built, which could recapitulate CADASIL pathology [225].

In general, all current iPSC-CADASIL BBB models were based on iPSC-derived vMCs and vECs without other BBB cell types, despite astrocytes and neurons may also paly vital role in BBB defect contributing to CADASIL pathologies as we discussed before. Moreover, all the EC differentiated from iPSCs in the three studies are peripheral rather than brain type ECs where CADASIL pathologies mainly happen.

6.1.2. BBB damage in vascular dementia and CADASIL

An increasing number of studies indicate that damage of the BBB may play a significant role in the pathogenesis of VaD. Wardlaw *et al*. suggested that chronic BBB leakage leads to neuronal damage, which may contribute to the development of lacunar stroke and dementia [368]. In the most common VaD CADASIL, leaking and microbleeds were found in relatively thin-walled vessels in the cortex [368, 369].

The current hypothetical pathogenetic mechanisms of BBB breakdown in CADASIL are showed in **Figure 6.1**. In healthy individuals, tight junctions between BMECs form the BBB that protects the brain from toxic substances. In CADASIL, several defects have been found in the interface between blood vessels and brain parenchyma or cerebrospinal fluid at the artery, arteriole, and capillary levels. This includes arterial wall was damage by vSMC degeneration, EC dysfunction and GOM deposition. Collectively these changes may impair the BBB functions [370]. However, the mechanisms underlying these changes and how these changes are related to BBB damage are unknown.

Evidence suggests that ECs dysfunction in the microvasculature is a more likely cause of stoke rather than arterial defect, which may occur subsequent to BBB failure and leading to toxic components to superflux into the brain [371-373]. Recent studies identified how tight junction deficiencies and macromolecule transporters, such as GLUT-1, disruption can influence cerebrovascular integrity [374, 375]. In AD patients, it was found Aβ oligomers disrupt tight junctions and increase permeability of the BBB through reduction in the expression of occludin, claudin-5, and ZO-1 by BMECs [376-378]. The association between dysfunction of tight junction proteins especially claudins and occludin leading to BBB dysregulation and VaD should be considered [373]. Claudins have a vital role in the sealing

function of tight junctions, with claudin-5 playing a critical role in BBB permeability. Claudin5-deficient mice revealed that the development and morphology of blood vessels were not altered, while the BBB barrier against small molecules rather than larger molecules was selectively loosened [170]. Interestingly, Mihaela *et al*. found that occludin expression was significantly increased in both AD and VaD patients [379]. Thus it is important to explore the prevalence of tight junctions and the abundance of tight junction proteins in the BBB to investigate the pathologies of VaDs such as CADASIL.

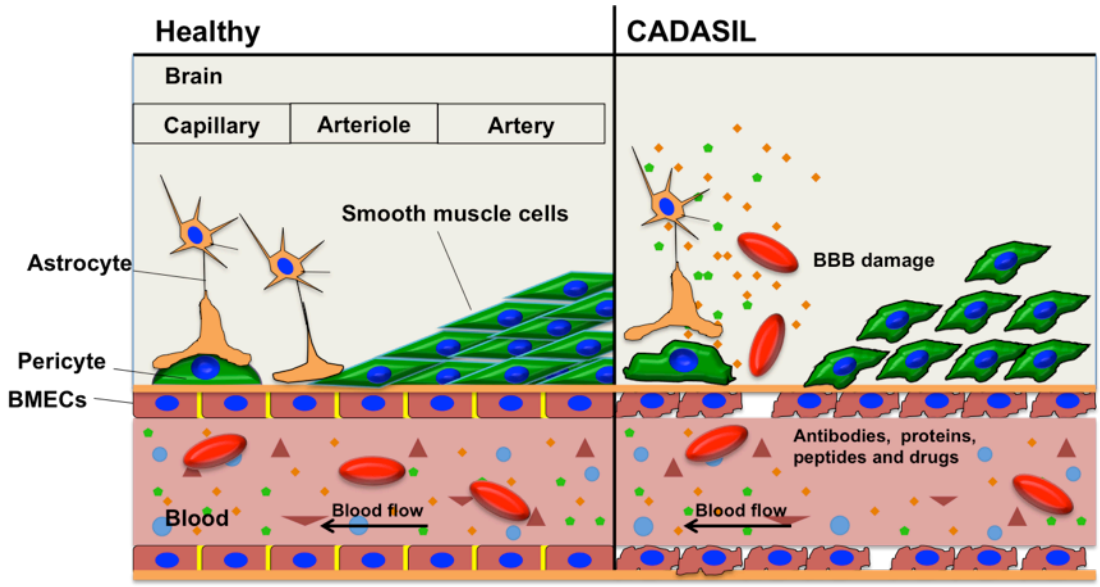

Figure 6.1 Hypothetical schematic drawing of BBB breakdown mechanisms in CADASIL.

In healthy individuals, tight junctions (yellow bars) between BMECs form the BBB, which protects the brain from toxic substances and helps to regulate the passage of drugs to the brain from the blood. In CADASIL patients, several changes happen in the interface between the blood and the brain parenchyma at small artery, arteriole, and capillary levels. Debris derived from the blood accumulates in disrupted BBB which prevent the normal transportation of molecules throughout the CNS across BMECs monolayer and interrupt the formation of interstitial fluid flow, which prevent antibodies, proteins, peptides, medicine and drugs from reaching their neuronal targets. The degeneration changes in vSMCs and pericytes and the GOM deposition in CADASIL patients likely damage BMECs, leading to BBB breakdown.

6.1.3. Notch3 mutation and BBB

In order to understand the neurovascular component of CADASIL it is important to explore the potential role of NOTCH3 deficiency on human neurovascular interactions and BBB function.

It has been demonstrated zebrafish pericytes express Notch3 and that Notch3 mutant zebrafish fail to form a tight BBB [192]. However, no differences were found in the expression of VE-cadherin, tight junction proteins claudin5 and ZO-1 between mutant and wild type zebrafish larvae, which indicates that Notch3 is required for BBB integrity independently of BMEC tight junction formation [192]. Mice models of CADASIL have shown that NOTCH signalling cooperated with TGF-β pathway gene SMAD4 to promote N-cadherin expression in BMECs. Inactivation of NOTCH signalling in BMECs caused impaired endothelial-pericyte adhesion resulting in BBB breakdown, indicating that NOTCH signalling pathways especially NOTCH3 and NOTCH1/NOTCH4 ICD in brain pericytes with ECs work together to ensure cerebral vascular integrity by promoting brain pericyte expansion as well as pericyte attachment to the endothelium [192, 380].

Current studies have found evidence of BBB breakdown in CADASIL, but the exact mechanism is unrevealed. Prevailing hypotheses indicate that pericyte dysfunction caused by *NOTCH3* mutation might damage tight junction proteins between BMECs thus leading to BBB leakage. However, these studies were based on animal models or knockdown/over-expression of *NOTCH3* genes in cell lines, which cannot faithfully mimic the disease pathology that happens in the human brain. Moreover, defects in neuronal cells or neurovascular interactions, which were not considered in any of the previous research, may also occur in CADASIL patients as migraine, a symptom of neural issues, happens at younger age then stroke appears.

Here it was hypothesised that defect may exist in cell-cell interactions among CADASIL iPSCs-derived NVU cells resulting in BBB leakage, which may be caused by tight junctions dysfunction related to *NOTCH3* mutation.

6.1.4. Aims and objectives

IPSCs provided a valuable platform to mimic the BBB *in vitro* with genetic background of the disease. The successfully establishment of a BBB model with NVU cell types differentiated from iPSCs were described in previous chapters. As was discussed before, studies have provided evidence of EC dysfunction and BBB breakdown in CADASIL but the exact mechanism is unrevealed. As one of the leading pathological changes in CADASIL is NOTCH3 mutation leading to vSMCs dysfunction, it is possible that this change could lead to BMEC barrier dysfunction. To reveal this question, the aim of this chapter is to compare the BBB barrier function between CADASIL and control iPSC-derived BBB models.

The objectives of this chapter are: (1) to compare the barrier functions between CADASIL and control iPSC-derived vMCs co-culturing with control BMECs via TEER measurement and sodium fluorescence permeability assay; (2) to compare the barrier function of CADASIL and control BMECs without co-culturing with other NVU cell type. (3) to compare the angiogenesis ability and junction and EC specific proteins expression between control and CADASIL BMECs. (4) to perform *NOTCH3* siRNA knockdown in control iPSC-BMECs and compare the barrier function between knockdown BMECs and scramble controls.

6.2. Results

6.2.1. CADASIL derived BMECs form BBB monolayers with poorer barrier properties that cannot be rescued by co-culture with healthy NVU cell types

A primary role of the BBB is to regulate the passage of molecules from the blood into the brain. To investigate whether defect exists in CADASIL BMECs thus affecting BBB function, CADASIL and control BMECs were differentiated from iPSCs and barrier function was measured.

When BMECs were seeded on the Transwell inserts on day 8, initial TEER of CADASIL iPSC-BMECs was 300 Ωxcm^2, which is significantly lower than control BMEC that was 800 Ωxcm^2 (24 hours' time point) ($p < 0.0001$) (**Figure 6.2)**. At 48 hours' time point, TEER of CADASIL BMECs increased to 600 Ωxcm^2 while control BMECs increased to 1,800 Ωxcm^2 ($p < 0.0001$). At 72 hours' time point, TEER of CADASIL BMECs decreased to 400 Ωxcm^2 while control BMECs decreased to 800 Ωxcm^2 ($p < 0.0005$) (**Figure 6.2)**. The maximum TEER in 6 control and CADASIL independent differentiation was summarised in **Figure 6.3.**

To determine if the normal NVU cells could rescue impaired barrier of CADASIL BMECs, indirect co-culture of BMECs with vMCs was performed, the TEER of CADASIL iPSC-BMECs with or without co-culture showed no significant difference at all time points (**Figure 6.4 A and B)**. The initial TEER of all groups was 400-600 Ωxcm^2 (24 hours' time point). At 48 hours' time point, the TEER of CADASIL iPSC-BMECs with or without co-culture in experiment A (**Figure 6.4 A)** and B (**Figure 6.4 B)** were 700 Ωxcm^2 and 300 Ωxcm^2 respectively, lower than control BMECs monoculture in relevant groups that are 800 Ωxcm^2 and 1,800 Ωxcm^2 respectively ($p < 0.0001$ and $p< 0.05$) and significantly lower than control BMECs co-culture with vMCs that are 2,800 Ωxcm^2 and 2,700 Ωxcm^2 respectively ($p < 0.0001$) (**Figure 6.4**).

Next, neurons from iPSCs were co-cultured with BMECs. Three independent experiment of control iPSC-neurons co-culturing with CADASIL and control iPSC-BMECs showed initial TEER of 300-500 Ωxcm^2 for all cultures **Figure 6.5**, with one exceptional of 1,000 Ωxcm^2 in control BMECs co-culture with neurons in **Figure 6.5 A.** At 48 hours' time point, the TEER of control BMECs monoculture and CADASIL BMECs with or without co-culture in experiment A were ~500 Ωxcm^2, much lower than control BMECs co-culture with neurons (**Figure 6.5 A)** ($p < 0.0001$). At 48 hours the TEER of control BMECs monoculture and

CADASIL BMECs co-culture with neurons were similar in experiment B and C (700 and 2,000 Ωxcm^2 respectively), much lower than control BMECs co-culture with neurons in both experiments (2,500 and 3,500 Ωxcm^2 respectively) (**Figure 6.5 B and C)** ($p < 0.0001$). This indicates neurons could not rescue CADASIL BMECs barrier function compared with control BMECs.

Finally, astrocytes were co-cultured with iPSC-BMECs. Three independent experiments of control iPSC-astrocytes co-culturing with CADASIL and control iPSC-BMECs showed initial TEER of 300-500 Ωxcm^2 for all cultures **Figure 6.6**. At 48 hours' time point, the TEER of control BMECs monoculture and CADASIL BMECs with or without co-culture in experiment 1 were ~700 Ωxcm^2, much lower than control BMECs co-culture with astrocytes (**Figure 6.6 A)** ($p < 0.0001$). At 48 hours, the TEER of patient BMECs monoculture was lower than control BMECs monoculture as well as CADASIL BMECs co-culture with astrocytes in experiment B and C ($p<0.005$), and much lower than control BMECs co-culture with astrocytes (5,000 and 3,300 Ωxcm^2 respectively) ($p < 0.0001$) (**Figure 6.6 B and C)**. The maximum TEER in all groups were summarised in **Figure 6.7.**

The permeability of control and CADASIL BMEC monolayers was measured using the passive diffusion of sodium fluorescein across the monolayers. Two out of the three independent experiments showed significant higher permeability of CADASIL BMECs compared with control BMECs ($p<0.05$ and $p<0.005$ respectively) (**Figure 6.8 A)**. The permeability in co-culture settings was measured. The results showed that CADASIL BMECs have higher permeability than control BMECs monoculture as well as co-culture with astrocytes and vMCs (**Figure 6.8 A)**. Moreover, control BMECs co-culture with vMCs or astrocytes could decrease the permeability more than CADASIL BMECs (**Figure 6.8 B)**.

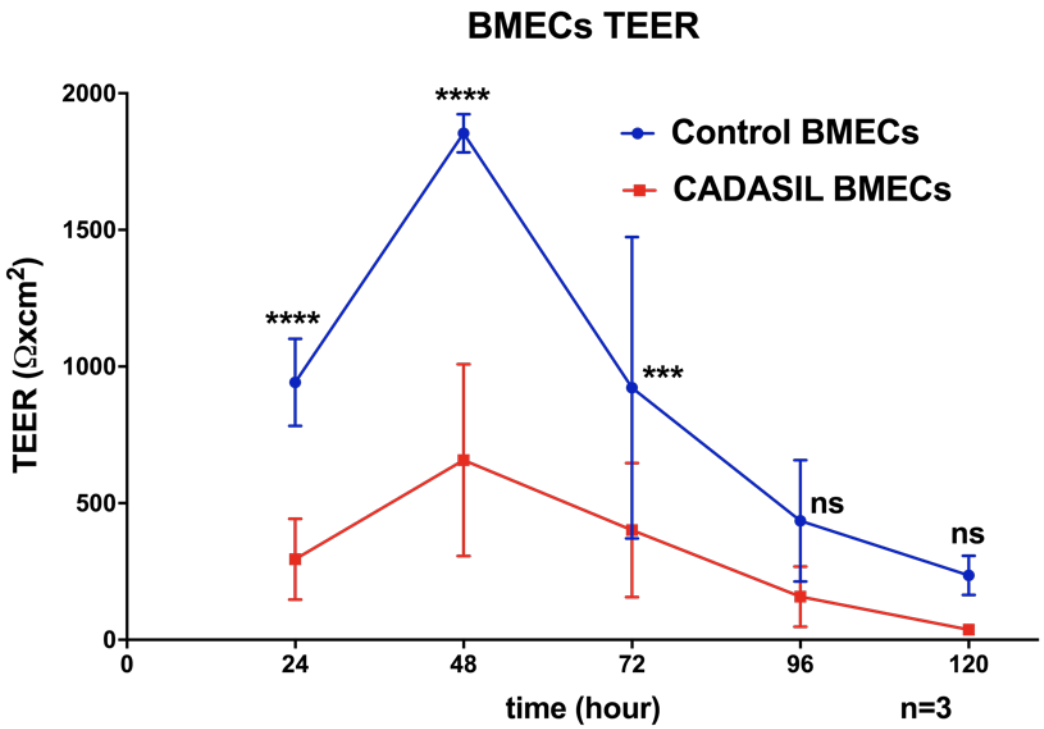

Figure 6.2 TEER of CADASIL iPSC-BMECs compared with control iPSC-BMECs.

Control and CADASIL BMECS were cultured on Transwells and TEER measured for 120 hours. Shown are mean data from 3 independent experiments with 3 control (AGD-14-02 C9/C3 and SW171A) and 3 CADASIL (AGD-14-04 C7/C10 and AGD-14-01 C1) BMEC lines. After 48 hours the maximum TEER achieved by monolayers of control BMECs was significantly higher than the patient BMEC monolayer counterpart. Statistical significance was calculated using unpaired T-Test. Values are reported as mean ± SEM, n=3. P<0.0005 ***, p<0.0001 **** versus control iPSC-BMECs at respective time point.

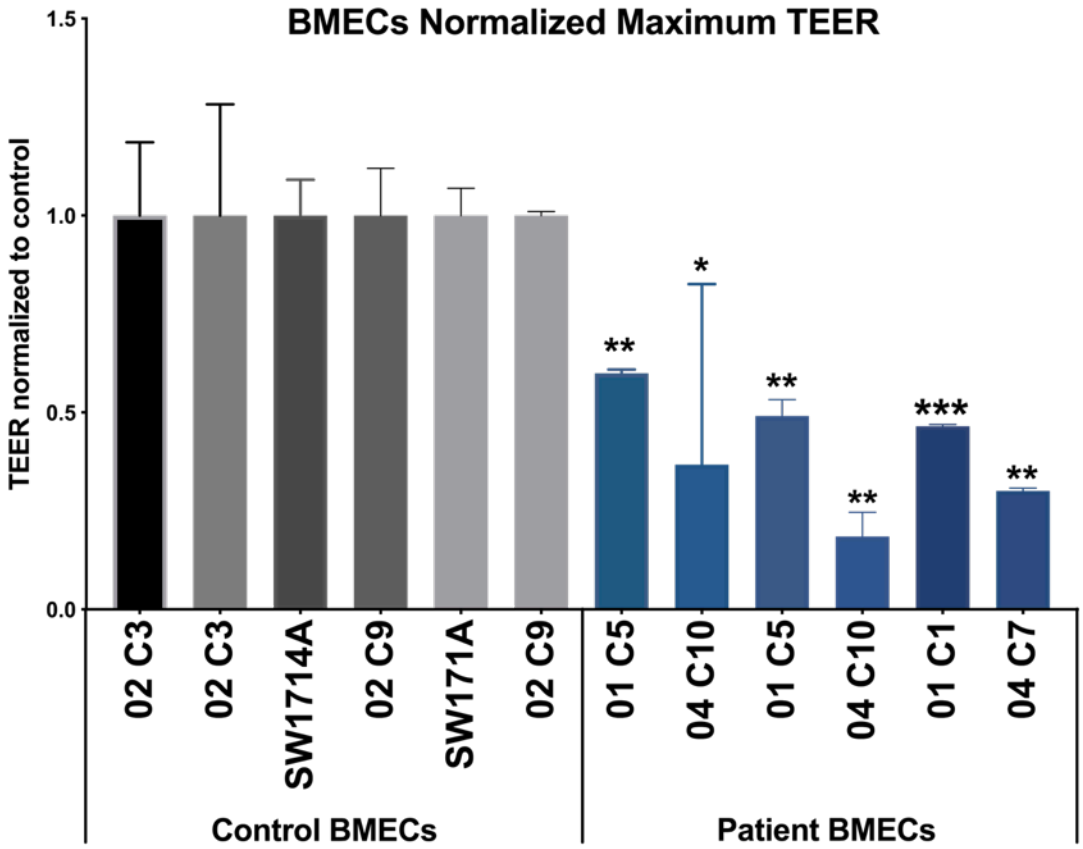

Figure 6.3 Maximum TEER of patient BMEC monolayers relative to a counterpart control BMEC monolayer

Maximum TEER of 6 control iPSC-BMEC lines were compared with 6 CADASIL iPSC-BMEC lines. Data displayed as maximum TEER of CADASIL BMECs relative to control BMECs monocultures.

Statistical significance was calculated using one-way ANOVA. Values are reported as mean ± SEM of these collective measurements. N=3. *p represents p value versus control iPSC-BMECs. * $p<0.05$, ** $p<0.005$ *** $P<0.0005$.

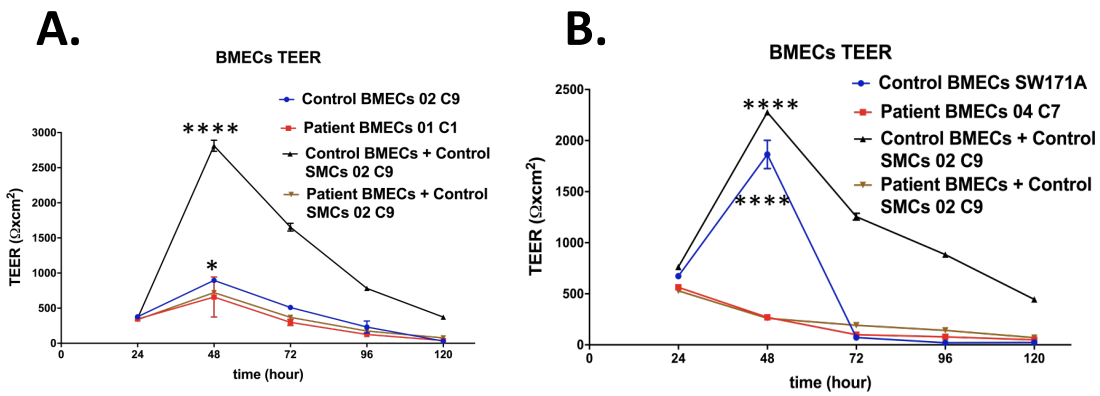

Figure 6.4 TEER measurements from CADASIL and control iPSC-BMEC monolayers indirectly co-cultured with control iPSC-derived vMCs.

Control or CADASIL BMECs were cultured on Transwell membranes with vMCs cultured on the bottom of the well. TEER was measured every 24 hours after seeding. Maximum TEER was achieved at 48 hours after BMECs seeding and was compared between control and co-culturing groups. **A-B**) data from two independent experiments.

Statistical significance was calculated using one-way ANOVA. The plot is the result of 3 biological replicates with each daily TEER measurement. Values are reported as mean ± SEM of these collective measurements. *$p<0.05$, **** $P<0.0001$ versus mean data of patient BMECs monoculture.

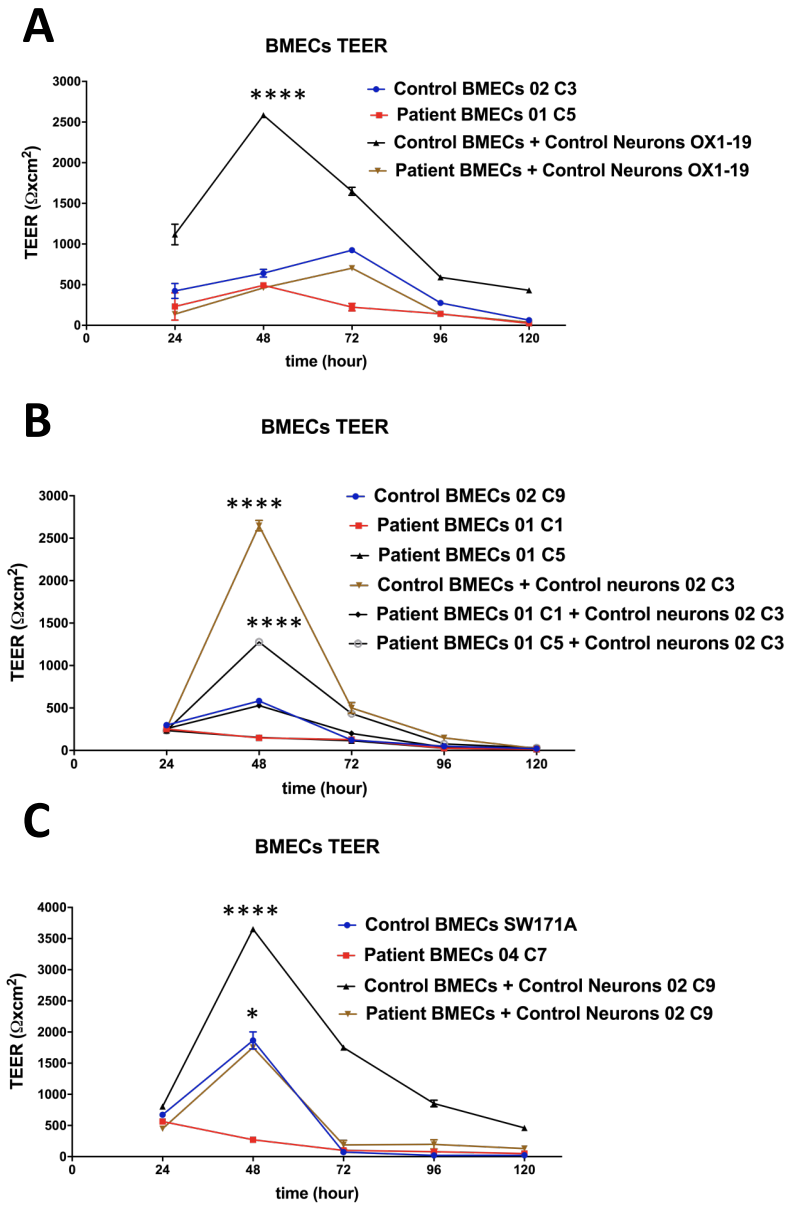

Figure 6.5 TEER measurements from CADASIL and control iPSC-BMEC monolayers indirectly co-cultured with control iPSC-derived neurons.

Control or CADASIL BMECs were cultured on Transwell membranes with neurons cultured on the bottom of the well. TEER was measured every 24 hours after seeding. Maximum TEER was achieved at 48 hours after BMECs seeding and was compared between control and co-culturing groups. **A-C**) data from three independent experiments.

Statistical significance was calculated using one-way ANOVA. The plot is the result of 3 biological replicates with each daily TEER measurement. Values are reported as mean ± SEM of these collective measurements. *P<0.05, **** P<0.0001 versus patient BMECs monoculture.

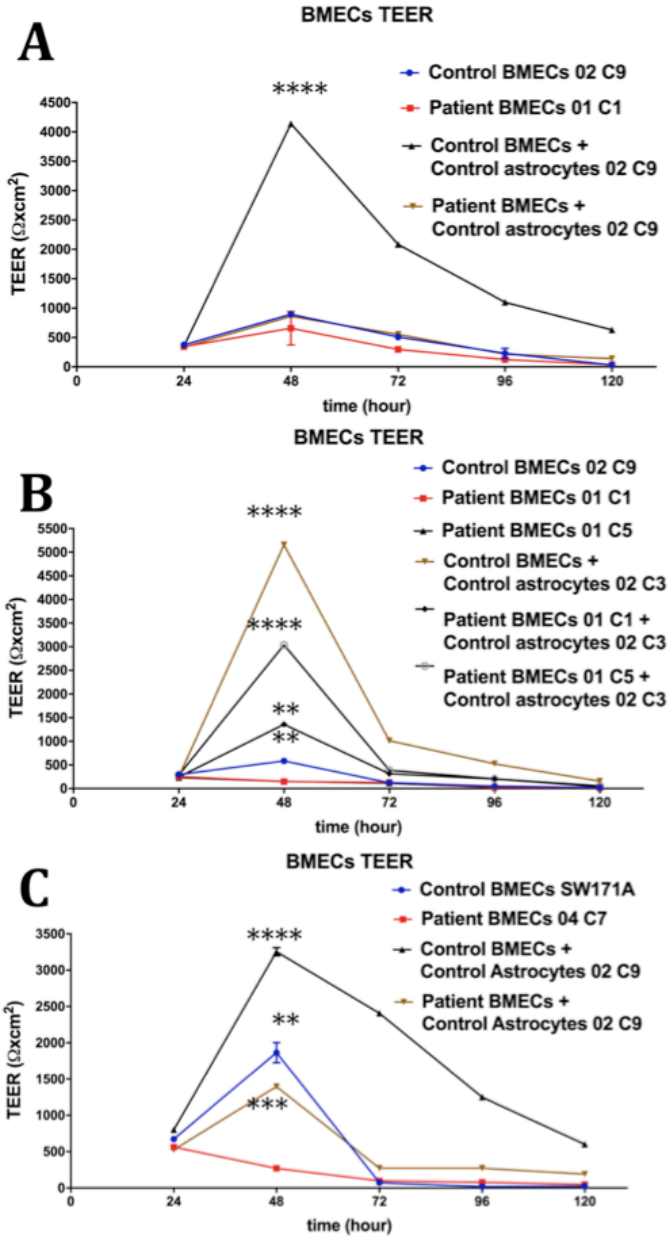

Figure 6.6 TEER measurements from CADASIL and control iPSC-BMEC monolayers indirectly co-cultured with control iPSC-derived astrocytes.

Control or CADASIL BMECs were cultured on Transwell membranes with astrocytes cultured on the bottom of the well. TEER was measured every 24 hours after seeding. Maximum TEER was achieved at 48 hours after BMECs seeding and was compared between control and co-culturing groups. **A-C**) data from three independent experiments. Statistical significance was calculated using one-way ANOVA. The plot is the result of 3 biological replicates with each daily TEER measurement. Values are reported as mean ± SEM of these collective measurements. *P<0.05, **** P<0.0001 versus patient BMECs monoculture.

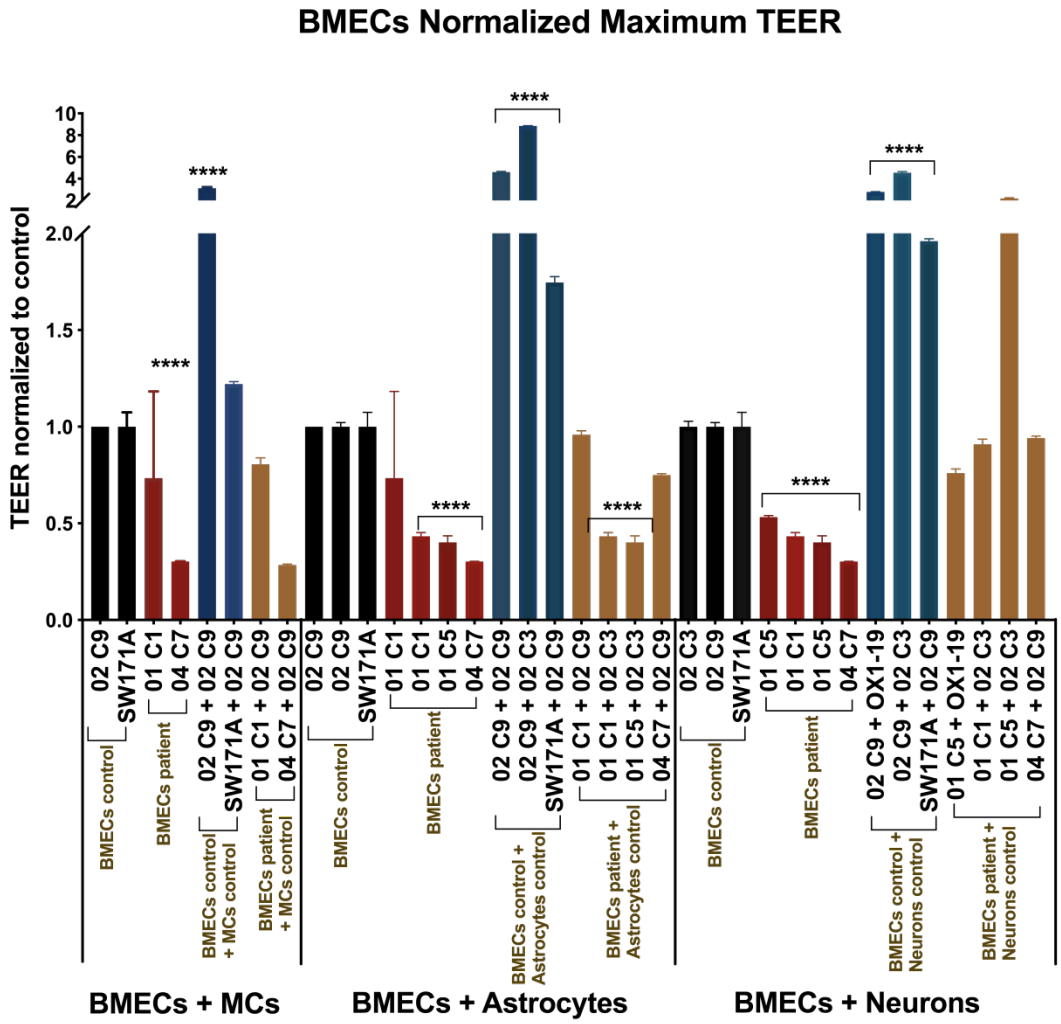

Figure 6.7 Maximum TEER summaries of CADASIL and control iPSC-BMECs co-culture with iPSC-vMCs/ neurons/ astrocytes.

Maximum TEER of control and CADASIL iPSC-BMECs co-culturing with control iPSC-vMCs/ neurons/ astrocytes directly or indirectly were compared with control iPSC-BMECs lines monoculture. Data showed maximum TEER of co-culture groups relative to control BMECs monocultures.

Statistical significance was calculated using one-way ANOVA. Values are reported as mean ± SEM of these collective measurements. N=3. *P < 0.05 (in blue colour) represent p value versus control BMECs monoculture. **** P<0.0001.

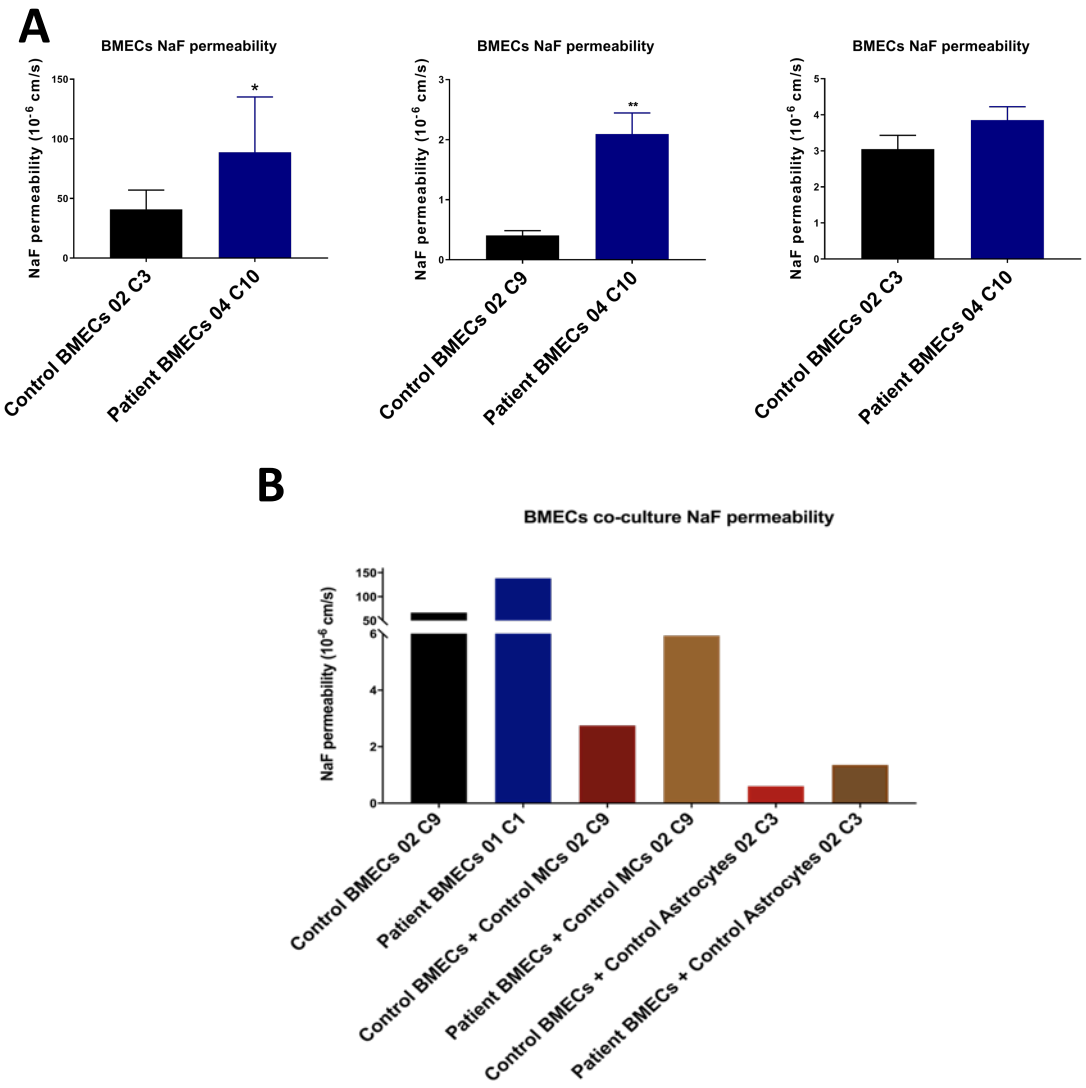

Figure 6.8 Permeability of sodium fluorescein for control and CADASIL iPSC-BMECs monolayers as well as co-culture with control iPSC-vMCs/ astrocytes.

The permeability of **(A)** control and CADASIL BMECs monolayers from 3 independent differentiation and **(B)** with indirect co-culture with control MCs/ astrocytes was measured using the passive diffusion of sodium fluorescein (pe) across the monolayers at 48 h after seeding, monocultured control iPSCs-BMECs were used as a control.

(A) Statistical significance was calculated using unpaired t-test. Values are mean ± SEM, n=3. *p < 0.05. **(B)** This graph shows the result from one experiment with one replicate.

6.2.2. CADASIL iPSC-derived mural cells can impair the barrier function of healthy iPSC-BMECs

In order to verify the hypothesis that CADASIL may disrupt the BBB as a result of vMCs dysfunction, CADASIL and healthy vMCs were co-cultured with control iPSC-BMECs in the established BBB model and barrier function was measured. Three independent experiment of indirect co-culture and one experiment of direct co-culture were performed. TEER measurements from control BMECs alone were used as a reference.

During indirect co-culture, the initial TEER of iPSC-BMECs derived from control AGD-14-02 C3 line was 500-1,200 Ωxcm^2 (24 hours' time point). At 48 hours' time point, both control groups of vMCs AGD-14-02 C9 (group 1) and AGD-14-02 C3 (group 2) co-culturing with BMECs exhibited significant increased TEER to 5,500 Ωxcm^2 and 4,500 Ωxcm^2 respectively compared with BMECs monoculture (nearly 2,000 Ωxcm^2) ($p < 0.005$) and ($p < 0.0005$) (**Figure 6.9A**). In comparison, TEER in co-culture with CADASIL iPSC-vMC lines AGD-14-04 C10 (group 1) and AGD-14-01 C1 (group 2) were 2,300 Ωxcm^2 and 3,000 Ωxcm^2 respectively, both of which did not show significant difference compared with BMECs monoculture, while both TEER were significantly lower than TEER of BMECs co-culturing with control iPSC-vMC co-culture lines ($p < 0.05$) and ($p < 0.005$) respectively (**Figure 6.9A**).

For another control iPSC-BMECs line SW171A, when co-culturing with CADASIL iPSC-MC line (AGD-14-01 C5) indirectly, the maximum TEER at 48 hours (1,400 Ωxcm^2) was less than that in co-culturing with control iPSC-vMC line AGD-14-02 C9 (2,300 Ωxcm^2) ($p < 0.0001$), while the TEER in monoculture was 1,250 Ωxcm^2 and showed no significant difference with CADASIL co-culture setting (**Figure 6.9B**).

TEER in monoculture of iPSC-BMEC lines EIPL1 (group 1) and SOJD3 (group 2) (both commercially purchased control iPSC lines) were both ~700 Ωxcm^2 at 48 hours' time point, both increased significantly in co-culturing with either control or CADASIL iPSC-vMCs ($P<0.0001$). However, in group 1, TEER of BMECs co-culturing indirectly with control iPSC-vMCs exhibited significant higher TEER compared with co-culturing with CADASIL iPSC-vMCs (3,700 and 1,800 Ωxcm^2 respectively) ($p < 0.0001$) (**Figure 6.9C, group 1**). Similarly, TEER of BMECs co-culturing with control iPSC-vMCs in group 2 showed much higher TEER compared with co-culturing with CADASIL iPSC-vMCs (4,700 and 1,700 Ωxcm^2 respectively) ($p < 0.0001$) (**Figure 6.9C, group 2**).

For the direct co-culture settings, TEER in monoculture of iPSC-BMEC lines EIPL1 (group 1) and SOJD3 (group 2) were both ~700 Ωxcm^2 at 48 hours' time point, both increased significantly in co-culturing with either control or CADASIL iPSC-vMCs (P<0.0001). In group 1, TEER of BMECs co-culturing indirectly with control iPSC-vMCs exhibited significant higher TEER compared with co-culturing with CADASIL iPSC-vMCs (3,700 and 1,900 Ωxcm^2 respectively) ($p < 0.0001$) (**Figure 6.10, group 1**). Similarly, TEER of BMECs co-culturing with control iPSC-MCs in group 2 showed much higher TEER compared with co-culturing with CADASIL iPSC-vMCs (4,600 and 1,600 Ωxcm^2 respectively) ($p < 0.0001$) (**Figure 6.10, group 2**). The maximum TEER in all groups were summarised in **Figure 6.11.**

The permeability of control BMEC monolayers with indirect co-culture with CADASIL or control iPSC-vMCs was measured using the passive diffusion of sodium fluorescein across the monolayers, monocultured control iPSCs-BMECs were used as a control. The permeability of control BMECs cultured with control vMCs was significantly decreased compared to control BMECs alone ($p<0.05$) (**Figure 6.12**). Furthermore, the permeability of the control BMEC monolayer was significantly increased when co-cultured with patient vMCs compared to co-culture with control vMCs ($p<0.05$) (**Figure 6.12**).

Immunofluorescence staining images showed discontinuous expression of junctional proteins to the tight junctions ZO-1 and GLUT1 in control BMEC line SW171A after co-culturing with CADASIL vMC line AGD-14-01 C5 (arrowed), while BMECs co-cultured with control iPSC-vMCs showed intact expression of GLUT1 and ZO-1 (**Figure 6.13**).

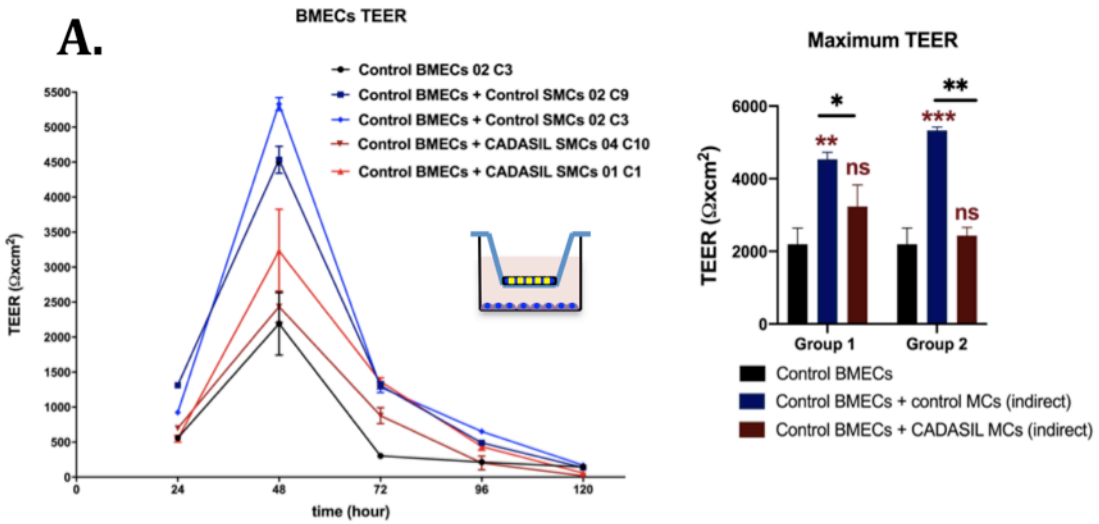
A.
BMECs TEER
Control BMECs 02 C3
Control BMECs + Control SMCs 02 C9
Control BMECs + Control SMCs 02 C3
Control BMECs + CADASIL SMCs 04 C10
Control BMECs + CADASIL SMCs 01 C1
TEER (Ωxcm²)
time (hour)
Maximum TEER
TEER (Ωxcm²)
Group 1
Group 2
Control BMECs
Control BMECs + control MCs (indirect)
Control BMECs + CADASIL MCs (indirect)

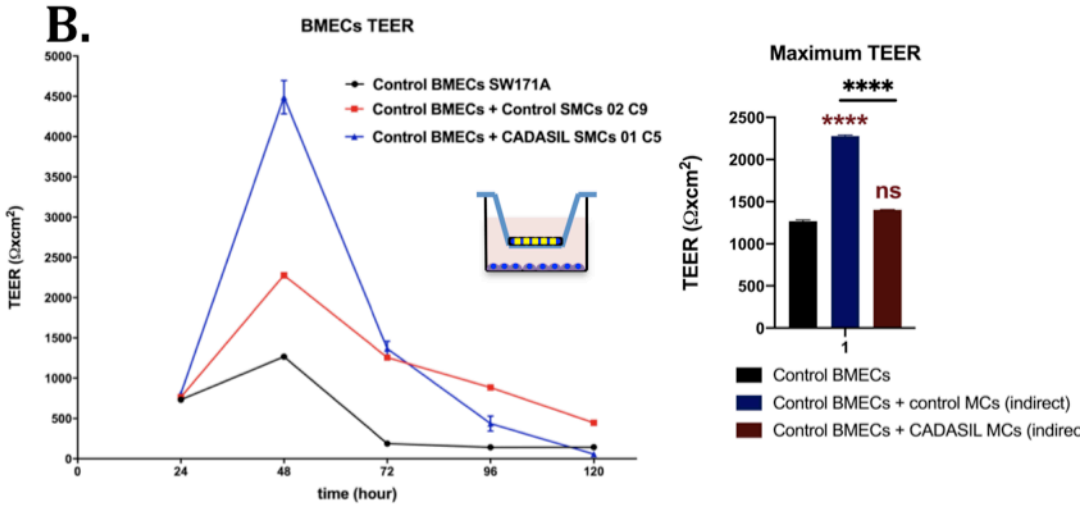
B.
BMECs TEER
Control BMECs SW171A
Control BMECs + Control SMCs 02 C9
Control BMECs + CADASIL SMCs 01 C5
TEER (Ωxcm²)
time (hour)
Maximum TEER
TEER (Ωxcm²)
Control BMECs
Control BMECs + control MCs (indirect)
Control BMECs + CADASIL MCs (indirec

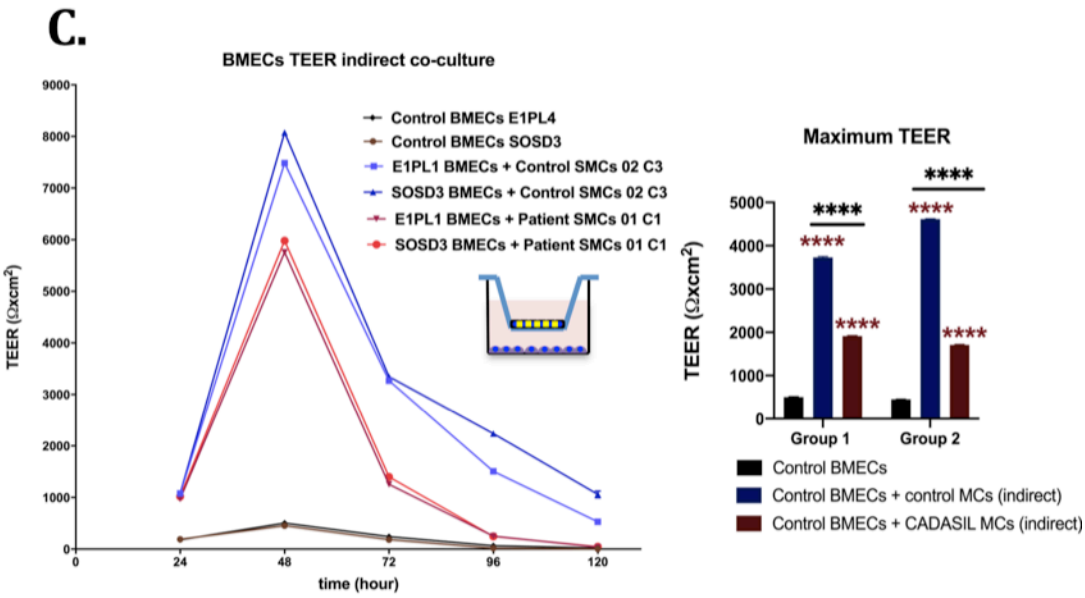
C.
BMECs TEER indirect co-culture
Control BMECs E1PL4
Control BMECs SOSD3
E1PL1 BMECs + Control SMCs 02 C3
SOSD3 BMECs + Control SMCs 02 C3
E1PL1 BMECs + Patient SMCs 01 C1
SOSD3 BMECs + Patient SMCs 01 C1
TEER (Ωxcm²)
time (hour)
Maximum TEER
TEER (Ωxcm²)
Group 1
Group 2
Control BMECs
Control BMECs + control MCs (indirect)
Control BMECs + CADASIL MCs (indirect)

Figure 6.9 TEER of iPSC-BMECs monolayers indirectly co-cultured with CADASIL and control iPSC-derived vMCs.

(A) iPSC-BMECs derived from AGD-14-02 C3 line were co-cultured indirectly with patient iPSC-vMC lines (AGD-14-04 C10 and AGD-14-01 C1) and control iPSC-vMC lines (AGD-14-02 C3 and AGD-14-02 C9) and TEER was monitored for 120 hours. **(B)** iPSC-BMECs derived from SW171A line were co-cultured indirectly with control iPSC-vMC line AGD-14-02 C9 and patient iPSC-vMC line AGD-14-01 C5 TEER was monitored for 120 hours. **(C)** iPSC-BMECs derived from EIPL1 line and SOJD3 line were co-cultured indirectly with control iPSC-vMC line AGD-14 -02 C3 and patient iPSC-vMC line AGD-14-01 C1 and TEER was monitored for 120 hours.

Statistical significance was calculated using one-way ANOVA. The plot is the result of 3 biological replicates (n=3) with each daily TEER measurement. Values are reported as mean ± SEM of these collective measurements. * $p<0.05$, ** $p<0.005$ *** $P<0.0005$, **** $P<0.0001$ (* in red, versus control BMEC monolayers; * in black versus control BMECs co-cultured with control vMCs).

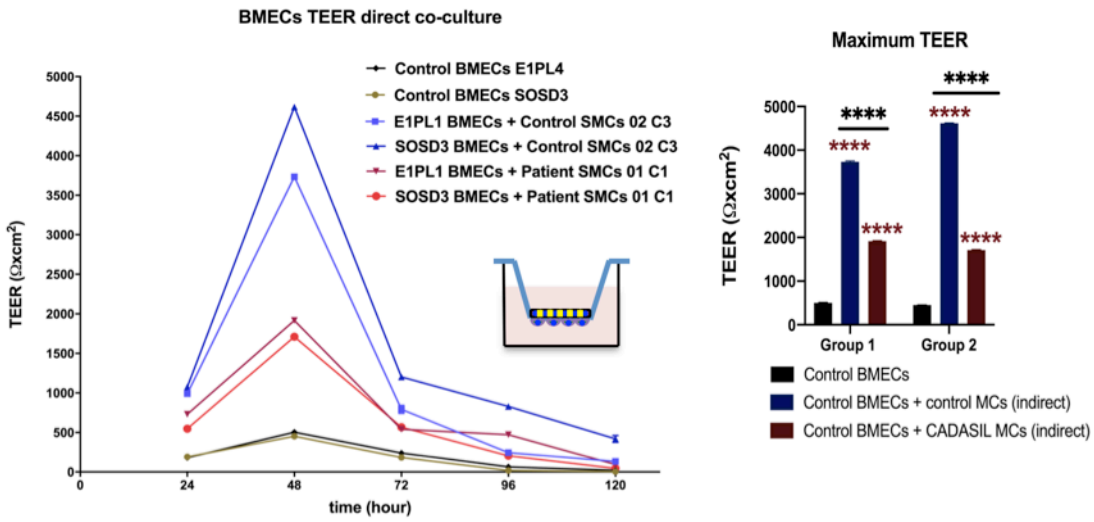

Figure 6.10 TEER of iPSC-BMECs directly co-cultured with CADASIL and control iPSC-derived MCs.

iPSC-BMECs derived from EIPL1 line and SOJD3 line were co-cultured directly with control iPSC-vMC line AGD-14-02 C3 and patient iPSC-vMC line AGD-14-01 C1 and TEER was monitored for 120 hours.

Statistical significance was calculated using one-way ANOVA. The plot is the result of 1 biological replicates (n=1) with each daily TEER measurement. Values are reported as mean ± SEM of three technical repeats. **** P<0.0001 (* in red, versus control BMEC monolayers; * in black versus control BMECs co-cultured with control vMCs).

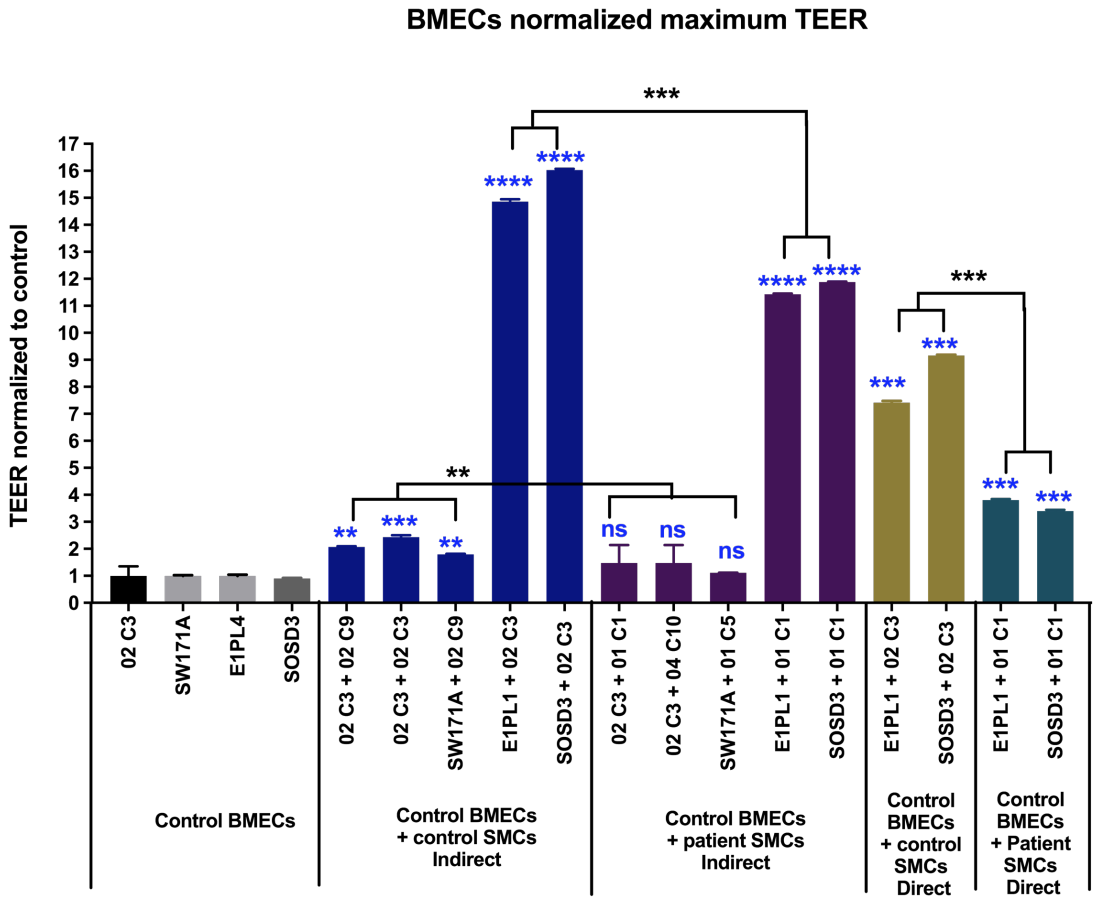

Figure 6.11 Maximum TEER summaries of control iPSC-BMECs co-culture with CADASIL and control iPSC-MCs.

Maximum TEER of control iPSC-BMECs co-culturing with CADASIL and control iPSC-MCs directly/indirectly were compared with 4 control iPSC-BMECs lines monoculture. Data showed maximum TEER of co-culture groups relative to control BMECs monocultures.

Statistical significance was calculated using one-way ANOVA. The plot is the result of 3 technical replicates with each daily TEER measurement. Values are reported as mean ± SEM of these collective measurements. ** $p<0.005$ *** $P<0.0005$, **** $P<0.0001$ (* in blue versus control BMEC monolayers, * in black versus control BMECs co-cultured with control vMCs).

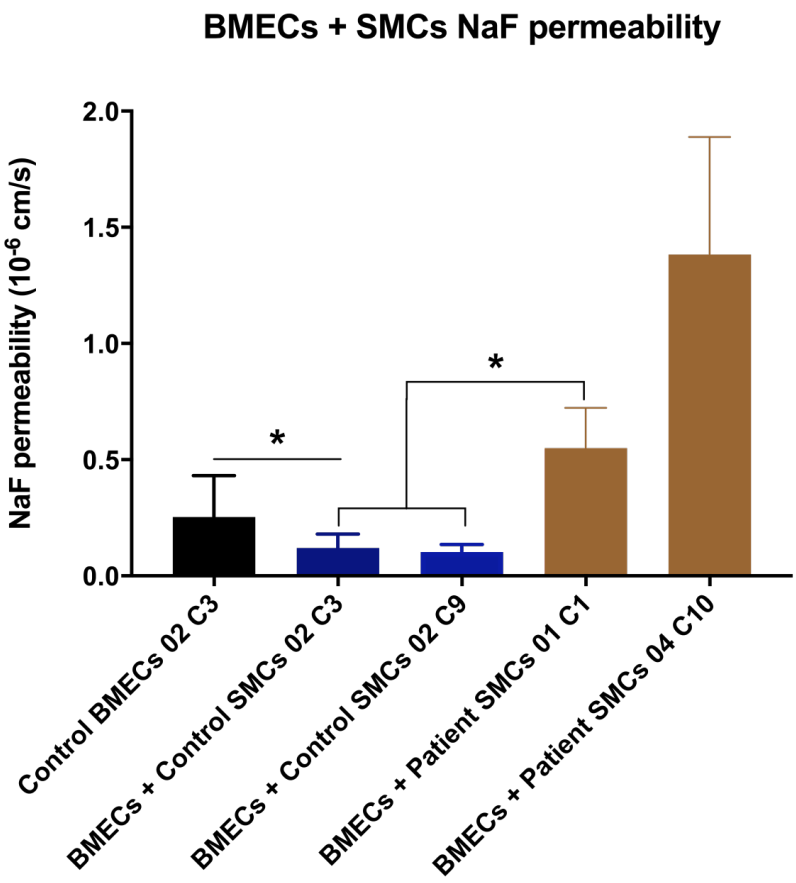

Figure 6.12 Permeability of sodium fluorescein for iPSC-BMECs co-culture with CADASIL and control iPSC-vMCs.

The permeability of control BMECs monolayers (AGD-14-02 C3 line) with indirect co-culture with CADASIL (AGD-14-01 C1 line and AGD-14-04 C10 line) or control MCs (AGD-14-02 C3 line and AGD-14-02 C9 line) was measured using the passive diffusion of sodium fluorescein across the monolayers at 48 h after seeding, monocultured control iPSCs-BMECs were used as a control.

Statistical significance was calculated using one-way ANOVA. Values are mean ± SEM of three replicates from a single differentiation. *$p < 0.05$.

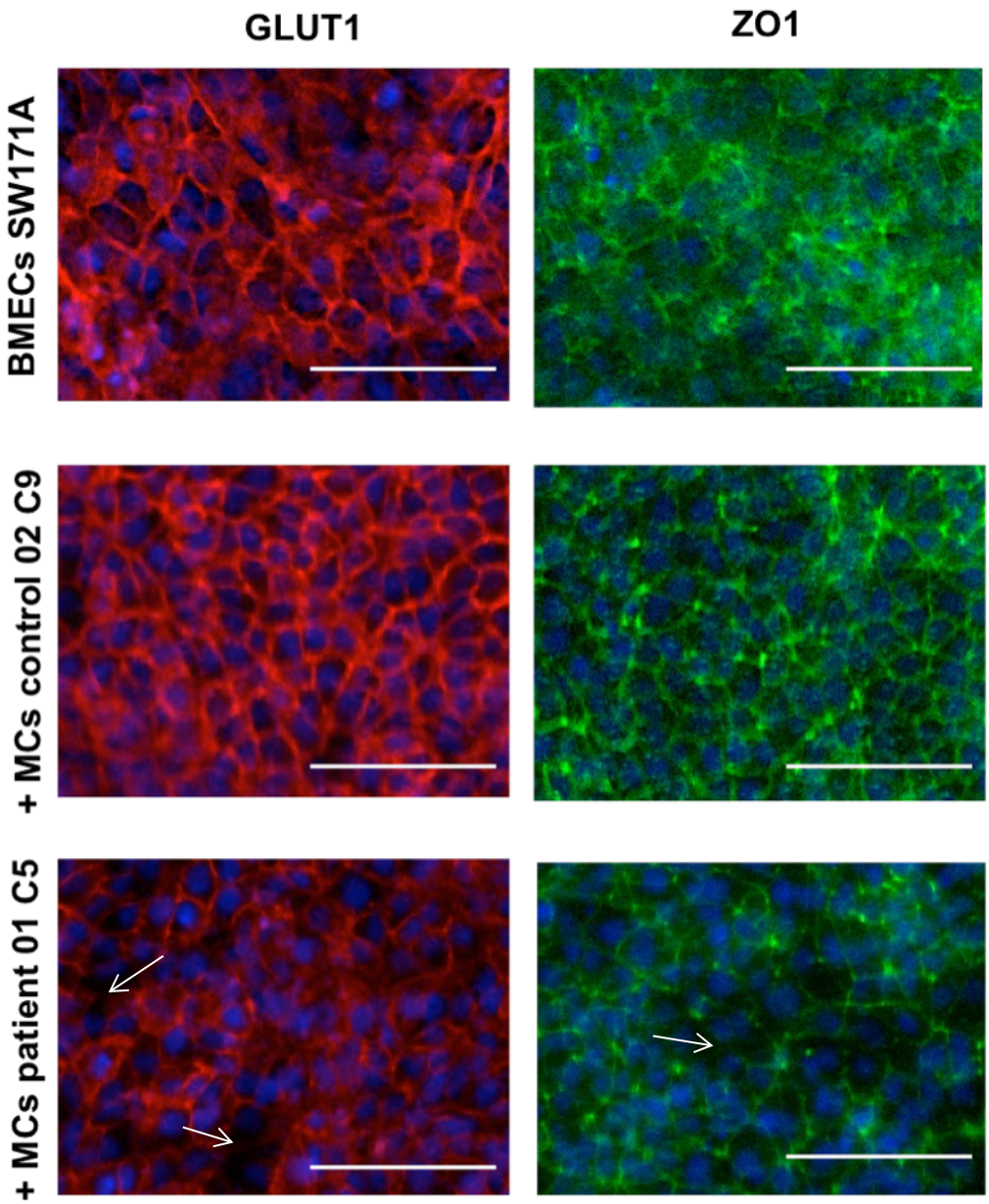

Figure 6.13 Immunofluorescence staining microscopy of control iPSC-BMECs co-culture with control iPSC-MCs compared to CADASIL iPSC-vMCs.

Immunofluorescence staining images shows BMECs and junction protein markers ZO-1 (green) and GLUT1 (red) with DAPI (blue) at day 10 of the differentiation. Scale bars, 100 μm.

6.2.3. Gene expression of junctional proteins in CADASIL and control BMECs

To investigate whether the barrier defects in CADASIL iPSC-BMECs was associated with known BMEC functional markers and junction proteins, mRNA expression of the related genes throughout differentiation was detected by qRT-PCR. The gene expression profile between CADASIL and control BMECs showed contradictory results on the expression of BMECs marker gene *SLC2A1* and tight junction marker genes *ZO-1*, *OCLDN* and *CLDN5* (**Figure 6.14 A, B, C and D**). No difference between CADASIL and control BMECs can be concluded. The mRNA expression of NOTCH3 in CADASIL and control BMECs was also assessed preliminarily. The results indicate that NOTCH3 mRNA expression in CADASIL cells is lower than in control cells d0 control vs CADASIL ($P<0.0001$), d5 control vs CADASIL ($P<0.0001$) and d8 control vs CADASIL ($P<0.0001$) (**Figure 6.14 E)**.

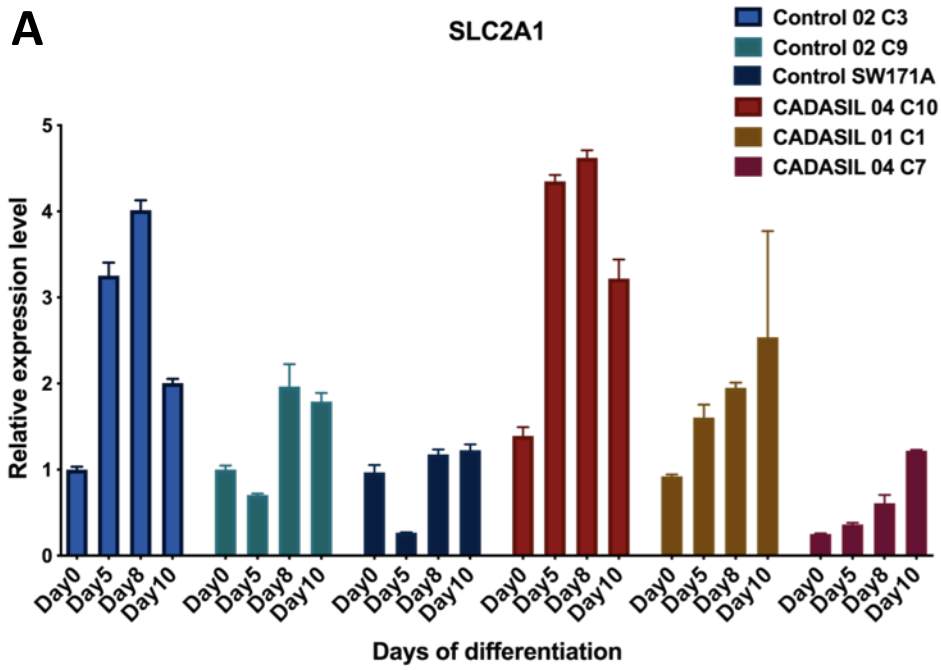
A
SLC2A1
Control 02 C3
Control 02 C9
Control SW171A
CADASIL 04 C10
CADASIL 01 C1
CADASIL 04 C7
Relative expression level
0
1
2
3
4
5
Day0
Day5
Day8
Day10
Days of differentiation

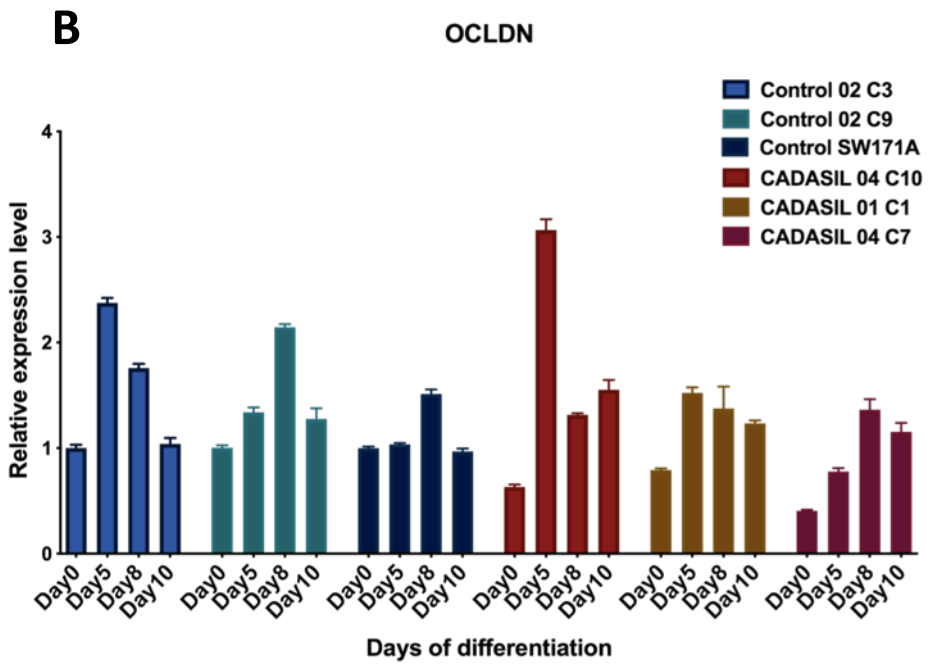
B
OCLDN
Control 02 C3
Control 02 C9
Control SW171A
CADASIL 04 C10
CADASIL 01 C1
CADASIL 04 C7
Relative expression level
0
1
2
3
4
Day0
Day5
Day8
Day10
Days of differentiation

C

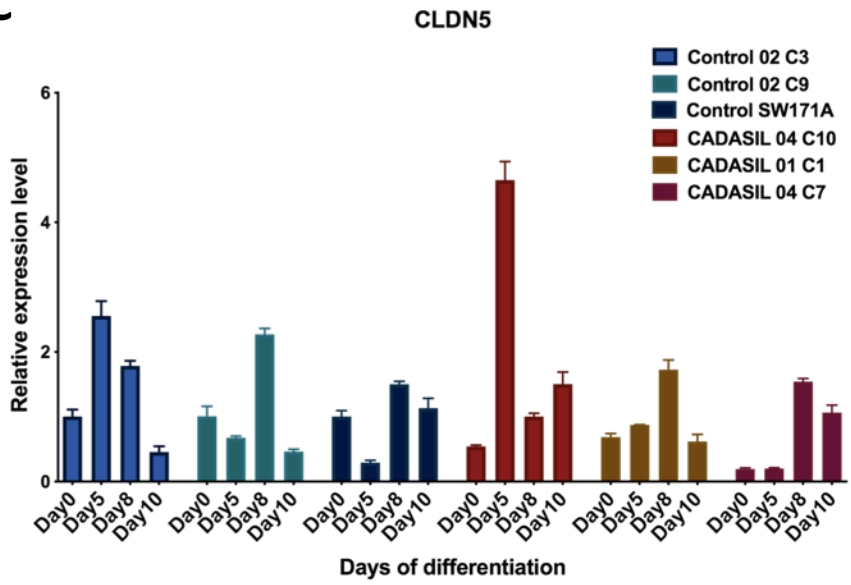
CLDN5
Control 02 C3
Control 02 C9
Control SW171A
CADASIL 04 C10
CADASIL 01 C1
CADASIL 04 C7
Relative expression level
0
2
4
6
Day0
Day5
Day8
Day10
Days of differentiation

D

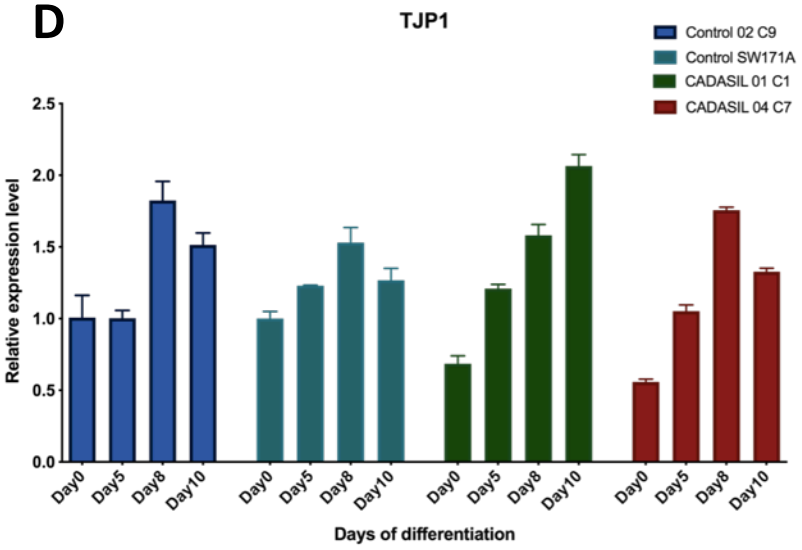
TJP1
Control 02 C9
Control SW171A
CADASIL 01 C1
CADASIL 04 C7
Relative expression level
0.0
0.5
1.0
1.5
2.0
2.5
Day0
Day5
Day8
Day10
Days of differentiation

E

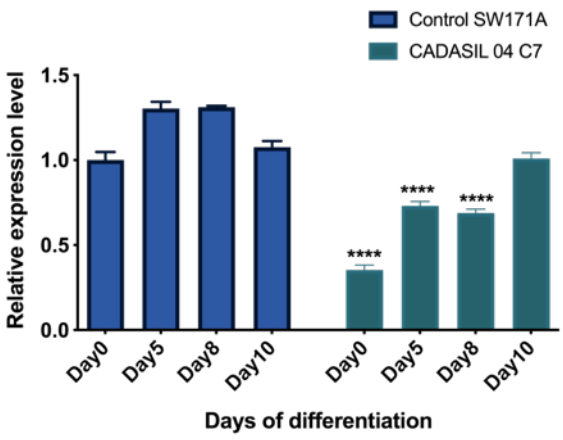
NOTCH3
Control SW171A
CADASIL 04 C7
Relative expression level
0.0
0.5
1.0
1.5
****
****
****
Day0
Day5
Day8
Day10
Days of differentiation

Figure 6.14 Gene expression profile of BMEC associated markers during differentiation of control and CADASIL iPSCs.

Expression of **(A)** transporter gene *SLC2A1* and tight junction marker genes **(B)** *OCLDN* **(C)** *CLDN5* and **(D)** *ZO-1*, and **(E)** *NOTCH3* gene measured during BMEC differentiation from control and CADASIL iPSCs. Gene expression was measured relative to GAPDH expression and normalised to day 0. Error bars represent the SEM. For **(A) (B) (C)** n=3, 3 biological repeats using control iPSCs (3 clones) and CADASIL iPSCs (3 clones). For **(D)** n=2, 2 biological repeats using control iPSCs (2 clones) and CADASIL iPSCs (2 clones). For **(E)** n=1. Statistical significance was determined by one-way Anova. **** $P<0.0001$.

6.2.4. Expression of BMEC associated marker proteins in CADASIL and control BMECs

Immunofluorescent staining was used to detect the expression GLUT1, ZO-1 and occludin in healthy and CADASIL iPSC-derived BMECs (n=4) at day 10 of differentiation when the barrier properties of the monolayers were at their peak. CADASIL and control BMECs from 4 CADASIL iPSCs and 4 control iPSCs accordingly were stained for the BMECs specific protein Glut1, ZO-1 and occludin at Day 10 of differentiation when TEER meets the maximum value. As shown in **Figure 6.15**, GLUT1, ZO-1 and occludin were expressed in both CADASIL and control BMECs in all cell lines. The localization of the staining for occludin, and ZO-1 is different between CADASIL AGD-14-04 C10 and control line (arrow) (**Figure 6.15 B and C**).

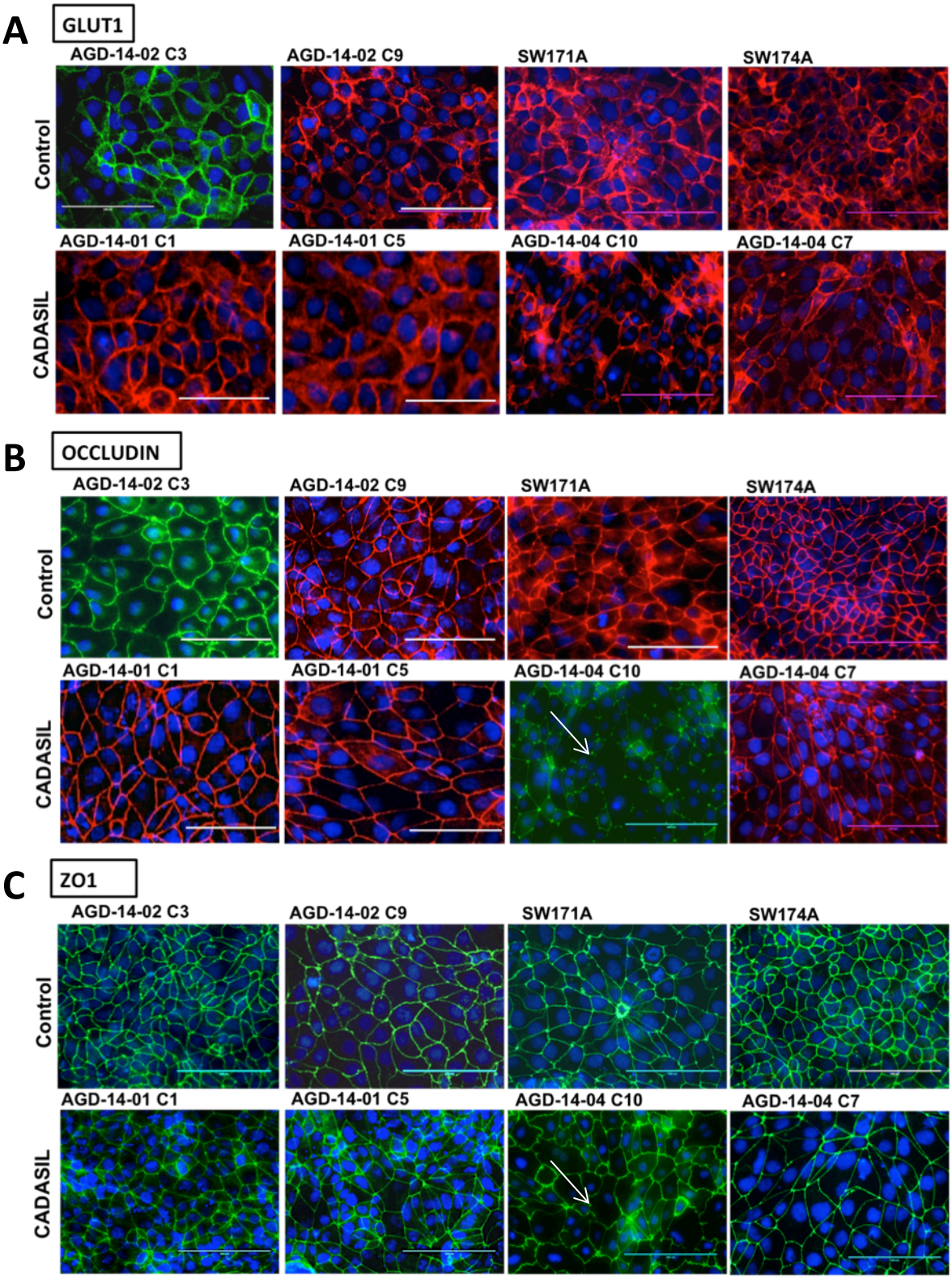
A
GLUT1
AGD-14-02 C3
AGD-14-02 C9
SW171A
SW174A
Control
AGD-14-01 C1
AGD-14-01 C5
AGD-14-04 C10
AGD-14-04 C7
CADASIL
B
OCCLUDIN
AGD-14-02 C3
AGD-14-02 C9
SW171A
SW174A
Control
AGD-14-01 C1
AGD-14-01 C5
AGD-14-04 C10
AGD-14-04 C7
CADASIL
C
ZO1
AGD-14-02 C3
AGD-14-02 C9
SW171A
SW174A
Control
AGD-14-01 C1
AGD-14-01 C5
AGD-14-04 C10
AGD-14-04 C7
CADASIL

Figure 6.15 Immunofluorescent staining of CADASIL and control iPSC-BMECs at day 10 of differentiation.

Control iPSC-BMECs (AGD-14-02 clones 3, 9, SW171A and SW174A) and CADASIL iPSC-BMECs (AGD-14-01 clones 1, 5 and AGD-14-04 clones 10, 7) were stained for GLUT1, occludin and ZO-1. DAPI (blue) as a counterstain. At day 10 of differentiation, N=4. Scale bars represent 100 μm.

6.2.5. CADASIL and control iPSC-BMECs display no difference in their ability to form endothelial-like tubes *in vitro*

Control and CADASIL iPSCs were differentiated to BMECs and characterised as described previously. CADASIL iPSC-BMECs AGD-14-04 C10 line and Control iPSC-BMECs AGD-14-02 C3 line were seeded on Matrigel coated culture plates to form endothelial-like tubular structures, monitored over 48 hours and network characteristics measured. Total network length, network branching points and mean mesh sizes were quantified with the 'Angiogenesis Analyser' function in ImageJ software and were compared between control and CADASIL iPSC-BMECs started to undergo tube formation within 6 hours of seeding. Complete tube network formation was observed within 18 hours and afterwards the total network length of both CADASIL and control iPSC-BMECs declined rapidly (**Figure 6.16 A**). However, control and CADASIL iPSC-BMECs exhibited no significant differences in network formation, stability and branching over the course of the angiogenesis assay at each time point (**Figure 6.16 B**).

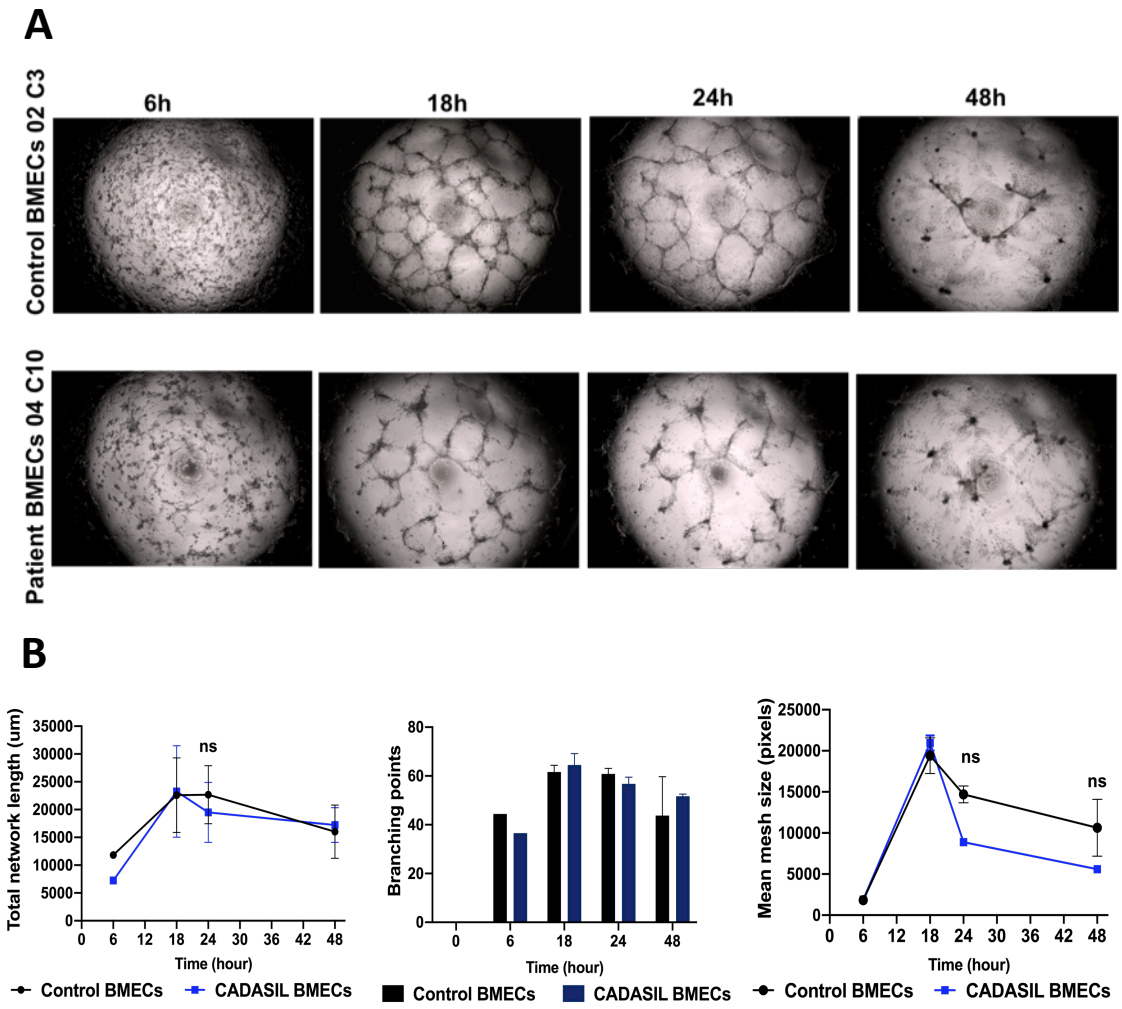

Figure 6.16 In vitro angiogenesis assay to assess endothelial-like tube formation of control and CADASIL iPSC-BMECs.

(A) Control-BMECs AGD-14-02 clone 3 and CADASIL-BMEC AGD-14-04 clone 10 were seeded in 96-wells plates pre-coated with Matrigel. Representative Images of iPSC-BMEC tube formation morphology at 6, 18, 24, 48 hours were captured after seeding. **(B)** Quantification of the total network length, branching points and mean mesh sizes over time for control AGD-14-02 clone 3 and CADASIL AGD-14-04 clone 10 iPSC-BMECs. Displayed is the mean ± SEM. n=2, 2 experimental repeats using 1 control and 1 CADASIL iPSC clones, 3 replicate wells for each experiment. Statistical significance was determined by one-way ANOVA.

6.2.6. *NOTCH3* siRNA knockdown in HCAECs

To further investigate whether impaired *NOTCH3* expression may diminish angiogenic potential siRNA was used to knockdown *NOTCH3* in HCAECs. HCAECs were treated with siRNA and a 50% decrease in *NOTCH3* expression was detected by qRT-PCR while HCAECs treated with scrambled siRNA showed no decrease in *NOTCH3* expression up to 48 hours after siRNA transfection (**Figure 6.17 B**). The expression of the EC specific marker *PECAM* in both *NOCTH3* siRNA and scrambled siRNA treated cells showed no change (**Figure 6.17 A**).

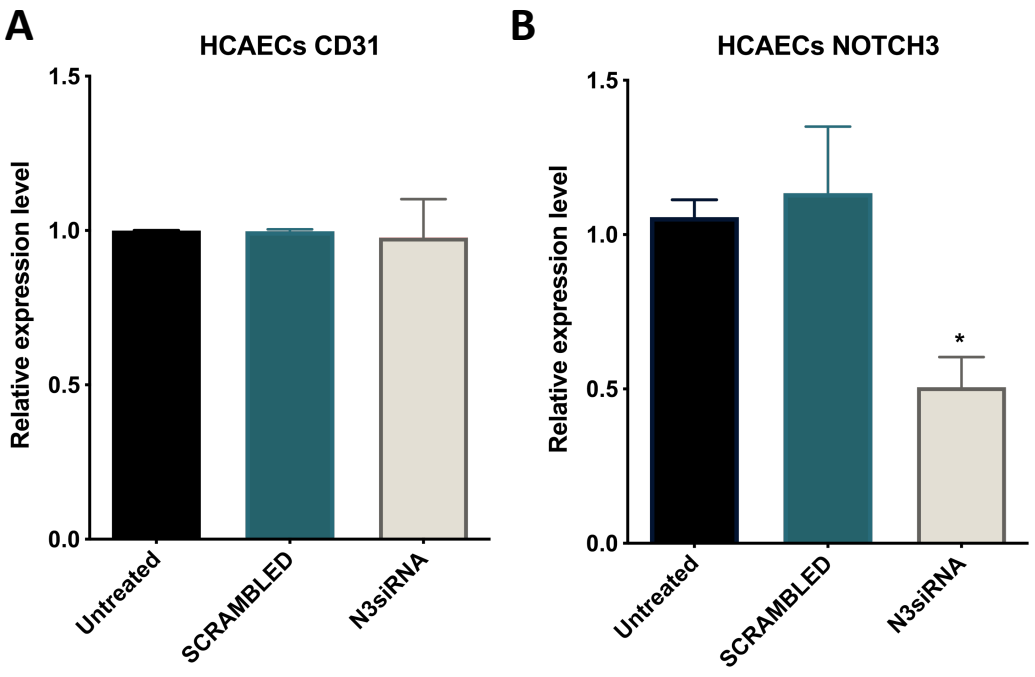

Figure 6.17 mRNA expression of *CD31* and *NOTCH3* after *NOTCH3* knockdown in HCAECs.

(A) Quantification of *CD31* and *NOTCH3* in untreated, scrambled and siRNA *NOTCH3* knockdown HCAECs. *GAPDH* was used as the endogenous control and data expressed relative to the untreated control. Data displayed as the mean ± SEM. n=3. One-way ANOVA analysis was performed to determine statistical significance. * P<0.05.

6.2.7. *NOTCH3* knockdown in control iPSC-BMECs may affect BMECs barrier function

In earlier sections of this Chapter, it was found that the barrier functions of the CADASIL iPSC-BMECs were significantly impaired as compared with the control iPSC-BMECs. CADASIL is caused by the *NOTCH3* mutation, but *NOTCH3* is not considered an important NOTCH receptor subtype in ECs as it is not highly expressed in this cell type. However, it is not known if NOTCH3 is functionally important for the barrier function of BMECs. To clarify this, *NOTCH3* was knocked down in the control iPSC-BMECs (AGD-14-02 C3) using siRNA. A significant decrease (70%) in *NOTCH3* expression was detected ($p<0.05$) following the siRNA treatment, control iPSC-BMECs (AGD-14-02 clone 3) were treated with siRNA and a significant 70% decrease in *NOTCH3* expression was detected ($p<0.05$) while control iPSC-BMECs treated with scrambled siRNA showed no decrease in *NOTCH3* expression up to 48 hours after siRNA transfection (**Figure 6.18 A**). The expression of the BMEC associated marker genes *PECAM* and *GLUT1*, *TJP-1* and *OCLN* were unaltered by *NOTCH3* knockdown. There may have been an increase in the expression of *CLDN5* but it was not statistically significant (**Figure 6.18 A**).

24 hours after siRNA transfection, iPSC-BMECs were seeded onto Transwell inserts and barrier function was assessed by TEER measurement. *NOTCH3* knockdown resulted in a significant reduction in TEER throughout the 96 hours of measurement in the *NOTCH3* knockout BMECs compared with scrambled siRNA treated iPSC-BMECs and the difference was maintained throughout the measurement ($p<0.0005$) (**Figure 6.18 B)**.

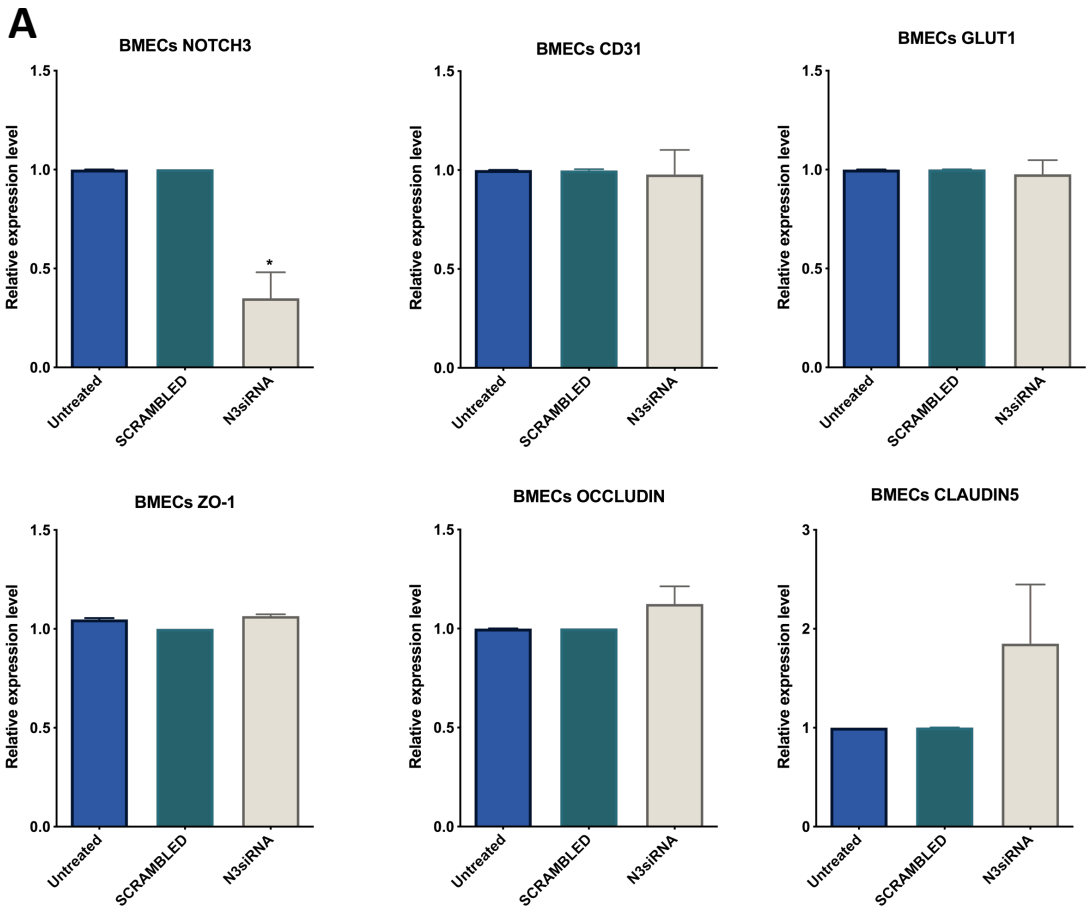
A
BMECs NOTCH3
BMECs CD31
BMECs GLUT1
BMECs ZO-1
BMECs OCCLUDIN
BMECs CLAUDIN5
Relative expression level
Untreated
SCRAMBLED
N3siRNA
*

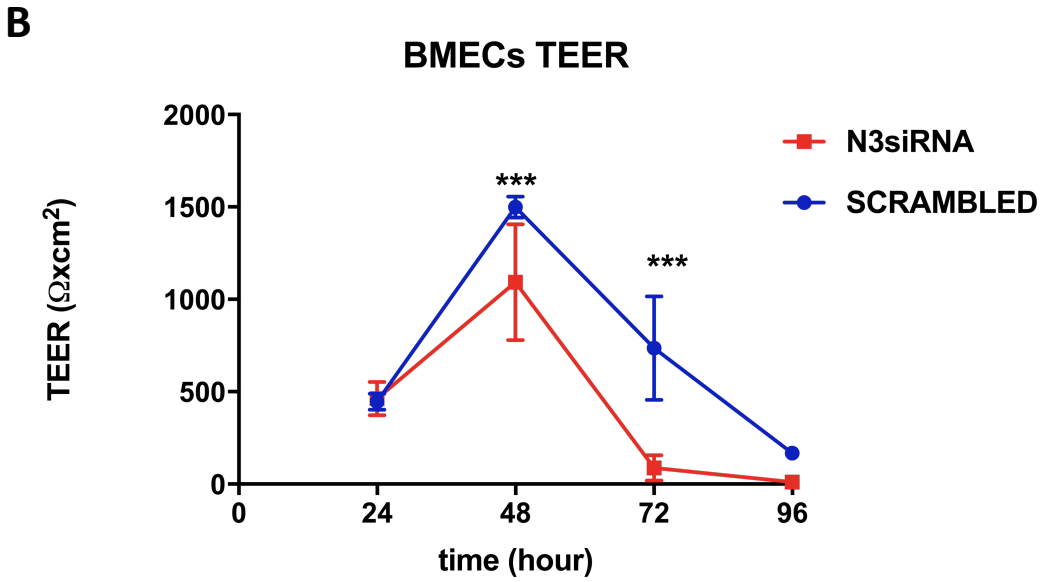
B
BMECs TEER
TEER (Ωxcm²)
time (hour)
N3siRNA
SCRAMBLED
***
***
0
500
1000
1500
2000
0
24
48
72
96

Figure 6.18 NOTCH3 knockdown in iPSC-BMECs may affect BMECs barrier function

(A) Expression of BMEC associated marker genes in untreated, scrambled and siRNA NOTCH3 knockdown BMECs. Gene expression was measured relative to GAPDH expression and normalised to non-treated control. Error bars represent the SEM. n=3, the plots are from 3 experimental repeats using one iPSC-BMEC line AGD-14-02 clone 3. One-way ANOVA analysis was performed to determine statistical significance. * $P<0.005$.

(B) TEER was measured for untreated, scrambled and siRNA NOTCH3 knockdown BMECs for 120 hours. Statistical significance was calculated using one-way ANOVA. The plot is the result of 3 biological replicates using one iPSC-BMEC line AGD-14-02 clone 3 with each daily TEER measurement. Values are reported as mean ± SEM of these collective measurements. *** $P<0.0005$.

6.3. Discussion

CADASIL is caused by *NOTCH3* mutation but the disease mechanisms are currently not fully understood. In previous chapters the differentiation of NVU cell types from iPSCs and the construction of an iPSC-BBB model were described. In this chapter the CADASIL and control BBB were compared based on this iPSC-BBB model.

6.3.1. CADASIL BMECs create BBB monolayers that exhibit poorer barrier properties than healthy BMECs

Previous studies into the molecular mechanisms underpinning CADASIL have focused on vMCs due to the prominent pathological changes observed in this cell type. However, abnormalities in EC function have also been observed in arteries of both CADASIL patients and CADASIL transgenic models of mice [87, 381]. It has been demonstrated that leaking and microbleeds were found in relatively thin-walled vessels in the cortex in CADASIL [382]. In fact, recent studies showed that not only vMCs (vSMCs and pericytes) are damaged in CADASIL, but also ECs, which could be another leading pathological change in CADASIL, makes the study of ECs as well as interaction between ECs and vMCs of vital importance in CADASIL [279, 383]. The iPSCs models on CADASIL recently published revealed new pathological changes in vMCs or in vMCs and ECs interactions in CADASIL [223, 240]. None of these studies were based on brain type ECs. CADASIL largely affects the cerebral vasculature, and the BBB function in CADASIL has yet to be investigated.

In this chapter barrier properties of CADASIL-derived BMEC monolayers and healthy iPSC-BMEC monolayers were compared. It was demonstrated for the first time that CADASIL derived iPSC-BMEC BBB possessed significantly lower TEER than the healthy iPSC-BMEC BBB and that co-culturing with vMCs, neurons and astrocytes could not increase the TEER as high as when co-cultured with healthy iPSC-BMECs (**Figure 6.1-6.6**). These results were further supported by sodium fluorescein permeability data of CADASIL BMECs, which was significantly higher than control BMECs, indicating a defect in the CADASIL BMECs barrier function (**Figure 6.8**). These data together indicate that CADASIL BMECs alone could have impaired barrier function and argue against the prevailing hypothesis that vMC defect is the primary driver of BBB dysfunction in CADASIL. This result of defect in CADASIL BMECs also has important implications for the pathologies of EC dysfunction in CADASIL, raising the hypothesis that BBB dysfunction in CADASIL may not only be affected by vMCs defect, but also be caused by

BMECs defect in itself. The future work can be focused on revealing whether the defect in BMECs leads to BBB damage.

6.3.2. CADASIL iPSC mural cells can impair the BBB properties of monolayers formed from healthy iPSC-BMECs

Studies have indicated that BBB damage may play a vital role in the pathogenesis of VaD. Current hypothetical mechanisms of BBB dysfunction in CADASIL indicate that MCs dysfunction in CADASIL might affect the interactions between NVU cells leading to the breakdown of junction proteins and BBB leakage. Previously it has been found that CADASIL iPSC-vMCs fail to promote the endothelial tube formation in iPSC-ECs and fail to stabilize vessel-like structures of iPSC-ECs *in vitro* [223], underlining the effects CADASIL may have on larger blood vessels. However, the effect CADASIL has on the brain microvasculature and the BBB has not been investigated.

In this chapter, it was demonstrated for the first time that CADASIL iPSC-vMCs failed to increase the TEER of control iPSC-BMEC monolayers compared with control iPSC-vMCs in the indirect co-culture Transwell settings (**Figure 6.9 and Figure 6.11)**. The direct co-culture experiments showed similar results though more repeats were needed to reach a conclusion (**Figure 6.10 and Figure 6.11,**). Sodium fluorescence permeability of control iPSC-BMECs co-culturing with CADASIL and control iPSC-vMCs confirmed the result by TEER, which also needs at least 2 more repeats (**Figure 6.12**). As line difference exists in BMECs differentiation among both control and CADASIL iPSC lines, the qRT-PCR results were displayed in separately lines rather than in average. It was not as expected to see a higher TEER of BMECs co-culture with CADASIL vMCs (EIPL1/ SOJD3 + 01 C1) compared with control MCs (02 C3/SW171A + 02 C3/02 C9) (**Figure 6.11)**, which is also caused by line difference during differentiation. As a result, the TEER comparison was made within the same experimental groups.

These results suggest that CADASIL vMCs may have detrimental effects on the barrier function of the BBB, while the underlying mechanisms are unknown. Also, more functional analysis comparison between control and CADASIL BMECs are needed in the future work such as efflux transporter activities measurement by the intracellular accumulation of rhodamine 123. Immunofluorescence staining of junction proteins on BMECs indicated abnormal expression of GLUT1 and ZO-1 following co-culturing with CADASIL vMCs compared to co-culturing with control BMECs (**Figure 6.13**). There's possibility that this

abnormality could be linked to the BBB dysfunction in CADASIL, which needs future work for further validation.

Impairment of the interactions between NVU cells leading to BBB damage has emerged to be an important feature in various neurodegenerative diseases. It is possible that *NOTCH3* mutation in CADASIL could cause similar pathological changes [384]. Current knowledge on *NOTCH3* research is still limited and more evidence of the impact of *NOTCH3* in vMCs on how it contributes to the integrity and function of the BBB is needed. For example, based on the disparities in the localization of tight junction proteins, the increased passive diffusion and decreased TEER in CADASIL derived BMEC monolayers, future studies should investigate whether the accumulation of mutant NOTCH3 extracellular domain protein interferes with the formation of tight junctions.

6.3.3. mRNA and protein expression did not show significant difference between CADASIL and control iPSC-BMECs

It has been reported that NOTCH3 is highly expressed in small arterial vSMCs and brain capillary pericytes where CADASIL presents, cells that are enriched with NOTCH3 receptors, compared with ECs and astrocytes [27, 385, 386]. One study on vSMCs differentiated from CADASIL iPSCs showed gene expression changes including activation of the NOTCH and NF-κB signaling pathway, which are associated with disease phenotypes. In comparison, these abnormalities were not observed in vECs derived from the patient's iPSCs [387]. But the ECs been used in the mentioned models are not brain microvessel ECs and fail to show barrier property, as we have demonstrated in chapter 5.

This model is the first to build iPSC-BBB models for CADASIL based on BMECs and the first to show defect barrier function in CADASIL BMECs. In order to reveal the mechanisms of BMECs defect in CADASIL that was observed in this research, in this chapter it was demonstrated that CADASIL and control iPSC-BMECs display no difference in angiogenic potential *in vitro* (**Figure 6.16.**), a result that is consistent with current findings on CADASIL iPSC-vECs [223]. mRNA expression of tight junction genes showed no significant difference between control and CADASIL iPSC-BMECs (**Figure 6.14.**). In one experiment *NOTCH3* mRNA expression was significantly decreased in CADASIL iPSC-BMECs but more repeats are needed to confirm (**Figure 6.14. E**). It is possible that NOTCH3 mutation may lead to CADASIL BMECs dysfunction but needs further confirmation. To conclude whether difference on tight junctions and NOTCH3 expression

exists between CADASIL and control iPSC-BMECs, future work can be applied to use more repeats of qRT-PCR on various clones and protein expression between CADASIL and control should also be stressed via western blotting.

6.4. Summary

In this chapter, barrier function between CADASIL and control iPSC-BMECs was compared. The data confirmed for the first time and provide strong evidence that defect in BMECs barrier function exists in CADASIL. Then barrier function between CADASIL and control vMCs co-culture with BMECs was compared and it was found that CADASIL MCs could damage the barrier function of control BMECs. These results indicate that BBB dysfunction exists in CADASIL and could be caused by BMEC dysfunction in its own and MCs dysfunction, which disrupts interaction with BMECs. Moreover, preliminary result that NOTCH3 mutation may affect BMECs barrier function provides new insights into CADASIL pathology. The role of NOTCH3 in BMECs requires further investigation.

7. Chapter 7: General discussion

7.1. The importance of developing an iPSC-derived NVU model for CADASIL

IPSCs can be differentiated into cells that constitute the NVU to model cerebral SVD, for example, CADASIL. This thesis demonstrated the development of the first iPSC-derived model of neurovascular interactions for genetic stroke CADASIL. Such a model can overcome the drawbacks of transgenic mice models that cannot fully recapitulate the disease pathologies which observed in CADASIL patients [388]. Due to species differences between humans and animals, animal models may not always demonstrate disease pathology especially the brain pathologies for SVD, particularly they do not always undergo spontaneous stroke [389]. Previous cell models for CADASIL have built based on non-NVU cell lines mostly HEK cells, which rely on overexpression of mutant NOTCH3 [390]. As the strategy of overexpression creates more than two fold change of Notch3 expression in CADASIL while Notch signalling is highly dosage dependent, these overexpression cell models may not reliably reflect the NVU pathological changes in CADASIL patients [391].

VaD has been associated with BBB dysfunction [356]. BBB is composed of NVU cell types includes vascular cells and neuronal/glia cells. CADASIL patients showed degeneration and loss of vSMCs in the brain [392], abnormal NOTCH3 accumulation and ECs dysfunction [38, 393, 394]. Previous studies have investigated the relationship between NOTCH3 and vSMC dysfunction [385], but the mechanism underlying these changes and how they result in EC dysfunction are poorly understood. Currently a few iPSC models were built for CADASIL [225, 240, 391], however, none of the current iPSC-derived CADASIL models were based on NVU cell types apart from ECs and MCs. Moreover, the ECs being investigated for CADASIL pathologies in previous studies were peripheral rather than brain microvascular ECs, which may not be able to faithfully recapitulate the brain pathologies in CADASIL [223]. Among iPSC-BBB models for other CNS disorders, pericytes are the least studied of the cellular components of the BBB despite their tight association with BMECs and important functions in the NVU [357].

While cell models and animal models have disadvantages to faithfully recapitulate CADASIL pathologies and human NVU cells are difficult to be isolated from the brain, iPSCs provide the possibility to investigate disease mechanisms using autologous cells with genetic background of the patient. Evidence was found that defects in BBB integrity might exist in CADASIL. However, most of the studies mainly revealed vMCs deficiency in CADASIL,

which left other NVU cell types in BBB dysfunction largely un-investigated. Collectively, these have prompted the need for other considerations in disease modelling. This thesis has addressed these considerations by investigating the NVU interactions and BBB barrier properties in iPSC-derived NVU model composed of vMC, BMECs, astrocytes and neurons in CADASIL. The iPSCs that sourced from CADASIL patient carrying the already known CADASIL *NOTCH3* mutation that have equal levels of expression in NOTCH3. The data has demonstrated important roles of NVU interaction in BBB barrier function and also revealed new insights into BBB defect in CADASIL.

7.2. IPSCs differentiation into vascular cell types

In this thesis, chapter 5 demonstrated the development of an *in vitro* model of neurovascular interactions. Building such a model relied on the differentiation of NVU cell types from iPSCs based on published protocols or already established protocols in our lab. The differentiation of vascular cells including BMECs and MCs were described in chapter 3. Attempt to replicate one of the most frequently cited protocols for iPSC-BMECs differentiation was successful, yielding quickly generated and highly reproducible BMECs with expression of junction proteins. The main optimisation was on the seeding cell number at starting of differentiation, which highlights the variations between different lineages of iPSCs. To address this issue a refined BMEC differentiation protocol was published recently through the replacement of serum with more defined supplements [395]. This advancement could minimize procedural variability, providing more reliable and robust iPSC-derived BMECs and could be applied for future CADASIL NVU disease modelling.

The vMCs differentiation was followed by a well-established protocol, which was refined by Kelleher et al. based on the manuscript by Cheung et al. [216, 223]. The original protocol described the cells differentiated as vSMCs, however Kelleher et al. found that these cells express both vSMCs markers and pericytes including NG2, α-SMA and CNN1 [223]. As current knowledge on defining pericytes behaviour with vSMCs is still controversial and by surface markers alone could not be able to distinguish the two cell populations [396], the cells differentiated was referred to as vMCs to reflect the heterogeneity of the cell populations [223]. Though pericytes are vital for NVU function, there had been few protocols for iPSC-pericytes differentiation until very recently, publications have reported methods for pericyte-like cells differentiation from iPSCs [334, 335]. For example, Stebbins et al. generated NCSCs (the embryonic precursor to forebrain pericytes) from iPSCs and differentiated

NCSCs to brain pericyte–like cells that could yield cells expressing pericytes markers NG2 and PDGFRβ rather than vSMCs marker α-SMA [334]. However, as these cells still sustained express the contractile-related proteins CNN1 and SM22α [334], which were recoded should not be expressed in brain pericytes [330], it is difficult to confirm these cells are definitely pericytes. In summary, future work for our model is required to characterise the differentiated population in a proper way to sort the population into vPCs and vSMCs.

7.3. IPSCs differentiation into astrocytes and neurons

Differentiation of astrocytes and neurons from iPSCs were demonstrated in chapter 4. As differentiation of astrocytes is not well defined and there are a limited number of protocols that differentiate iPSCs into certain sub-types of astrocytes [397], attempts to replicate and refine some of the published differentiation protocols were demonstrated with limit success in some of them. These differentiation processes rely on the generation of NPCs, like most of other astrocytes differentiation protocols. This process can be promoted only after the occurrence of gliogenesis during NPCs differentiating into neurons [398]. Successfully differentiation of astrocytes was achieved via the protocol from StemCell Technologies with the commercially available medium. Though this protocol could generate abundant astrocytes with functional abilities and thus was chosen for building the NVU model, drawback exists including the medium is costly and proprietary without known of detailed factors inside the medium. One of the optimisation protocols showed great promising in quick generation of astrocytes through SMAD signalling inhibition and TGF-β1 method. However the optimisation takes a long time and has not finished. Future work should be addressed on functional analysis of these astrocytes such as calcium imaging, glutamate uptake and promotion of neuronal synaptogenesis to finish the optimisation of this protocol.

Neurons differentiation from iPSCs was followed by a well-defined, already established protocol [291]. The data demonstrates the successful generation of neurons from iPSCs. As this thesis is focused mainly on barrier function of CADASIL BBB and BMECs are the main cell type for barrier function, neurons were not investigated into details and only control neurons were differentiated from iPSCs to build the model. CADASIL are young and mid-aged onset and natural history of CADASIL shows migraine can happen at very young age (20 years age) [39], indicating that dysfunction in CADASIL neurons may exist. Future direction on iPSC-CADASIL model can be addressed on investigating the potential neuronal defect in CADASIL. Instead of day 80 neurons that were applied in this iPSC-NVU model,

earlier neurons after day 35 could be used to investigate the early onset of migraine in CADASIL pathologies.

7.4. Development of an iPSC-BBB model for neurovascular interaction

In chapter 5, the development of an *in vitro* BBB model with iPSC-derived NVU cell types was described. It was demonstrated that iPSC-derived vMCs, astrocytes and neurons could be co-cultured with iPSC-derived BMECs to form a completely human iPSC-derived BBB model consists of four key NVU cell types. Most of current BBB models are based on cells of the NVU from different species and the isolations of each cell type are using tissue from differently aged animals with distinct protocols [399-401]. BBB modelling using animal sourced cells have limitations include the differences between the human BBB and the BBB in other species [402]. Moreover, many of the immortalized brain endothelial cell lines fail to form tight barriers [402]. These drawbacks result in the cells isolated may not be able to fully recapitulate the human BBB especially the disease BBB. Moreover, while the differentiation of each single cell type of NVU has been reported, no BBB model incorporating all of iPSC-derived BMECs, vMCs, astrocytes and neurons has yet been reported [403, 404]. Thus, using iPSC tools to differentiate all BBB cell types from the same human source with identical genetic background can provide a useful tool for BBB disease modelling.

The major phenotypic change after co-culture was the increased barrier function measured through TEER and passive permeability [360]. Importantly, the BMECs demonstrated barrier function and co-culturing with other NVU cell types help increase the barrier ability. Such increase was first confirmed in barrier tightness in co-cultured rat BMECs [360]. Interestingly, the data in chapter 5 shows that BMECs co-culturing with iPSC-astrocytes yielded enhanced barrier function compared to co-culture with iPSC-neurons, which is consistent with previous reports of BBB models with immortalized rat cells co-culture with rat primary astrocytes and neurons, which indicates that astrocyte co-cultures were more inductive of BMEC barrier properties than neuronal co-cultures [405].

In chapter 5 we demonstrated for the first time a triple-culture iPSC-BBB model with vMCs seeded on the apical side of the Transwell to mimic the direct contact of NVU cells *in vitro.* Previous BBB models usually build up triple-culture by co-culture a mixture of neurons and astrocytes together in non-direct contact co-culture with BMECs [350, 360]. While such models cannot faithfully reproduce the direct contact between NVU cells, our iPSC-BBB models allow the direct interaction between vMCs and BMECs for cell-cell communications.

Future attempt could be on more combinations of direct co-culture between NVU cell including astrocytes and BMECs and astrocytes and neurons.

7.5. BBB dysfunction in CADASIL

Based on this iPSC-BBB model, we observed for the first time that the CADASIL iPSC-BMECs showed lower barrier function than that of control iPSC-BMECs as measured by TEER and permeability. This result confirms the abnormalities observed in EC function in arteries of both CADASIL patients and CADASIL transgenic models of mice [87, 381]. The co-culture experiment further indicated that co-culture with NVU cells failed to rescue the CADASIL iPSC-BMECs barrier function. Gene expression profiles did not show significant abnormalities in the expression of tight junction genes, and immune-staining of these proteins showed possible difference in the integrity of the junction between the CADASIL and control iPSC-BMECs as well. However, a limitation of our research is that the immune-staining images were not taken by high-resolution microscopies, for example confocal, which makes it difficult to determine the tight junction continuity between CADASIL and control BMECs. Previous studies on iPSC-BBB models revealed that, tight junction continuity and not protein levels are likely responsible for the observed barrier induction upon co-culture [360]. It can be hypothesised that tight junction continuity might be altered in CADASIL BMECs and could be confirmed by future work in high resolution confocal microscopy comparisons for the immune-staining of junction proteins between CADASIL and patient.

It was also observed CADASIL iPSC-vMCs failed to support the control iPSC-BMECs barrier function. Previously it has been reported that CADASIL iPSC-vMCs fail to promote the endothelial tube formation by iPSC-ECs and fail to stabilize vessel-like structures of iPSC-ECs *in vitro* [223]. Our result is consistent with the previous finding. This defect could be caused by CADASIL vMCs releasing detrimental factors that breakdown the junction protein in BMECs leading to barrier function defect as it happened in both direct and indirect co-culture of vMCs with BMECs. Future direction for this work can be addressed on a protein transciptomic study using the concentrated co-culture medium to screen for candidate genes potentially responsible for the defect.

7.6. NOTCH3 mutation in CADASIL

Previous studies on iPSC-derived AD model has found that mutations in one of the causative genes for early onset Alzheimer's disease, *PSEN1* rather than *PSEN2*, could impair the development and the maintenance of the iPSC-BMECs, both by an impairment of the barrier function, vesicle trafficking and bioenergetics [406]. Such findings lead us to consider similar mechanisms the observed barrier defect in our CADASIL iPSC-BMECs. In chapter 6 we demonstrated *NOTCH3* is successfully knockdown in control BMECs and lead to decreased TEER in BMECs. This preliminary data indicates the BMECs barrier function defect could be linked with *NOTCH3* mutation.

Previous research has mostly focused on the pathology of vSMCs, which express NOTCH3, in CADASIL [223]. However, there is evidence that *NOTCH3* is also expressed in ECs and glial cells, which have so far not been investigated in detail in CADASIL. RNA-seq data from public database for *NOTCH3* gene expression in the human brain demonstrated higher level in purified human ECs compared with astrocytes, and neurons, which indicate *NOTCH3* mutations may potentially affect function of these cells in the disease brain (**Figure 7.1**) [407]. Besides, it is interesting to observe the expression of *Notch3/NOTCH3* shows obvious difference expression between mouse and human brain, which provide evidence on the gene level that mouse model for CADASIL could not faithfully mimic the disease pathology.

Thus, the iPSCs generated in this study can be differentiated to both CADASIL and control cell types of NVU in the future to determine alteration in these cell behaviours, which will shed light on how the *NOTCH3* mutation alter CADASIL NVU biology.

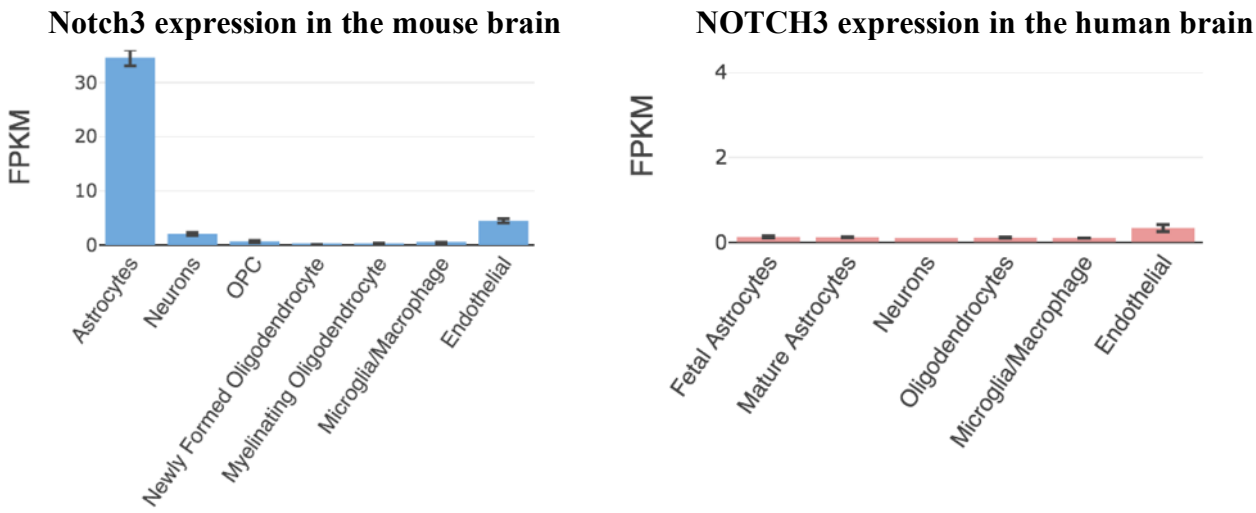

Figure 7.1 *Notch3/NOTCH3* expressions in the mouse/human brain.

Notch3/NOTCH3 RNA expression in immunopanned purified mice (left) and human (right) cells from the Barres lab database. Data are expressed as FPKM. (https://www.brainrnaseq.org/)

7.7. Conclusions

CADASIL is the most common cerebral SVD, with the pathologies of degeneration and loss of vSMCs in the brain, abnormal *NOTCH3* accumulation and endothelial cell dysfunction. Previous studies have investigated the interaction between *NOTCH3* and vSMC dysfunction, but the mechanism underlying these changes and how EC dysfunction happens are poorly understood. The symptom of migraine that is young age onset indicates defects in neuronal cell may exist apart from vascular cells that most of current studies have been focused on. It is of great importance to develop a CADASIL BBB model to investigate the neurovascular interactions in CADASIL.

Human *in vitro* BBB models using iPSCs derived from CADASIL patients are required, as current animal and cell models cannot faithfully simulate the CADASIL phenotype due to species differences. Current iPSC-CADASIL BBB models were all based on iPSC-derived vMCs and vECs without other BBB cell types, despite astrocytes and neurons may also paly vital role in BBB defect contributing to CADASIL pathologies. Besides, the vECs involved in these models are not brain microvascular ECs that exhibit BBB properties. It is of great importance to build a BBB model using NVU cells derived from patient iPSCs.

This thesis has demonstrated the development of an *in vitro* iPSC-derived NVU model of neurovascular interactions that can mimic BBB in CADASIL. To build the model, NVU cells including vMCs, BMECs, astrocytes and neurons were differentiated from CADASIL and control iPSCs. All these cell types were then co-cultured in a Transwell to mimic neurovascular interactions and functional analysis was performed. Using this model, we have identified barrier function defect in CADASIL BMECs that could not be rescued by co-culture with other NVU cells. Moreover we showed CADASIL vMCs failed to support BMECs barrier function. The defect may have relations with NOTCH3 mutation in CADASIL.

The nature of the BBB barrier functions makes the model adaptable to high throughput screening of chemicals, drugs and therapies to identify molecules that can rescue the disease phenotype. This model could be applied to identify specific treatments for CADASIL, as well as identifying key pathways in disease pathogenesis in help understanding genetic stroke, which may have implications for the prevention and find therapies for ischemic stroke and other SVDs or neurodegenerative diseases more generally.

References

1. McKhann, G.M., et al., *The diagnosis of dementia due to Alzheimer's disease: Recommendations from the National Institute on Aging-Alzheimer's Association workgroups on diagnostic guidelines for Alzheimer's disease.* Alzheimer's & Dementia, 2011. **7**(3): p. 263-269.
2. Organization, W.H., *Dementia: a public health priority*. 2012: World Health Organization.
3. Skoog, I., et al., *15-year longitudinal study of blood pressure and dementia.* The Lancet, 1996. **347**(9009): p. 1141-1145.
4. Luchsinger, J.A. and R. Mayeux, *Cardiovascular risk factors and Alzheimer's disease.* Current atherosclerosis reports, 2004. **6**(4): p. 261-266.
5. *2018 Alzheimer's disease facts and figures.* Alzheimer's & Dementia, 2018. **14**(3): p. 367-429.
6. Schneider, J.A., et al., *Mixed brain pathologies account for most dementia cases in community-dwelling older persons.* Neurology, 2007. **69**(24): p. 2197-204.
7. Schneider, J.A., et al., *The neuropathology of probable Alzheimer disease and mild cognitive impairment.* Ann Neurol, 2009. **66**(2): p. 200-8.
8. Ferri, C.P., et al., *Global prevalence of dementia: a Delphi consensus study.* The lancet, 2006. **366**(9503): p. 2112-2117.
9. Ueda, K., et al., *Prevalence and etiology of dementia in a Japanese community.* Stroke, 1992. **23**(6): p. 798-803.
10. Gorelick, P.B., et al., *Vascular contributions to cognitive impairment and dementia: a statement for healthcare professionals from the American Heart Association/American Stroke Association.* Stroke, 2011. **42**(9): p. 2672-2713.
11. Román, G.C., *Vascular dementia: distinguishing characteristics, treatment, and prevention.* Journal of the American Geriatrics Society, 2003. **51**(5s2): p. S296-S304.
12. Duron, E. and O. Hanon, *Vascular risk factors, cognitive decline, and dementia.* Vascular health and risk management, 2008. **4**(2): p. 363-381.
13. Justin, B.N., M. Turek, and A.M. Hakim, *Heart disease as a risk factor for dementia.* Clinical epidemiology, 2013. **5**: p. 135-145.
14. Souza, D., et al., *Association of apolipoprotein E polymorphism in late-onset Alzheimer's disease and vascular dementia in Brazilians.* Brazilian journal of medical and biological research, 2003. **36**(7): p. 919-923.
15. Folin, M., et al., *Apolipoprotein E as vascular risk factor in neurodegenerative dementia.* International journal of molecular medicine, 2004. **14**: p. 609-614.
16. Vijayan, M. and P.H. Reddy, *Stroke, Vascular Dementia, and Alzheimer's Disease: Molecular Links.* Journal of Alzheimer's disease : JAD, 2016. **54**(2): p. 427-443.
17. Sudlow, C.L. and C.P. Warlow, *Comparable studies of the incidence of stroke and its pathological types: results from an international collaboration. International Stroke Incidence Collaboration.* Stroke, 1997. **28**(3): p. 491-9.
18. Gorelick, P.B., et al., *Vascular contributions to cognitive impairment and dementia: a statement for healthcare professionals from the american heart association/american stroke association.* Stroke, 2011. **42**(9): p. 2672-713.
19. Li, Q., et al., *Cerebral Small Vessel Disease.* Cell transplantation, 2018. **27**(12): p. 1711-1722.
20. Pantoni, L., *Cerebral small vessel disease: from pathogenesis and clinical characteristics to therapeutic challenges.* The Lancet Neurology, 2010. **9**(7): p. 689-701.
21. Charidimou, A., L. Pantoni, and S. Love, *The concept of sporadic cerebral small vessel disease: A road map on key definitions and current concepts.* Int J Stroke, 2016. **11**(1): p. 6-18.
22. Tan, R., et al., *New insights into mechanisms of small vessel disease stroke from genetics.* Clin Sci (Lond), 2017. **131**(7): p. 515-531.
23. Choi, J.C., *Genetics of cerebral small vessel disease.* Journal of stroke, 2015. **17**(1): p. 7-16.

24. Kubo, M., et al., *A nonsynonymous SNP in PRKCH (protein kinase C η) increases the risk of cerebral infarction.* Nature Genetics, 2007. **39**(2): p. 212-217.
25. Fornage, M., et al., *Genome-wide association studies of cerebral white matter lesion burden.* Annals of Neurology, 2011. **69**(6): p. 928-939.
26. Woo, D., et al., *Meta-analysis of genome-wide association studies identifies 1q22 as a susceptibility locus for intracerebral hemorrhage.* Am J Hum Genet, 2014. **94**(4): p. 511-21.
27. Joutel, A., et al., *Notch3 mutations in CADASIL, a hereditary adult-onset condition causing stroke and dementia.* Nature, 1996. **383**(6602): p. 707-10.
28. Choi, J.C., *Cerebral autosomal dominant arteriopathy with subcortical infarcts and leukoencephalopathy: a genetic cause of cerebral small vessel disease.* J Clin Neurol, 2010. **6**(1): p. 1-9.
29. Chabriat, H., et al., *Clinical spectrum of CADASIL: a study of 7 families. Cerebral autosomal dominant arteriopathy with subcortical infarcts and leukoencephalopathy.* Lancet, 1995. **346**(8980): p. 934-9.
30. Nozaki, H., M. Nishizawa, and O. Onodera, *Features of cerebral autosomal recessive arteriopathy with subcortical infarcts and leukoencephalopathy.* Stroke, 2014. **45**(11): p. 3447-53.
31. Hara, K., et al., *Association of HTRA1 mutations and familial ischemic cerebral small-vessel disease.* N Engl J Med, 2009. **360**(17): p. 1729-39.
32. Gould, D.B., et al., *Role of COL4A1 in small-vessel disease and hemorrhagic stroke.* N Engl J Med, 2006. **354**(14): p. 1489-96.
33. Richards, A., et al., *C-terminal truncations in human 3'-5' DNA exonuclease TREX1 cause autosomal dominant retinal vasculopathy with cerebral leukodystrophy.* Nat Genet, 2007. **39**(9): p. 1068-70.
34. Jen, J., et al., *Hereditary endotheliopathy with retinopathy, nephropathy, and stroke (HERNS).* Neurology, 1997. **49**(5): p. 1322-30.
35. Di Donato, I., et al., *Cerebral Autosomal Dominant Arteriopathy with Subcortical Infarcts and Leukoencephalopathy (CADASIL) as a model of small vessel disease: update on clinical, diagnostic, and management aspects.* BMC Medicine, 2017. **15**(1): p. 41.
36. Dunn, P.J., et al., *Investigating diagnostic sequencing techniques for CADASIL diagnosis.* Human genomics, 2020. **14**(1): p. 2-2.
37. Ishiko, A., et al., *Notch3 ectodomain is a major component of granular osmiophilic material (GOM) in CADASIL.* Acta Neuropathol, 2006. **112**(3): p. 333-9.
38. Joutel, A., et al., *The ectodomain of the Notch3 receptor accumulates within the cerebrovasculature of CADASIL patients.* J Clin Invest, 2000. **105**(5): p. 597-605.
39. Chabriat, H., et al., *Cadasil.* Lancet Neurol, 2009. **8**(7): p. 643-53.
40. Ruchoux, M.-M. and C.-A. Maurage, *CADASIL: cerebral autosomal dominant arteriopathy with subcortical infarcts and leukoencephalopathy.* Journal of Neuropathology & Experimental Neurology, 1997. **56**(9): p. 947-964.
41. Ihalainen, S., et al., *Proteome analysis of cultivated vascular smooth muscle cells from a CADASIL patient.* Mol Med, 2007. **13**(5-6): p. 305-14.
42. Takahashi, K., et al., *Mutations in NOTCH3 cause the formation and retention of aggregates in the endoplasmic reticulum, leading to impaired cell proliferation.* Hum Mol Genet, 2010. **19**(1): p. 79-89.
43. Fiúza, U.M. and A.M. Arias, *Cell and molecular biology of Notch.* J Endocrinol, 2007. **194**(3): p. 459-74.
44. Wharton, K.A., et al., *Nucleotide sequence from the neurogenic locus notch implies a gene product that shares homology with proteins containing EGF-like repeats.* Cell, 1985. **43**(3 Pt 2): p. 567-81.

45. Yochem, J., K. Weston, and I. Greenwald, *The Caenorhabditis elegans lin-12 gene encodes a transmembrane protein with overall similarity to Drosophila Notch.* Nature, 1988. **335**(6190): p. 547-550.
46. Cordle, J., et al., *Localization of the delta-like-1-binding site in human Notch-1 and its modulation by calcium affinity.* J Biol Chem, 2008. **283**(17): p. 11785-93.
47. Mumm, J.S., et al., *A ligand-induced extracellular cleavage regulates gamma-secretase-like proteolytic activation of Notch1.* Mol Cell, 2000. **5**(2): p. 197-206.
48. Sanchez-Irizarry, C., et al., *Notch subunit heterodimerization and prevention of ligand-independent proteolytic activation depend, respectively, on a novel domain and the LNR repeats.* Molecular and cellular biology, 2004. **24**(21): p. 9265-9273.
49. Struhl, G. and A. Adachi, *Nuclear access and action of notch in vivo.* Cell, 1998. **93**(4): p. 649-660.
50. Schroeter, E.H., J.A. Kisslinger, and R. Kopan, *Notch-1 signalling requires ligand-induced proteolytic release of intracellular domain.* Nature, 1998. **393**(6683): p. 382-386.
51. Lecourtois, M. and F. Schweisguth, *Indirect evidence for Delta-dependent intracellular processing of notch in Drosophila embryos.* Current Biology, 1998. **8**(13): p. 771-775.
52. Kopan, R. and M.X.G. Ilagan, *The canonical Notch signaling pathway: unfolding the activation mechanism.* Cell, 2009. **137**(2): p. 216-233.
53. van Tetering, G., et al., *Metalloprotease ADAM10 is required for Notch1 site 2 cleavage.* The Journal of biological chemistry, 2009. **284**(45): p. 31018-31027.
54. Wang, T., M. Baron, and D. Trump, *An overview of Notch3 function in vascular smooth muscle cells.* Progress in Biophysics and Molecular Biology, 2008. **96**(1): p. 499-509.
55. Monet-Leprêtre, M., et al., *Distinct phenotypic and functional features of CADASIL mutations in the Notch3 ligand binding domain.* Brain, 2009. **132**(6): p. 1601-1612.
56. Le Borgne, R., A. Bardin, and F. Schweisguth, *The roles of receptor and ligand endocytosis in regulating Notch signaling.* Development, 2005. **132**(8): p. 1751-1762.
57. Roca, C. and R.H. Adams, *Regulation of vascular morphogenesis by Notch signaling.* Genes & development, 2007. **21**(20): p. 2511-2524.
58. Jain, R.K., *Molecular regulation of vessel maturation.* Nature medicine, 2003. **9**(6): p. 685-693.
59. Fouillade, C., et al., *Notch signalling in smooth muscle cells during development and disease.* Cardiovascular Research, 2012. **95**(2): p. 138-146.
60. Huppert, S.S., et al., *Embryonic lethality in mice homozygous for a processing-deficient allele of Notch1.* Nature, 2000. **405**(6789): p. 966-970.
61. Krebs, L.T., et al., *Notch signaling is essential for vascular morphogenesis in mice.* Genes Dev, 2000. **14**(11): p. 1343-52.
62. Limbourg Florian, P., et al., *Essential Role of Endothelial Notch1 in Angiogenesis.* Circulation, 2005. **111**(14): p. 1826-1832.
63. Domenga, V., et al., *Notch3 is required for arterial identity and maturation of vascular smooth muscle cells.* Genes Dev, 2004. **18**(22): p. 2730-5.
64. Liu, H., S. Kennard, and B. Lilly, *NOTCH3 expression is induced in mural cells through an autoregulatory loop that requires endothelial-expressed JAGGED1.* Circulation research, 2009. **104**(4): p. 466-475.
65. Carmeliet, P., *Angiogenesis in health and disease.* Nature medicine, 2003. **9**(6): p. 653-660.
66. Gridley, T., *Chapter Nine - Notch Signaling in the Vasculature*, in *Current Topics in Developmental Biology*, R. Kopan, Editor. 2010, Academic Press. p. 277-309.
67. Byrne, A.M., D.J. Bouchier-Hayes, and J.H. Harmey, *Angiogenic and cell survival functions of vascular endothelial growth factor (VEGF).* J Cell Mol Med, 2005. **9**(4): p. 777-94.
68. Jakobsson, L., et al., *Endothelial cells dynamically compete for the tip cell position during angiogenic sprouting.* Nat Cell Biol, 2010. **12**(10): p. 943-53.

69. Tung, J.J., I.W. Tattersall, and J. Kitajewski, *Tips, stalks, tubes: notch-mediated cell fate determination and mechanisms of tubulogenesis during angiogenesis.* Cold Spring Harbor perspectives in medicine, 2012. **2**(2): p. a006601-a006601.
70. Liu, Z.-J., et al., *Regulation of Notch1 and Dll4 by vascular endothelial growth factor in arterial endothelial cells: implications for modulating arteriogenesis and angiogenesis.* Molecular and cellular biology, 2003. **23**(1): p. 14-25.
71. Lawson, N.D., A.M. Vogel, and B.M. Weinstein, *sonic hedgehog and vascular endothelial growth factor act upstream of the Notch pathway during arterial endothelial differentiation.* Dev Cell, 2002. **3**(1): p. 127-36.
72. Jan, Y.N. and L.Y. Jan, *Genetic control of cell fate specification in Drosophila peripheral nervous system.* Annual review of genetics, 1994. **28**(1): p. 373-393.
73. Poulson, D.F., *Chromosomal Deficiencies and the Embryonic Development of Drosophila Melanogaster.* Proceedings of the National Academy of Sciences of the United States of America, 1937. **23**(3): p. 133-137.
74. Louvi, A. and S. Artavanis-Tsakonas, *Notch signalling in vertebrate neural development.* Nature Reviews Neuroscience, 2006. **7**(2): p. 93-102.
75. Ables, J.L., et al., *Not(ch) just development: Notch signalling in the adult brain.* Nature reviews. Neuroscience, 2011. **12**(5): p. 269-283.
76. Hitoshi, S., et al., *Notch pathway molecules are essential for the maintenance, but not the generation, of mammalian neural stem cells.* Genes & development, 2002. **16**(7): p. 846-858.
77. Ohtsuka, T., et al., *Hes1 and Hes5 as notch effectors in mammalian neuronal differentiation.* The EMBO journal, 1999. **18**(8): p. 2196-2207.
78. Woo, S.-M., et al., *Notch signaling is required for maintaining stem-cell features of neuroprogenitor cells derived from human embryonic stem cells.* BMC neuroscience, 2009. **10**: p. 97-97.
79. Woo, H.-N., et al., *Alzheimer's disease and Notch signaling.* Biochemical and Biophysical Research Communications, 2009. **390**(4): p. 1093-1097.
80. Joutel, A., et al., *Pathogenic mutations associated with cerebral autosomal dominant arteriopathy with subcortical infarcts and leukoencephalopathy differently affect Jagged1 binding and Notch3 activity via the RBP/JK signaling Pathway.* American journal of human genetics, 2004. **74**(2): p. 338-347.
81. Peters, N., et al., *CADASIL-associated Notch3 mutations have differential effects both on ligand binding and ligand-induced Notch3 receptor signaling through RBP-Jk.* Experimental Cell Research, 2004. **299**(2): p. 454-464.
82. Low, W.C., et al., *CADASIL-causing mutations do not alter Notch3 receptor processing and activation.* Neuroreport, 2006. **17**(10): p. 945-9.
83. Takahashi, K., et al., *Mutations in NOTCH3 cause the formation and retention of aggregates in the endoplasmic reticulum, leading to impaired cell proliferation.* Human molecular genetics, 2010. **19**(1): p. 79-89.
84. Opherk, C., et al., *CADASIL mutations enhance spontaneous multimerization of NOTCH3.* Human Molecular Genetics, 2009. **18**(15): p. 2761-2767.
85. Arboleda-Velasquez, J.F., et al., *Hypomorphic Notch 3 alleles link Notch signaling to ischemic cerebral small-vessel disease.* Proc Natl Acad Sci U S A, 2011. **108**(21): p. E128-35.
86. Ghosh, M., et al., *Pericytes are involved in the pathogenesis of cerebral autosomal dominant arteriopathy with subcortical infarcts and leukoencephalopathy.* Ann Neurol, 2015. **78**(6): p. 887-900.
87. Ruchoux, M.M., et al., *Transgenic Mice Expressing Mutant Notch3 Develop Vascular Alterations Characteristic of Cerebral Autosomal Dominant Arteriopathy with Subcortical Infarcts and Leukoencephalopathy.* The American Journal of Pathology, 2003. **162**(1): p. 329-342.

88. Lundkvist, J., et al., *Mice carrying a R142C Notch 3 knock–in mutation do not develop a CADASIL-like phenotype.* genesis, 2005. **41**(1): p. 13-22.
89. Werkman, I.L., D.H. Lentferink, and W. Baron, *Macroglial diversity: white and grey areas and relevance to remyelination.* Cellular and Molecular Life Sciences, 2020.
90. Zhang, J.H., et al., *The vascular neural network--a new paradigm in stroke pathophysiology.* Nat Rev Neurol, 2012. **8**(12): p. 711-6.
91. Ginsberg, M.D., *Neuroprotection for ischemic stroke: past, present and future.* Neuropharmacology, 2008. **55**(3): p. 363-89.
92. Lo, E.H., J.P. Broderick, and M.A. Moskowitz, *tPA and proteolysis in the neurovascular unit.* Stroke, 2004. **35**(2): p. 354-6.
93. Lo, E.H., T. Dalkara, and M.A. Moskowitz, *Mechanisms, challenges and opportunities in stroke.* Nat Rev Neurosci, 2003. **4**(5): p. 399-415.
94. Iadecola, C., *Neurovascular regulation in the normal brain and in Alzheimer's disease.* Nat Rev Neurosci, 2004. **5**(5): p. 347-60.
95. Harder, D.R., C. Zhang, and D. Gebremedhin, *Astrocytes function in matching blood flow to metabolic activity.* News Physiol Sci, 2002. **17**: p. 27-31.
96. Armstead, W.M. and R. Raghupathi, *Endothelin and the neurovascular unit in pediatric traumatic brain injury.* Neurological research, 2011. **33**(2): p. 127-132.
97. Abbott, N.J. and A. Friedman, *Overview and introduction: the blood–brain barrier in health and disease.* Epilepsia, 2012. **53**(s6): p. 1-6.
98. Muoio, V., P.B. Persson, and M.M. Sendeski, *The neurovascular unit - concept review.* Acta Physiol (Oxf), 2014. **210**(4): p. 790-8.
99. Najjar, S., et al., *Neurovascular unit dysfunction with blood-brain barrier hyperpermeability contributes to major depressive disorder: a review of clinical and experimental evidence.* J Neuroinflammation, 2013. **10**: p. 142.
100. Abbott, N.J. and S.R. Yusof, *Structure and function of the blood-brain barrier.* Frontiers in Pharmacology.
101. Aird, W.C., *Phenotypic heterogeneity of the endothelium: I. Structure, function, and mechanisms.* Circ Res, 2007. **100**(2): p. 158-73.
102. Reese, T.S. and M.J. Karnovsky, *Fine structural localization of a blood-brain barrier to exogenous peroxidase.* J Cell Biol, 1967. **34**(1): p. 207-17.
103. Komarova, Y. and A.B. Malik, *Regulation of endothelial permeability via paracellular and transcellular transport pathways.* Annual review of physiology, 2010. **72**: p. 463-493.
104. Brightman, M. and T. Reese, *Junctions between intimately apposed cell membranes in the vertebrate brain.* The Journal of cell biology, 1969. **40**(3): p. 648-677.
105. Coomber, B.L. and P.A. Stewart, *Morphometric analysis of CNS microvascular endothelium.* Microvasc Res, 1985. **30**(1): p. 99-115.
106. Cornford, E.M. and S. Hyman, *Localization of brain endothelial luminal and abluminal transporters with immunogold electron microscopy.* NeuroRx, 2005. **2**(1): p. 27-43.
107. Kubo, Y., et al., *Quantitative determination of luminal and abluminal membrane distributions of transporters in porcine brain capillaries by plasma membrane fractionation and quantitative targeted proteomics.* Journal of pharmaceutical sciences, 2015. **104**(9): p. 3060-3068.
108. Cordon-Cardo, C., et al., *Multidrug-resistance gene (P-glycoprotein) is expressed by endothelial cells at blood-brain barrier sites.* Proceedings of the National Academy of Sciences, 1989. **86**(2): p. 695-698.
109. Löscher, W. and H. Potschka, *Blood-brain barrier active efflux transporters: ATP-binding cassette gene family.* NeuroRx, 2005. **2**(1): p. 86-98.
110. Simpson, I.A., A. Carruthers, and S.J. Vannucci, *Supply and demand in cerebral energy metabolism: the role of nutrient transporters.* Journal of Cerebral Blood Flow & Metabolism, 2007. **27**(11): p. 1766-1791.

111. Daneman, R., et al., *The mouse blood-brain barrier transcriptome: a new resource for understanding the development and function of brain endothelial cells.* PloS one, 2010. **5**(10): p. e13741.
112. Sims, D.E., *The pericyte--a review.* Tissue Cell, 1986. **18**(2): p. 153-74.
113. Brown, L.S., et al., *Pericytes and Neurovascular Function in the Healthy and Diseased Brain.* Frontiers in cellular neuroscience, 2019. **13**: p. 282-282.
114. Mazzoni, J., T. Cutforth, and D. Agalliu, *Dissecting the Role of Smooth Muscle Cells versus Pericytes in Regulating Cerebral Blood Flow Using In Vivo Optical Imaging.* Neuron, 2015. **87**(1): p. 4-6.
115. Hill, R.A., et al., *Regional Blood Flow in the Normal and Ischemic Brain Is Controlled by Arteriolar Smooth Muscle Cell Contractility and Not by Capillary Pericytes.* Neuron, 2015. **87**(1): p. 95-110.
116. Armulik, A., et al., *Pericytes regulate the blood-brain barrier.* Nature, 2010. **468**(7323): p. 557-61.
117. Liu, S., et al., *The role of pericytes in blood-brain barrier function and stroke.* Curr Pharm Des, 2012. **18**(25): p. 3653-62.
118. Hellstrom, M., et al., *Role of PDGF-B and PDGFR-beta in recruitment of vascular smooth muscle cells and pericytes during embryonic blood vessel formation in the mouse.* Development, 1999. **126**(14): p. 3047-3055.
119. Etchevers, H.C., et al., *The cephalic neural crest provides pericytes and smooth muscle cells to all blood vessels of the face and forebrain.* Development, 2001. **128**(7): p. 1059-1068.
120. Korn, J., B. Christ, and H. Kurz, *Neuroectodermal origin of brain pericytes and vascular smooth muscle cells.* Journal of Comparative Neurology, 2002. **442**(1): p. 78-88.
121. Kurz, H., *Cell lineages and early patterns of embryonic CNS vascularization.* Cell adhesion & migration, 2009. **3**(2): p. 205-210.
122. Winkler, E.A., R.D. Bell, and B.V. Zlokovic, *Central nervous system pericytes in health and disease.* Nat Neurosci, 2011. **14**(11): p. 1398-405.
123. Pfaltzgraff, E.R. and D.M. Bader, *Heterogeneity in vascular smooth muscle cell embryonic origin in relation to adult structure, physiology, and disease.* Developmental dynamics : an official publication of the American Association of Anatomists, 2015. **244**(3): p. 410-416.
124. Bergwerff, M., et al., *Neural crest cell contribution to the developing circulatory system: implications for vascular morphology?* Circ Res, 1998. **82**(2): p. 221-31.
125. Quelhas, P., G. Baltazar, and E. Cairrao, *The Neurovascular Unit: Focus on the Regulation of Arterial Smooth Muscle Cells.* Curr Neurovasc Res, 2019. **16**(5): p. 502-515.
126. Attwell, D., et al., *Glial and neuronal control of brain blood flow.* Nature, 2010. **468**(7321): p. 232-243.
127. Hall, C.N., et al., *Capillary pericytes regulate cerebral blood flow in health and disease.* Nature, 2014. **508**(7494): p. 55-60.
128. Sengillo, J.D., et al., *Deficiency in Mural Vascular Cells Coincides with Blood–Brain Barrier Disruption in A lzheimer's Disease.* Brain pathology, 2013. **23**(3): p. 303-310.
129. Ma, Q., et al., *Blood-brain barrier-associated pericytes internalize and clear aggregated amyloid-β42 by LRP1-dependent apolipoprotein E isoform-specific mechanism.* Molecular neurodegeneration, 2018. **13**(1): p. 1-13.
130. Davson, H. and W. Oldendorf, *Symposium on membrane transport. Transport in the central nervous system.* Proceedings of the Royal Society of Medicine, 1967. **60**(4): p. 326.
131. Abbott, N.J., L. Rönnbäck, and E. Hansson, *Astrocyte–endothelial interactions at the blood–brain barrier.* Nature Reviews Neuroscience, 2006. **7**(1): p. 41-53.
132. Daneman, R. and A. Prat, *The blood-brain barrier.* Cold Spring Harbor perspectives in biology, 2015. **7**(1): p. a020412-a020412.
133. Volterra, A. and J. Meldolesi, *Astrocytes, from brain glue to communication elements: the revolution continues.* Nature Reviews Neuroscience, 2005. **6**(8): p. 626-640.

134. Cabezas, R., et al., *Astrocytic modulation of blood brain barrier: perspectives on Parkinson's disease.* Frontiers in cellular neuroscience, 2014. **8**: p. 211-211.
135. Iadecola, C. and M. Nedergaard, *Glial regulation of the cerebral microvasculature.* Nat Neurosci, 2007. **10**(11): p. 1369-76.
136. Noell, S., et al., *Evidence for a role of dystroglycan regulating the membrane architecture of astroglial endfeet.* Eur J Neurosci, 2011. **33**(12): p. 2179-86.
137. Rossi, A., et al., *Super-resolution imaging of aquaporin-4 orthogonal arrays of particles in cell membranes.* J Cell Sci, 2012. **125**(Pt 18): p. 4405-12.
138. Haj-Yasein, N.N., et al., *Glial-conditional deletion of aquaporin-4 (Aqp4) reduces blood-brain water uptake and confers barrier function on perivascular astrocyte endfeet.* Proc Natl Acad Sci U S A, 2011. **108**(43): p. 17815-20.
139. Halliday, G.M. and C.H. Stevens, *Glia: initiators and progressors of pathology in Parkinson's disease.* Mov Disord, 2011. **26**(1): p. 6-17.
140. Oberheim, N.A., S.A. Goldman, and M. Nedergaard, *Heterogeneity of astrocytic form and function.* Methods Mol Biol, 2012. **814**: p. 23-45.
141. Koehler, R.C., D. Gebremedhin, and D.R. Harder, *Role of astrocytes in cerebrovascular regulation.* Journal of applied physiology, 2006. **100**(1): p. 307-317.
142. Stewart, P.A. and M.J. Wiley, *Developing nervous tissue induces formation of blood-brain barrier characteristics in invading endothelial cells: A study using quail-chick transplantation chimeras.* Developmental Biology, 1981. **84**(1): p. 183-192.
143. Yoshida, Y., et al., *Endothelial fenestrae in the rat fetal cerebrum.* Brain Res Dev Brain Res, 1988. **44**(2): p. 211-9.
144. Tontsch, U. and H.-C. Bauer, *Glial cells and neurons induce blood-brain barrier related enzymes in cultured cerebral endothelial cells.* Brain Research, 1991. **539**(2): p. 247-253.
145. Shabir, O., J. Berwick, and S.E. Francis, *Neurovascular dysfunction in vascular dementia, Alzheimer's and atherosclerosis.* BMC neuroscience, 2018. **19**(1): p. 62.
146. Lecrux, C. and E. Hamel, *The neurovascular unit in brain function and disease.* Acta Physiologica, 2011. **203**(1): p. 47-59.
147. Zhao, Z., et al., *Establishment and Dysfunction of the Blood-Brain Barrier.* Cell, 2015. **163**(5): p. 1064-1078.
148. Gulbenkian, S., R. Uddman, and L. Edvinsson, *Neuronal messengers in the human cerebral circulation.* Peptides, 2001. **22**(6): p. 995-1007.
149. Ballabh, P., A. Braun, and M. Nedergaard, *The blood–brain barrier: an overview: structure, regulation, and clinical implications.* Neurobiology of disease, 2004. **16**(1): p. 1-13.
150. Navarro-Sobrino, M., et al., *The angiogenic gene profile of circulating endothelial progenitor cells from ischemic stroke patients.* Vascular cell, 2013. **5**(1): p. 1.
151. Hartmann, C., et al., *The impact of glia-derived extracellular matrices on the barrier function of cerebral endothelial cells: an in vitro study.* Experimental cell research, 2007. **313**(7): p. 1318-1325.
152. Hawkins, B.T. and T.P. Davis, *The blood-brain barrier/neurovascular unit in health and disease.* Pharmacol Rev, 2005. **57**(2): p. 173-85.
153. Obermeier, B., R. Daneman, and R.M. Ransohoff, *Development, maintenance and disruption of the blood-brain barrier.* Nat Med, 2013. **19**(12): p. 1584-96.
154. Stamatovic, S.M., R.F. Keep, and A.V. Andjelkovic, *Brain endothelial cell-cell junctions: how to "open" the blood brain barrier.* Current neuropharmacology, 2008. **6**(3): p. 179-192.
155. Larsen, J.M., D.R. Martin, and M.E. Byrne, *Recent advances in delivery through the blood-brain barrier.* Curr Top Med Chem, 2014. **14**(9): p. 1148-60.
156. Zlokovic, B.V., *The blood-brain barrier in health and chronic neurodegenerative disorders.* Neuron, 2008. **57**(2): p. 178-201.
157. Pardridge, W.M., *Drug transport across the blood-brain barrier.* J Cereb Blood Flow Metab, 2012. **32**(11): p. 1959-72.

158. Farrington, G.K., et al., *A novel platform for engineering blood-brain barrier-crossing bispecific biologics.* FASEB J, 2014. **28**(11): p. 4764-78.
159. Prades, R., et al., *Applying the retro-enantio approach to obtain a peptide capable of overcoming the blood-brain barrier.* Angew Chem Int Ed Engl, 2015. **54**(13): p. 3967-72.
160. Pardridge, W., *Targeted delivery of protein and gene medicines through the blood–brain barrier.* Clinical Pharmacology & Therapeutics, 2015. **97**(4): p. 347-361.
161. Lajoie, J.M. and E.V. Shusta, *Targeting receptor-mediated transport for delivery of biologics across the blood-brain barrier.* Annu Rev Pharmacol Toxicol, 2015. **55**: p. 613-31.
162. Parrish, K.E., J.N. Sarkaria, and W.F. Elmquist, *Improving drug delivery to primary and metastatic brain tumors: strategies to overcome the blood-brain barrier.* Clin Pharmacol Ther, 2015. **97**(4): p. 336-46.
163. Stamatovic, S.M., et al., *Junctional proteins of the blood-brain barrier: New insights into function and dysfunction.* Tissue barriers, 2016. **4**(1): p. e1154641-e1154641.
164. Anderson, J.M. and C.M. Van Itallie, *Physiology and function of the tight junction.* Cold Spring Harbor perspectives in biology, 2009. **1**(2): p. a002584-a002584.
165. Kniesel, U. and H. Wolburg, *Tight Junctions of the Blood–Brain Barrier.* Cellular and Molecular Neurobiology, 2000. **20**(1): p. 57-76.
166. Li, Y., et al., *Structure of the conserved cytoplasmic C-terminal domain of occludin: identification of the ZO-1 binding surface.* J Mol Biol, 2005. **352**(1): p. 151-64.
167. Nusrat, A., et al., *Multiple protein interactions involving proposed extracellular loop domains of the tight junction protein occludin.* Mol Biol Cell, 2005. **16**(4): p. 1725-34.
168. Cording, J., et al., *In tight junctions, claudins regulate the interactions between occludin, tricellulin and marvelD3, which, inversely, modulate claudin oligomerization.* J Cell Sci, 2013. **126**(Pt 2): p. 554-64.
169. Ohtsuki, S., et al., *mRNA expression levels of tight junction protein genes in mouse brain capillary endothelial cells highly purified by magnetic cell sorting.* J Neurochem, 2008. **104**(1): p. 147-54.
170. Nitta, T., et al., *Size-selective loosening of the blood-brain barrier in claudin-5-deficient mice.* J Cell Biol, 2003. **161**(3): p. 653-60.
171. Itoh, M., et al., *Junctional adhesion molecule (JAM) binds to PAR-3: a possible mechanism for the recruitment of PAR-3 to tight junctions.* J Cell Biol, 2001. **154**(3): p. 491-7.
172. Bazzoni, G. and E. Dejana, *Endothelial cell-to-cell junctions: molecular organization and role in vascular homeostasis.* Physiol Rev, 2004. **84**(3): p. 869-901.
173. Sobocki, T., et al., *Genomic structure, organization and promoter analysis of the human F11R/F11 receptor/junctional adhesion molecule-1/JAM-A.* Gene, 2006. **366**(1): p. 128-44.
174. Williams, L.A., et al., *Identification and characterisation of human Junctional Adhesion Molecule (JAM).* Mol Immunol, 1999. **36**(17): p. 1175-88.
175. Ebnet, K., et al., *The junctional adhesion molecule (JAM) family members JAM-2 and JAM-3 associate with the cell polarity protein PAR-3: a possible role for JAMs in endothelial cell polarity.* J Cell Sci, 2003. **116**(Pt 19): p. 3879-91.
176. Fanning, A.S., et al., *The unique-5 and -6 motifs of ZO-1 regulate tight junction strand localization and scaffolding properties.* Mol Biol Cell, 2007. **18**(3): p. 721-31.
177. Utepbergenov, D.I., A.S. Fanning, and J.M. Anderson, *Dimerization of the scaffolding protein ZO-1 through the second PDZ domain.* J Biol Chem, 2006. **281**(34): p. 24671-7.
178. White, T.W. and D.L. Paul, *GENETIC DISEASES AND GENE KNOCKOUTS REVEAL DIVERSE CONNEXIN FUNCTIONS.* Annual Review of Physiology, 1999. **61**(1): p. 283-310.
179. Ivanova, E., T. Kovacs-Oller, and B.T. Sagdullaev, *Domain-specific distribution of gap junctions defines cellular coupling to establish a vascular relay in the retina.* J Comp Neurol, 2019. **527**(16): p. 2675-2693.

180. Ivanova, E., T. Kovacs-Oller, and B.T. Sagdullaev, *Vascular Pericyte Impairment and Connexin43 Gap Junction Deficit Contribute to Vasomotor Decline in Diabetic Retinopathy.* J Neurosci, 2017. **37**(32): p. 7580-7594.
181. Hirst-Jensen, B.J., et al., *Characterization of the pH-dependent interaction between the gap junction protein connexin43 carboxyl terminus and cytoplasmic loop domains.* Journal of biological chemistry, 2007. **282**(8): p. 5801-5813.
182. Lagrée, V., et al., *Specific amino-acid residues in the N-terminus and TM3 implicated in channel function and oligomerization compatibility of connexin43.* Journal of cell science, 2003. **116**(15): p. 3189-3201.
183. Kameritsch, P., K. Pogoda, and U. Pohl, *Channel-independent influence of connexin 43 on cell migration.* Biochim Biophys Acta, 2012. **1818**(8): p. 1993-2001.
184. Abbruscato, T.J. and T.P. Davis, *Protein expression of brain endothelial cell E-cadherin after hypoxia/aglycemia: influence of astrocyte contact.* Brain Res, 1999. **842**(2): p. 277-86.
185. Luo, Y. and G.L. Radice, *N-cadherin acts upstream of VE-cadherin in controlling vascular morphogenesis.* J Cell Biol, 2005. **169**(1): p. 29-34.
186. Li, W., et al., *The Role of VE-cadherin in Blood-brain Barrier Integrity Under Central Nervous System Pathological Conditions.* Current neuropharmacology, 2018. **16**(9): p. 1375-1384.
187. Carmeliet, P., et al., *Targeted deficiency or cytosolic truncation of the VE-cadherin gene in mice impairs VEGF-mediated endothelial survival and angiogenesis.* Cell, 1999. **98**(2): p. 147-57.
188. Andrae, J., R. Gallini, and C. Betsholtz, *Role of platelet-derived growth factors in physiology and medicine.* Genes & development, 2008. **22**(10): p. 1276-1312.
189. Daneman, R., et al., *Pericytes are required for blood-brain barrier integrity during embryogenesis.* Nature, 2010. **468**(7323): p. 562-6.
190. Henshall Tanya, L., et al., *Notch3 Is Necessary for Blood Vessel Integrity in the Central Nervous System.* Arteriosclerosis, Thrombosis, and Vascular Biology, 2015. **35**(2): p. 409-420.
191. Bell, R.D., et al., *Pericytes control key neurovascular functions and neuronal phenotype in the adult brain and during brain aging.* Neuron, 2010. **68**(3): p. 409-27.
192. Wang, Y., et al., *Notch3 establishes brain vascular integrity by regulating pericyte number.* Development (Cambridge, England), 2014. **141**(2): p. 307-317.
193. Wallin, A., et al., *Blood brain barrier function in vascular dementia.* Acta neurologica Scandinavica, 1990. **81**(4): p. 318-322.
194. Skoog, I., et al., *A population study on blood-brain barrier function in 85-year-olds: relation to Alzheimer's disease and vascular dementia.* Neurology, 1998. **50**(4): p. 966-971.
195. Kalaria, R.N., et al., *The pathogenesis of CADASIL: an update.* J Neurol Sci, 2004. **226**(1-2): p. 35-9.
196. Singhal, S. and H.S. Markus, *Cerebrovascular reactivity and dynamic autoregulation in nondemented patients with CADASIL (cerebral autosomal dominant arteriopathy with subcortical infarcts and leukoencephalopathy).* J Neurol, 2005. **252**(2): p. 163-7.
197. Craggs, L.J., et al., *Immunolocalization of platelet‐derived growth factor receptor‐β (PDGFR‐β) and pericytes in cerebral autosomal dominant arteriopathy with subcortical infarcts and leukoencephalopathy (CADASIL).* Neuropathology and applied neurobiology, 2015. **41**(4): p. 557-570.
198. Joutel, A., et al., *Cerebrovascular dysfunction and microcirculation rarefaction precede white matter lesions in a mouse genetic model of cerebral ischemic small vessel disease.* The Journal of clinical investigation, 2010. **120**(2): p. 433-445.
199. Capone, C., et al., *Mechanistic insights into a TIMP3-sensitive pathway constitutively engaged in the regulation of cerebral hemodynamics.* Elife, 2016. **5**: p. e17536.
200. Huneau, C., et al., *Altered dynamics of neurovascular coupling in CADASIL.* Annals of Clinical and Translational Neurology, 2018. **5**(7): p. 788-802.

201. Ghosh, M., et al., *Pericytes are involved in the pathogenesis of cerebral autosomal dominant arteriopathy with subcortical infarcts and leukoencephalopathy.* Annals of Neurology, 2015. **78**(6): p. 887-900.
202. Takahashi, K. and S. Yamanaka, *Induction of pluripotent stem cells from mouse embryonic and adult fibroblast cultures by defined factors.* Cell, 2006. **126**(4): p. 663-76.
203. Wernig, M., et al., *In vitro reprogramming of fibroblasts into a pluripotent ES-cell-like state.* Nature, 2007. **448**(7151): p. 318-24.
204. Dimos, J.T., et al., *Induced pluripotent stem cells generated from patients with ALS can be differentiated into motor neurons.* Science, 2008. **321**(5893): p. 1218-21.
205. Sun, N., et al., *Feeder-free derivation of induced pluripotent stem cells from adult human adipose stem cells.* Proc Natl Acad Sci U S A, 2009. **106**(37): p. 15720-5.
206. Ebert, A.D., P. Liang, and J.C. Wu, *Induced pluripotent stem cells as a disease modeling and drug screening platform.* Journal of cardiovascular pharmacology, 2012. **60**(4): p. 408-416.
207. Crook, J.M. and N.R. Kobayashi, *Human stem cells for modeling neurological disorders: accelerating the drug discovery pipeline.* J Cell Biochem, 2008. **105**(6): p. 1361-6.
208. Nat, R., et al., *Neurogenic neuroepithelial and radial glial cells generated from six human embryonic stem cell lines in serum-free suspension and adherent cultures.* Glia, 2007. **55**(4): p. 385-99.
209. Cai, S., X. Fu, and Z. Sheng, *Dedifferentiation: a new approach in stem cell research.* Bioscience, 2007. **57**(8): p. 655-662.
210. Cheung, C. and S. Sinha, *Human embryonic stem cell-derived vascular smooth muscle cells in therapeutic neovascularisation.* J Mol Cell Cardiol, 2011. **51**(5): p. 651-64.
211. Lippmann, E.S., et al., *Derivation of blood-brain barrier endothelial cells from human pluripotent stem cells.* Nature biotechnology, 2012. **30**(8): p. 783-791.
212. Lippmann, E.S., et al., *A retinoic acid-enhanced, multicellular human blood-brain barrier model derived from stem cell sources.* Sci Rep, 2014. **4**: p. 4160.
213. Qian, T., et al., *Directed differentiation of human pluripotent stem cells to blood-brain barrier endothelial cells.* Science advances, 2017. **3**(11): p. e1701679.
214. Workman, M.J. and C.N. Svendsen, *Recent advances in human iPSC-derived models of the blood–brain barrier.* Fluids and Barriers of the CNS, 2020. **17**(1): p. 30.
215. Korn, J., B. Christ, and H. Kurz, *Neuroectodermal origin of brain pericytes and vascular smooth muscle cells.* J Comp Neurol, 2002. **442**(1): p. 78-88.
216. Cheung, C., et al., *Generation of human vascular smooth muscle subtypes provides insight into embryological origin–dependent disease susceptibility.* Nature Biotechnology, 2012. **30**(2): p. 165-173.
217. Shi, Y., P. Kirwan, and F.J. Livesey, *Directed differentiation of human pluripotent stem cells to cerebral cortex neurons and neural networks.* Nature Protocols, 2012. **7**(10): p. 1836-1846.
218. Roybon, L., et al., *Human stem cell-derived spinal cord astrocytes with defined mature or reactive phenotypes.* Cell Rep, 2013. **4**(5): p. 1035-1048.
219. Cecchelli, R., et al., *A stable and reproducible human blood-brain barrier model derived from hematopoietic stem cells.* PLoS One, 2014. **9**(6): p. e99733.
220. Lippmann, E.S., et al., *Derivation of blood-brain barrier endothelial cells from human pluripotent stem cells.* Nat Biotechnol, 2012. **30**(8): p. 783-91.
221. Vatine, G.D., et al., *Modeling Psychomotor Retardation using iPSCs from MCT8-Deficient Patients Indicates a Prominent Role for the Blood-Brain Barrier.* Cell Stem Cell, 2017. **20**(6): p. 831-843.e5.
222. Ling, C., et al., *Modeling CADASIL vascular pathologies with patient-derived induced pluripotent stem cells.* Protein & cell, 2019. **10**(4): p. 249-271.
223. Kelleher, J., et al., *Patient-Specific iPSC Model of a Genetic Vascular Dementia Syndrome Reveals Failure of Mural Cells to Stabilize Capillary Structures.* Stem Cell Reports, 2019. **13**(5): p. 817-831.

224. Kelleher, J., et al., *187 Induced Pluripotent Stem Cell (IPSC) Model of Cerebral Autosomal Dominant Arteriopathy with Subcortical Infarcts and Leukoencephalopathy (CADASIL).* Heart, 2015. **101**(Suppl 4): p. A105.
225. Yamamoto, Y., et al., *Human iPS cell-derived mural cells as an in vitro model of hereditary cerebral small vessel disease.* Molecular Brain, 2020. **13**(1): p. 38.
226. Wilgenburg, B.v., et al., *Efficient, Long Term Production of Monocyte-Derived Macrophages from Human Pluripotent Stem Cells under Partly-Defined and Fully-Defined Conditions.* PLOS ONE, 2013. **8**(8): p. e71098.
227. Chambers, S.M., et al., *Highly efficient neural conversion of human ES and iPS cells by dual inhibition of SMAD signaling.* Nature biotechnology, 2009. **27**(3): p. 275-280.
228. Stebbins, M.J., et al., *Differentiation and characterization of human pluripotent stem cell-derived brain microvascular endothelial cells.* Methods, 2016. **101**: p. 93-102.
229. Joutel, A., et al., *Strong clustering and stereotyped nature of Notch3 mutations in CADASIL patients.* The Lancet, 1997. **350**(9090): p. 1511-1515.
230. Joutel, A., et al., *Skin biopsy immunostaining with a Notch3 monoclonal antibody for CADASIL diagnosis.* The Lancet, 2001. **358**(9298): p. 2049-2051.
231. Ruchoux, M.M., et al., *Transgenic mice expressing mutant Notch3 develop vascular alterations characteristic of cerebral autosomal dominant arteriopathy with subcortical infarcts and leukoencephalopathy.* Am J Pathol, 2003. **162**(1): p. 329-42.
232. Wang, T., M. Baron, and D. Trump, *An overview of Notch3 function in vascular smooth muscle cells.* Prog Biophys Mol Biol, 2008. **96**(1-3): p. 499-509.
233. Lundkvist, J., et al., *Mice carrying a R142C Notch 3 knock-in mutation do not develop a CADASIL-like phenotype.* Genesis, 2005. **41**(1): p. 13-22.
234. Takahashi, K., et al., *Induction of Pluripotent Stem Cells from Adult Human Fibroblasts by Defined Factors.* Cell, 2007. **131**(5): p. 861-872.
235. Fernández-Susavila, H., et al., *Adult Stem Cells and Induced Pluripotent Stem Cells for Stroke Treatment.* Frontiers in Neurology, 2019. **10**(908).
236. Israel, M.A., et al., *Probing sporadic and familial Alzheimer's disease using induced pluripotent stem cells.* Nature, 2012. **482**(7384): p. 216-220.
237. Kondo, T., et al., *Modeling Alzheimer's disease with iPSCs reveals stress phenotypes associated with intracellular Abeta and differential drug responsiveness.* Cell Stem Cell, 2013. **12**(4): p. 487-96.
238. Kikuchi, T., et al., *Human iPS cell-derived dopaminergic neurons function in a primate Parkinson's disease model.* Nature, 2017. **548**(7669): p. 592-596.
239. Szlachcic, W.J., et al., *The Generation of Mouse and Human Huntington Disease iPS Cells Suitable for In vitro Studies on Huntingtin Function.* Front Mol Neurosci, 2017. **10**: p. 253.
240. Ling, C., et al., *Modeling CADASIL vascular pathologies with patient-derived induced pluripotent stem cells.* Protein Cell, 2019. **10**(4): p. 249-271.
241. Chabriat, H., et al., *CADASIL.* The Lancet Neurology, 2009. **8**(7): p. 643-653.
242. Shabir, O., J. Berwick, and S.E. Francis, *Neurovascular dysfunction in vascular dementia, Alzheimer's and atherosclerosis.* BMC Neurosci, 2018. **19**(1): p. 62.
243. Zlokovic, B.V., *Neurovascular pathways to neurodegeneration in Alzheimer's disease and other disorders.* Nat Rev Neurosci, 2011. **12**(12): p. 723-38.
244. Armulik, A., et al., *Pericytes regulate the blood-brain barrier.* Nature, 2010. **468**(7323): p. 557-61.
245. Winkler, E.A., R.D. Bell, and B.V. Zlokovic, *Central nervous system pericytes in health and disease.* Nat Neurosci, 2011. **14**(11): p. 1398-1405.
246. Butt, A.M., H.C. Jones, and N.J. Abbott, *Electrical resistance across the blood-brain barrier in anaesthetized rats: a developmental study.* The Journal of physiology, 1990. **429**: p. 47-62.
247. Lippmann, E.S., et al., *Modeling the blood–brain barrier using stem cell sources.* Fluids and Barriers of the CNS, 2013. **10**(1): p. 2.

248. Smith, Q.R. and S.I. Rapoport, *Cerebrovascular permeability coefficients to sodium, potassium, and chloride.* J Neurochem, 1986. **46**(6): p. 1732-42.
249. Montesano, R., et al., *Increased proteolytic activity is responsible for the aberrant morphogenetic behavior of endothelial cells expressing the middle T oncogene.* Cell, 1990. **62**(3): p. 435-445.
250. Weksler, B.B., et al., *Blood-brain barrier-specific properties of a human adult brain endothelial cell line.* Faseb j, 2005. **19**(13): p. 1872-4.
251. Naik, P. and L. Cucullo, *In vitro blood-brain barrier models: current and perspective technologies.* J Pharm Sci, 2012. **101**(4): p. 1337-54.
252. Boyer-Di Ponio, J., et al., *Instruction of circulating endothelial progenitors in vitro towards specialized blood-brain barrier and arterial phenotypes.* PLoS One, 2014. **9**(1): p. e84179.
253. Fusaki, N., et al., *Efficient induction of transgene-free human pluripotent stem cells using a vector based on Sendai virus, an RNA virus that does not integrate into the host genome.* Proc Jpn Acad Ser B Phys Biol Sci, 2009. **85**(8): p. 348-62.
254. van Wilgenburg, B., et al., *Efficient, long term production of monocyte-derived macrophages from human pluripotent stem cells under partly-defined and fully-defined conditions.* PloS one, 2013. **8**(8): p. e71098-e71098.
255. Lei, Y. and D.V. Schaffer, *A fully defined and scalable 3D culture system for human pluripotent stem cell expansion and differentiation.* Proceedings of the National Academy of Sciences, 2013. **110**(52): p. E5039.
256. Patel, R. and A.J. Alahmad, *Growth-factor reduced Matrigel source influences stem cell derived brain microvascular endothelial cell barrier properties.* Fluids and Barriers of the CNS, 2016. **13**(1): p. 6.
257. Hollmann, E.K., et al., *Accelerated differentiation of human induced pluripotent stem cells to blood–brain barrier endothelial cells.* Fluids and Barriers of the CNS, 2017. **14**(1): p. 9.
258. Lauschke, K., L. Frederiksen, and V.J. Hall, *Paving the Way Toward Complex Blood-Brain Barrier Models Using Pluripotent Stem Cells.* Stem Cells and Development, 2017. **26**(12): p. 857-874.
259. Minami, H., et al., *Generation of Brain Microvascular Endothelial-Like Cells from Human Induced Pluripotent Stem Cells by Co-Culture with C6 Glioma Cells.* PLoS One, 2015. **10**(6): p. e0128890.
260. Wilson, H.K., et al., *Exploring the effects of cell seeding density on the differentiation of human pluripotent stem cells to brain microvascular endothelial cells.* Fluids and Barriers of the CNS, 2015. **12**(1): p. 13.
261. Abbott, N.J., et al., *Structure and function of the blood-brain barrier.* Neurobiol Dis, 2010. **37**(1): p. 13-25.
262. Vorbrodt, A.W. and D.H. Dobrogowska, *Molecular anatomy of intercellular junctions in brain endothelial and epithelial barriers: electron microscopist's view.* Brain Res Brain Res Rev, 2003. **42**(3): p. 221-42.
263. Suga, M., T. Kondo, and H. Inoue, *Modeling Neurological Disorders with Human Pluripotent Stem Cell-Derived Astrocytes.* International journal of molecular sciences, 2019. **20**(16): p. 3862.
264. Miller, R.H. and M.C. Raff, *Fibrous and protoplasmic astrocytes are biochemically and developmentally distinct.* J Neurosci, 1984. **4**(2): p. 585-92.
265. Lundgaard, I., et al., *White matter astrocytes in health and disease.* Neuroscience, 2014. **276**: p. 161-73.
266. Sofroniew, M.V., *Astrogliosis.* Cold Spring Harb Perspect Biol, 2014. **7**(2): p. a020420.
267. Gordon, G.R., S.J. Mulligan, and B.A. MacVicar, *Astrocyte control of the cerebrovasculature.* Glia, 2007. **55**(12): p. 1214-21.
268. Koehler, R.C., R.J. Roman, and D.R. Harder, *Astrocytes and the regulation of cerebral blood flow.* Trends Neurosci, 2009. **32**(3): p. 160-9.

269. Beck, D.W., et al., *Glial Cells Influence Polarity of the Blood-Brain Barrier.* Journal of Neuropathology & Experimental Neurology, 1984. **43**(3): p. 219-224.
270. Haseloff, R.F., et al., *In search of the astrocytic factor(s) modulating blood-brain barrier functions in brain capillary endothelial cells in vitro.* Cell Mol Neurobiol, 2005. **25**(1): p. 25-39.
271. Abbott, N.J., L. Ronnback, and E. Hansson, *Astrocyte-endothelial interactions at the blood-brain barrier.* Nat Rev Neurosci, 2006. **7**(1): p. 41-53.
272. Oksanen, M., et al., *Astrocyte alterations in neurodegenerative pathologies and their modeling in human induced pluripotent stem cell platforms.* Cellular and molecular life sciences : CMLS, 2019. **76**(14): p. 2739-2760.
273. Nedergaard, M., B. Ransom, and S.A. Goldman, *New roles for astrocytes: redefining the functional architecture of the brain.* Trends Neurosci, 2003. **26**(10): p. 523-30.
274. Sofroniew, M.V. and H.V. Vinters, *Astrocytes: biology and pathology.* Acta neuropathologica, 2010. **119**(1): p. 7-35.
275. Ezan, P., et al., *Deletion of astroglial connexins weakens the blood-brain barrier.* J Cereb Blood Flow Metab, 2012. **32**(8): p. 1457-67.
276. Heinemann, U., D. Kaufer, and A. Friedman, *Blood-brain barrier dysfunction, TGFβ signaling, and astrocyte dysfunction in epilepsy.* Glia, 2012. **60**(8): p. 1251-1257.
277. Price, B.R., et al., *An emerging role of astrocytes in vascular contributions to cognitive impairment and dementia.* J Neurochem, 2018. **144**(5): p. 644-650.
278. Brennan-Krohn, T., et al., *Glial vascular degeneration in CADASIL.* J Alzheimers Dis, 2010. **21**(4): p. 1393-402.
279. Hase, Y., et al., *Severe white matter astrocytopathy in CADASIL.* Brain Pathol, 2018. **28**(6): p. 832-843.
280. Oberheim, N.A., et al., *Uniquely hominid features of adult human astrocytes.* J Neurosci, 2009. **29**(10): p. 3276-87.
281. Hol, E.M. and M. Pekny, *Glial fibrillary acidic protein (GFAP) and the astrocyte intermediate filament system in diseases of the central nervous system.* Current Opinion in Cell Biology, 2015. **32**: p. 121-130.
282. Malik, N., et al., *Comparison of the gene expression profiles of human fetal cortical astrocytes with pluripotent stem cell derived neural stem cells identifies human astrocyte markers and signaling pathways and transcription factors active in human astrocytes.* PLoS One, 2014. **9**(5): p. e96139.
283. Tyzack, G., A. Lakatos, and R. Patani, *Human Stem Cell-Derived Astrocytes: Specification and Relevance for Neurological Disorders.* Current Stem Cell Reports, 2016. **2**(3): p. 236-247.
284. Zhang, S.-C., et al., *In vitro differentiation of transplantable neural precursors from human embryonic stem cells.* Nature Biotechnology, 2001. **19**(12): p. 1129-1133.
285. Reubinoff, B.E., et al., *Neural progenitors from human embryonic stem cells.* Nat Biotechnol, 2001. **19**(12): p. 1134-40.
286. Itsykson, P., et al., *Derivation of neural precursors from human embryonic stem cells in the presence of noggin.* Mol Cell Neurosci, 2005. **30**(1): p. 24-36.
287. Krencik, R., et al., *Specification of transplantable astroglial subtypes from human pluripotent stem cells.* Nature Biotechnology, 2011. **29**(6): p. 528-534.
288. Jones, V.C., et al., *Aberrant iPSC-derived human astrocytes in Alzheimer's disease.* Cell Death & Disease, 2017. **8**(3): p. e2696-e2696.
289. Shaltouki, A., et al., *Efficient Generation of Astrocytes from Human Pluripotent Stem Cells in Defined Conditions.* STEM CELLS, 2013. **31**(5): p. 941-952.
290. Krencik, R. and S.-C. Zhang, *Directed differentiation of functional astroglial subtypes from human pluripotent stem cells.* Nature Protocols, 2011. **6**(11): p. 1710-1717.
291. Shi, Y., P. Kirwan, and F.J. Livesey, *Directed differentiation of human pluripotent stem cells to cerebral cortex neurons and neural networks.* Nat Protoc, 2012. **7**(10): p. 1836-46.

292. Tcw, J., et al., *An Efficient Platform for Astrocyte Differentiation from Human Induced Pluripotent Stem Cells.* Stem Cell Reports, 2017. **9**(2): p. 600-614.
293. Goncalves, C.A., M.C. Leite, and P. Nardin, *Biological and methodological features of the measurement of S100B, a putative marker of brain injury.* Clin Biochem, 2008. **41**(10-11): p. 755-63.
294. Lovatt, D., et al., *The Transcriptome and Metabolic Gene Signature of Protoplasmic Astrocytes in the Adult Murine Cortex.* The Journal of Neuroscience, 2007. **27**(45): p. 12255.
295. Dossi, E., F. Vasile, and N. Rouach, *Human astrocytes in the diseased brain.* Brain Research Bulletin, 2018. **136**: p. 139-156.
296. Kobayashi, E., et al., *Activated forms of astrocytes with higher GLT-1 expression are associated with cognitive normal subjects with Alzheimer pathology in human brain.* Sci Rep, 2018. **8**(1): p. 1712.
297. Waring, S.C. and R.N. Rosenberg, *Genome-wide association studies in Alzheimer disease.* Arch Neurol, 2008. **65**(3): p. 329-34.
298. Oksanen, M., et al., *PSEN1 Mutant iPSC-Derived Model Reveals Severe Astrocyte Pathology in Alzheimer's Disease.* Stem cell reports, 2017. **9**(6): p. 1885-1897.
299. di Domenico, A., et al., *Patient-Specific iPSC-Derived Astrocytes Contribute to Non-Cell-Autonomous Neurodegeneration in Parkinson's Disease.* Stem Cell Reports, 2019. **12**(2): p. 213-229.
300. Juopperi, T.A., et al., *Astrocytes generated from patient induced pluripotent stem cells recapitulate features of Huntington's disease patient cells.* Mol Brain, 2012. **5**: p. 17.
301. Schlageter, K.E., et al., *Microvessel Organization and Structure in Experimental Brain Tumors: Microvessel Populations with Distinctive Structural and Functional Properties.* Microvascular Research, 1999. **58**(3): p. 312-328.
302. Zlokovic, B.V., *Neurovascular mechanisms of Alzheimer's neurodegeneration.* Trends in Neurosciences, 2005. **28**(4): p. 202-208.
303. Savettieri, G., et al., *Neurons and ECM regulate occludin localization in brain endothelial cells.* Neuroreport, 2000. **11**(5): p. 1081-4.
304. Bickler, P.E. and P.H. Donohoe, *Adaptive responses of vertebrate neurons to hypoxia.* Journal of Experimental Biology, 2002. **205**(23): p. 3579.
305. Li, Y.N., et al., *Ischemic neurons activate astrocytes to disrupt endothelial barrier via increasing VEGF expression.* J Neurochem, 2014. **129**(1): p. 120-9.
306. Man, S., E.E. Ubogu, and R.M. Ransohoff, *Inflammatory Cell Migration into the Central Nervous System: A Few New Twists on an Old Tale.* Brain Pathology, 2007. **17**(2): p. 243-250.
307. Pehar, M., et al., *Complexity of Astrocyte-Motor Neuron Interactions in Amyotrophic Lateral Sclerosis.* Neurodegenerative Diseases, 2005. **2**(3-4): p. 139-146.
308. Haseloff, R.F., et al., *In Search of the Astrocytic Factor(s) Modulating Blood–Brain Barrier Functions in Brain Capillary Endothelial Cells In Vitro.* Cellular and Molecular Neurobiology, 2005. **25**(1): p. 25-39.
309. Livesey, F.J., *Human stem cell models of dementia.* Human molecular genetics, 2014. **23**(R1): p. R35-R39.
310. Penney, J., W.T. Ralvenius, and L.-H. Tsai, *Modeling Alzheimer's disease with iPSC-derived brain cells.* Molecular Psychiatry, 2020. **25**(1): p. 148-167.
311. Arber, C., C. Lovejoy, and S. Wray, *Stem cell models of Alzheimer's disease: progress and challenges.* Alzheimer's Research & Therapy, 2017. **9**(1): p. 42.
312. Yagi, T., et al., *Modeling familial Alzheimer's disease with induced pluripotent stem cells.* Hum Mol Genet, 2011. **20**(23): p. 4530-9.
313. Wang, D.S., D.W. Dickson, and J.S. Malter, *beta-Amyloid degradation and Alzheimer's disease.* J Biomed Biotechnol, 2006. **2006**(3): p. 58406.

314. Byers, B., H.-l. Lee, and R. Reijo Pera, *Modeling Parkinson's Disease Using Induced Pluripotent Stem Cells.* Current Neurology and Neuroscience Reports, 2012. **12**(3): p. 237-242.
315. Lee, S. and E.J. Huang, *Modeling ALS and FTD with iPSC-derived neurons.* Brain Research, 2017. **1656**: p. 88-97.
316. Kril, J.J., et al., *Patients with vascular dementia due to microvascular pathology have significant hippocampal neuronal loss.* Journal of Neurology, Neurosurgery & Psychiatry, 2002. **72**(6): p. 747.
317. Kurosawa, H., *Methods for inducing embryoid body formation: in vitro differentiation system of embryonic stem cells.* Journal of Bioscience and Bioengineering, 2007. **103**(5): p. 389-398.
318. Tao, Y. and S.C. Zhang, *Neural Subtype Specification from Human Pluripotent Stem Cells.* Cell Stem Cell, 2016. **19**(5): p. 573-586.
319. Jarosz-Griffiths, H.H., et al., *Proteolytic shedding of the prion protein via activation of metallopeptidase ADAM10 reduces cellular binding and toxicity of amyloid-β oligomers.* Journal of Biological Chemistry, 2019. **294**(17): p. 7085-7097.
320. Majumder, A., et al., *Inhibition of DNA methyltransferases and histone deacetylases induces astrocytic differentiation of neural progenitors.* Stem Cell Research, 2013. **11**(1): p. 574-586.
321. Plachez, C., et al., *Astrocytes repress the neuronal expression of GLAST and GLT glutamate transporters in cultured hippocampal neurons from embryonic rats.* Neurochem Int, 2004. **45**(7): p. 1113-23.
322. Perego, C., et al., *The GLT-1 and GLAST glutamate transporters are expressed on morphologically distinct astrocytes and regulated by neuronal activity in primary hippocampal cocultures.* J Neurochem, 2000. **75**(3): p. 1076-84.
323. Gomes, F.C., O. Sousa Vde, and L. Romao, *Emerging roles for TGF-beta1 in nervous system development.* Int J Dev Neurosci, 2005. **23**(5): p. 413-24.
324. Baghdassarian, D., et al., *Effects of transforming growth factor-beta 1 on the extracellular matrix and cytoskeleton of cultured astrocytes.* Glia, 1993. **7**(3): p. 193-202.
325. Laping, N.J., et al., *Transforming growth factor-beta 1 induces neuronal and astrocyte genes: tubulin alpha 1, glial fibrillary acidic protein and clusterin.* Neuroscience, 1994. **58**(3): p. 563-72.
326. Stipursky, J., et al., *TGF-β1 promotes cerebral cortex radial glia-astrocyte differentiation in vivo.* Frontiers in cellular neuroscience, 2014. **8**: p. 393-393.
327. Li, L., et al., *GFAP Mutations in Astrocytes Impair Oligodendrocyte Progenitor Proliferation and Myelination in an hiPSC Model of Alexander Disease.* Cell Stem Cell, 2018. **23**(2): p. 239-251.e6.
328. Dai, C., et al., *PDGF autocrine stimulation dedifferentiates cultured astrocytes and induces oligodendrogliomas and oligoastrocytomas from neural progenitors and astrocytes in vivo.* Genes & development, 2001. **15**(15): p. 1913-1925.
329. Shi, Y., P. Kirwan, and F.J. Livesey, *Directed differentiation of human pluripotent stem cells to cerebral cortex neurons and neural networks.* Nature protocols, 2012. **7**(10): p. 1836.
330. Vanlandewijck, M., et al., *A molecular atlas of cell types and zonation in the brain vasculature.* Nature, 2018. **554**(7693): p. 475-480.
331. Dziewulska, D. and E. Lewandowska, *Pericytes as a new target for pathological processes in CADASIL.* Neuropathology, 2012. **32**(5): p. 515-21.
332. Taura, D., et al., *Induction and isolation of vascular cells from human induced pluripotent stem cells--brief report.* Arteriosclerosis, Thrombosis, and Vascular Biology, 2009: p. 1100-1103.
333. Lee, T.-H., et al., *Functional Recapitulation of Smooth Muscle Cells Via Induced Pluripotent Stem Cells From Human Aortic Smooth Muscle Cells.* Circulation Research, 2010. **106**(1): p. 120-128.

334. Stebbins, M.J., et al., *Human pluripotent stem cell–derived brain pericyte–like cells induce blood-brain barrier properties.* Science Advances, 2019. **5**(3): p. eaau7375.
335. Faal, T., et al., *Induction of Mesoderm and Neural Crest-Derived Pericytes from Human Pluripotent Stem Cells to Study Blood-Brain Barrier Interactions.* Stem Cell Reports, 2019. **12**(3): p. 451-460.
336. Cheung, C., et al., *Modeling Cerebrovascular Pathophysiology in Amyloid-β Metabolism using Neural-Crest-Derived Smooth Muscle Cells.* Cell Reports, 2014. **9**(1): p. 391-401.
337. Wang, A., et al., *Derivation of Smooth Muscle Cells with Neural Crest Origin from Human Induced Pluripotent Stem Cells.* Cells Tissues Organs, 2012. **195**(1-2): p. 5-14.
338. Cheung, C., et al., *Generation of human vascular smooth muscle subtypes provides insight into embryological origin-dependent disease susceptibility.* Nature biotechnology, 2012. **30**(2): p. 165-173.
339. Sweeney, M.D., A.P. Sagare, and B.V. Zlokovic, *Blood–brain barrier breakdown in Alzheimer disease and other neurodegenerative disorders.* Nature Reviews Neurology, 2018. **14**(3): p. 133-150.
340. Syvänen, S., et al., *Species Differences in Blood-Brain Barrier Transport of Three Positron Emission Tomography Radioligands with Emphasis on P-Glycoprotein Transport.* Drug Metabolism and Disposition, 2009. **37**(3): p. 635.
341. Hoshi, Y., et al., *Quantitative Atlas of Blood–Brain Barrier Transporters, Receptors, and Tight Junction Proteins in Rats and Common Marmoset.* Journal of Pharmaceutical Sciences, 2013. **102**(9): p. 3343-3355.
342. Bernas, M.J., et al., *Establishment of primary cultures of human brain microvascular endothelial cells to provide an in vitro cellular model of the blood-brain barrier.* Nat Protoc, 2010. **5**(7): p. 1265-72.
343. Weksler, B.B., et al., *Blood-brain barrier-specific properties of a human adult brain endothelial cell line.* Faseb j, 2005. **19**(13): p. 1872-4.
344. Rahman, N.A., et al., *Immortalized endothelial cell lines for in vitro blood-brain barrier models: A systematic review.* Brain Res, 2016. **1642**: p. 532-545.
345. Osipova, E.D., et al. *Designing in vitro Blood-Brain Barrier Models Reproducing Alterations in Brain Aging*. Frontiers in aging neuroscience, 2018. **10**, 234 DOI: 10.3389/fnagi.2018.00234.
346. Miranda-Azpiazu, P., et al., *A novel dynamic multicellular co-culture system for studying individual blood-brain barrier cell types in brain diseases and cytotoxicity testing.* Scientific Reports, 2018. **8**(1): p. 8784.
347. Mantle, J.L. and K.H. Lee, *A differentiating neural stem cell-derived astrocytic population mitigates the inflammatory effects of TNF-α and IL-6 in an iPSC-based blood-brain barrier model.* Neurobiology of Disease, 2018. **119**: p. 113-120.
348. Appelt-Menzel, A., et al., *Establishment of a Human Blood-Brain Barrier Co-culture Model Mimicking the Neurovascular Unit Using Induced Pluri- and Multipotent Stem Cells.* Stem Cell Reports, 2017. **8**(4): p. 894-906.
349. Lippmann, E.S., et al., *A retinoic acid-enhanced, multicellular human blood-brain barrier model derived from stem cell sources.* Scientific Reports, 2014. **4**(1): p. 4160.
350. Appelt-Menzel, A., et al., *Establishment of a Human Blood-Brain Barrier Co-culture Model Mimicking the Neurovascular Unit Using Induced Pluri- and Multipotent Stem Cells.* Stem Cell Reports, 2017. **8**(4): p. 894-906.
351. Delsing, L., et al., *Barrier Properties and Transcriptome Expression in Human iPSC-Derived Models of the Blood-Brain Barrier.* Stem Cells, 2018. **36**(12): p. 1816-1827.
352. Vatine, G.D., et al., *Human iPSC-Derived Blood-Brain Barrier Chips Enable Disease Modeling and Personalized Medicine Applications.* Cell Stem Cell, 2019. **24**(6): p. 995-1005.e6.
353. Katt, M.E., et al., *The role of mutations associated with familial neurodegenerative disorders on blood–brain barrier function in an iPSC model.* Fluids and Barriers of the CNS, 2019. **16**(1): p. 20.

354. Lim, R.G., et al., *Huntington's Disease iPSC-Derived Brain Microvascular Endothelial Cells Reveal WNT-Mediated Angiogenic and Blood-Brain Barrier Deficits.* Cell Reports, 2017. **19**(7): p. 1365-1377.
355. Lee, C.A.A., et al., *Modeling and rescue of defective blood–brain barrier function of induced brain microvascular endothelial cells from childhood cerebral adrenoleukodystrophy patients.* Fluids and Barriers of the CNS, 2018. **15**(1): p. 9.
356. Iadecola, C., *The Pathobiology of Vascular Dementia.* Neuron, 2013. **80**(4): p. 844-866.
357. Jamieson, J.J., et al., *Role of iPSC-derived pericytes on barrier function of iPSC-derived brain microvascular endothelial cells in 2D and 3D.* Fluids and barriers of the CNS, 2019. **16**(1): p. 15-15.
358. Qian, T., et al., *Directed differentiation of human pluripotent stem cells to blood-brain barrier endothelial cells.* Science advances, 2017. **3**(11): p. e1701679-e1701679.
359. Weidenfeller, C., C.N. Svendsen, and E.V. Shusta, *Differentiating embryonic neural progenitor cells induce blood–brain barrier properties.* Journal of Neurochemistry, 2007. **101**(2): p. 555-565.
360. Canfield, S.G., et al., *An isogenic blood–brain barrier model comprising brain endothelial cells, astrocytes, and neurons derived from human induced pluripotent stem cells.* Journal of Neurochemistry, 2017. **140**(6): p. 874-888.
361. Cheung, C., et al., *Generation of human vascular smooth muscle subtypes provides insight into embryological origin-dependent disease susceptibility.* Nat Biotechnol, 2012. **30**(2): p. 165-73.
362. Lindskog, H., et al., *New insights to vascular smooth muscle cell and pericyte differentiation of mouse embryonic stem cells in vitro.* Arterioscler Thromb Vasc Biol, 2006. **26**(7): p. 1457-64.
363. Potjewyd, G., et al., *Tissue Engineering 3D Neurovascular Units: A Biomaterials and Bioprinting Perspective.* Trends in Biotechnology, 2018. **36**(4): p. 457-472.
364. Bernard-Patrzynski, F., et al., *Isolation of endothelial cells, pericytes and astrocytes from mouse brain.* PloS one, 2019. **14**(12): p. e0226302-e0226302.
365. Thomsen, L.B., A. Burkhart, and T. Moos, *A Triple Culture Model of the Blood-Brain Barrier Using Porcine Brain Endothelial cells, Astrocytes and Pericytes.* PLOS ONE, 2015. **10**(8): p. e0134765.
366. Canfield, S.G., et al., *An isogenic blood-brain barrier model comprising brain endothelial cells, astrocytes, and neurons derived from human induced pluripotent stem cells.* J Neurochem, 2017. **140**(6): p. 874-888.
367. Joutel, A. and F.M. Faraci, *Cerebral small vessel disease: insights and opportunities from mouse models of collagen IV-related small vessel disease and cerebral autosomal dominant arteriopathy with subcortical infarcts and leukoencephalopathy.* Stroke, 2014. **45**(4): p. 1215-21.
368. Wardlaw, J.M., et al., *Is Breakdown of the Blood-Brain Barrier Responsible for Lacunar Stroke, Leukoaraiosis, and Dementia?* Stroke, 2003. **34**(3): p. 806-812.
369. Anamnart, C., D. Songsaeng, and S. Chanprasert, *A large number of cerebral microbleeds in CADASIL patients presenting with recurrent seizures: a case report.* BMC Neurology, 2019. **19**(1): p. 106.
370. Yamamoto, Y., et al., *Brain Microvascular Accumulation and Distribution of the NOTCH3 Ectodomain and Granular Osmiophilic Material in CADASIL.* Journal of Neuropathology & Experimental Neurology, 2013. **72**(5): p. 416-431.
371. Mead, G.E., et al., *Severe ipsilateral carotid stenosis and middle cerebral artery disease in lacunar ischaemic stroke: innocent bystanders?* J Neurol, 2002. **249**(3): p. 266-71.
372. Wardlaw, J.M., et al., *Is breakdown of the blood-brain barrier responsible for lacunar stroke, leukoaraiosis, and dementia?* Stroke, 2003. **34**(3): p. 806-12.

373. Srinivasan, V., et al., *Genetic and environmental factors in vascular dementia: an update of blood brain barrier dysfunction.* Clinical and Experimental Pharmacology and Physiology, 2016. **43**(5): p. 515-521.
374. Greene, C. and M. Campbell, *Tight junction modulation of the blood brain barrier: CNS delivery of small molecules.* Tissue barriers, 2016. **4**(1): p. e1138017-e1138017.
375. Winkler, E.A., et al., *GLUT1 reductions exacerbate Alzheimer's disease vasculo-neuronal dysfunction and degeneration.* Nat Neurosci, 2015. **18**(4): p. 521-530.
376. Marco, S. and S.D. Skaper, *Amyloid beta-peptide1-42 alters tight junction protein distribution and expression in brain microvessel endothelial cells.* Neurosci Lett, 2006. **401**(3): p. 219-24.
377. Kook, S.Y., et al., *Aβ$_{1-42}$-RAGE interaction disrupts tight junctions of the blood-brain barrier via Ca^{2+}-calcineurin signaling.* J Neurosci, 2012. **32**(26): p. 8845-54.
378. Wan, W., et al., *Aβ(1-42) oligomer-induced leakage in an in vitro blood-brain barrier model is associated with up-regulation of RAGE and metalloproteinases, and down-regulation of tight junction scaffold proteins.* J Neurochem, 2015. **134**(2): p. 382-93.
379. Romanitan, M.O., et al., *Occludin is overexpressed in Alzheimer's disease and vascular dementia.* J Cell Mol Med, 2007. **11**(3): p. 569-79.
380. Li, F., et al., *Endothelial Smad4 Maintains Cerebrovascular Integrity by Activating N-Cadherin through Cooperation with Notch.* Developmental Cell, 2011. **20**(3): p. 291-302.
381. Stenborg, A., et al., *Impaired endothelial function of forearm resistance arteries in CADASIL patients.* Stroke, 2007. **38**(10): p. 2692-7.
382. Dichgans, M., et al., *Cerebral microbleeds in CADASIL: a gradient-echo magnetic resonance imaging and autopsy study.* Stroke, 2002. **33**(1): p. 67-71.
383. Pescini, F., et al., *Circulating Biomarkers in Cerebral Autosomal Dominant Arteriopathy with Subcortical Infarcts and Leukoencephalopathy Patients.* J Stroke Cerebrovasc Dis, 2017. **26**(4): p. 823-833.
384. Kisler, K., et al., *Pericyte degeneration leads to neurovascular uncoupling and limits oxygen supply to brain.* Nature Neuroscience, 2017. **20**(3): p. 406-416.
385. Joutel, A., *Pathogenesis of CADASIL: transgenic and knock-out mice to probe function and dysfunction of the mutated gene, Notch3, in the cerebrovasculature.* Bioessays, 2011. **33**(1): p. 73-80.
386. Joutel, A., et al., *The ectodomain of the Notch3 receptor accumulates within the cerebrovasculature of CADASIL patients.* The Journal of clinical investigation, 2000. **105**(5): p. 597-605.
387. Qin, W., et al., *Melatonin protects blood-brain barrier integrity and permeability by inhibiting matrix metalloproteinase-9 via the NOTCH3/NF-κB pathway.* Aging, 2019. **11**(23): p. 11391-11415.
388. Ayata, C., *CADASIL: experimental insights from animal models.* Stroke, 2010. **41**(10_suppl_1): p. S129-S134.
389. Huang, Z., et al., *Effects of cerebral ischemia in mice deficient in neuronal nitric oxide synthase.* Science, 1994. **265**(5180): p. 1883-1885.
390. Bentley, P., et al., *CADASIL with cord involvement associated with a novel and atypical NOTCH3 mutation.* J Neurol Neurosurg Psychiatry, 2011. **82**(8): p. 855-60.
391. Kelleher, J., et al., *Patient-Specific iPSC Model of a Genetic Vascular Dementia Syndrome Reveals Failure of Mural Cells to Stabilize Capillary Structures.* Stem Cell Reports, 2019.
392. Salloway, S. and J. Hong, *CADASIL syndrome: a genetic form of vascular dementia.* J Geriatr Psychiatry Neurol, 1998. **11**(2): p. 71-7.
393. Stenborg, A., et al., *Impaired Endothelial Function of Forearm Resistance Arteries in CADASIL Patients.* Stroke, 2007. **38**(10): p. 2692-2697.
394. Dubroca, C., et al., *Impaired Vascular Mechanotransduction in a Transgenic Mouse Model of CADASIL Arteriopathy.* Stroke, 2005. **36**(1): p. 113-117.

395. Neal, E.H., et al., *A Simplified, Fully Defined Differentiation Scheme for Producing Blood-Brain Barrier Endothelial Cells from Human iPSCs.* Stem cell reports, 2019. **12**(6): p. 1380-1388.
396. Kumar, A., et al., *Specification and Diversification of Pericytes and Smooth Muscle Cells from Mesenchymoangioblasts.* Cell reports, 2017. **19**(9): p. 1902-1916.
397. Li, X., et al., *Fast Generation of Functional Subtype Astrocytes from Human Pluripotent Stem Cells.* Stem Cell Reports, 2018. **11**(4): p. 998-1008.
398. Tao, Y. and S.-C. Zhang, *Neural Subtype Specification from Human Pluripotent Stem Cells.* Cell stem cell, 2016. **19**(5): p. 573-586.
399. Deli, M.A., et al., *Permeability studies on in vitro blood-brain barrier models: physiology, pathology, and pharmacology.* Cell Mol Neurobiol, 2005. **25**(1): p. 59-127.
400. Syvänen, S., et al., *Species differences in blood-brain barrier transport of three positron emission tomography radioligands with emphasis on P-glycoprotein transport.* Drug Metab Dispos, 2009. **37**(3): p. 635-43.
401. Lippmann, E.S., et al., *Modeling the blood–brain barrier using stem cell sources.* Fluids and Barriers of the CNS, 2013. **10**(1): p. 1-14.
402. Delsing, L., et al., *Models of the blood-brain barrier using iPSC-derived cells.* Molecular and Cellular Neuroscience, 2020. **107**: p. 103533.
403. Kim, Y.H., et al., *A 3D human neural cell culture system for modeling Alzheimer's disease.* Nat Protoc, 2015. **10**(7): p. 985-1006.
404. Kumar, A., et al., *Specification and Diversification of Pericytes and Smooth Muscle Cells from Mesenchymoangioblasts.* Cell Rep, 2017. **19**(9): p. 1902-1916.
405. Schiera, G., et al., *Permeability properties of a three‐cell type in vitro model of blood‐brain barrier.* Journal of cellular and molecular medicine, 2005. **9**(2): p. 373-379.
406. Al-Ahmad, A., R. Patel, and S. Raut, *PSEN1, but not PSEN2, mutation in familial form of Alzheimer's disease is associated with impaired barrier phenotype in a stem cell-based model of the blood-barrier.* 2019.
407. Zhang, Y., et al., *An RNA-sequencing transcriptome and splicing database of glia, neurons, and vascular cells of the cerebral cortex.* J Neurosci, 2014. **34**(36): p. 11929-47.